Rock Stability under Different Fluid Flow Conditions

by

Gang Han

A thesis
presented to the University of Waterloo
in fulfillment of the
thesis requirement for the degree of
Doctor of Philosophy
in
Chemical Engineering

Waterloo, Ontario, Canada, 2003

©Gang Han, 2003

I hereby declare that I am the sole author of this thesis. This is a true copy of the thesis, including any required final revisions, as accepted by my examiners.

I understand that my thesis may be made electronically available to the public.

Acknowledgements

This thesis would not be completed without acknowledgement of the efforts of those people who helped throughout this research. First I would like to thank my supervisor, Prof. Maurice B. Dusseault, for his consistent technical, moral, and financial support; for trusting my decisions and allowing me the flexibility to achieve my project goals. His efforts, enthusiasm, and encouragement motivated the author throughout the study.

Special thanks to the members of my PhD committee, Prof. John Chatzis, Prof. Leo Rothenburg, Prof. Mario Ioannidis, and Dr. Euripides Papamichos, for their technical help during my study, and for their critical reviews and useful suggestions on this thesis.

The author deeply appreciates the generous financial support from Schlumberger. In particular, I would like to thank Dr. Denis Heliot, Dr. Steve Chang, and Dr. John Cook from Schlumberger for having initiated this study, and Dr. John Cook, Dr. Hongren Gu, Dr. Chang Liu, and Dr. Ian Walton for providing valuable technical discussions and inspirations.

My extended gratefulness to the technical communications with Dr. Bernald Tremblay, Dr. Jian-Yang Yuan, and Dr. Ernie H. Perkins from Alberta Research Council, Dr. Luis C.B. Bianco from PetroBras, Dr. Neal Nagel from Philips Petroleum Company, and Dr. Andreas Kronenberg from Texas A&M University. Mr. Kirby Hayes' arrangement for my field study of sand production in Lloydminster oil fields is particularly recognized.

This thesis is dedicated to my great parents, Benli Han and Xiangdong Qi, and my beautiful wife, Xingmei Diao, for always being there

Abstract

It is widely known in oil industry that changes in fluid flow conditions such as water breakthrough or unsteady flow due to well shut-in can lead to sand destabilization, with a possible consequent sand production. In this research, different flow situations are incorporated into stress and stability analysis for the region around a wellbore producing oil from weak or unconsolidated sands, and the analyses involve strength weakening, stress redistribution, and decrease of rock stiffness.

Two main mechanisms, chemical reactions of rock with formation water and variations of rock capillary strength, are identified and analyzed to study strength weakening after water breakthrough, both qualitatively and quantitatively. Using theories from particle mechanics, rock mechanics, and interfacial science, four novel capillarity models are developed and verified to analytically capture the physical behaviors of capillary strength at the grain scale. Based on model calculations, significantly better understanding of strength behavior in two-phase fluid environments is achieved.

Based on a simplified model that can conservatively but efficiently quantify capillary strength with only two input parameters (i.e. particle radius and water saturation), a verified new method that physically calculates pore pressure in a multiphase environment, and a coupled poro-inelastic stress model, the redistributions of effective stresses with water saturation around a wellbore are solved. In terms of stress changes and growth of a plastic radius defining shear-failure zone, the effects of different stability factors, including capillarity through water-oil menisci, pore pressure changes due to the variations of fluid relative permeabilities, and loss of strength through chemical reactions of water-sensitive cementation materials, are quantified and compared in order to clarify when and how they contribute to sand production after water breakthrough.

The nonlinearities of rock elastic properties in stressed and biphasic fluid environments is analytically addressed, based on an improved nonlinear theory that considers both a failure-based mechanism and a confining-stress-based mechanism, the strength model, and the coupled stress model. The calculations demonstrate the redistributions of stress-dependent rock stiffness around a wellbore and its evolution with increase of water saturation, clarify the relative importance of each mechanism in reducing rock stiffness, and fundamentally explain why current predictive technologies are invalid when water appears in a flowing wellbore.

To quantify the effect of well shut-down on rock stability, the redistributions of fluid pressure in reservoir are analytically solved and coupled with the stress model, while the water hammer equations provide a boundary condition for the bottom-hole pressure. This approach allows direct solution of the relationships among fluid properties, rock properties and production parameters, within the context of rock stability.

The proposed new approaches and models can be applied to evaluate sand production risk in multiphase and unsteady fluid flow environment. They can also serve as points of departure to develop more sophisticated models, or to develop more useful constitutive laws for numerical solutions.

Nomenclature

a	Half distance between two particles, m
a_w	Wave speed of fluid transient, m/s
A	Area, m^2
A_{iw}	Area of wellbore internal cross-section, m^2
B_K	Bulk modulus, Pa
C	Rock compressibility, 1/Pa
C_{bc},	Effective bulk compressibility, 1/Pa
C_{bp}	Pesudo-bulk compressibility, 1/Pa
C_{pc},	Formation compaction coefficient, 1/Pa
C_{pp}	Effective pore compressibility, 1/Pa
C_l,	Fluid compressibility, 1/Pa
C_m	Rock matrix compressibility, 1/Pa
C_t	Formation total compressibility ($=\phi C_l + C_m$), 1/Pa
C_o	Cohesive shear strength, Pa
C_{o_ch}	Chemically reduced cohesive strength, Pa
C_{o_init}	Rock initial cohesive strength, Pa
D_{iw}	Internal radius of wellbore, m
D_φ	Change rate of friction angle with confining stress
D_v	Change rate of Poisson's ratio with confining stress
e	Thickness of tubing wall, m
E	Young's modulus, Pa
E_i, E_o	Young's moduli in reservoir conditions and at atmospheric pressure, Pa
f	Friction factor of tubing
f_w, f_o	Water and oil cuts in fluid production
F	Force, N
F_c	Cohesive capillary force, N
F_f	Fluid seepage force, N
F_v,	Viscous drag force, N
F_b	Buoyancy force, N
g	Gravity, m/s^2
G	Shear rigidity, Pa
h	Thickness of oil formation, m

H	Piezometric head, m
k	Permeability of reservoir, m^2
k_i	Initial reservoir permeability, m^2
k_{rw}, k_{row}	Water and oil relative permeabilities, m^2
$\overline{K}$	A parameter used in pressure calculation, $= \frac{Q\mu}{2\pi kh}$
L	Length of wellbore, m
n	Size ratio (the ratio of two particles radii)
	Total number of discrete length
P	Fluid pressure, Pa
P_1, P_2	Fluid pressures at inner (wellbore) and outer boundary of reservoir, Pa
P_a	Atmospheric pressure, Pa
P_w, P_O	Water and oil pressures, Pa
P_e, P_w	Pressures at external boundary and wellbore (used only in Chapter 6), Pa
ΔP	Pressure difference between two immiscible fluids, Pa
P_c	Capillary pressure, Pa
q	Production rate per unit thickness, m^2/s
Q	Production rate, m^3/s
Q_o, Q_w	Oil and water production rate, m^3/s
	Water volume in the liquid bridge, m^2
r	Radius of curvature of the liquid bridge in the vertical plane, m
	Radius from wellbore, m
R	The radius of particle spheres, m
R_1, R_2	Inner (wellbore) and outer boundary radii of reservoir, m
R_c	The critical radius defining the plastic zone, m
R_w, R_e	Wellbore radius and external radii, m
R_f	A parameter describing residual strength after stress reaches the peak
S	Specific surface area, 1/m
S_w, S_O	Water and oil saturations
S_{wc}	Connate water saturation
S_{oi}	Immobile oil saturation
u, v, w	Displacements in r, θ, z directions, m
V	Volume of the unit, m^2
V_b, V_p	Bulk and pore volumes, m^3

x_p, y_p	Spatial coordinates of point p(x,y), m
z	Vertical direction
	Depth from wellhead, m
α	Biot coefficient
β	Failure angle (= $\pi/4 + \varphi/2$), radian
β_v	The angle describing the extent of particle overlap, radian
β_w	Water volume angle, radian
ε	Normal strain
ε_r, ε_θ, ε_z	Normal strains in radial, tangential, and vertical directions
ε_v	Volumetric strain
ξ	Dimensionless radius
θ	Contact angle between fluid and solid, radian
λ	Lamé elastic constant
	Eigenvalue of first order Bessel function
	A factor accounting for non-uniform particle size effects on rock strength
χ	The ratio of interparticle space and the particle radius (= a/R)
η	A balance parameter (= ϕ^o/ϕ)
ρ	Material density, kg/m^3
γ	Surface-free energy of the material, N/m
	Surface tension between two fluids, N/m
μ	Fluid viscosity, Pa·s
ν	Poisson's ratio
ν_i, ν_o	Poisson's ratios at initial reservoir conditions and at atmospheric pressure
ω	Dimensionless time
σ	Total stress, Pa
σ'	Effective stress, Pa
σ'_1, σ'_2, σ'_3	Maximum, medium, minimum effective stresses, Pa
σ_r, σ_θ, σ_z	Total radial, tangential, and vertical stresses, Pa
σ'_r, σ'_θ, σ'_z	Effective radial, tangential, and vertical stresses, Pa
σ'_h	Horizontal effective stress in far field, Pa
σ'_e, σ'_p	Effective elastic and plastic stresses, Pa
σ_T	Tensile strength, Pa

σ_{UCS}	Uniaxial (unconfined) compressive strength, Pa
σ_m	Molecular cohesive strength, Pa
τ	Shear stress, Pa
Γ	Shear strain
φ	Internal friction angle, radian
φ_0	Friction angle at atmosphere pressure, radian
ϕ	Rock porosity
ϕ_i	Initial rock porosity
Φ	Dimensionless pressure

Table of Contents

Chapter 1 Introduction and Structure of Thesis

Each year, wellbore stability problems cost the petroleum upstream industry more than $6 billion US dollars (Powers, 2000). Starting from drilling operations, completion and production, workovers, to EOR (Enhanced Oil Recovery), oil operators have to expect various rock stability problems such as borehole breakout or collapse, sand production, formation compaction, casing shear, etc. Also, sand production is a common challenge, especially in unconsolidated and weakly consolidated sand where seventy percent of world oil production is achieved (Bianco and Halleck, 2001). Sand production is the main focus in this research.

Veeken et al. (1991) pointed out that unconsolidated sandstone reservoirs with permeabilities of 0.5 to 8 Darcy are the most susceptible to sand production, which may "…start during initial inflow or later, when reservoir pressure has fallen or when water breaks through". Despite insufficient studies of the mechanisms of sand failure, it is generally believed that the disturbance caused by drilling activities, wellbore introduction, workover operations, or production strategies leads to stress alterations in the formations near the well. After stresses are elevated above rock strength, failure (or fabric deterioration) occurs and fluid flow starts to erode and carry failed sands into the wellbore. Hence sand production can be divided into two processes: sand failure and failed sand transportation. In this research the first process is focused upon, involving strength weakening, stress overloading, and decrease of rock stiffness when fluid conditions vary from monophasic to biphasic, or from steady-state to unsteady-state flow. All of these are important aspects of sand production prediction.

1.1 Fundamental Theories and Concepts in Stability Analysis

Before discussing any details of rock stability, some important concepts and theories should be clarified and emphasized as their overuse and frequent misuse lead to a great deal of confusion (Dusseault et al., 1989).

1.1.1 Theory of effective stress

The most fundamental principle of soil mechanics is the Terzaghi principle of effective stress as defined by the following equations:

$$\begin{bmatrix} \sigma'_x & \tau_{xy} & \tau_{xz} \\ \tau_{yx} & \sigma'_y & \tau_{yz} \\ \tau_{zx} & \tau_{zy} & \sigma'_z \end{bmatrix} = \begin{bmatrix} \sigma_x & \tau_{xy} & \tau_{xz} \\ \tau_{yx} & \sigma_y & \tau_{yz} \\ \tau_{zx} & \tau_{zy} & \sigma_z \end{bmatrix} - \begin{bmatrix} P & 0 & 0 \\ 0 & P & 0 \\ 0 & 0 & P \end{bmatrix} \tag{1.1}$$

where σ is total normal stress, σ' is effective normal stresses, τ is shear stress, and P is pore pressure. The above equation expresses the principle that effective stresses are the difference between total stresses in the rock skeleton and pore pressure in the interconnected voids. The pore pressure must always act normal to the surface of sand particles because it is a hydrostatic force; therefore it contributes nothing to the shear stress that acts parallel to a plane.

In Petroleum Geomechanics, a form of $\sigma' = \sigma - \alpha P$ has generally been used, where α is called Biot's poroelastic constant. Physically it means that the rock skeleton carries the part σ' of the total external stress σ, while the remaining part, αP, is carried by the fluid in the porous medium. Expressed as $\alpha = 1 - \frac{C_m}{C_{bc}}$, ($C_m$ and C_{bc} are the compressibilities of rock matrix and rock bulk, respectively), α is extremely difficult to measure, given the inherently complex nature of a porous medium (Chen et al, 1995). However, α is restricted to the region $\phi < \alpha \leq 1$, and for unconsolidated or weak rocks, α is undoubtedly close to 1 (Fjær et al., 1992).

The concept of effective stress lays the foundation for rock stability investigation in reservoir conditions because it is effective stresses that eventually act on the rock particles (interparticle forces at the grain scale) to stabilize or mobilize them. Meanwhile the method that pore pressure effects, which may result from reservoir depletion, fluid saturation changes, adjustment of production strategy, and so on, are incorporated into stresses calculation reveals the importance of coupled analysis between fluid flow and rock stresses when issues of reservoir rock stability are involved. For example, it is found that the effective stress level at reservoir abandonment often will be approximately two times higher that that encountered at the start of production (Burton et al., 1998), and the increased effective stresses can result in shear failure of even well consolidated (strong) rock.

1.1.2 Stress components and equilibrium

For cases involving cylindrical or axial symmetry, e.g. stress and pressure analysis around a wellbore that penetrates an oil reservoir, the system of cylindrical coordinates r, θ, z are used, in which the stress components become

normal stresses: σ_r, σ_θ, σ_z

shear stresses: $\tau_{r\theta}$, τ_{rz}, $\tau_{\theta z}$

The components of strain are

$$\varepsilon_r = \frac{\partial u}{\partial r}; \qquad \varepsilon_\theta = \frac{1}{r}\left(u + \frac{\partial v}{\partial \theta}\right); \qquad \varepsilon_z = \frac{\partial w}{\partial z}$$

$$2\Gamma_{r\theta} = \frac{1}{r}\left(\frac{\partial u}{\partial \theta} - v\right) + \frac{\partial v}{\partial r}; \qquad 2\Gamma_{\theta z} = \frac{1}{r}\frac{\partial w}{\partial \theta} + \frac{\partial v}{\partial z}; \qquad 2\Gamma_{rz} = \frac{\partial w}{\partial r} + \frac{\partial u}{\partial z} \tag{1.2}$$

where ε and Γ are normal strain and shear strain, u, v, w are displacements in r, θ, z directions, respectively. The relations between stress and strain for an elastic material can be written as

$$\sigma_r = \lambda\Delta + 2G\varepsilon_r; \qquad \sigma_\theta = \lambda\Delta + 2G\varepsilon_\theta; \qquad \sigma_z = \lambda\Delta + 2G\varepsilon_z$$

$$\tau_{r\theta} = 2G\Gamma_{r\theta}; \qquad \tau_{\theta z} = 2G\Gamma_{\theta z}; \qquad \tau_{rz} = 2G\Gamma_{rz} \tag{1.3}$$

where Δ is volumetric strain that can be determined by

$$\Delta = \varepsilon_r + \varepsilon_\theta + \varepsilon_z = \frac{\partial u}{\partial r} + \frac{1}{r}\left(u + \frac{\partial v}{\partial \theta}\right) + \frac{\partial w}{\partial z} \tag{1.4}$$

In these expressions, λ and G are the Lamé elastic constants (G is also called shear rigidity), which can be related to Young's modulus (E) and Poisson's ratio (ν) by:

$$\lambda = \frac{E\nu}{(1+\nu)(1-2\nu)}, \; G = \frac{E}{2(1+\nu)} \tag{1.5}$$

Without fluid influence, the stress equilibrium equation in a 3-D cylindrical coordinate system can be written as (Jaeger and Cook, 1979)

$$\frac{\partial \sigma_r}{\partial r} + \frac{1}{r}\frac{\partial \tau_{r\theta}}{\partial \theta} + \frac{\partial \tau_{rz}}{\partial z} + \frac{\sigma_r - \sigma_\theta}{r} + \rho F_r = 0$$

$$\frac{\partial \tau_{r\theta}}{\partial r} + \frac{1}{r}\frac{\partial \sigma_\theta}{\partial \theta} + \frac{\partial \tau_{\theta z}}{\partial z} + \frac{2\tau_{r\theta}}{r} + \rho F_\theta = 0$$

$$\frac{\partial \tau_{rz}}{\partial r} + \frac{1}{r}\frac{\partial \tau_{\theta z}}{\partial \theta} + \frac{\partial \sigma_z}{\partial z} + \frac{\tau_{rz}}{r} + \rho F_z = 0 \tag{1.6}$$

where F is internal force and ρ is medium density. In 2-D situation, the above equations (without consideration of body force) can be simplified to:

$$\frac{\partial \sigma_r}{\partial r} + \frac{1}{r}\frac{\partial \tau_{r\theta}}{\partial \theta} + \frac{\sigma_r - \sigma_\theta}{r} = 0$$

$$\frac{\partial \tau_{r\theta}}{\partial r}+\frac{1}{r}\frac{\partial \sigma_{\theta}}{\partial \theta}+\frac{2\tau_{r\theta}}{r}=0 \tag{1.7}$$

This can be further simplified if only a 1-D axisymmetric situation is considered:

$$\frac{d\sigma_r}{dr}+\frac{\sigma_r-\sigma_{\theta}}{r}=0 \tag{1.8}$$

Replacing stresses in the equilibrium equation (Eq. 1.6) with Eq. (1.3) result in

$$(\lambda+G)\frac{\partial \Delta}{\partial r}+G\left\{\frac{\partial^2 u}{\partial r^2}+\frac{1}{r}\frac{\partial u}{\partial r}-\frac{u}{r^2}+\frac{1}{r^2}\frac{\partial^2 u}{\partial \theta^2}-\frac{2}{r^2}\frac{\partial v}{\partial \theta}+\frac{\partial^2 u}{\partial z^2}\right\}+\rho F_r=0$$

$$(\lambda+G)\frac{\partial \Delta}{r\partial \theta}+G\left\{\frac{\partial^2 v}{\partial r^2}+\frac{1}{r}\frac{\partial v}{\partial r}-\frac{v}{r^2}+\frac{1}{r^2}\frac{\partial^2 v}{\partial \theta^2}+\frac{2}{r^2}\frac{\partial u}{\partial \theta}+\frac{\partial^2 v}{\partial z^2}\right\}+\rho F_{\theta}=0$$

$$(\lambda+G)\frac{\partial \Delta}{\partial z}+G\left\{\frac{\partial^2 w}{\partial r^2}+\frac{1}{r}\frac{\partial w}{\partial r}+\frac{1}{r^2}\frac{\partial^2 w}{\partial \theta^2}+\frac{\partial^2 w}{\partial z^2}\right\}+\rho F_z=0 \tag{1.9}$$

For the 1-D case it can be rewritten as

$$\frac{d^2 u}{dr^2}+\frac{1}{r}\frac{du}{dr}-\frac{u}{r^2}=0 \tag{1.10}$$

In this research (Chapter 4), coupled stress approaches for 1-D studies around a wellbore will be developed based on Eq. (1.8) and Eq. (1.10).

1.1.3 Rock strength

Mechanical strength is the most crucial rock property in stability analysis, and it appears in different forms: uniaxial compressive strength (UCS), shear strength, tensile strength, and residual strength:

- As shown in Fig 1.1, a typical rock response to external uniaxial stress, UCS is the peak stress that rock can sustain during a uniaxial compression test with no lateral confinement. Usually, it is treated as a benchmark for sand stability because it is easy to measure. The higher the UCS value, the more stable sands are assumed to be.
- Another strength concept defined in the figure is the residual strength: the strength rock has left after losing its cohesive strength component. Its importance for rock stability analysis will be demonstrated in Chapter 5.

- Tensile strength prevents solids from being pulled apart by fluid flow or other driving forces from their original positions. For unconsolidated sand, it is usually negligible unless capillarity exists through fluid menisci acting on the particle-fluid contact surface, as it is shown that the magnitude of capillary force at least can match that of fluid seepage force (Han and Dusseault, 2002 a).
- Shear strength, also called compressive strength, is the maximum compressive stress that rock can sustain in uniaxial unconfined test. The resistive forces come from two contributions: one is the cohesive resistive force (cohesive strength); the other is the frictional resistive force (frictional strength). Cohesion comes from not only mineral cementation (e.g. quartz, calcareous, and ferruginous materials) and cohesive bonding (e.g. capillary force), but can also be related to the intergranular fabric, that is, the nature of the contacts among particles (i.e. interlocking leads to breakage of mineral grains before sliding can occur).

Rock strength is not a constant: it is affected by numerous internal factors, including grain size, mineral cement type, contact fabric (e.g. point contact, long contact…), original cracks and fissures, anisotropy, etc., as well as external conditions such as water saturation, stress state, loading path and so on. This leads to great difficulties in obtaining accurate rock strength data, especially for in-situ conditions.

Based on the magnitude of stress perturbation and its rate of change, strength determination can be divided into static (or experimental) methods and dynamic (or logging-derived correlation) methods. Usually both lab and wireline log data are incorporated if possible, since none of them could be claimed superior than the other. The most reliable approach is triaxial tests of core samples in laboratory. However it is time-consuming and costly, and the samples provided are always damaged to some unknown amount by stress relief.

Well logs can reflect the in-situ stress conditions and provide continuous curves that reveal strength trends of the formation. Unfortunately, since no logging tool directly yields static strength value, dynamic methods have to face formidable difficulties in order to interpret and calibrate the logs in terms of strength, and "…no one should be offended by the statement that it is far from being solved, even today." (Raaen et al, 1996) In case of a lack of both experimental and logging data, an analogue material from an existing database may be worth a try (Chalaturnyk et al., 1992).

1.1.4 Rock failure theory

Besides UCS and residual strength, there are several other important concepts defined in Fig. 1.1:

- Elastic region, within which rock will recover its original state if loading stress is relieved;
- Plastic region, where rock undergoes plastic or irrecoverable deformation, such as grain sliding and rearrangement, cementation breakage, fracture generation, grain crushing, etc.;
- Yield point, delineating the onset of plastic fabric changes and deviation of the stress-strain curve from elastic behavior (point A); and,
- Failure point, where the structure loses its designated functionality (point B). Clearly failure and yield are different concepts. For stability analysis, the accumulation of shear bands is a process of yield, but cannot be termed as failure until rock collapse and the loading stresses have shifted to the vicinity. All of these are important aspects of sand production prediction.

Corresponding to strength classifications, two types of rock failure are mainly expected in sand production scenarios: shear failure (also called compressive failure) and tensile failure. The former destroys most of the weak mineral bonds between particles and is largely blamed for rock cohesion loss, while tensile failure results in sand grains being plucked out of the rock skeleton at the low- or no-cohesion stage and those grains are carried by fluid flow into the wellbore. As a special form of tensile failure, the term "erosive failure" is sometime used to describe the transportation of disintegrated particles.

Numerous empirical criteria have been developed to describe the onset of rock failure, among which the Mohr-Coulomb failure criterion (M-C criterion) remains the most popular because it clearly captures and describes both frictional and cohesive strength factors in shear failure, and it is easy to apply and is relatively reliable (Fig. 1-2):

$$\sigma_1' = 2C_o \tan\beta + \sigma_3' \tan^2\beta \tag{1.11}$$

where C_o is cohesive shear strength, β is failure angle and is related to the friction angle (φ) through $\beta = \pi/4 + \varphi/2$. For a cylindrical wellbore system, maximum effective stress (σ'_1) and minimum effective stress (σ'_3) are usually effective tangential stress (σ'_θ) and effective radial stress (σ'_r), respectively.

There are, however, some controversial points about the M-C criterion:

- Mohr's circle analysis assumes that the intermediate principal stress (σ'_2) does not affect rock stability, which is not necessarily true;

- It neglects the development of microfractures and the gradual accumulation of damage before failure; and,
- It doesn't account easily for the case of a deviated hole with dipping formation beds passing through perforation tunnels at various angles (i.e. it is difficult to express the M-C criterion for the case of anisotropic rocks).

To overcome these limitations, other criteria have been developed. For example, the Drucker-Prager criterion considers the effect of intermediate principal stress:

$$(\sigma'_1 - \sigma'_2)^2 + (\sigma'_2 - \sigma'_3)^2 + (\sigma'_3 - \sigma'_1)^2 = C^2 \tag{1.12}$$

where C is a characteristic of the rock. The Griffith criterion was developed to study the stability of rocks where the yield and failure mechanisms are dominated by the development and coalescence of microcracks:

$$(\sigma'_1-\sigma'_3)^2 = 8\sigma_T(\sigma'_1+\sigma'_3) \qquad \text{if } \sigma'_1+3\sigma'_3 >= 0$$

$$\sigma'_3 = -\sigma_T \qquad \text{if } \sigma'_1+3\sigma'_3 < 0 \tag{1.13}$$

Tensile failure arises when the radial hydrodynamic drag force, i.e. the radial effective stress, exceeds the rock tensile strength σ_T, and is likely triggered exclusively by the case where the drawdown pressure P exceeds the tensile-failure criterion:

$$P - \sigma_r > \sigma_T \tag{1.14}$$

1.2 Structure of Thesis

1.2.1 Research goals

Most predictive models developed for sand production focus on the effect of steady pressure depletion in a monophase fluid environment. The effects of water breakthrough and unsteady flow on sand stability have been less studied and remain poorly quantified despite the fact that oil companies, on average, produce three barrels of water for each barrel of oil (Bailey et al., 2000), seventy percent of which comes from unconsolidated or weakly consolidated rock. Unfortunately those models are "…invalid when the well being analyzed produces free water…" (Ghalambor et al., 1994), and, to the author's knowledge, there is no analytical or numerical model for sand production when fluid flow becomes unsteady.

For the first time, based on experiment findings and field evidence, two important problems are comprehensively and analytically studied and answered in this research:

- Why does sand fail after water breakthrough?
- Why does sand fail after the well is abruptly shut down?

More specifically, for water effects on sand stability, new insights and quantifications of the following questions are addressed:

- Will rock strength be weakened after water breakthrough, and how?
- Will rock elastic properties such as Young's modulus and Poisson's ratio be altered by water, and how?
- How do stress-dependent porosity and permeability occur around the wellbore, and is it necessary to incorporate their effects into pressure calculations?
- How do effective stresses become redistributed with increasing water saturation?
- Why are current predictive models useless in the presence of water?
- What kind of role does capillarity play in stabilizing sand, and how to quantify it?
- What are the most important factors that should be accounted for in studying destabilizing of sand in a biphasic environment?

For the effect of unsteady pressure distributions on wellbore stability, a new framework is elaborated to tackle problems such as:

- How much hammer energy (in terms of pressure fluctuations) can be generated when a well is abruptly shut down?
- How much hammer energy can reach the bottom hole and propagate into reservoir?
- What are the possible magnitudes of stress and pressure fluctuations in the reservoir?

Those new findings can serve as a basis for developing new tools to evaluate sand stability in biphasic environments, when production strategies are adjusted, or for upgrading the current predictive tools to overcome their limitations. It should be noted that it is not the intention of this research to cover all the complicated processes of sand production as discussed in Chapter 2. For example, liquefied sand flowing with oil and water (three-phase flow) in a porous medium whose transport properties (e.g. porosity, permeability, etc.) and elastic properties (e.g. Young's modulus, Poisson's ratio, cohesive strength, etc.) are constantly changing with sand disintegration requires more intensive theoretical and experimental studies, and is not addressed in this research. Furthermore, the rigorous development of analytical or numerical relation for stress and the critical drawdown pressure at which an oil well will start to produce sand can be seriously compromised without adequate study of the physics of the sand failure phenomenon. Hence instead of using empirical approaches, which are commonly adopted by current oil industry, this

research leaves such issues for future exploration and focuses on rock failure processes that can be analyzed from a reasonably competent physical basis.

1.2.2 Steps and approaches

There are seven chapters in the thesis, throughout which new analytical approaches are pursued, based on current physical understanding and theoretical developments in analyses of rock strength, transport and elastic properties, pore pressure, and stresses.

Chapter 1 contains a fundamental knowledge review for rock stability analysis. Crucial concepts and theories are introduced with emphasis on fluid influence, such as effective stress theory, stress components and equilibrium in cylindrical coordinates, classification, influential factors, rock strength determination, and rock failure theory. Also, the research scope is defined, and the research goals and steps are clarified.

To better understand the importance of the studies, brief discussions of sand production scenarios and current prediction technologies are included in Chapter 2. After demonstrating the benefits and drawbacks associated with sand production, sanding mechanisms from sand failure to failed sand transport are discussed while the difference between the onset of sand failure and that of sand production is emphasized. A review of current prediction technologies and their limitations is briefly carried out.

Chapter 3 is dedicated to the study of strength variation with fluid saturation, as strength is treated as the most important rock property in stability analysis. After reviewing laboratory and field findings, geochemical reactions between rock and formation water and variations of capillary strength are discussed, both qualitatively and quantitatively. Inspired by theories from particle mechanics, rock mechanics, and interfacial science, five novel capillarity models are developed and verified to analytically capture the physical behaviors of capillary strength at the grain scale. Significantly better understanding of sand behavior is achieved, based on model calculations.

The appeal of these models is not fully revealed until a simplified capillary model is proposed in Chapter 4 for stress calculations. With only two parameters as input requirement (i.e. particle radius and water saturation), the model can conservatively but efficiently quantify capillary strength. More importantly in Chapter 4, based on a coupled poro-inelastic stress model, a pore pressure model, and a strength model, for the first time the redistributions of pore pressure and stresses around a wellbore after water breakthrough are solved. Combined with strength reduction mechanisms discussed in Chapter 3, these new results reveal the mechanisms

by which sand fails in two-phase fluid flow environments. In the stress models, different boundary conditions are compared and some inappropriate conditions that are currently used in geomechanics analysis are criticized. Based on the simplified capillarity model, pore pressure is calculated microscopically, and the results confirm the conventional pressure calculations in multiphase environments. Another important theoretical contribution in the chapter is the modelling of stress-dependent porosity and permeability around a wellbore. With input of different relations of compressibility and stress, the proposed method can depict stress-dependent conductivity properties for different types of rock. As an application, a new approach for unconsolidated sand is formulated based on nonlinear theory.

Chapter 5 investigates the nonlinearities of rock elastic properties in stressed and biphasic fluid environments. Nonlinear theories are classified and analyzed into two types: one is based on confining stress; the other is on shear damage. For the first time, with the aid of the stress models in Chapter 4, redistributions of rock stiffness around a wellbore with both stresses and fluid saturation are analytically delineated. Moreover, the calculations clarify the fundamental reasons why current predictive technologies are invalid when water appears in a flowing wellbore. The limitations of the models are discussed and recommendations are made regarding the method to incorporate rock nonlinearities into stress calculations.

A new framework to address the issues of unsteady flow is developed in Chapter 6. Three models, including a pressure wave model inside the wellbore, a pressure recovery model in the reservoir, and a model for stress fluctuations around the wellbore, are developed and interlaced through the variable of fluid pressure. By resorting to analytical and semi-analytical solutions, the new approach enables a direct relationship to be established among fluid properties, rock properties and production parameters. The mechanisms for rock failure after well shut-in, including shear stress elevation, seepage force increase, and cyclic fatigue, are elucidated.

Chapter 7 summarizes main theoretical developments and discoveries in this research. The two research goals, i.e. why sand fails after water breakthrough or after a well is abruptly shut down, are answered. The limitations of the models are restated and further improvements are recommended for future research.

1.3 Tables and Figures

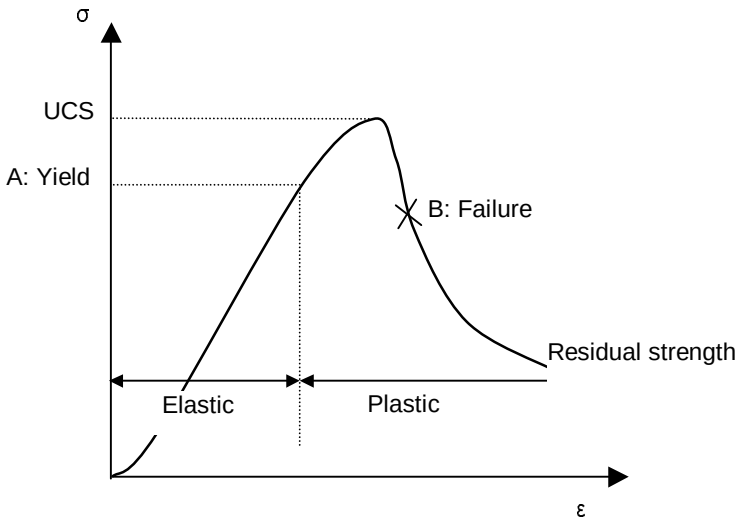

Fig 1-1: Stress vs. strain in a uniaxial compression test

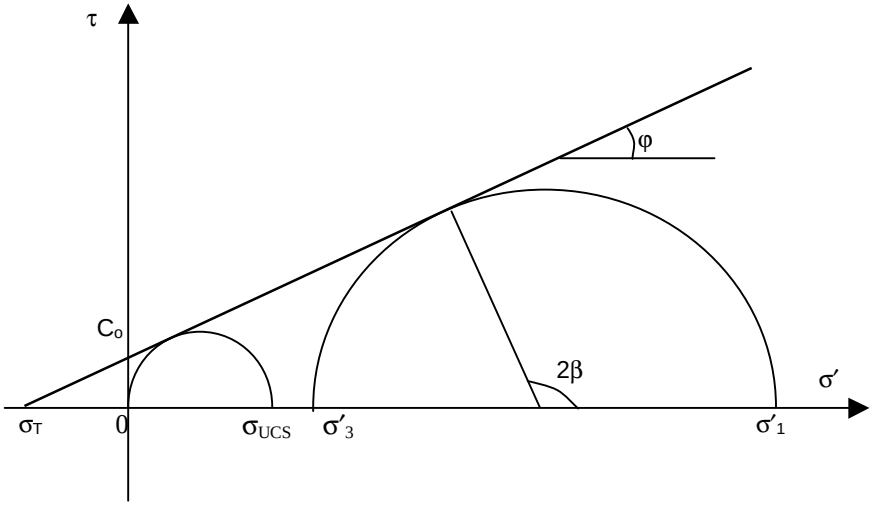

Fig. 1-2: Mohr-Coulomb criteria

Chapter 2 Sand Production and Prediction

2.1 Sand Production: a Benefit or a Nightmare?

For a long time, sand production becomes a cost source and a safety hazard for oil industry because it

- erodes equipment, include tubing, pump stator, surface pipes, valves, etc.;
- blocks wells such as tubing assemblage blocking and surface facilities plugging;
- leads to more workovers to replace or repair equipment or clean wells;
- decreases formation conductivity and therefore reservoir recovery efficiency;
- causes formation subsidence and casing collapse; and,
- generates additional need for sand disposal.

Many methods have been tried to prevent sand mobilization, which are referred to as "sand control". These exclusion methods range from chemical consolidation such as resin injection to physical exclusion methods such as slotted liners, prepacked screens, gravel pack placement, frac-and-pack treatments, etc. However, all these methods normally reduce well productivity and involve expensive workovers if problems arise. Thus, optimization of sand prediction techniques and their use in completion and production designs to minimize sanding risks have great economical value.

In the 1980s, people began to realize that sand production could lead to many benefits: in the heavy oil (10°-20°API gravity) deposits of Alberta (Canada), field cases show a significant boost in oil production because of sand production. For many oil wells in the Lloydminster region, a new concept of sand management, Cold Heavy Oil Production with Sand (CHOPS or CHOP), instead of sand control, has been widely and successfully implemented to keep heavy oil production economic. The benefits mainly result from (Dusseault and Santarelli, 1989):

- porosity and permeability enhancement from both sand subtraction from the matrix and the removal of negative permeability factors;
- increase of oil mobility and therefore production rate, from the relative velocity aspects of Darcy's law (if sand can move, resistance to liquid movement is reduced);
- foamy oil behavior (the exsolution and growth of gas bubbles in the oil); and,
- enlarged compressibility and porosity dilation, leading to formation compression.

What constitutes an acceptable level of sand production depends on how much sand will come out, what the benefit to oil production is, and operational constraints like tubular goods erosion, sand separator capacity, ease and cost of sand disposal, and the capability of artificial lift equipment to remove oil and sand from the well.

2.2 Mechanisms for Sand Production

Sand production involves many complicated processes such as stress concentrations and redistribution, shear dilation, strength weakening, non-linear elastic behavior, hydraulic erosion, solid transportation, sand recapture, stress arching, perforation blockage, failure propagation, etc. Most of these are not fully understood despite the tremendous efforts that have been devoted to them. Assuming that all processes involved are isothermal, brief discussions of each are carried out below.

2.2.1 First stage of sand production: sand failure

The introduction of a wellbore into an elastic formation leads to stress concentrations sketched in Fig. 2-1, calculated from the well-known Kirsch elastic solutions (Brady and Brown, 1985). Shear stress reaches a maximum in the formation adjacent to the wellbore, leading these sands to most likely experience shear failure and cohesion loss (damage). Furthermore, the maximum shear stress at the direction of $\theta = 0$ ($= 3\sigma'_1 - \sigma'_3$) will be always greater than the stress at the direction of $\theta = \pi/2$ ($= 3\sigma'_3 - \sigma'_1$); therefore, as shown in Fig. 2-2, the direction of $\theta = 0$ (i.e. σ'_3) is more favorable for shear failure in the form of shear bands, whereas the direction of $\theta = \pi/2$ (i.e. σ'_1) favors tensile failure in the form of extensional fractures normal to the cavity surface.

Kirsch's solutions assume rock is an elastic material and fluid flow has no influence on rock stability. In a real case when a critical stress (such as the one defined in the M-C criterion) is reached, the material will yield and behave plastically instead of elastically (Fig. 1-1). With increasing deformation, the strength of the material may be further reduced, but still can carry some load, which could restrict unimpeded sand movement toward the well. Thus there will be a gradual transition zone with reduced strength and stiffness and altered permeability, which is called the "Coulomb zone" and has been shown to usually exist around a wellbore or perforation channels by Bratli and Risnes (1981). The stresses, in contrast to Fig. 2-1 where they constantly decline with radius, first increase within the Coulomb zone before their difference reaches a maximum (Fig. 2-3), and then declines with radius.

When subjected to local shearing, the sand particles will rearrange themselves. Microscopically, two effects may occur: closure or shrinkage of voids or cracks (a process of volume decrease), or, on the contrary, opening of void space in the form of porosity or microfissures (a process of volume increase). The former is called compaction while the latter is called shear dilation (Fig. 2-4). Compaction makes the rock denser and stronger, thus it is a form of "work hardening". Even though expressed through a hardening parameter in plasticity theory (Fjær, 1992), it attracts less attention than shear dilation, mainly because it is a safe process, generally leading to strength enhancement and greater stability.

Shear dilation becomes of interest in sand stability analysis because, on one hand, it decreases rock strength and leads to larger deformations; and, on the other hand, it increases rock porosity and permeability (Wong and Li, 2000), enhances flow efficiency (Tronvoll and Fjær, 1994) and seepage force, and facilitates the detachment of particles from the rock skeleton. It is generally believed that dilation initiates after some initial compression and before total rock failure as the shear stress is increased. However, things are far from so simple: first, shear dilation and compaction may happen at the same time and volumetric and strength changes then are a conjunctive result of both; second, dilatancy depends on numerous factors such as rock type, confining stress, porosity, water saturation, temperature, and so on. Jaeger and Cook (1979) pointed out that dilatancy begins when stresses reach the value of about half the strength of the low-porosity rock, while Dusseault and Rothenburg (1988) suggested that it does not happen in high-porosity rock until it deforms 60% to 80% of the yield strain. Larsen et al. (1998) argued that the shear stress level for the onset of dilation (τ_{onset}) should satisfy

$$\tau_{onset} = A\sigma_{conf} + (B\phi_o + C)\sigma_{in-situ} \tag{2.1}$$

where A, B, C are constants, σ_{conf} is confining stress and $\sigma_{in\text{-}situ}$ is in-situ horizontal stress, in effective stress terms.

Dilation can cause two major changes of rock mechanical properties as damage accumulates: one is decreasing rock strength, which is called strength weakening; the other is increasing rock deformability or declining rock stiffness.

- As implied by the empirical correlation, $\sigma_{UCS}(MPa) = 258e^{-9\phi}$ (Sarda et al., 1993), the strength will drop as long as the porosity increases. Tronvoll and Fjær (1994) found in their experiments that under relatively low fluid flow rate conditions, even for ultra-weak sandstones with UCS of 1-2 MPa, material weakening is a necessary condition for the onset of sand production. But how much strength will be destroyed by shear distortion or dilation? It seems this has not been convincingly answered yet. Some empirical correlations of

strength and deformation used in the elastoplastic description of sand post-yield behavior may help, such as the one suggested by Van Den Hoek et al. (2000)

$$\tau_{strength}(\varepsilon_p) = \tau_o(1+\frac{\varepsilon_p}{a}) \qquad \text{for } 0 \le \varepsilon_p \le \varepsilon_p^{peak}$$

$$\tau_{strength}(\varepsilon_p) = \tau_{peak}(1-\frac{\varepsilon_p - \varepsilon_p^{peak}}{b}) \qquad \text{for } \varepsilon_p^{peak} \le \varepsilon_p \qquad (2.2)$$

where $\tau_{strength}(\varepsilon_p)$ is the rock shear strength changing with plastic shear strain ε_p; τ_o and τ_{peak} are the rock shear strength at the yield and peak, respectively; ε_p^{peak} is maximum shear strain at the peak stress; and, a and b are parameters calibrated from triaxial compression tests.

- Many rock properties such as Young's modulus, Poisson's ratio, bulk modulus, etc., are stress-sensitive. The detailed discussion and modelling of this phenomenon are included in Chapter 5. In general, corresponding to strength weakening, the Young's modulus and friction angle decrease while bulk modulus increases, which is called rock softening in this research. Even though strength weakening and rock softening are usually substituted for each other in current geomechanics analyses (e.g. Wang, 1990; Bradford and Cook, 1994; Van Den Hoek et al., 2000), both of them should be incorporated.

2.2.2 Sand failure is not the same as sand production

After rock is weakened enough and cannot support the original loads, shear failure may appear. However, failed sands (characterized by shear bands) will not flow into wellbore until fluid flow is able to disintegrate the particles from the rock skeleton, suspend them in a form of slurry (containing fluid and solids), and carry them through the porous formation that has changed dramatically from the original due to sand movement. In fact, the whole formation may be extruding plastically, or there may be channels that are carrying slurry to the wellbore. Also, the sand transport issue may be characterized by repeated episodes of capture and re-liquefaction of sand on its transit to the wellbore.

Fluid flow is an indispensable precondition for sand fluidization. After sand loses its cohesion in the process of shear failure, the rock may remain stable due to frictional strength and residual strength or capillary forces from fluid menisci between particles. If fluid is viscous and flowing, a driving force resulting from the gradient of pore pressure, called seepage force, becomes the main contributor to pluck particles out of the rock skeleton. Experiments show that, for a given flow rate, sand cavity growth progresses and then stabilizes while additional growth requires a further increase in pressure gradient (Bruno et al., 1996). Furthermore, progressive failure propagates parallel to the direction of fluid flow (Tronvoll and Fjær, 1994). Based on a

tensile failure criterion and Darcy flow law (Eq. 1.14), Bratli and Risnes (1981) calculated a critical production rate (q) at which the inner shell of a cavity (with radius of R_w) will start sanding, triggered by radial fluid flow:

$$\frac{\mu q}{4\pi k R_w} > 4C_o \tan\beta \tag{2.3}$$

Detached from the rock matrix, the sand particles will then flow toward the wellbore, carried by the fluid. Some of the particles may be recaptured when they pass through or interact with stable parts of the porous media: when the size of a pore throat is smaller than that of the particles suspended in the slurry flowing through the pores, the particles will be trapped locally. Also, the sand will gradually settle down and sediment into a more compact mass with renewed grain-to-grain contact (and therefore possible frictional strength) if the fluid flow cannot suspend them fully for their entire trip to the wellbore. These capture mechanisms may be described as (Zhang and Dusseault, 2000):

$$S_c(t) = -\alpha_c \phi \nabla P + \gamma\phi \frac{C}{\rho_s} \tag{2.4}$$

where α_c and γ are empirically determined parameters and ρ_s is solid density. It shows the amount of captured sands (S_c) is increased with the increase of porosity and sand content of the slurry (C), and decreased with fluid velocity (∇P).

Another significant post-failure process during sand production is sand arching. Hall and Harrisberger (1970) observed that under confining stress dry angular sand would form an arch, and a cohesive force resulting from a residual fluid saturation was necessary in a well-rounded sand to allow an arch to form. There are two places most likely for developing sand arches near the wellbore: one is around the perforation channel, especially around its tip where the radius of the cavity reaches the smallest value; the other is around the perforation hole in the casing, which could block the sand grains from being carried into the tubing as long as the arches are stable (Fig. 2-5). With the fluid rate increasing, the stability of arches has been increased to some extent too; then they become instable due to high dilation. When the porosity exceeds some critical point, i.e. porosity is in the range of 0.4 to 0.53 for different shapes of grains (Perkins and Weingarten, 1988), sand arches break and sands will flow into the wellbore with the fluid. After that, a new larger size arch will form and experience the same process. Besides flow rate, there are many other factors affecting arch stability, including stress level and distribution, particles' size and shape, fluid saturation, completion strategies and induced damage, arch size and perforation opening diameter, etc.

When the process arrives at a point where the pressure gradients and the stresses cannot stabilize an arch any longer, massive sand production is expected. The collapse-formation-collapse arching cycles fits well with the "sand burst" phenomenon (see Fig. 2-6) that happens quite often in both laboratory and the field (Veeken et al., 1991; Dusseault et al., 2000). Unfortunately, currently available technologies based on either continuum or non-continuum theories face serious challenges to mathematically describe sand bursts because they are chaotically episodic, and because the stability of arches is scale-dependent.

2.2.3 Failure propagation

How will the formation change after sanding initiation? This is a very controversial and obscure subject. Based on experiments and field experience, different damage evolution models have been proposed. transportation of disintegrated particles.

Enlarged and cone-shaped cavities shown in Fig. 2-7 are found in some experiments (Vaziri et al., 1997; Bianco and Halleck, 2001). The cavities grow upward due to gravity influence as failure propagates. After sufficient enlargement, separate perforation cavities may merge and form one bigger cavity round the wellbore. Some researchers claimed the existence of large cavities around wellbore by analyzing the changes in density log data (Edward et al., 1983) and inflow performance. Though the cavity assumption can lead to convenience, e.g. using effective wellbore radius to calculate well flow performance, it may only be valid when a bed with good cohesion exists above the cavities, e.g. shale or silt layer. For many CHOPS wells, geophysical data shows low seismic velocity zones that extend as far as 50 m or more. If it were a true cavity of 50 m diameter formed underground, it would definitely cause casing collapse or formation subsidence. Also it is unlikely that large cavities (greater than 5 – 20 cm?) in cementation-free sands could be indefinitely stable at depths of 500-1000 m.

Tubular piping channels, termed "wormholes", are reported in lab experiments during cold heavy oil production (Tremblay et al., 1999). As the wormhole is developing, the produced sand cut is high; when it reaches the fixed boundary, the sand cut decreases sharply because the wormhole has nowhere else to propagate. Two conditions must be fulfilled for wormhole propagation: first, the pressure gradient at the tip must be large enough to pluck the sand grains from the rock around it, which have already experienced shear failure; second, there must be enough pressure gradient distributed along the wormhole axis to carry the failed sands into the wellbore. Wormhole model can be classified into three types for modelling convenience: constant density, constant number, and combined model (Fig. 2-8). Some progress has been

made in numerical simulations to relate continuous sand production to wormhole propagation, such as by Yuan et al. (2000). However this model has never been conclusively confirmed by geophysical logging or well testing in field, while the experiment conditions such as boundary conditions or confining stress level for wormhole development in the lab are considerably different from reality. A simple calculation reveals its controversy: if 1000 m^3 volume of sands were produced from a CHOPS well, assuming the diameter of the wormholes is 0.05 m, there would be about 127 kilometers length of wormholes under the ground, which is obviously absurd.

Dusseault and Santarelli (1989) suggested a compact growth model for failure propagation in late stages of massive sand production (Fig. 2-9). Four regions have been classified according to rock behavior:

- Liquefied zone, where the sands have been disintegrated already and are being carried to the wellbore by oil in the form of slurry flow;
- Yielded zone, where rock has been yielded but not liquefied or suspended;
- Transition zone, where rock begins to elastically deform upon stress loading, but no plastic deformation occurs; and,
- Intact region, where rock remains in its original in-situ status and is not disturbed yet.

This model facilitates theoretical descriptions of sanding formation; for example, elastoplastic and poroelastic theories can be applied separately to the yielded zone and the transition zone. However, perhaps this model is only applicable for massive sand production in heavy oils and determination of the region boundaries will be very difficult.

Now the question "which one of those propagation models is true?" arises. Unfortunately, since no one can see the real case underground, each of those modes is possible, or they may appear as a combination, depending on rock strength and consolidation state, stresses level and direction, perforation pattern and density, rock anisotropy, fluid gradient, and so on. For example, if sand strength is low, i.e. loose sands, the wormholes maybe cannot stabilize themselves and a compact growth model or cavity model is more suitable; wormholes may occur around individual perforation channels if conditions can stabilize them but hardly be expected around an open hole or a densely perforated casing.

2.3 Current Predictive Techniques and their Limitations

Because of the complex and as yet unclear mechanisms, the diversities of reservoir and rock properties, and many other inherent uncertainties, the history of predictive models for sand

production is relatively short: only about 30 years. The goals of these models are to answer two questions that oil industry concerns most:

- When and why will the sand come out?
- How much sand will come out?

Solving the second question requires a three-dimensional description of failure propagation and other complicated post-failure processes discussed above, which is extremely difficult. Therefore, most efforts have been focused on the first question. A critical and brief review is carried out as follows.

2.3.1 Models based on continuum theories

Poroelastic and elastoplastic theories, expressed in terms of effective stresses, are two common approaches in geomechanics to describe underground stress and strain distributions. Since sand production involves many inelastic processes, elastic theory is considered too conservative (Veeken et al., 1989).

Elastoplastic theory arises from the separation of elastic strain ε_e, calculated by poroelastic theory, and plastic strain ε_p, determined by plastic theory, from the total strain ε: $\varepsilon = \varepsilon_e + \varepsilon_p$. Because it can describe some rock post-yield behaviors through the "plastic flow rule", especially strength evolution such as work hardening and strain weakening, many advanced predictive models are based on this technique (e.g. Morita et al., 1989; Bradford and Cook, 1994) even though it does not obey basic thermodynamical laws (Fjær et al., 1992). Unfortunately for the case of sand production around a well, the changes of rock properties (e.g. permeability, stiffness, etc.) during plastic deformation are neglected due to the increased difficulties in solving partial differential equations that may lead to numerical models of poor stability.

Nevertheless, facilitated with the Finite Element Method (FEM) and sophisticated computing technologies, some models can update rock properties at each iteration based on some empirical correlations (e.g. Vaziri, 1995; Chin et al., 2000). Because strain is the focus of these models, a critical strain (defined by Morita, 1989), above which sand production starts, replaces the failure criteria based on the critical stress developed by Bratli and Rinses (1981):

$$\varepsilon_c^p = \sqrt{\frac{2}{3}\left[(\varepsilon_{11}^p)^2 + (\varepsilon_{22}^p)^2 + (\varepsilon_{33}^p)^2\right]} \tag{2.5}$$

While it avoids physical descriptions of complicated failure processes, this type of model creates a big challenge for laboratory calibration before applying into the oilfield, as strain, a rock response to stress changes, is sensitive to many factors such as stress level, loading path, rate, and

history, sample size and shape, etc, which are hardly considered simultaneously during lab measurements.

Though many researchers have tried to extend elastoplastic theory by relaxing and accounting for the impaired assumptions, the theory becomes more and more complicated and thereby needs more and more parameters and calibrations:

- Papamichos and Vardoulakis (1993) proposed noncoaxial, kinematical-hardening flow theory to relax the coaxial assumption between the principal plastic strain difference and the principal stress directions. This introduces a new variable of relative stress describing the translation of the yield surface.
- A Cosserat continuum model was proposed to account for particle rotation effects (Mühlhaus and Vardoulakis 1987), but it needs the determination of an internal characteristic length.
- Continuum Damage Mechanics can successfully record the influence of loading history, using a damage parameter to 'remember' the changed status of the rock (Cheng and Dusseault, 2002), but the mathematical sophistications deter its further development and widespread adoption.

The main challenge when those theories are applied into field cases may be a lack of calibration and the amount of data required. It is useful to remember that plastic theory is essentially an empirical theory instead of the one based on precise descriptions of physical changes in the rock mass fabric. Therefore accuracy is not the only goal here: some balance should be involved, bearing practical available sources in mind.

2.3.2 Models based on non-continuum theories

Discrete Element Method (DEM) is closer to reality than any other approaches, through numerical simulating, at the grain scale, discrete particle behaviors of discontinuous systems such as porous media. Some DEM models can convincingly capture sand arching effects based on the description of local stress concentrations (Rothenburg and Bruno, 1997), while others are demonstrated to be promising to quantify post-failure sanding processes such as slurry flow (Zhang and Dusseault, 2000). But, studying rock behavior in great detail requires significant simplifications of particles (round or elliptic smooth surface) and structures, a huge amount of formation information, and a thorough understanding of failure mechanisms, which makes DEM models unrealistic for solving field problem such as sand failure prediction. These drawbacks limits them only to study of physical mechanisms and the evolution of rock fabric and anisotropy, and it appears that at some level, these must be accommodated into a continuum approach.

Strength-based models were once popular in 1970s and early 1980s, mainly because of their simplicity: sanding was assumed to start if the values of rock strength (Stein and Hilchie, 1972; Coates and Denoo, 1981) or strength-related rock properties (e.g. the ratio of shear modulus to bulk compressibility, Trixier et al., 1975) exceeded a certain limit. The simplification and lack of physics, on the other hand, greatly compromises the model applicabilities when unsteady or multiphase fluid conditions are involved, as neither stress nor fluid pressure is calculated at all.

Other approaches have been tried for sand production prediction, e.g. Artificial Neural Networks (ANN) (Kan and Roegiers, 1998), system dynamics theory (Chang, 2000), automaton theory, etc. These models are relatively new and still need a lot of improvements before they can gain any acceptance.

2.4 Summary

In this chapter, a brief review of sand production mechanisms and prediction technologies was carried out.

Sand production does not always mean a nightmare for the oil industry even though it causes a lot of problems. What constitutes an acceptable level of sand production depends on sanding amount, its effects on oil production, and operational constraints.

Even though many issues are unclear and controversial, sand production generally can be divided into two stages: first is sand failure, which involves complicated processes such as stress concentration, shear dilation, strength weakening, decrease of stiffness, and so on; then sand grains or groups of grains are detached from the rock skeleton as a result of erosional failure (liquefaction or fluidization), suspended and carried by fluid flow into the wellbore. More efforts should be devoted both at lab and in field to clarify how failure propagates (cavity, wormhole, compact growth, etc.), based on sanding rates that are quantified through careful monitoring strategies.

Many approaches have been developed to predict sand failure, based on continuum theories (poroelastic and elastoplastic) or non-continuum theories (e.g. DEM, ANN, strength-based models, etc.). Besides insufficient physical understanding and description, the main challenge for prediction technologies is finding a balance among accuracy, sophistication, and the resources needed to apply the models into the field (such as calibration efforts and the complexity of required inputs to the models).

2.5 Tables and Figures

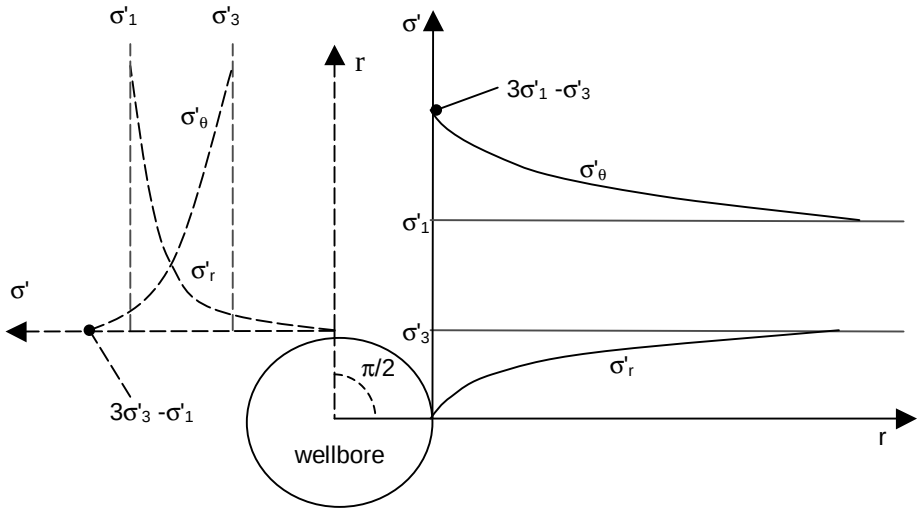

Fig. 2-1: Stress distribution in the directions of θ=0 and θ=π/2 around a cavity

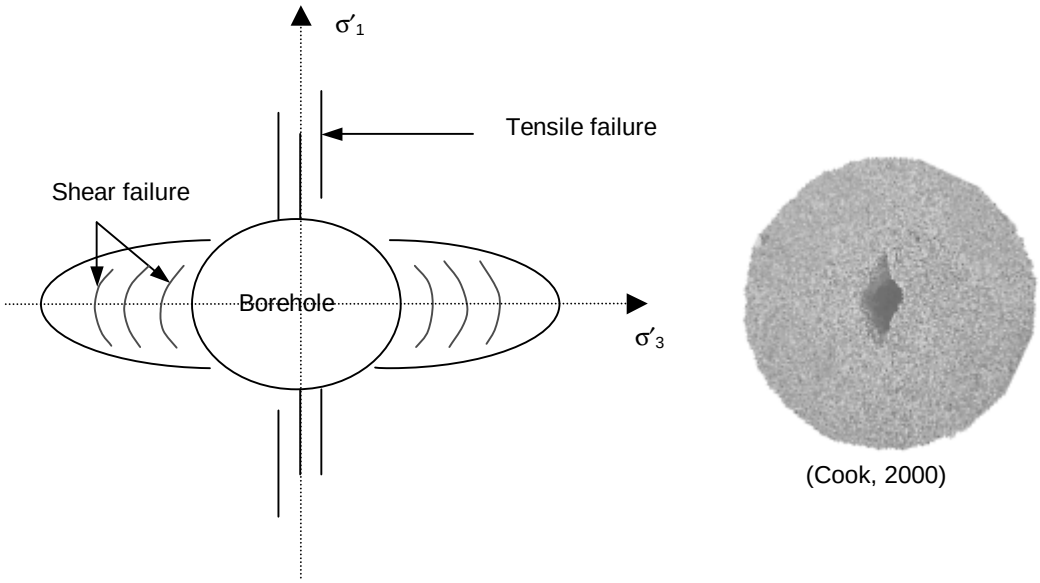

Fig. 2-2: Rock failure around a cavity

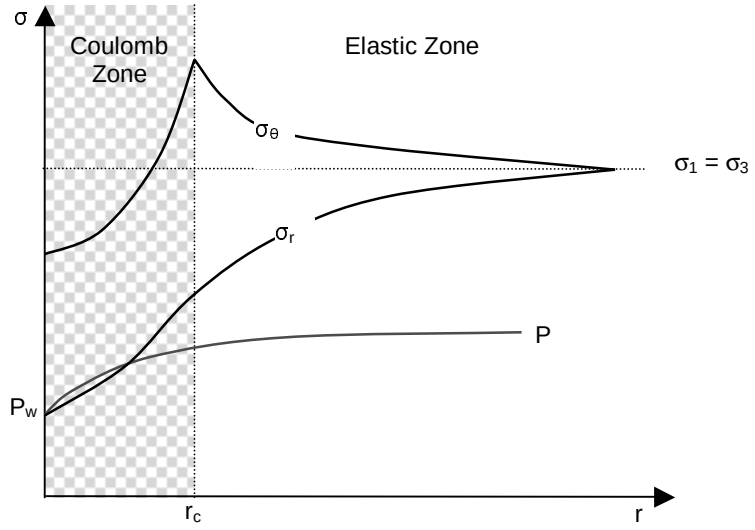

Fig. 2-3: Stress distribution in the Coulomb Zone
(After Bratli and Risnes, 1981)

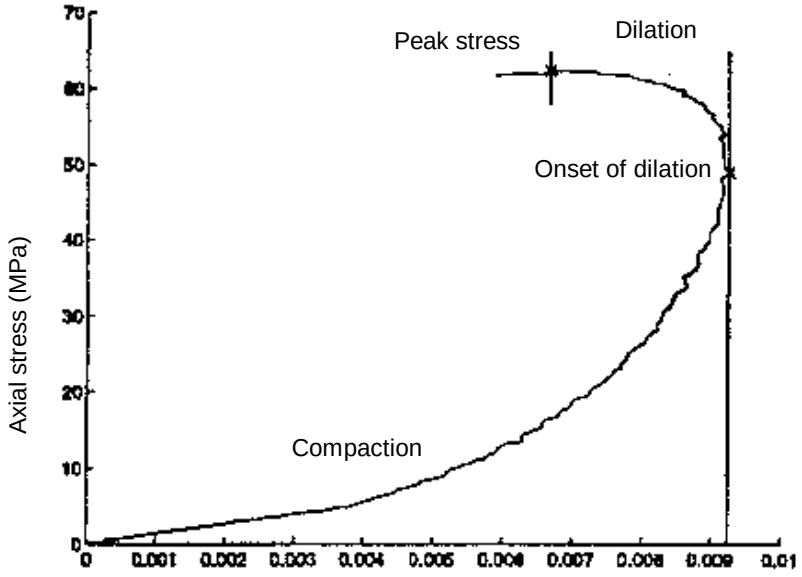

Fig. 2-4: Definition of Shear dilation (After Larsen et al., 1998)

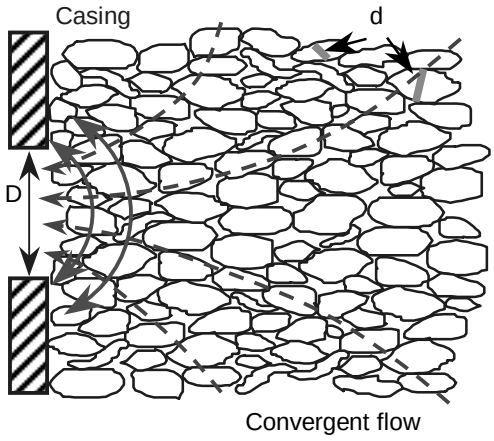

Fig. 2-5: Sand arching around a perforation hole
(After Dusseault, 2000)

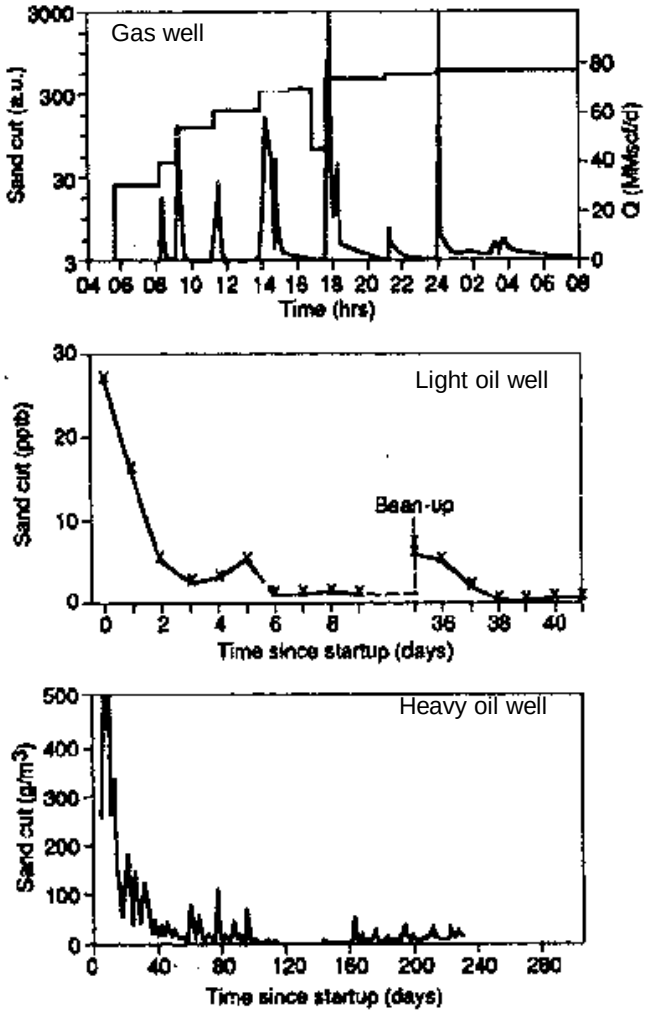

Fig. 2-6: Sand bursts for different reservoirs
(After Veeken et al., 1991)

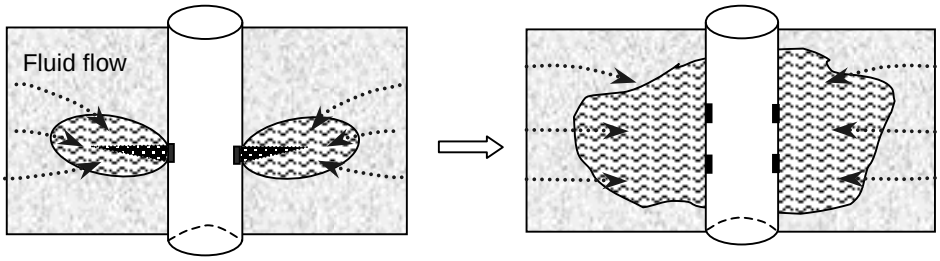

Fig. 2-7: Cavity model

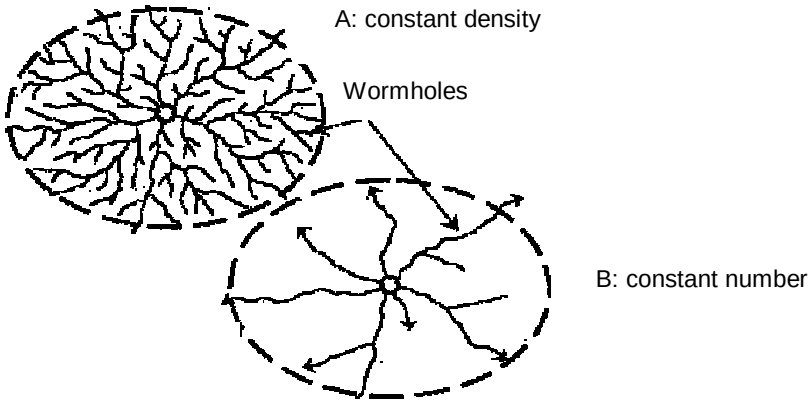

Fig. 2-8: Wormhole model

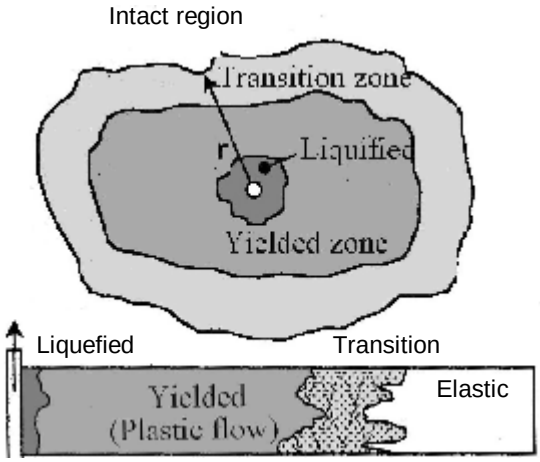

Fig. 2-9: Compact growth model (after Dusseault, 1989)

Chapter 3 Influence of Fluid Saturation on Rock Strength

Besides the contribution to effective stresses through the agency of fluid pressure, the fluid type and saturation may affect the rock strength. Along with the intrusion of more of the wetting fluids, e.g. formation water entering water-wetted but oil-saturated sand, which is the usual case in oil fields, the rock may become weaker and easier to fail. The main possible reasons are:

- Chemical reactions between water and solids and the dissolution of cementation materials may weaken the rock;
- Changes in the surface tension and capillary force may lower the cohesive strength;
- A higher pressure gradient may develop since the relative permeability of oil is decreased with the increase of water saturation. Therefore, there is a higher fluid velocity and drag force that may destabilize the sand, even though the viscosity of water is lower than oil; and,
- The particles plucked out of the rock skeleton by fluid flow and the swelling of clay materials may block pore throats and locally increase the pressure gradient and thus increase the destabilizing force.

The influence of water influx on sand stability has been realized for a long time, but few attempts have been made to quantitatively predict this influence, as compared with work on single-phase frictional sand production models (without capillarity). It will be extremely difficult to quantitatively describe all possible physical and chemical reasons. In this research, the first two reasons are discussed in detail, while the third will be addressed separately in the context of a geomechanical fluid model.

3.1 Experimental and Field Observations

3.1.1 Water-related sand production

Sand production with water ingress is a common problem in oil fields, especially for weakly consolidated sand and chalk reservoirs. Studies of 43 North Sea sand producers show that (Skjærstein et al., 1997):

- In 21% of the cases the onset of sand production coincided with the onset of water production, within a period of +/- 100 days (Fig. 3-1);
- For 70% of the wells, the onset occurred before that of water breakthrough; and,
- In only 9% of cases did the onset occurred more than 100 days after water breakthrough.

Also it was found that the average sanding rate during water breakthrough is higher than the one before breakthrough, while the average sanding rate 100 days after water breakthrough is the smallest (Fig. 3-2, Fig. 3-3). In Judge Digby Field (Louisiana, USA), some high-pressure-high-

temperature (HPHT) gas wells produced sand right after water production started, even though no wells experienced sanding under high levels of drawdown and flow rate (Vaziri et al., 2002).

Hall and Harrisberger (1970) (Test 11 and 12 in Table 3-1) showed that oil-water interfacial tension provided enough cohesion to stabilize a sand arch in flow tests. The arch was stable to outward flow of the non-wetting liquid phase (oil) at a limited rate at residual saturation of the wetting phase (water). However, outflow of the wetting phase (i.e. increase in wetting phase saturation) destroyed the arch. In sand cavity experiments (Bruno et al., 1996), it was found that the critical global pressure gradient that activates sanding dropped from 4 psi/ft to 2 psi/ft when water saturation was increased to 27%, compared with the irreducible water saturation (<23%). With further increases in water saturation to 30%, sanding occurred at a pressure gradient of 1 psi/ft. Furthermore, sanding appeared in an episodic manner: at a given flow rate and saturation condition, a sand cavity started to grow and then stabilized. Additional cavity growth required either an increase of pressure gradient or a change in water saturation.

3.1.2 Alteration of rock strength

Macroscopically, different rock behaviour before and after water breakthrough results from the changes of rock properties, including both deformation properties (e.g. Young's modulus, Poisson's ratio, bulk modulus, etc.) and rock strength properties. The detailed discussions of deformation properties are carried out in Chapter 5, while this chapter is dedicated to the study of rock strengths.

Many experiments have been done to study the changes of rock strength with water saturation (or moisture content). Parameters studied include uniaxial compressive strength (UCS), tensile strength, compressive strength, friction angle, etc. Different rock types have been tested, such as sandstone, chalk, and shale. Although there may be several physical and chemical processes involved, the general trend is that an increase in water saturation reduces rock strength.

Dube and Singh (1972) showed that the tensile strength of five different types of sandstone decreases from 11 to 48% of the dry strength under fully saturated conditions. Boretti-Onyszkiewicz (1966) tested the strength of five sets of sandstones parallel and perpendicular to the stratification and found that the compressive strengths of the water-saturated sandstones were about 7 to 46% lower than the ones in a dry condition (Table 3-2). In oil sands, the cohesive and UCS of water-saturated sand were determined to be 2.5 kPa and 16 kPa respectively, which are only 35% of the corresponding strength of water-wetted, oil-flooded sand of the same porosity (Tremblay et al., 1997). Colback and Wiid (1965) tested quartzitic shale and indicated that the UCS in the wet condition was approximately half of that in the dry condition (Fig. 3-4, Fig. 3-5). They believed the reduction in strength with increasing moisture content is primarily due to a

reduction in uniaxial tensile strength that in turn is a function of molecular cohesive strength of material. Skjærstein et al. (1997) found a UCS reduction of 50% due to brine saturation in triaxial compression tests on Red Wildmoor sandstone; their cavity failure tests indicate that this effect is more important than, for example, possible erosion effects (Table 3-3, Table 3-4).

While most strength parameters change with water saturation, the coefficient of internal friction, or frictional angle, is altered little or remains unchanged (Colback and Wild, 1965; Swolfs, 1972; Skjærstein et al., 1997): for different moisture contents the M-C envelopes are displaced parallel to each other (Fig. 3-6). However, some researchers (Gutierrez et al., 2000; Horn and Deere, 1962) found it varies with water saturation (up to 10°) if the rock surface chemically reacted with water, thus causing a change in the surface smoothness. Another interesting phenomenon is that the weakening is reversible: the data from the Pennant sandstone indicates that drying a previously saturated rock with a clayey matrix will lead to a significant increase in mechanical strength, provided that the rock had not been stressed up to the peak of the σ-ε curve whilst in a saturated state (Hadizadeh and Law, 1991).

The magnitude of strength changes with water saturation is closely related to rock lithology and mineralogy components. Hadizadeh and Law (1991) tested quartzitic ganister and sandstone under dry and water-saturated environment. There is little difference in mechanical behaviour between wet and dry Oughtibridge ganister (quartzite, Fig. 3-7), whereas a pronounced difference (around 100 MPa) in uniaxial strength between water-saturated and oven-dried sandstone specimens was observed at all stress rates: the wet rock strength is about 55% of the dry one (Fig. 3-8). They believed the difference mainly comes from the fact that quartz grains in ganister are bonded by epitaxial quartz cement overgrowths. In contrast, for Pennant sandstone, the matrix, forming 25% of the rock and composed of clay mineral, is locally cemented by ferruginous and calcareous material.

3.2 Possible Chemical Reactions of Formation Water and Sand

Sandstone is a type of formation-water-compatible agent since it lives with formation water for a long time during digenesis, i.e. formation water is in a state of chemical equilibrium relative to its original environment. However, as a powerful chemical agent, if water moves into a new environment, because of different compositions, density, or concentrations of active ions such as sodium, potassium or carbonate, etc., chemical reactions and physical changes have to take place in order to reach a new equilibrium.

Chemical reactions can be divided into two types: one group is interaction between rock skeleton and water; the other is between cementation minerals and water. Both of them could

play a role in the reduction of rock stability either through decreasing the rock strength or increasing the acting force (pressure drawdown). There are two limiting cases for water-sensitive cementation: they take part of the loads from the skeleton, or else they form only as bridges among the particles and do not appreciably share in the compressive load carrying capacity. For example, in Red Wildmoor sandstone (Skjærstein et al., 1997), X-ray diffraction (XRD) analysis of the fine-grained fraction shows a Smectite/Illite content of 72%, which acts partly as a cementation bond between grains and is very water-sensitive. For this case, a much lower rock strength is expected after water breakthrough because the bridges will become weaker; thus, it becomes much easier to release the particles from their original positions.

3.2.1 Formation water analysis

Most rocks in their natural environment contain water and salts in solution. The aqueous phase occurs either as free pore fluid, as absorbed water on grain boundaries and fracture surfaces, or as an impurity within the atomic structure of constituent minerals (Swolfs, 1972). The mobilized water during oil production comes mainly from water-bearing formations in the area surrounding the oil reservoirs, and is driven into the oil reservoirs by pressure drawdown during depletion. The formation waters range widely in composition (Perkins, 2001), from quite dilute (e.g. 1000 mg/l Total Dissolved Solid) to near salt saturation (>200,000 mg/l TDS). Compositionally, they are generally sodium chloride based solutions, but many have potassium, calcium or magnesium as the main cations, and sulphate, bicarbonate, or carbonate as the dominant anions.

Costin (1987) suggested that in most rocks absorbed and free water held along grain boundaries and in pores will be readily available for transport to crack tips, thus facilitating stress corrosion weakening at all applied strain rates. Similarly, results from Pennant sandstone demonstrated that water held within the clay matrix would be available to enter intergranular crack tips at all times (Hadizadeh and Law, 1991).

3.2.2 Quartz hydrolysis and water-related actions

For sand reservoirs, the main mineral is almost always quartz; furthermore, quartz overgrowths are common as cementation. There are several possible reactions that may happen when quartz contacts with invading formation water. Swolfs' (1972) summary noted that that formation water with solutions of aluminium and ferric iron salts react with quartz and silicates, weakening the surface silicon-oxygen bonds by hydrolysis, and reducing surface energy and cohesion. The common mode of hydrolysis is:

$$\text{-Si-O-Si-} + H_2O \rightarrow \text{-Si-OH} + \text{HO-Si-}$$

The -Si-O-Si- bridges break up into two silanol groups: -Si-OH and OH-Si-. In such a hydrolysed bridge, the hydrogen bond is weaker by an order of magnitude than the Si-O bond, and this is believed to be the source of the hydrolytic weakening. Since all silicates have -Si-O-Si- or -Si-O-M bridges (where M is a metal ion) that are susceptible to this type of hydrolysis, this water weakness may apply to silicates in general. Griggs (1967) tested different silicates, e.g. feldspar, olivine, hypersthene, tourmaline and beryl, and found that the rock strength in wet experiments was always about an order of magnitude weaker than the dry experimental strength.

Though hydrolysis occurrence and rate depend on the temperature, for example in Griggs' experiments the temperature was usually from 200°C to 500°C, which is too high compared with the typical reservoir situation, high in-situ stresses may trigger the occurrence of silicate hydrolysis in reservoir. Furthermore, it is believed that the hydrolysed bridges and dislocations do not of themselves cause weakening (Griggs and Blacic, 1965). Based on the assumption that "…the easy glide which occurs in the hydrolytic state can only occur when the hydrolysed dislocation can move by exchanging hydrogen bonds with a neighbouring silicon-oxygen bridge which has become hydrolysed", the weakening process is shown to be as follows:

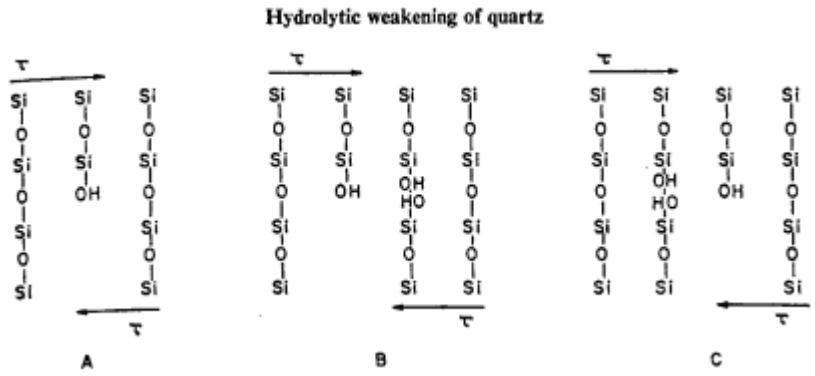

Frank-Griggs model of dislocation motion by hydrolysis and hydrogen bond exchange

Besides hydrolysis, quartz may participate in other forms of reactions under certain conditions in reservoirs.

- In steamflood processes, quartz and other minerals can generate smectitic minerals through the reaction:

$$\text{Quartz} \pm \text{Kaolinite} + \text{Siderite} + Na^+ + H_2O = \text{smectite} + H^+ + CO_2(g)$$

Even small amounts of smectite (<5%) can dramatically reduce the permeability (1-2 orders of magnitude, Nadeau, 1990) and rock strength, since smectite has high surface area, good stability, and a propensity to migrate and block pore throats. However, the reaction will apparently not happen if the temperature is under 150°C (Keith et al., 1998).

- Geochemical reactions in fault zones are generally fluid-induced and tend to soften and weaken the zones. Breaking down the relatively strong feldspars to easily deformable and sliding mica is the main reason. The possible hydration reactions are (Christoffersen, 1995):

$$\underset{\text{(microcline, or orthoclase)}}{3KAlSi_3O_8} + 2H^+ = \underset{\text{(muscovite, or sericite)}}{KAl_3Si_3O_{10}(OH)_2} + 6SiO_2$$

$$\underset{\text{(albite)}}{3NaAlSi_3O_8} + K^+ + 2H^+ = \underset{\text{(muscovite or sericite)}}{KAl_3Si_3O_{10}(OH)_2} + 6SiO_2 + 2K^+$$

$$\underset{\text{(microcline or orthoclase)}}{2KAlSi_3O_8} + 5Mg^+ + 8H_2O = \underset{\text{(clinochlore)}}{Mg_5Al_2Si_3O_{10}(OH)_8} + 3SiO_2 + 2K^+ + 8H^+$$

$$\underset{\text{(microcline or orthoclase)}}{KAlSi_3O_8} + 3Mg^{++} + 4H_2O = \underset{\text{(muscovite or sericite)}}{KMg_3AlSiO_{10}(OH)_2} + 6H^+$$

However, those reactions need a long time and should not be considered in the time frame of sand production issues (Kronenberg, 2001).

3.2.3 Carbonate dissolution

Carbonate minerals in reservoir rock exist either as a rock mass like chalk, oolitic strata, limestones and dolomite or as a cementation material in sandstone. The effect of chemical reactions between calcareous material and formation water on rock stability can be significant: chemical reactions may dissolve rock cementation, collapse the rock skeleton, and thus change the pore structures and rock properties (Brignoli et al., 1994; Papamichos et al., 1997; Lord et al., 1998; Gutierrez et al., 2000).

Chemically, calcareous minerals react with water in a form of

$$CaCO_3^- + H^+ \Leftrightarrow Ca^{2+} + HCO_3^- + e^-$$

where H^+ may originate from:

$$H_2O + CO_2 = H_2CO_3$$

$$H_2CO_3 \Leftrightarrow H^+ + HCO_3^-$$

$$HCO_3^- \Leftrightarrow H^+ + CO_3^{2-}$$

The overall rate of calcite dissolution depends on the activities at the calcite surface area and is given by (Plummer et al., 1978):

$$\text{Rate} = k_1(H^+) + k_2(H_2CO_3) + k_3(H_2O) - k_4(Ca^{2+})(HCO_3^-)$$

where k_i are rate constants. Therefore, to calculate the rate, the surface area and the activities of each item (in the brackets) at the surface area are needed.

3.2.4 Ferruginous deposits and clay swelling

In the normal pH range of formation water (pH = 5-8), dissolved iron is present as Fe^{2+}, whereas Fe^{3+} is essentially insoluble (Appelo and Postma, 1993). Therefore, ferruginous cement will most likely remain stable (relatively insoluble) as formation water comes in, while for formation water itself, since iron is a common constituent, the chemical reaction may occur as:

$$Fe^{2+} + 3H_2O \Leftrightarrow Fe(OH)_3 + 3H^+ + e^-$$

That is, there may be some Fe^{3+} deposits in the pore system arising from invading formation water.

Clay usually tends to deposit in the voids among rock particles rather than being a part of the cement deposited near grain contacts; therefore it carries little to no load and does not directly contribute to the strength decrease by water weakening. However, the existence of clay, even in small fractions, increases the strength of silicate rock substantially. Also, when in contact with water, the swelling behaviour of smectite clay makes it an important factor in rock failure. The swelling clay volume decreases the path diameter (permeability) for fluid flow and increases the local pressure drawdown, which can cause increased seepage forces to destabilize sand. Consequently, sand production may be more easily triggered by water breakthrough in clay-cemented materials if there are enough clay-sensitive cations in formation water.

3.2.5 Effects on rock surface energy and strength

Before continue the discussion, some concepts must be clarified. As discussed above, weakening of the sand skeleton (largely SiO_2) may result from the changes of bond type by hydrolysis. In order to describe the relationship between bond strength and a rock's ability to resist deformation, a term in material mechanics is introduced: the surface free energy (or surface energy). It is a measure of the work required to produce a unit area of surface of solid (or fluid) by a reversible and isothermal process; this means surface energy can be only measured in a totally inert environment, e.g. under high vacuum. In fluid mechanics, another similar concept is widely used: the surface tension, a tension per unit length along an arbitrary line on the surface. In a coherent set of units, it must be equal to the work done in creating a unit area of free surface of a fluid (Rowlinson and Widom, 1982). In this research the concept of surface energy is restricted to rock (solid) while the concept of surface tension is reserved for fluid.

The effect of all surface-energy related interactions is defined as the "Rebinder effect". For sandstone, the effect mainly refers to hydrolysis of silicon dioxide and dissolution of carbonate cement (since both ferruginous deposition and shale swelling tend to locally increase driving pressure instead of decreasing rock strength). As a matter of fact, liquids that wet the rock

surface invariably decrease the surface energy of the rock (Vutukuri et al. 1974). For example, the surface energy of dry quartz is estimated to be 1×10^{-4} Jcm^{-2} (Dunning, 1983), whereas in a H_2O environment it becomes 7.15×10^{-5} Jcm^{-2} when the work of absorption is -2.85×10^{-5} Jcm^{-2} (Young and Bush, 1960) or 8.25×10^{-5} Jcm^{-2} when the work of absorption is -1.75×10^{-5} Jcm^{-2} (Schuyler et al., 1982).

Rabinowicz (1965) and Brace (1963) have called attention to the close relation of surface energy and strength parameters, e.g. hardness, cohesive strength, tensile and compressive strength, etc. All available data indicate that the breaking strength of rocks, in a similar way as surface tension, is lower if measured in chemically active fluid environments than in dry or inert ones (Swolfs, 1972). There are some empirical relations that have been established between two quantities. For example, fracture will occur when the tensile stress exceeds (Griffith, 1924):

$$\sigma_T = \sqrt{\frac{2\gamma E}{\pi c}} \tag{3.1}$$

where σ_T is tensile strength, γ is the surface-free energy of the material, E is Young's modulus, and c is the length of an interior or surface crack. In a similar way, Orowan (1949) defined the molecular cohesive strength, σ_m, of an elastic material as:

$$\sigma_m = \sqrt{\frac{2\gamma E}{a}} \tag{3.2}$$

where a is the space between neighbouring atomic planes. Colback and Wiid (1965) showed that UCS is inversely proportional to the surface tension of different liquids into which specimens were submerged (see Fig. 3-9) as the immersion fluid can reduce rock surface energy and hence its strength.

3.2.6 Possibility to quantify those phenomena

In order to quantify the influence of those reactions on rock stability, attention must be focused on critical issues. The first issue is choosing the most important "part" of the rock with respect to rock strength. Because loading stress tends to concentrate around the boundaries of rock particles while the connection between cement and rock particles is usually the weakest part of rock, the cementation part plays a more important role than the rock skeleton in resisting failure, unless there is very little cement in the rock (e.g. an unconsolidated sand) and crushing occurs. Slight changes in cement strength may result in significant changes in rock behaviour. Griggs and Blacic (1965) found that even if only small proportion of the silicon-oxygen bonds are weakened by hydrolysis, e.g. fewer than 1 percent, significant weakening will be expected if these hydrolysed bridges are located in the cementing minerals.

For cementing agents, as discussed above, the mechanisms accounting for possible water-weakening reactions are various: quartz hydrolysis decreases rock strength through reducing the bond energy of silica to hydrogen; calcareous cement is dissolved into the water and physically changes the shape and size of cement; both new ferruginous material forming in the rock pore system and clay swelling will locally increase the driving force and therefore the rock instability. Additionally, those reactions can easily reach a geochemical equilibrium state within the time period of sand production.

However, even with the assumption that the change in cementation is a dominant factor in rock instability, and there are mainly three types of possible chemical reactions, rigorously quantifying those mechanisms with respect to sand instability is extremely difficult or impossible for a number of reasons.

- The speed and effects of reactions depend not only on the types, amount, and distribution of rock minerals and the active chemical ions, salinity, and concentrations of formation water, but also on the environment such as temperature, pressure, etc. As an illustration, the speed could range from seconds to months or even years for equilibrium within the range of conditions found in reservoirs (Perkins, 1997), and their effects may become significant in steamflood conditions in contrast to ordinary reservoir conditions (Keith et al., 1997). Nevertheless, time factors in chemical reactions may be the reason why some North Sea sand producers (about 9%) did not produce any sand until sometime (more than 100 days) after water breakthrough.
- There are several factors affecting the changes of both surface energy and rock strength, including:
    - type and strength of particle bonds, density of bonds per unit area;
    - structural resistance of the grain surfaces or boundaries to the rearrangement of the surface atoms (e.g. high friction angle); and,
    - presence and locations of defects such as cracks.

Unfortunately none of these factors can be mathematically described.

Nevertheless, as an important effect resulting from water-rock interactions, surface energy could serve as a simulation tool to justify the analytical results developed next, in order to match the sophisticated reservoir situations. Furthermore the description of possible reactions between cementation materials and water still could be useful as a reference. For example, if there is no calcareous or silicate cement in the rock (e.g. unconsolidated sand), the reduction of rock strength in a short period most likely comes from capillary force changes, which can be quantitatively studied.

3.3 Mathematical Models for Capillarity

Besides chemically or physically weakening the rock, two-phase fluids in porous media, such as oil and water, oil and gas, or gas and water, result in the generation of liquid menisci among particles where capillary forces cohesively bond particles, acting like a weak cementation. While some doubt the significance of capillary effect on rock stability (Lord et al., 1998), many people believe capillarity plays an important role in sand production after water breakthrough into an oil well (Papamichos et al., 1997; Bianco and Halleck, 2001; Vaziri et al., 2002). However, none of the current modelling techniques can convincingly capture the rock physics involved (i.e. changes of rock strength and elastic properties with fluid saturation).

Although there are clear practical difficulties in developing analytical or semi-analytical models in particulate systems, there are also important practical merits in pursuing such solutions. In the grain capillarity models that are described below, a quantitative description of how rock capillary strength behaves is undertaken. This is formulated at the grain-scale level, with various fluid properties (water saturation, surface tension, and contact angle), rock properties (grain size, contact fabric, and grain heterogeneity), and deformations (compaction and extension).

3.3.1 Basic model: uniform particles contacting tangentially

Before further discussion, some capillary concepts must be clarified. Capillary pressure, the most commonly used concept in capillarity, refers to the pressure difference across the free surface formed between wetting and non-wetting fluid phases; capillary force is a cohesive force that results from capillary pressure and acts on the surface of particles surrounded by liquid bridges; capillary strength is a part of rock strength resulting from the cohesive capillary forces thereby generated between solid particles. To simplify the problem, a water-wetted but oil-saturated rock is envisioned, but any two-phase system (e.g. gas-oil, gas-water, air-oil) can be treated similarly.

3.3.1.1 Capillary strength

The rock tensile strength can be related to cohesive force F_c of a single bond in the following manner (Schubert, 1984):

$$\sigma_T = \lambda \frac{1-\phi}{\phi} \frac{F_c}{4R^2} \tag{3.3}$$

where R is the radius of solid spheres representing particles, ϕ is rock porosity, σ_T is tensile strength, and λ is a factor accounting for non-uniform particle size effects on total rock strength. A value of λ = 6~8 is suggested for packs of particles with a narrow size range, and λ=1.9~14.5 for packs with wider particle size distributions (Schubert, 1984). The above equation is based on several assumptions (Schubert, 1975; Capes, 1980):

- A large number of bonds exists in the stressed cross-section, and the stresses are transmitted by liquid bridges at the contact points of the particles;
- A statistical distribution of bonds at different directions in space exists over the cross-section;
- The particles consist of a large number of monosized spheres that are randomly distributed in the agglomerate (i.e. there are no preferred fabric directions);
- The bond strength between individual particles can be replaced by a mean value that is statistically applicable throughout the whole assembly (homogeneity); and,
- The number of contact points between one particle and its neighbours (k) can be correlated directly with porosity as an approximation: $k\phi \approx \pi$. (Rumpf, 1962).

Based on a Mohr-Coulomb criterion, UCS can be approximately expressed as (Fig. 1-2)

$$\sigma_{UCS} = 2\sigma_T \frac{\sin\varphi}{1-\sin\varphi} \tag{3.4}$$

where φ is the friction angle. Substituting Eq. (3.3) into (3.4), the UCS can be expressed as a function of cohesive force F_c:

$$\sigma_{UCS} = \lambda \frac{1-\phi}{\phi} \frac{\sin\varphi}{1-\sin\varphi} \frac{F_c}{2R^2} \tag{3.5}$$

which illustrates, for unconsolidated sand, that rock strength is related to rock porosity, friction angle, the particle size, and the cohesive force in single capillary bonds.

3.3.1.2 Capillary forces

There are several methods to describe cohesive forces resulting from capillary pressure:

- Gillespie (1967) and Marmur (1993) proposed that the cohesive force results from the pressure difference ΔP (also called as capillary pressure P_c) between two fluids:

  $$F_c{}^o = \pi(R\sin\beta_w)^2 \Delta P \tag{3.6}$$

  where R is the radius of solid spheres and β_w is the wetting fluid volume angle (Fig. 3-11).
- Schubert (1984) and Lazzer et al. (1999) believed that besides the pressure difference across the free surface, there is another vertical component of the surface tension forces acting tangentially to the interface along the contact line, $F_s = 2\pi x_p \gamma \sin(\beta_w + \theta)$, where θ is contact angle, and x_p is the x-coordinate of point p (Fig. 3-11). In this case, the cohesive force will be:

  $$F_c = \pi(R\sin\beta_w)^2 \Delta P + F_s \tag{3.7}$$

Mason and Clark (1965) used the middle point (b) of the curvature to replace the contact point between solid and liquid (p), and derived:

$$F_c = \pi x_b^2 \Delta P_b + 2\pi x_b \gamma \tag{3.8}$$

where x_b is the x-coordinate of point b, and ΔP_b is the pressure difference at the point.

- Hotta and Takeda (1974) considered the influence of gravity forces by introducing an additional item, $F_G = \frac{1}{3}\rho g R^3 \sin^2\beta_w(\tan^2\frac{\beta_w}{2} + 2\sin^2\frac{\beta_w}{2})$, into Eq. (3.8):

$$F_c = F_c^{\ o} + F_s - F_G \tag{3.9}$$

However this gravity influence may be neglected if the particle size d < 1 mm (Schubert, 1984). Therefore, in the following research, the gravity influence on capillary force is not taken into account. As for the discrepancy between Eq. (3.6) and Eq. (3.8), both of them will be used to calculate the cohesive forces before arriving at a conclusion as to which one is more preferred in rock stability analysis.

3.3.1.3 Capillary pressure

Now the focus is turned to the calculation of the pressure difference ΔP. Though the Laplace-Young equation relates the mean curvature of the liquid bridge to the pressure deficiency, it cannot be solved analytically (Hotta et al., 1974):

$$\frac{\Delta P}{\gamma} = \frac{d^2y/dx^2}{[1+(dy/dx)^2]^{3/2}} - \frac{1}{y[1+(dy/dx)^2]^{1/2}} \tag{3.10}$$

The most widely accepted simplification is to assume that the shape of the liquid bridge is a toroid characterized by a radius r (Fig. 3-11). Therefore the pressure difference can be

$$\Delta P = \gamma(\frac{1}{r_1} - \frac{1}{r}) \tag{3.11}$$

, where r_1 is the radius of curvature of the liquid bridge at point q in the horizontal plane ($r_1 = x_p - r + r\sin(\beta_w)$), and r is the radius of the curvature in the vertical plane going through the axis of symmetry. The precision of the toroidal approximation is within 10% of the value obtained by numerical solution of the Laplace-Young equation (Lian et al., 1993).

Replacing ΔP in Eq. (3.8) by Eq. (3.11), the complete description of the cohesive forces can be derived:

$$F_c = \pi x_p^{\ 2}\gamma(\frac{1}{r_1} - \frac{1}{r}) + 2\pi x_p \gamma \sin(\beta_w + \theta) \tag{3.12}$$

In this equation, r_1, r, α and θ are unknown factors that are correlated with each other in a geometrical way. The coordinates of point p are:

$$x_p = R\sin\beta_w \; ; \; y_p = R - R\cos\beta_w \tag{3.13}$$

The radius of curvature at the free interface between the two fluids is:

$$r = \frac{R - R\cos\beta_w}{\cos(\beta_w + \theta)} \tag{3.14}$$

If the wetting phase in the unit cell is only filled in the liquid bridge (i.e. low water saturation), the water saturation is equal to the ratio of the volume of liquid bridge to the void volume ($V\phi$):

$$S_w = \frac{4[x_p y_p - (A_1 + A_2)]}{V\phi} \tag{3.15}$$

where

$$A_1 = \frac{\beta_w}{2}R^2 - \frac{1}{2}(R - y_p)x_p$$

$$A_2 = (\frac{\pi}{4} - \frac{\beta_w + \theta}{2})r^2 - \frac{1}{2}y_p r\sin(\beta_w + \theta) \tag{3.16}$$

Since the contact angle θ is solely determined by rock and fluid properties instead of water saturation, it is reasonable to assume $\theta = 0$, i.e. the rock is fully wetted by water (which appears to be an excellent assumption for the great majority of unconsolidated sandstone reservoirs). The areas A_1 and A_2 then become:

$$A_1 = \frac{1}{2}R^2(\beta_w - \cos\beta_w \sin\beta_w) \tag{3.17}$$

$$A_2 = (\frac{\pi}{4} - \frac{\beta_w}{2})R^2(\frac{1-\cos\beta_w}{\cos\beta_w})^2 - \frac{1}{2}R^2\frac{(1-\cos\beta_w)^2}{\cos\beta_w}\sin\beta_w \tag{3.18}$$

Substituting Eqs. (3.13), (3.14), (3.17), and (3.18) into Eq. (3.15), a relationship between the volume angle of wetting liquid (water) and water saturation is established:

$$\frac{V\phi S_w}{4R^2} = -\frac{\beta_w}{2} + \frac{1}{2}\tan\beta_w + (\frac{\beta_w}{2} - \frac{\pi}{4})(\frac{1-\cos\beta_w}{\cos\beta_w})^2 \tag{3.19}$$

If the unit studied is defined as in Fig. 3-12 (2D), its volume (area) will be $4R^2$, and the above equation will become:

$$\phi S_w = -\frac{\beta_w}{2} + \frac{1}{2}\tan\beta_w + (\frac{\beta_w}{2} - \frac{\pi}{4})(\frac{1-\cos\beta_w}{\cos\beta_w})^2 \tag{3.20}$$

However, taking Fig. 3-13 into account, the porosity of the unit is easily determined as a constant: $\phi^o = 1 - \frac{\pi R^2}{4R^2}$ = 0.2146. This obviously conflicts with the real situation where porosity is a variable. The conflict results from the simplification of the defined model: i.e. identical spheres contacting tangentially. In order to get rid of this conflict and match the "real" microscopic porosity, a balance parameter, $\eta = \phi^o/\phi$, has been introduced into Eq. (3.20):

$$\eta\phi \cdot S_w = -\frac{\beta_w}{2} + \frac{1}{2}\tan\beta_w + (\frac{\beta_w}{2} - \frac{\pi}{4})(\frac{1-\cos\beta_w}{\cos\beta_w})^2 \tag{3.21}$$

Corresponding to each value of water saturation, the water volume angle (β_w) can be analytically determined, as well as the toroid radii of curvature (r, x_p), the capillary pressure (Δp), and the capillary strength (in terms of tensile strength and UCS) resulting from capillary cohesive forces.

3.3.1.4 Contact angle (θ)

When the contact angle θ is not zero, Eq. (3.17) and Eq. (3.18) will be:

$$A_1 = \frac{1}{2}R^2(\beta_w - \cos\beta_w \sin\beta_w) \tag{3.22}$$

$$A_2 = (\frac{\pi}{4} - \frac{\beta_w + \theta}{2})R^2\frac{(1-\cos\beta_w)^2}{\cos^2(\beta_w + \theta)} - \frac{1}{2}R^2\frac{(1-\cos\beta_w)^2}{\cos(\beta_w + \theta)}\sin(\beta_w + \theta) \tag{3.23}$$

Therefore Eq. (3.21) could be rewritten as:

$$\eta\phi \cdot S_w = -\frac{\beta_w}{2} + \sin\beta_w - \frac{1}{4}\sin 2\beta_w - [\frac{\pi}{2} - (\beta_w + \theta) - \frac{\sin 2(\beta_w + \theta)}{2}] \cdot \frac{(1-\cos\beta_w)^2}{1+\cos 2(\beta_w + \theta)} \tag{3.24}$$

Also, the principal radius r_1 can be expressed as $r_1 = x_p - r + r\cdot\sin(\beta_w+\theta)$.

3.3.2 Non-uniform particles contacting tangentially

Assuming the contact angle $\theta = 0$ and the particles are tangentially in contact, for particle 1, the coordinates of contact point P_1 are (see i) in Fig. 3-13)

$$x_1 = R\sin\beta_{w1}; \qquad y_1 = r\cos\beta_{w1} \tag{3.25}$$

while those of contact point P_2 for particle 2 are

$$x_2 = nR\sin\beta_{w2}; \qquad y_2 = r\cos\beta_{w2} \tag{3.26}$$

where n is the ratio of two particle radii, and α_1, α_2 are water volume angles of particle 1 and particle 2, respectively. From triangle O_1O_3C, the distance between the x-axis and point O_3 is $\Delta y = (R+r)\cos\beta_{w1} - R$, comparing with $\Delta y = nR - (nR+r)\cos\beta_{w2}$ established in triangle O_1O_2C. The relation of r, β_{w1}, and β_{w2} can thus be determined as

$$(n+1)R = (R+r)\cos\beta_{w1} + (nR+r)\cos\beta_{w2} \tag{3.27}$$

Based on the cosine rule for Triangle $O_1O_2O_3$, the relationship between α_1 and r can be

$$\cos\beta_{w1} = \frac{1+\frac{1-n}{1+n}\cdot\frac{r}{R}}{1+\frac{r}{R}}, \text{ or } r = \frac{1-\cos\beta_{w1}}{\cos\beta_{w1}-\frac{1-n}{1+n}}\cdot R \tag{3.28}$$

Substituting r from Eq (3.28) into Eq (3.27), the relationship between two water volume angles (β_{w1}, β_{w2}) can be determined as

$$\cos\beta_{w2} = \frac{(n^2+1)\cos\beta_{w1} + (n^2-1)}{(n^2-1)\cos\beta_{w1} + (n^2+1)} \tag{3.29}$$

The water volume in the unit cell (see ii) in Fig. 3-13) is equal to the one determined by water saturation, i.e. $V\phi S_w$, where $V\phi$ is the porous volume of the unit

$$V\phi = 2(1-\frac{\pi}{4})\cdot(1+n^2)R^2 \tag{3.30}$$

Hence

$$V\phi S_w = R^2(n+1)(r/R+1)\sin\beta_{w1} - R^2(\beta_{w1}+\beta_{w2}\cdot n^2) - (\pi-(\beta_{w1}+\beta_{w2}))r^2 \tag{3.31}$$

where r, β_{w2} can be expressed by β_{w1} through Eqs. (3.28) and (3.29). Corresponding to each saturation, the liquid bridge radius r can be explicitly determined by Eq (3.28).

In order to determine capillary pressure from Eq. (3.11), the other radius of the liquid bridge (r_1) must be specified. Neither x_1 nor x_2 is suitable since the capillary pressure should be uniform inside the liquid bridge. In this model, the point Q where the interface crosses the x-axis is selected as a "median" point of the bridge, while its x coordinate, $r_1 = (R+r)\sin\beta_{w1} - r$, will served as its "median" radius. Therefore the capillary force can be expressed as

$$F_{ci} = \pi x_i^2 \Delta p \quad (i = 1,2) \tag{3.32}$$

F_{c1}, F_{c2} are the capillary forces acting on the interfaces between particle 1 and the liquid bridge and between particle 2 and the liquid bridge, respectively. Because the capillary bond always

breaks at the weakest part, the smaller capillary force, i.e. $\overline{F_c} = F_{c2}$, should be selected as the value used in the following equation

$$\sigma_T = \lambda \frac{1-\phi}{\phi} \frac{F_{c2}}{4\overline{R}^2} \tag{3.33}$$

where $\overline{R} = (R + nR)/2$.

3.3.3 Detached uniform particles

Besides tangential contact, there are many other possible contact fabrics between particles, such as floating contact, sutured contact, convex-concave contact, and long contact, as summarized by Taylor (1950) and shown in Fig. 3-14. Because fluid tends to fill out any void space regardless its shape, contact fabrics can be generalized in two microscopic cases for the purpose of capillarity analysis: the particles are detached from each other, which may simply be an artifact of the sampling and preparation procedure, or squeezed and overlapped to form convex-concave contacts and long contacts.

Fig. 3-15 illustrates two detached particles. Assuming two identical particles and a contact angle $\theta \neq 0$, the coordinates of point p are

$$x_p = R\sin\beta_w \; ; \; y_p = R + a - R\cos\beta_w \tag{3.34}$$

where a is the half distance between the particles. The radius r can be expressed as

$$r = \frac{R + a - R\cos\beta_w}{\cos(\beta_w + \theta)} = \frac{1 + \chi - \cos\beta_w}{\cos(\beta_w + \theta)} \cdot R \tag{3.35}$$

where χ is the ratio of interparticle space and the particle radius, i.e. χ = a/R. Therefore A_1 and A_2 in Eq. (3.15) can be rewritten as

$$A_1 = \frac{\beta_w}{2} R^2 - \frac{1}{2}(R + a - y_p)x_p \; ; \; A_2 = (\frac{\pi}{4} - \frac{\beta_w + \theta}{2})r^2 - \frac{1}{2} y_p r \sin(\beta_w + \theta) \tag{3.36}$$

where the porosity ϕ^o of the unit (the shaded area in part ii) of Fig. 3-15) is

$$\phi^o = 1 - \frac{\pi R^2}{2R \cdot (2R + 2a)} = 1 - \frac{\pi}{4(1+\chi)} \tag{3.37}$$

Consequently, Eq. (3.15) becomes

$$(1+\chi)\left[1 - \frac{\pi}{4(1+\chi)}\right] S_w = -\frac{\beta_w}{2} + (1+\chi)\sin\beta_w - \frac{1}{4}\sin 2\beta_w$$

$$-\left[\frac{\pi}{4}-\frac{\beta_w+\theta}{2}-\frac{1}{4}\sin 2(\beta_w+\theta)\right]\left[\frac{1+\chi-\cos\beta_w}{\cos(\beta_w+\theta)}\right]^2 \qquad (3.38)$$

When the contact angle $\theta = 0$, the above equation becomes

$$(1+\chi)\left[1-\frac{\pi}{4(1+\chi)}\right]S_w = -\frac{\pi}{4}+(1+\chi)\sin\beta_w-\left(\frac{\pi}{4}-\frac{\beta_w}{2}-\frac{1}{4}\sin 2\beta_w\right)\left[\left(\frac{1+\chi}{\cos\beta_w}\right)^2-\frac{2(1+\chi)}{\cos\beta_w}\right] \qquad (3.39)$$

Combining with Eqs. (3.6), (3.3) and (3.5), capillary strength (and force) can be determined.

3.3.4 Squeezed uniform particles

When two particles are squeezed together due to overburden pressure or tectonic movement (Fig. 3-16), another angle β_v, which accounts for the extent of particle overlap, is introduced to calculate the relationship between water saturation and water volume angle β_w. In the figure, β_v can be determined by

$$\beta_v = \arccos(1-\chi) \qquad (3.40)$$

where $\chi = a/R$. The other required parameters can be written as well

$$x_p = R\sin\beta_w\,;\; y_p = R-a-R\cos\beta_w \qquad (3.41)$$

$$r = \frac{R-a-R\cos\beta_w}{\cos(\beta_w+\theta)} = \frac{1-\chi-\cos\beta_w}{\cos(\beta_w+\theta)}\cdot R \qquad (3.42)$$

Therefore

$$A_1 = \left(\frac{\beta_w-\beta_v}{2}\right)R^2-\frac{1}{4}R^2(\sin 2\beta_w-\sin 2\beta_v)$$
$$A_2 = \left(\frac{\pi}{4}-\frac{\beta_w+\theta}{2}\right)r^2-\frac{1}{4}r^2\sin(2(\beta_w+\theta)) \qquad (3.43)$$

and

$$\phi^o = 1-\frac{\pi R^2-R^2(2\beta_v-\sin 2\beta_v)}{2R\cdot(2R-2a)} = 1-\frac{\pi-2\beta_v+\sin 2\beta_v}{4(1-\chi)} \qquad (3.44)$$

Following the same steps as before, with the definition of unit volume in part ii) of Fig. 3-16, Eq. (3.15) can be rewritten as

$$(1-\chi)\left[1-\frac{\pi-2\beta_v+\sin 2\beta_v}{4(1-\chi)}\right]S_w = (1-\chi-\cos\beta_w)\sin\beta_w-\left(\frac{\beta_w-\beta_v}{2}\right)+\frac{1}{4}(\sin 2\beta_w-\sin 2\beta_v)$$

$$-\frac{1}{2}\left[\frac{1-\chi-\cos\beta_w}{\cos(\beta_w+\theta)}\right]^2\left[\frac{\pi}{2}-\beta_w-\theta-\frac{1}{2}\sin 2(\beta_w+\theta)\right]$$

i.e. $$(1-\chi)\left[1-\frac{\pi-2\beta_v+\sin 2\beta_v}{4(1-\chi)}\right]S_w=\frac{-\beta_w+\beta_v}{2}+(1-\chi)\sin\beta_w-\frac{1}{4}(\sin 2\beta_w+\sin 2\beta_v)$$

$$-\left[\frac{\pi}{4}-\frac{\beta_v+\theta}{2}-\frac{1}{4}\sin 2(\beta_v+\theta)\right]\left[\frac{1-\chi-\cos\beta_v}{\cos(\beta_v+\theta)}\right]^2 \qquad (3.45)$$

Finally, for each water saturation, the volume angle β_w can be determined, as well as the other parameters needed for calculating capillary force and capillary strength.

3.3.5 Loaded uniform particles

One character of capillary force is that it does not break abruptly with rock deformation, as does mineral cohesion, which is very sensitive to strain. It has been shown that the critical separation distance at which tensile failure of the static liquid bridge occurs approximately equals to the cube root of the liquid volume (Lian et al., 1993), or is at least six orders of magnitude lower than the particle radius (Johnson et al., 1971). This means that before the sands deform to a certain extent and grains are fully disaggregated, the capillary force still exists during weakening, dilation and separation processes. For brittle mineral whose mineral cohesion is destroyed by shearing, capillary cohesion remains unaffected.

In Fig. 3-15, the volumetric deformation of the particles can be expressed as

$$\varepsilon=\frac{\Delta V}{V}=\frac{2R(2R+2a)-2R\cdot 2R}{2R\cdot 2R}=\frac{a}{R}=\chi \qquad (3.46)$$

Coincidently, it is equal to the ratio of distance between particles and particle radius. Therefore the models developed to calculate capillary strength for detached and squeezed particles can be used to describe the variations of capillary strength with rock deformation, except that water volume in the liquid bridge between particles should remain constant instead of water saturation (as the total unit volume will change upon loading). For the extended case, the water volume (Q_w) in the liquid bridge can be calculated as

$$Q_w=4R^2(1+\frac{a}{R}-\frac{\pi}{4})\cdot S_w \qquad (3.47)$$

and for compressed case,

$$Q_w=4R^2\left[(1-\frac{a}{R})(1-\frac{1}{2}\sin\beta_v)-\frac{\pi}{4}+\frac{1}{2}\beta_v\right]\cdot S_w \qquad (3.48)$$

3.4 Calculations and Verifications of Capillary Models

Based on rock properties and contact fabrics, four microscopic models, are presented here to analytically describe the behaviours of capillary strength under different rock, fluid, and loading conditions:

- uniform particles contacting tangentially,
- non-uniform particles contacting tangentially,
- detached uniform particles, and
- squeezed uniform particles.

In the following discussions, capillary strength factors such as surface tension, contact angle, rock heterogeneity, detached or squeezed extent of particles, and rock deformation are analyzed, as well as water saturation.

3.4.1 Model inputs and simplifications

The parameters used in the calculations are listed in Table 3-5, unless otherwise specified. This list shows the inherent simplicity of the models: only particle radius, surface tension, contact angle, porosity, and friction angle are needed to estimate the magnitude of capillary strength.

Besides the variations of surface tension due to the replacement of oil by water and chemical reactions between water and rock (e.g. hydrolysis), there may exist other changes affecting the magnitude of capillary force. For example, the softening and collapse of rock cementation changes the pore structure in chalk reservoirs and therefore changes the radius of capillary menisci (Papamichos et al., 1997). This influence depends on rock properties and geochemically active water components, and is extremely hard to describe in an analytical way. Thus this research assumes stable pore structure. However, some other assumptions made during the model development should be clearly restated, such as:

- The liquid bridge formed between particles can be described as a toroid;
- The variable bond strength between particles can be replaced by a mean value that is applicable throughout the whole rock mass;
- The water content is distributed evenly inside the particulate rock mass; and,
- The particles deform elastically upon compressive loading (squeezing).

Whereas these may be viewed as limitations to the models' applicability, the author believes that because the models capture the essential physics, adjustments and calibrations can easily be incorporated so as to give useful results in practice.

3.4.2 Behaviors of capillary pressure and forces

Table 3-6 lists calculation results of the proposed model of uniform particles contacting tangentially. The negative sign of P_c means the direction of capillary force is opposite to the y-direction. Notice that the calculated capillary pressure changes from negative to positive, which indicates that at some critical water saturation (33.19%) capillary pressure does not exist anymore. Physically, this means that the interface between water and oil collapses and water in the bridge begins to flow through the particles. Therefore the positive P_c data in the table (marked as red) are meaningless and should not be considered.

The relationship between water saturation (S_w) and water volume angle (β_w) is plotted in Fig. 3-17. Water volume angle increases with the increase of water saturation, and the increase rate is very fast at the beginning (S_w<0.55%). (The dashed part of the curve is based on the positive P_c data in Table 3-6, which should not be considered, as discussed in the previous paragraph.) Correspondingly, capillary pressure in Fig. 3-18 decreases very quickly with saturation when S_w<0.55%, and its value can be as high as 34 kPa, a value that is reached almost instantaneously as soon as water saturation is not zero. Fig. 3-19 describes the typical relationship between capillary pressure and water saturation degree, i.e. the ratio of water volume to oil volume, for a white chalk from Haubourdin in the north of France. Fig. 3-20 contains experimental results of the effect of different fluid combinations on capillary pressure. Not only in trend but also in magnitude the model-developed capillary pressure curve fits well with field and experimental data. Considering the influence of connate water saturation (the model assumes there is no connate water, i.e. S_w starts from zero), the proposed model appears to be promising.

However, plotting the capillary forces resulting from both pressure differences, i.e. F_c^o from Eq. (3.6), and surface tension, i.e. F_s from Eq. (3.7), in the same graph can be confusing: F_c^o decreases while F_s increases steadily with water saturation. As a result, the sum of them F_c (= $|F_c^o|+F_s$) only slightly decreases with the increase of water saturation. This is contradictory to reality where capillary forces and thus capillary strength decreases with water saturation and will eventually disappear when there are no capillary menisci at all. Therefore F_s should not be incorporated into F_c, as it is believed to be only a part of F_c^o and already included in Eq. (3.6) (Gillespie and Settineri, 1967).

3.4.3 Capillary cohesive force vs. fluid driving forces

After solving the capillary force at grain scale level, a question arises: should it be taken into account during the analysis of rock stability, since it is usually treated as negligible? In order to

answer this question, a comparison between the fluid destabilizing force (i.e. seepage force resulting from fluid gradient) and resistant force (i.e. capillary force) is carried out.
At the particle scale, fluid gradient results in a seepage force that pushes the particles in the direction of fluid flow. It is one of the major forces that mobilize (liquefy) weak, disaggregated sand into a slurried condition. An analytical description of the one-dimension seepage force can be given as (Asgian and Cundall, 1994)

$$F_f = -\frac{4}{3}\pi \frac{dP}{dx} R^3 \tag{3.49}$$

by assuming the particle is spherical with radius R (and a shape factor can be added to this equation to account for deviations from sphericity). Capillary force among particles only resists tensile failure; it makes little contribution to resist shear deformation. Fig. 3-21 summarizes the values of capillary cohesive bond force F_c calculated by the model and the seepage force F_f calculated by Eq. (3.49), assuming fluid gradient is 20 kPa/m (about 1 psi/ft). It turns out that the seepage force is always lower than the capillary bond force, on the order of 1 to 3, depending on the particle size and water saturation. The bigger the particles and the higher the water saturation, the lower the ratio. Even if the pressure gradient at the sand surface is 1000 psi/ft (due to massive restrictive formation damage near the wellbore, for example), the capillary force still could match it when the particle radius is small (R < 0.05 mm) and water saturation is low (<5%).

There are some other forces that fluids may induce on particles, such as viscous drag force (F_v) and buoyancy force (F_b). By assuming that the fluid flow rate is very slow (creeping flow), they can be calculated through

$$F_v = 6\pi R \mu v \quad \text{and} \quad F_b = \frac{4}{3}\pi R^3 g \tag{3.50}$$

where μ is fluid viscosity and v is fluid velocity. However, both of them are too small to be considered, compared with either seepage driving force or capillary force. (i.e. F_v is about two orders of magnitude lower than the seepage force, Walton, 2000).

In summary, capillary force (F_c) appears to be important enough to deserve attention in the analysis of rock stability, especially for unconsolidated sandstones. Furthermore, considering the effect of connate water saturation, capillary pressure and capillary forces most likely have already reached their peaks before a well produces significant amounts of water.

3.4.4 Behaviour of capillary strength and influential factors

3.4.4.1 Capillary strength vs. water saturation

Comparing to the rapid decrease of capillary pressure, the reduction rate of capillary strength with water saturation is smaller (see Fig.3-22). Its magnitude can reach several kPa. Based on tests of medium to fine-grained sandstones poorly cemented with clay, Dyke and Dobereiner (1991) developed a relation between rock strength and moisture content (Fig. 3-23), and found that most strength reduction occurs within a limited moisture content range (1%). The model calculations agree with their experimental results: capillary strength decreases quickly with water saturation before it increases to some critical value (as low as 5% in the model). Furthermore, this specific value is closely related to contact angle (Fig. 3-22), size ratio between particles (Fig. 3-29), and contact fabrics (Figs. 3-30 and 3-31). This may explain why some experiments showed that outflowing wetting fluid could destroy a formerly stable sand arch immediately (Hall and Harrisberger, 1970), and the critical fluid pressure gradient destabilizing sand will decrease to some extent when water saturation increases (Bruno et al., 1996).

3.4.4.2 Contact angle (θ)

Based on Eqs. (3.5), (3.6), (3.24), the effect of contact angle between fluid and rock on variations of capillary strength is calculated and plotted in Fig. 3-22. It is shown that capillary force decreases with an increase of contact angle, and the bigger the angle, the faster the decrease. Comparing to zero contact angle at which the maximum capillary tensile strength can be as high as 1.4 kPa and diminishes as saturation reaches 28%, when the angle $\theta = 1$, the strength only reaches 0.6 kPa and it quickly decreases to zero if the saturation rises to 3%. However, at any saturation there is no significant difference of the magnitude of capillary forces when the changes of the angle are small (<0.2).

3.4.4.3 Particle size (R)

The particle size has significant impact not only on the ratio of F_c/F_f (Fig. 3-21), but also on rock capillary strength, as shown in Fig. 3-24. Rock capillary strength (UCS) increases dramatically (up to 10 kPa) when particle size is smaller than some critical value (around R = 0.15mm), even at the same time that capillary cohesive force decreases (Fig. 3-25). The main reason for this dramatic effect, i.e. rock strength increases while capillary force decreases in unconsolidated sand, is that the interactions among rock particles become more dominant to determine rock strength than the fluid-rock interactions: the finer-grained the sand particles, the denser the particle contacts, the higher the rock strength. Since the radii of sand particles in oil-producing

formations are usually between 0.05 mm and 0.5 mm, the magnitude of capillary strength resulting from capillary force can be expected to be as high as in the range of kPa.

3.4.4.4 Surface tension (γ)

In experiments it is found that the cohesive strength and UCS of a water-wet, silicone-oil-flooded sand was about three times larger than those of the same water-wet, heavy-oil-flooded sand under the same stress (Tremblay et al., 1997). The difference is believed to result from the higher interfacial tension between water and silicone oil (38 dynes/cm, measured by Adamson, 1982) than between water and heavy oil (15 to 20 dynes/cm, measured by Takamura and Isaacs, 1989).

With inputs of γ = 0.015 N/m and γ = 0.036 N/m, respectively, the model-calculated relations of surface tension and capillary force (and therefore capillary strength) are listed in Table 3-7, while other parameters used are unchanged (Table 3-5). It is demonstrated that at the same water saturation, such as S_w = 0.5%, UCS can be 1327 Pa for γ = 0.036N/m and 552.9 Pa for γ = 0.015N/m, corresponding to the capillary forces of 3.94 dyne and 1.64 dyne respectively. The ratio of UCS values is about 2.4, which matches the above experimental results, and this may be viewed as evidence of model validity. Furthermore, as shown in Fig. 3-26, rock capillary strength is found to be linearly related to the surface tension between wetting and non-wetting fluids, but the rate of increase (slope of lines) becomes less when water saturation increases.

3.4.4.5 Size difference

Based on Eqs. (3.28), (3.29), (3.31), Fig. 3-24 illustrates the effect of non-uniform size (size ratio n = 0.1, 0.5, 1) on the variations of water volume angles (β_{w1}, β_{w2}): at the same water saturation, the greater difference between particles size (i.e. lower value of n) leads to a greater difference between two angles; in addition, the angles tends to stop increasing with water saturation more rapidly when the size ratio is small (n = 0 in Fig. 3-27). As a result the capillary force diminishes more rapidly (i.e. the liquid bridge breaks more easily) when the particles' size is more different: for a size ratio n = 1, the capillary force becomes zero when water saturation reaches 30%, while for n = 0.1, only a water saturation of 1.7% is needed (Fig. 3-28).

The size difference also can affect the magnitude of capillary force and strength. In Fig. 3-29, at the same water saturation (1%), both capillary force and strength keep increasing when the difference between particles becomes small (i.e. size ratio increases), despite the fact that capillary pressure does not increase after reaching a maximum value when the size ratio n is around 0.5. The reason for different trends of capillary pressure (or tensile strength) and capillary force is that the force (or strength) is not only determined by the pressure, but also dependent on

the area being acted upon by the pressure. When the area increase overwhelms the pressure decrease, their product, the capillary force, will track the area changes.

3.4.4.6 Contact fabrics

Figs. 3-30, 3-31, 3-32, and 3-33 illustrate calculated results for the detached and squeezed models developed in Sections 3.3.4 and 3.3.5.

Compared to tangentially contacting particles, the relationship between capillary strength and water saturation is quite different when particles become detached or squeezed: instead of continuously decreasing with water saturation (e.g. χ=0 in Fig. 3-30 and Fig. 3-31), the capillary strength increases to a peak at an early stage and then decreases (e.g. χ=0.01 in Fig. 3-30). The peak strength is strongly affected by the distance between particles (Fig. 3-32 and 3-33): the greater the distance between particles, the lower the value of peak strength. Furthermore, a greater distance, either positive (detachment) or negative (squeeze), results in a higher water saturation needed to attain the maximum capillary strength. This is reasonable because there will be more water needed for widely spaced particles to form a strong liquid bridge than for more closely spaced particles.

Experiments with unconsolidated sand (Bianco and Halleck, 2001) show that a stable arch starts to develop even with a small increase in water saturation (S_w > 3%) in a two-phase environment, whereas such an arch cannot be stable in a monophasic condition. Furthermore, the sand starts to flow into the wellbore when S_w > 20%, and massive sand production occurs if S_w > 32%. The models developed for detached and squeezed particles (Fig. 3-30, Fig. 3-31) can explain these phenomena directly: the strength from capillary force first increases to a peak value (therefore stable sand arches form) before continuously decreasing and disappearing as water saturation increases (hence the sand arches collapse).

When the extent of detachment and squeeze are the same, e.g. χ = 0.01 in Fig. 3-32 and χ = -0.01 in Fig. 3-33, the capillary strength of separated particles is much higher (about twice) than that of the squeezed arrays, given the same water saturation of 5%.

3.4.5 Strength evolution with rock deformation

As discussed in 3.3.5, detached and squeezed fabric models can be applied to describe behaviours of rock capillary strength upon loading. Following the conventions of rock mechanics, i.e. negative sign of deformation means compression while positive sign means extension, Fig. 3-34 summarizes the calculation results. In general, capillary tensile strength is a maximum when there is no deformation (i.e. ε = 0), and decreases with both compressive and extensional deformation, while there is a slight increase when extension of low magnitude occurs. This

agrees well with the experimental observations by Mason and Clark (1965): the curves in Fig. 3-35 generally decrease with the detached distance shortly after a slight increase (each curve corresponds to a constant water volume in the liquid bridge), even though there is a large difference of particle properties between their experiments and the analytical model developed above (the spheres they used are oil-wetted and water-immersed, with radii of 15 mm).

The strength decrease for compressed rock is much faster than when the rock is pulled apart. For example, when the water bridge volume is 1.72×10^{-9} m^3 and the deformation $\varepsilon = 0.02$, the tensile strength will decrease from 380 Pa to 95 Pa for rock in a compressional condition, and from 380 Pa to 315 Pa for rock in an extension condition. As in reservoir situations rock inevitably has to experience compression due to the changes of stresses in surrounding rocks during depletion, capillary strength may decrease rapidly with water saturation. On the other hand, if rock has experienced considerably compaction beforehand and particles are originally in a squeezed state when oil production starts, the capillary strength can be relatively small.

3.5 Conclusions

Among the mechanisms that may destabilize unconsolidated sand after an oil well starts to produce water, two main reasons are identified and analyzed in detail to clarify the effect of water saturation on sand strength: one is chemical reactions of rock with formation water, the other is variations of rock capillary strength.

There are mainly two kinds of chemical reactions that are likely to lower rock stability when water breakthrough occurs: quartz hydrolysis and carbonate dissolution that lower the surface energy of rock, whereas ferruginous deposition and shale swelling change the rock pore structure and affect local fluid gradients, thus enhancing seepage forces that may destabilize the sand. Since the rock strength changes from these reactions are environmentally dependent and are related to numerous parameters that cannot realistically be determined, it will be extremely hard to quantify the effects of those reactions.

Four novel models are developed to account for the variations and behaviors of rock strength resulting from capillary forces in two-phase fluid environments, including uniform particles in tangential contact, non-uniform particles in tangential contact, uniform particles in squeezed contact, and uniform particles in detached contact. Using these models, the effects of fluid properties (contact angle and surface tension), rock properties (particle size, size ratio, contact fabric), and deformation of loaded rock on capillary strength have, for the first time, been mathematically expressed and quantified. These models fit available experimental and field data and can explain many published reports about the influence of water saturation on rock strength.

Based on the model calculations, several novel conclusions are made:

- At the grain scale, capillary pressure among the particles can reach the order of kPa and capillary cohesive force is one to three orders of magnitude higher than the fluid seepage force when the fluid gradient is about 1 psi/ft. The smaller the particles, the greater the effect; therefore capillary force should not be neglected in the analysis of sand instability, especially for unconsolidated sand.
- Capillary induced strength, such as UCS or tensile strength resulting from capillary cohesive force, can decrease quickly with water saturation, from several kPa to near zero within only a 5% change of water saturation.
- For all the models, capillary strength increases linearly with increasing surface tension of the interface between the fluids.
- Contact angle affects both the magnitude of capillary strength and its variation with saturation. At the same water saturation, the larger the contact angle, the smaller the strength, and the faster the strength decrease with increasing saturation.
- If the particle size is uniform, small particle size results in high capillary strength. If particles have different size, the size ratio has an influence on the capillary strength similar to that of the fluid contact angle: it affects both the magnitude of capillary strength and its variation rate with saturation. However, the relations are different: the smaller the size difference, the higher the capillary strength and the faster its decrease. Furthermore, at the same saturation, more homogeneity in particle size leads to greater values of the capillary force and strength.
- For detached and squeezed contact models, the capillary strength first increases to a peak with water saturation, then decreases after a critical saturation, in contrast to the tangential contact model where capillary force always decreases with water saturation. The peak strength is closely related to the distance between particles, contact angle, and size homogeneity of particles. At the same saturation, the strength decrease becomes more significant for squeezed particles than for detached ones.
- By introducing strain into the models, capillary strength is also found to vary greatly with rock deformation: it reaches a maximum when particles are tangentially contacted and decreases with either compression or extension. Comparing with extended particles, the strength of compressed particles decreases much faster with deformation.

These new insights into the capillarity variations are essential to create a quantitative prediction model for sand production in poorly consolidated or unconsolidated sand. It also should be noted that, besides the description of rock capillary strength in unconsolidated sand after water breakthrough, these models could be used as the basis of any calculation of capillary force (and strength) between two spheres in two-phase fluid environments.

3.6 Tables and Figures

Table 3-1: Test results of arch stability by changing fluid types
(Hall and Harrisberger, 1970)

Test no.	Step	Initial situation	Flow	Load (psi.)	Results
9 (water wettable)		Water moistened	None	2,000	Arched
10 (oil wettable)	a	Kerosene	None	1,000	No arch
	b		Air in		Arched
	c		None		Held
11 (water wettable)	a	Kerosene at residual water	None	1,000	Arched
	b		Kerosene out		Held
	c		Water out		Failed
12 (oil wettable)	a	water at residual oil	None	1,000	Arched
	b		Water out		Held
	c		Oil out		Failed
13 (water wettable)		Water moistened	None	3,450	Arch held

Note: Ottawa sands of 20-40 mesh size, Krumbein Roundness 0.8 (high), grain density 2.64 gm/cc, porosity 34.6%, friction angle: 34.0. Arch formed at 500 psi; load (average vertical stress) increased to failure or to apparatus limit of 3,450 psi.

Table 3-2: Compressive Strength of Sandstones in MPa (lbf/in^2)
(after Boretti-Onyszkiewicz, 1966)

State	1		2		3		4		5	
	⊥	‖	⊥	‖	⊥	‖	⊥	‖	⊥	‖
Air-dry	150.2	137.3	125.6	88.4	93.9	99.4	93.5	83.2	69.2	54.5
Water saturated	103.7	92.5	87.9	76.5	63.4	53.5	81.4	65.1	55.2	50.3
Percent (%) (Dry-Sw)/Dry	31	32.6	30	13.5	32.7	46.2	12.9	21.8	20.2	7.7

Note: ‖, parallel to stratification; ⊥, perpendicular to stratification

Table 3-3: Properties of the materials applied in Skjærstein's experiments
(After Skjærstein *et al.,* 1997)

Material	Mean grain size [μm]	Horizontal permeability [mD]	Vertical permeability [mD]	Porosity [%]	Uniaxial compressive strength [MPa]
Red Wildmoor	100	350	350	0.25	~10
Red Wildmoor brine saturated, 10% NaCl	100	-	-	0.25	3.4
Red Wildmoor brine saturated, 10% KCl	100	-	-	0.25	5.8
Core material 1	100	481-988	485-462	0.286-0.345	5.5-7.5
Core material 2	-	~2000	~2000	32.5	~1.2

Table 3-4: External stress at initial cavity failure and onset of sand production
(After Skjærstein *et al.,* 1997)

Test id.	Cavity failure [MPa]		Onset of sand production [MPa]	Flowing fluid
	Wall	Roof		
RW01	No	No	No	σ_c=10 MPa, two phase flow
RW02	No	No	15	σ_c=15 MPa, two-phase flow
RW03	No	No	20	σ_c=20 MPa, two-phase flow
RW04	24.0	25.2	--	Humid, no flow
RW05	27.5	*	24.3	Oil flow
RW06	23.5	22.8	25	σ_c=25 MPa, two-phase flow
RW07	15	14.0	15	Brine flow
RW08	15	*	15	Two-phase flow

* missing
♦ bellow failure

Table 3-5: Input parameters for capillary models

R (m)	γ (N/m)	ϕ (%)	φ (°)	θ
0.0002	0.036	30	30	0

Table 3-6: The calculations from proposed capillary force model

Volume angle (β_w)	Saturation (S_w)	r_1 (m)	R (m)	Capillary pressure $-P_c$	Capillary force (Dyne)		
					F_c^o	F_s	F_c
0	0	0	0	0	0	0	0
0.1	0.000693369	1.90628E-05	1.00418E-06	33961.52	4.25352306	0.045088339	4.2986114
0.15	0.002218033	2.79558E-05	2.27129E-06	14562.28	4.08660105	0.101026482	4.187627532
0.2	0.004992964	3.64742E-05	4.06777E-06	7863.062	3.89998761	0.178555825	4.078543434
0.3	0.015281115	5.25169E-05	9.35032E-06	3164.642	3.47303252	0.395081531	3.868114046
0.4	0.033069497	6.74178E-05	1.71409E-05	1566.258	2.98473557	0.686033261	3.67076883
0.5	0.059334436	8.13617E-05	2.78988E-05	847.9102	2.44907479	1.039811687	3.48888648
0.6	0.094730187	9.45017E-05	4.23257E-05	469.6023	1.88142603	1.44231278	3.323738806
0.7	0.139727311	0.000106966	6.14919E-05	248.8873	1.29800968	1.877490091	3.17549977
0.8	0.194704415	0.000118863	8.70648E-05	110.6149	0.71530812	2.327994474	3.043302598
0.9	0.260010661	0.000130286	0.000121745	19.38547	0.1494763	2.775865741	2.925342044
0.927	0.279460592	0.000133301	0.000133202	0.19938	0.0016028	2.894009566	2.895612365
1	0.336009935	0.000141318	0.000170163	-2.34944	-0.0209051	3.203248679	3.22415381
1.1	0.423113736	0.000152031	0.000240921	-52.5465	-0.5244590	3.593104877	4.117563907

Table 3-7: Influence of surface tension on capillary strength

Surface tension γ = 0.015N/m				water Saturation	Surface tension γ = 0.036N/m			
Capillary Pressure (Pa)	Capillary Force (Dyne)	Capillary Strength			Capillary Pressure (Pa)	Capillary Force (Dyne)	Capillary Strength	
		σ_T (Pa)	UCS (Pa)				σ_T (Pa)	UCS (Pa)
0	0	0	0	0	0	0	0	0
14186.25	1.7768	259.1113	598.3918	0.0006933	34047.01	4.2642	621.8670	1436.1404
6102.301	1.7125	249.7371	576.7432	0.002218	14645.52	4.11	599.3691	1384.1838
3310.013	1.6417	239.4187	552.9138	0.004992	7944.032	3.9401	574.6049	1326.9931
1350.433	1.482	216.1296	499.1299	0.01528	3241.04	3.5569	518.7110	1197.9117
682.5057	1.3006	189.6731	438.0313	0.03307	1638.014	3.1215	455.2155	1051.2751
381.2206	1.1011	160.5777	370.8384	0.05933	914.9294	2.6427	385.3866	890.0121
221.5675	0.8877	129.4553	298.9642	0.09473	531.762	2.1305	310.6927	717.5141
127.5145	0.6650	96.9821	223.9705	0.1397	306.0348	1.596	232.7570	537.5292
67.7348	0.43802	63.8775	147.5189	0.1947	162.5635	1.0512	153.3061	354.0452
27.4627	0.21176	30.8813	71.3174	0.2600	65.91052	0.5082	74.1152	171.1618
0.23745	0.00210	0.30613	0.7070	0.3319	0.569877	0.005038	0.7347	1.6968

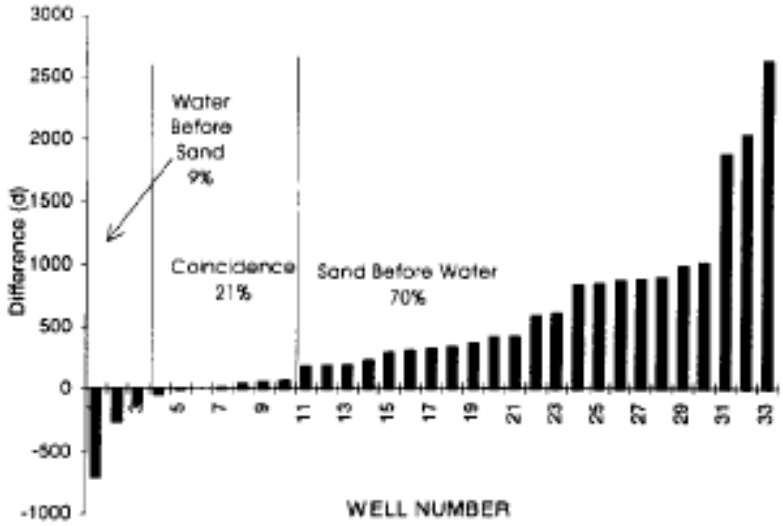

Fig. 3-1: Difference between onset of sand production and water breakthrough for 33 wells (After Skjærstein et al., 1997)

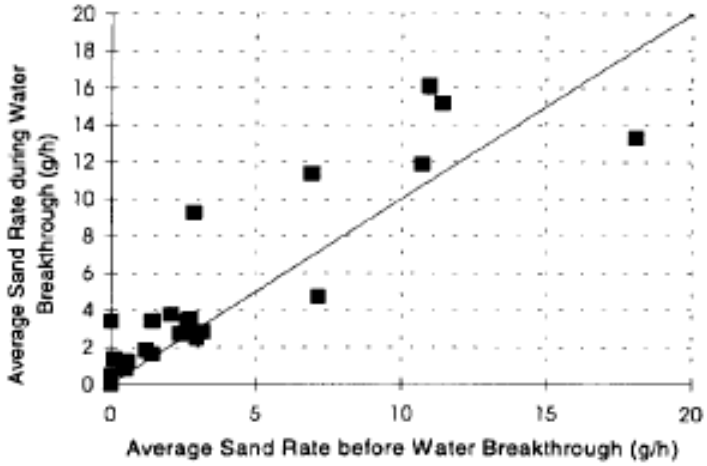

Fig. 3-2: Average sand rate during vs. before water breakthrough (After Skjærstein et al., 1997)

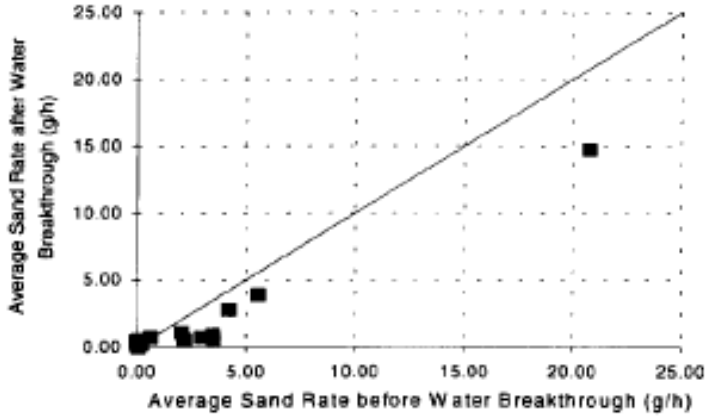

Fig. 3-3: Average sand rate after vs. before water breakthrough (After Skjærstein et al., 1997)

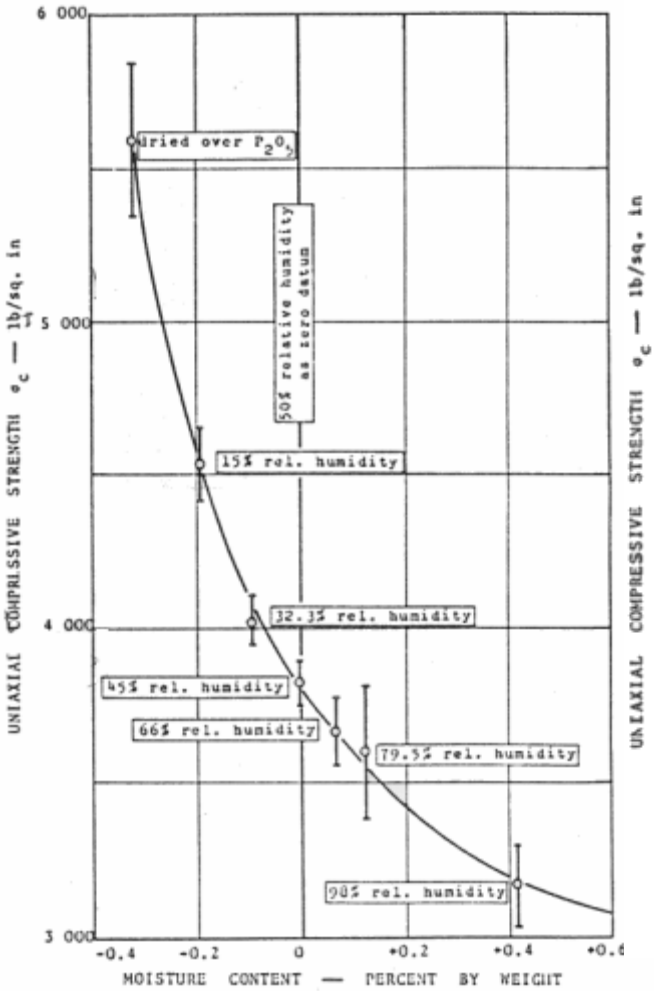

Fig. 3-4: UCS vs. moisture content for quartzitic sandstone (After Colback and Wiid, 1965)

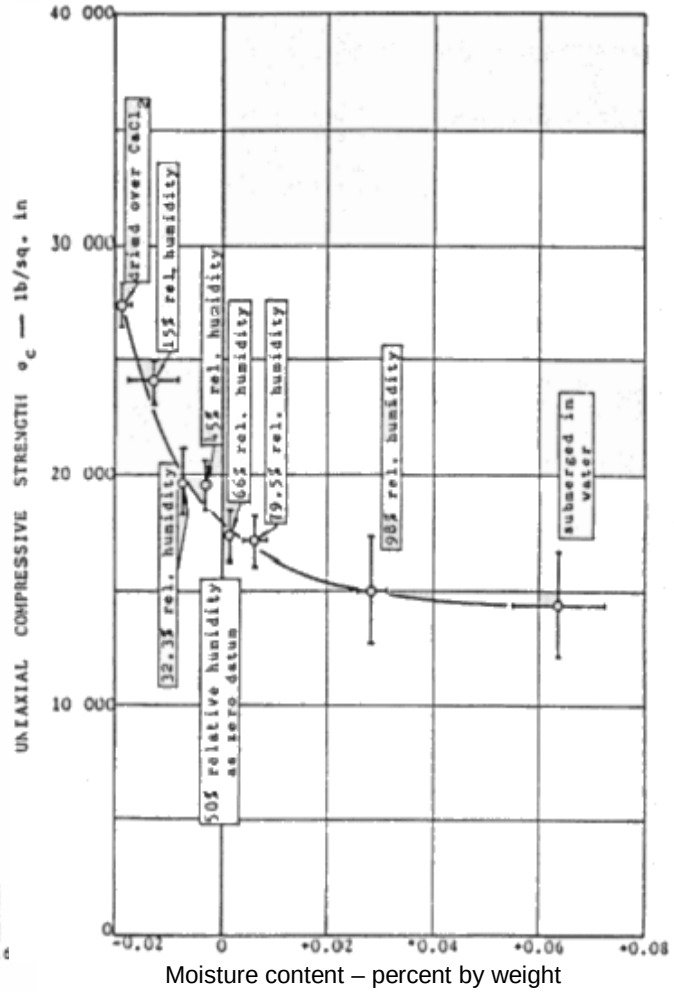

Fig. 3-5: UCS vs. moisture content for quartzitic shale (After Colback and Wiid, 1965)

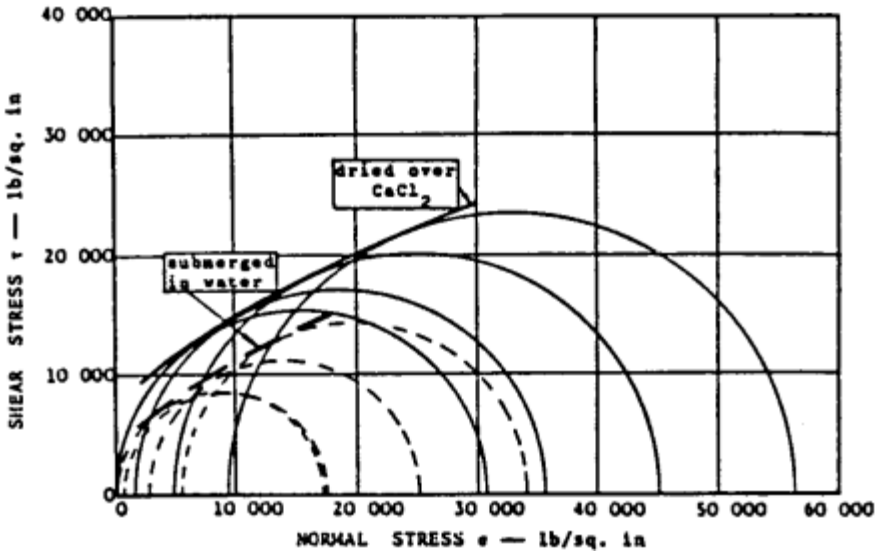

Fig. 3-6: Mohr fracture envelopes for quartzitic shale at two saturation status (After Colback and Wiid, 1965)

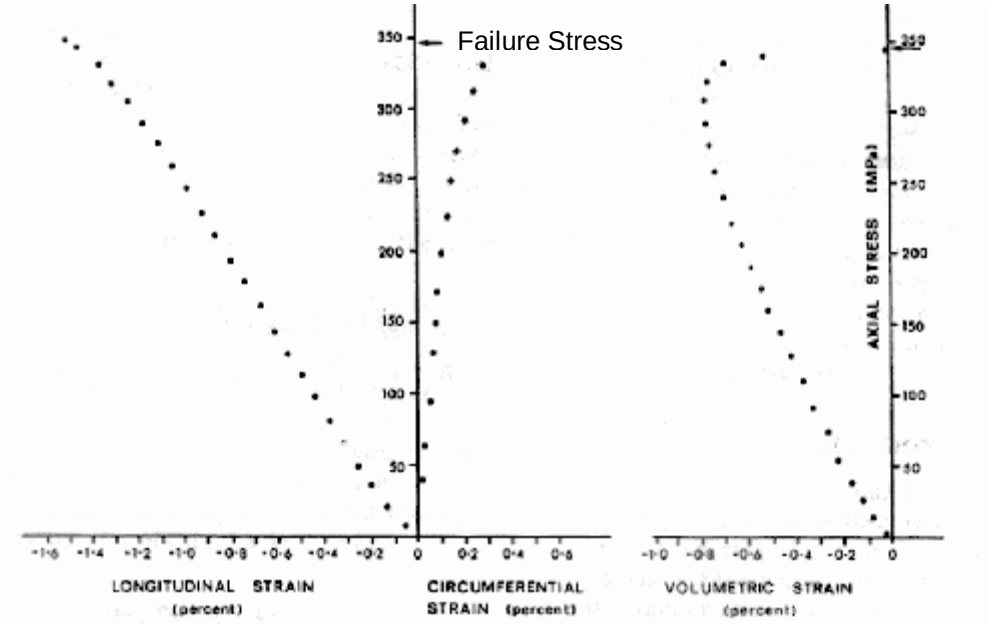

Fig. 3-7: Stress vs. strain curves for oven-dried Oughtibridge ganister (quartzite)
Strain curves for water-saturated quartzite specimens deformed at the same strain rate were found to be almost coincident with the oven-dried ones (After Hadizadeh and Law, 1991)

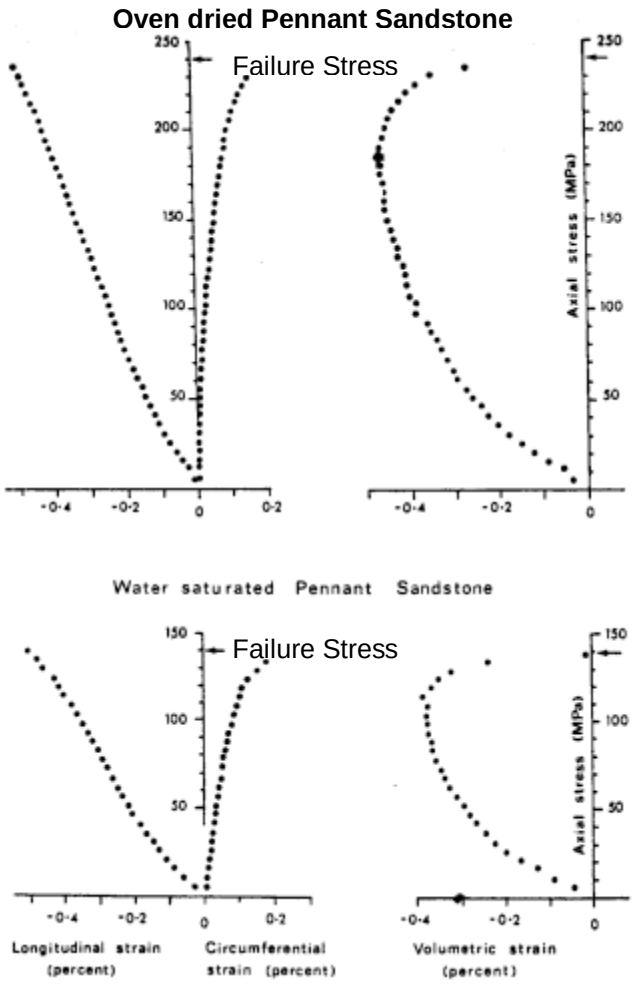

Fig. 3-8: Stress vs. strain in oven-dried and water-saturated Pennant sandstone
(After Hadizadeh and Law, 1991)

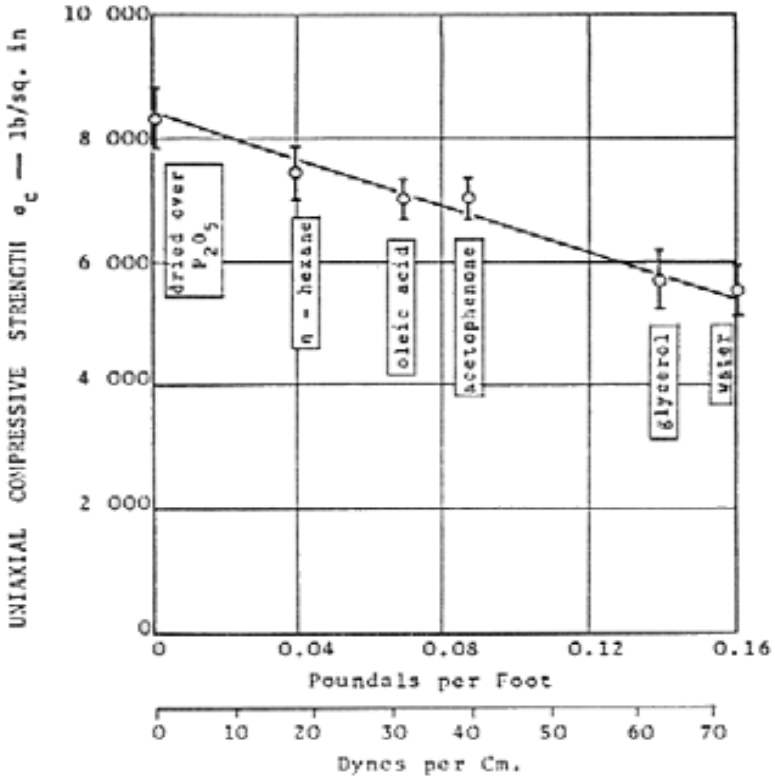

Fig. 3-9: Influence of the surface tension of immersion liquids on the strength of quartzitic sandstone (After Colback and Wiid, 1965)

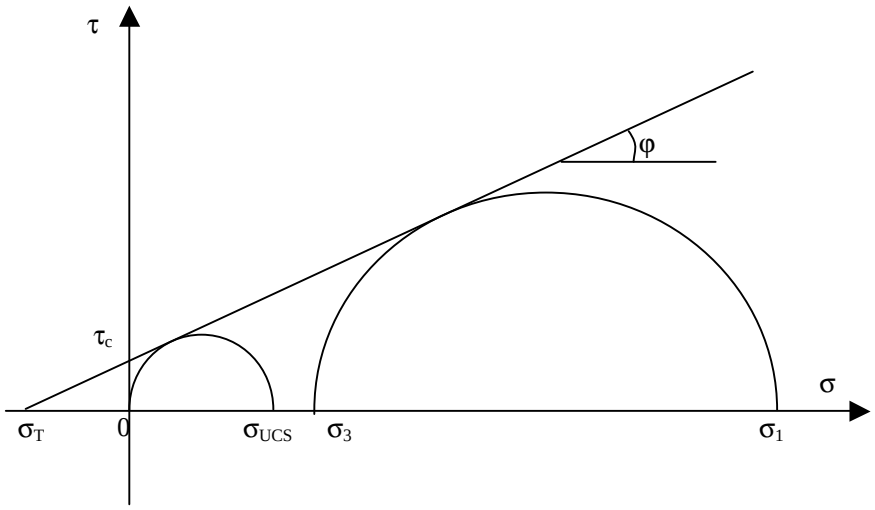

Fig. 3-10: Mohr-Columb criteria

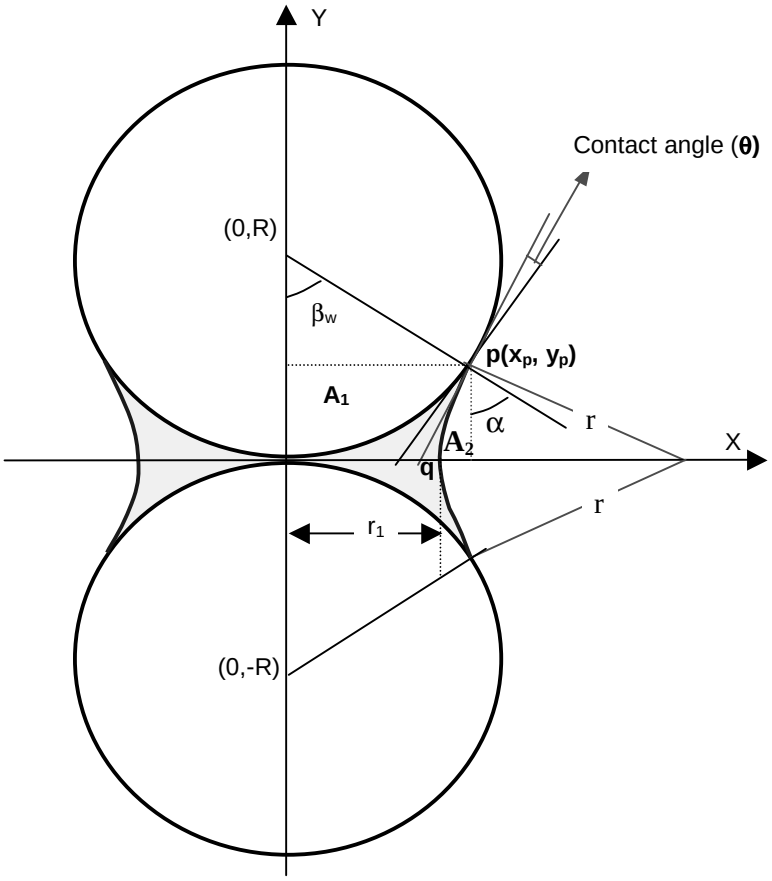

Fig. 3-11: Basic capillarity model

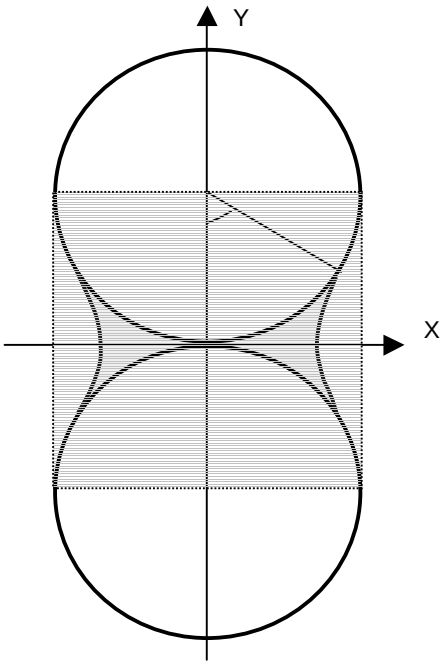

Fig. 3-12: Definition of unit volume

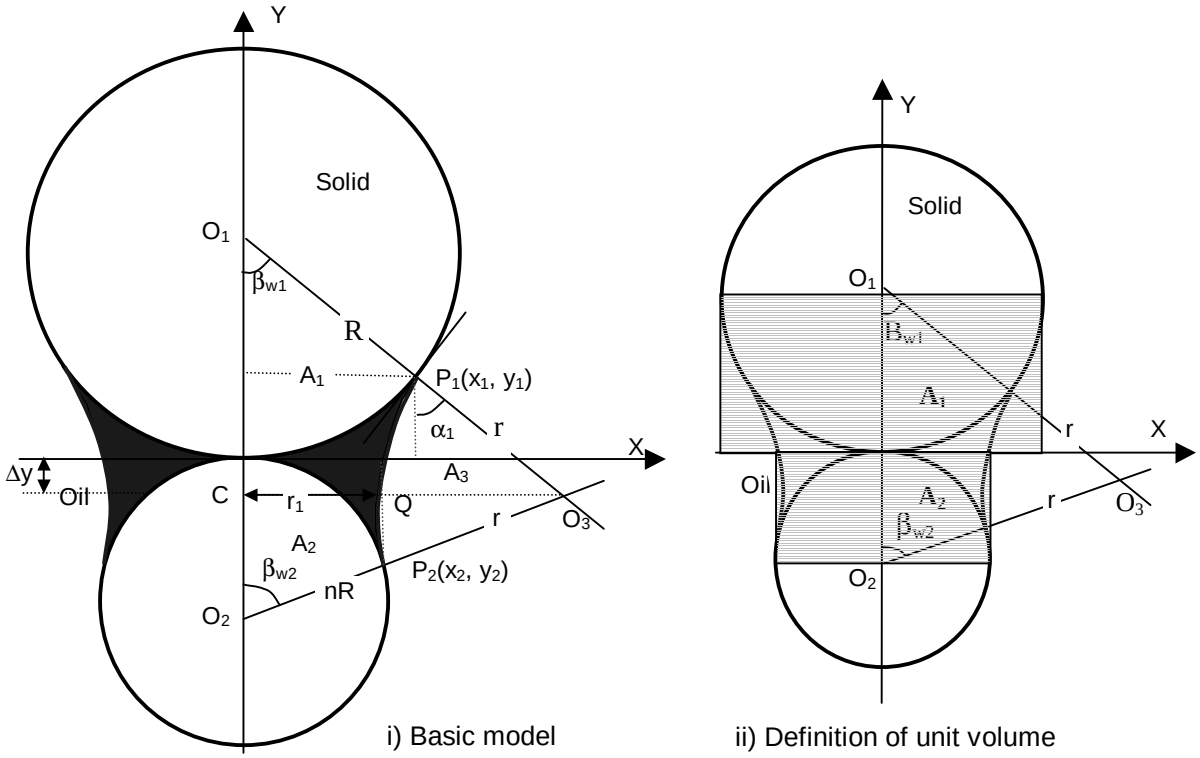

Fig. 3-13: Models for non-uniform particles contacting tangentially

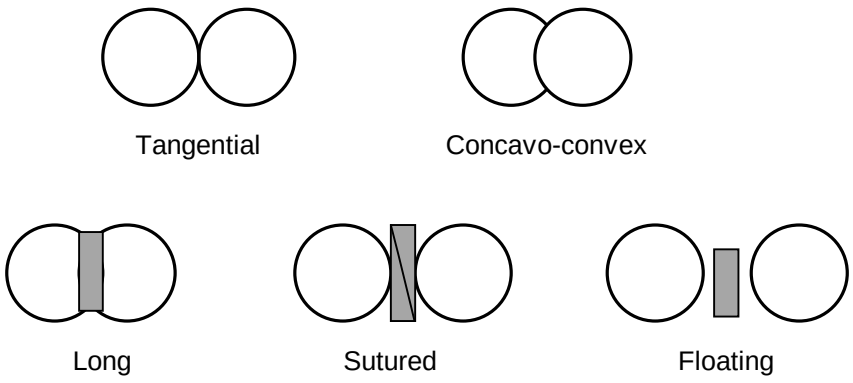

Fig. 3-14: Schematic Contact fabric for rock particles

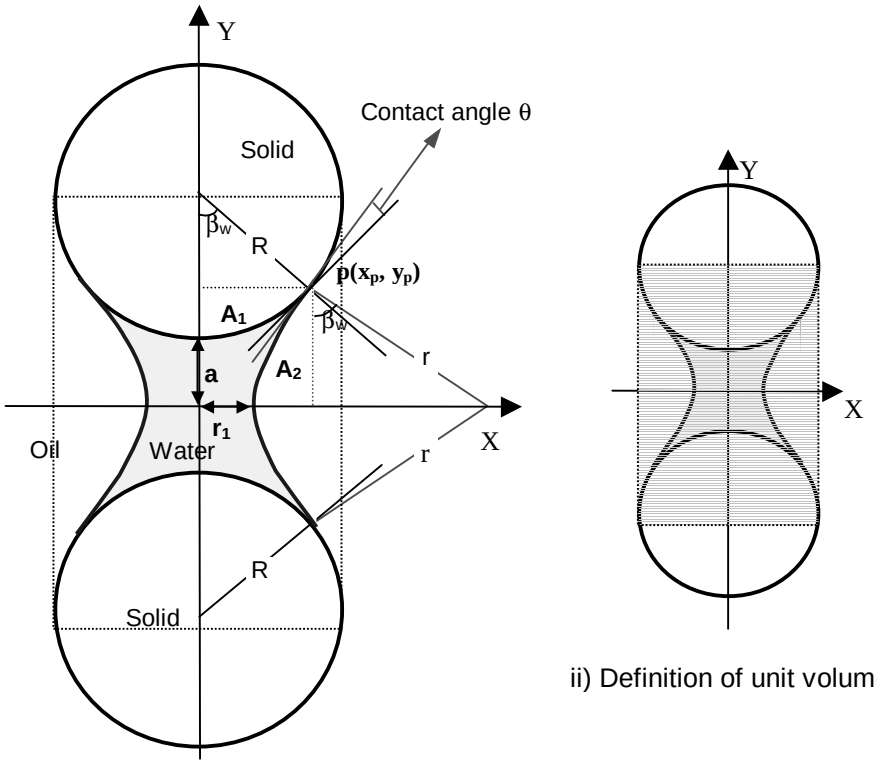

i) Basic model

ii) Definition of unit volume

Fig. 3-15: Detached uniform particles (a>0)

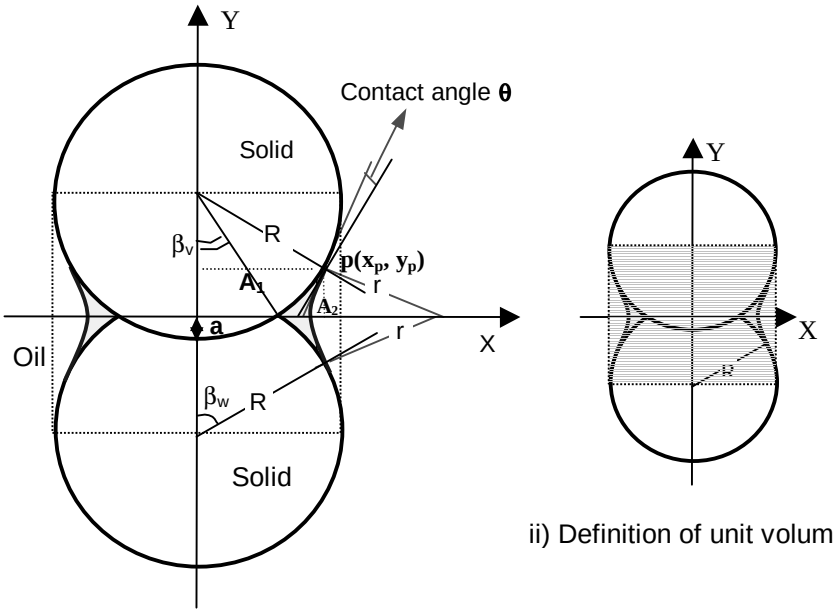

i) Basic model

ii) Definition of unit volume

Fig. 3-16: Squeezed uniform particles (a<0)

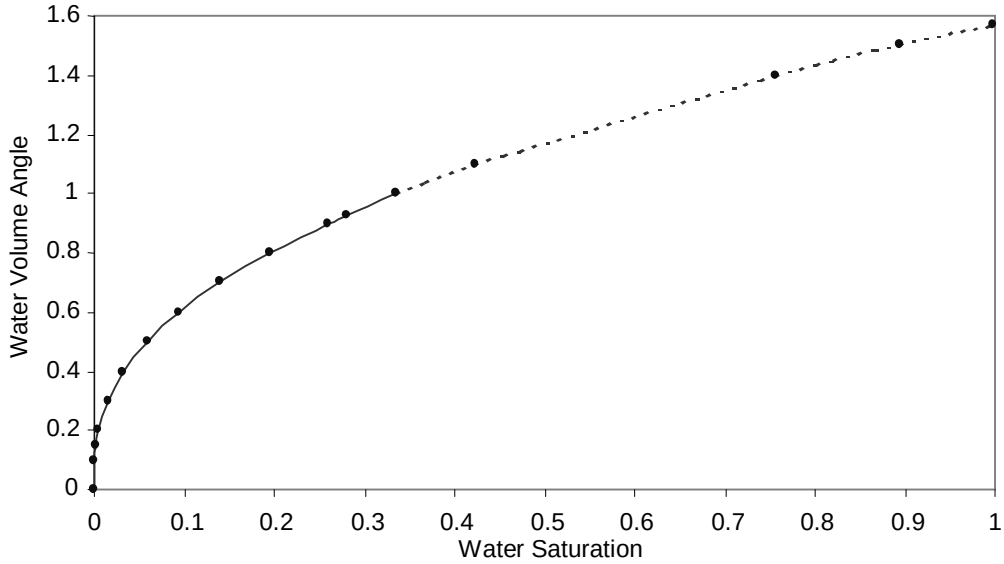

Fig. 3-17: Water saturation vs. volume angle (Data in Table 3-6)

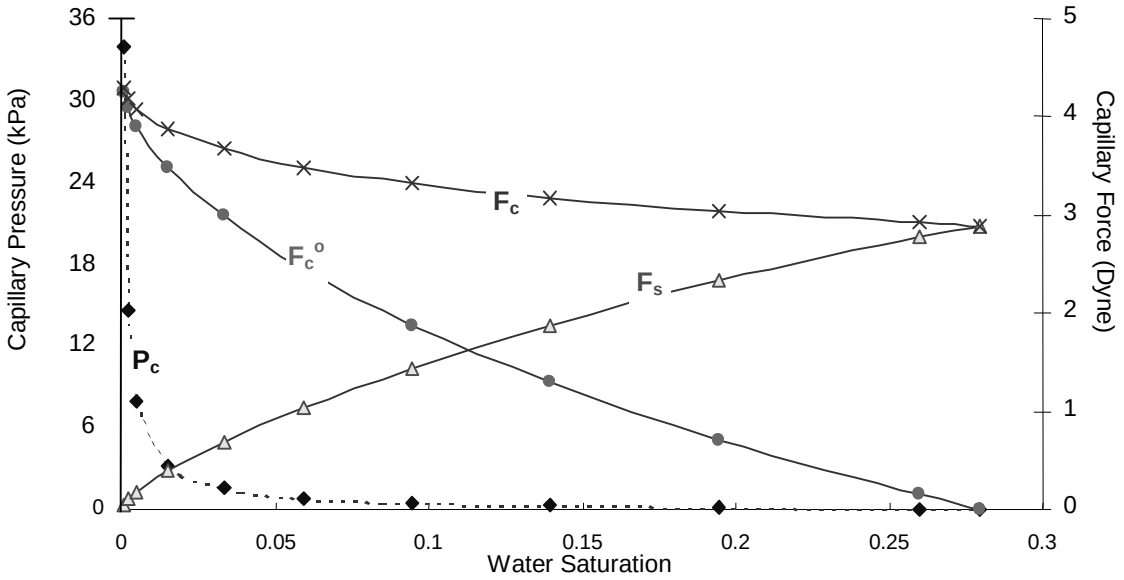

Fig. 3-18: Water saturation vs. capillary forces

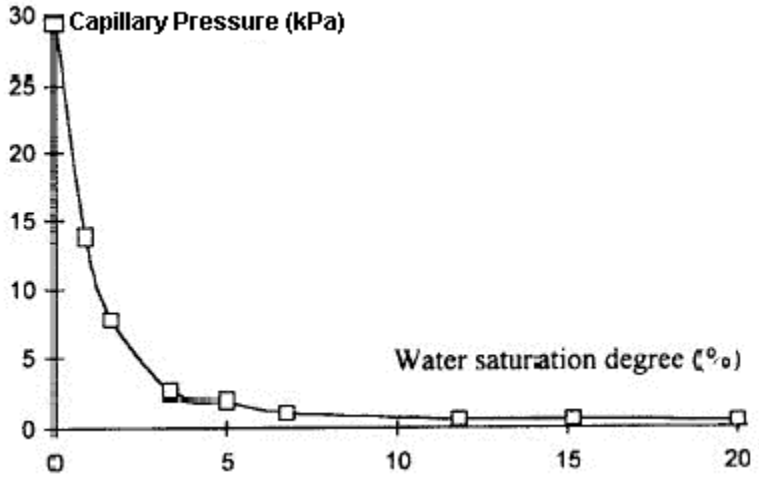

Fig. 3-19: capillary force vs. water saturation for a white porous chalk
(After Homand et al., 1997)

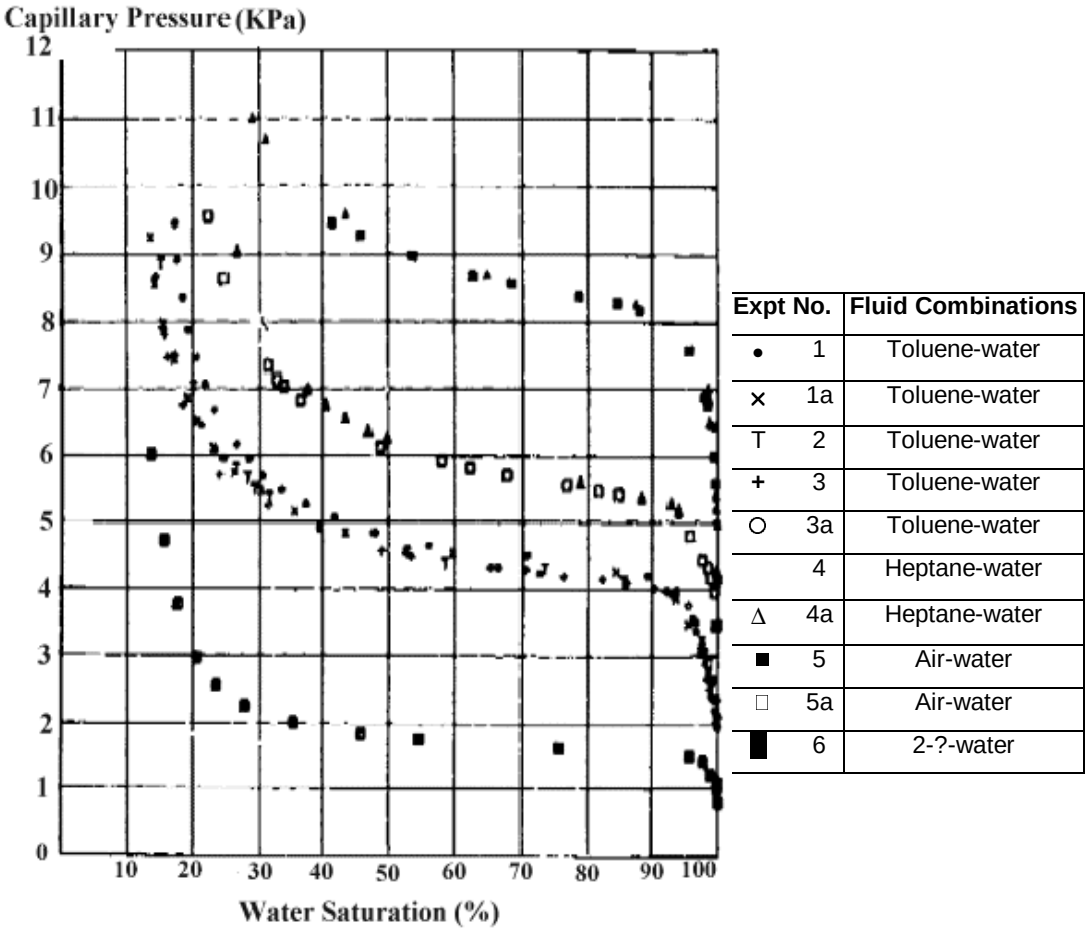

Expt No.		Fluid Combinations
•	1	Toluene-water
×	1a	Toluene-water
T	2	Toluene-water
+	3	Toluene-water
○	3a	Toluene-water
	4	Heptane-water
△	4a	Heptane-water
■	5	Air-water
□	5a	Air-water
▮	6	2-?-water

Fig. 3-20: Drainage capillary pressure for different fluid-fluid combinations
(After Dumore and Schols, 1974)

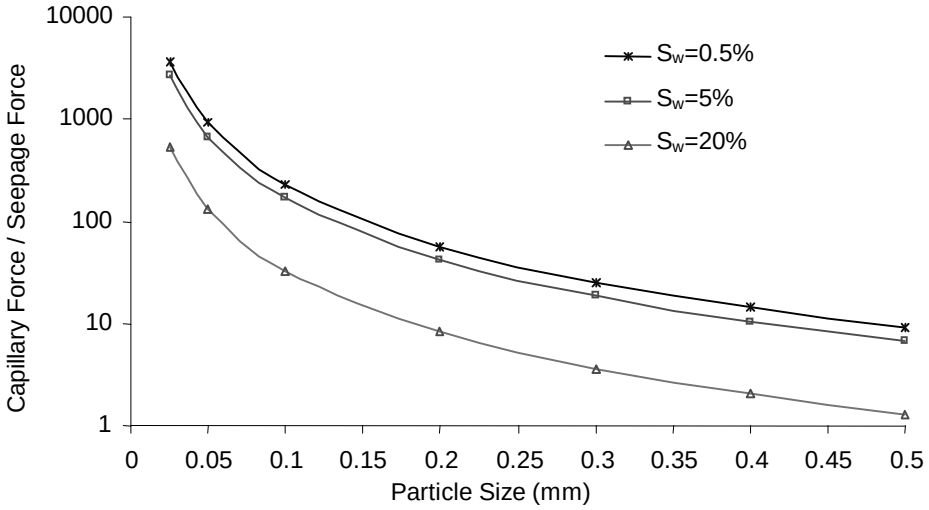

Fig. 3-21: The ratio of capillary force and seepage force vs. particle size

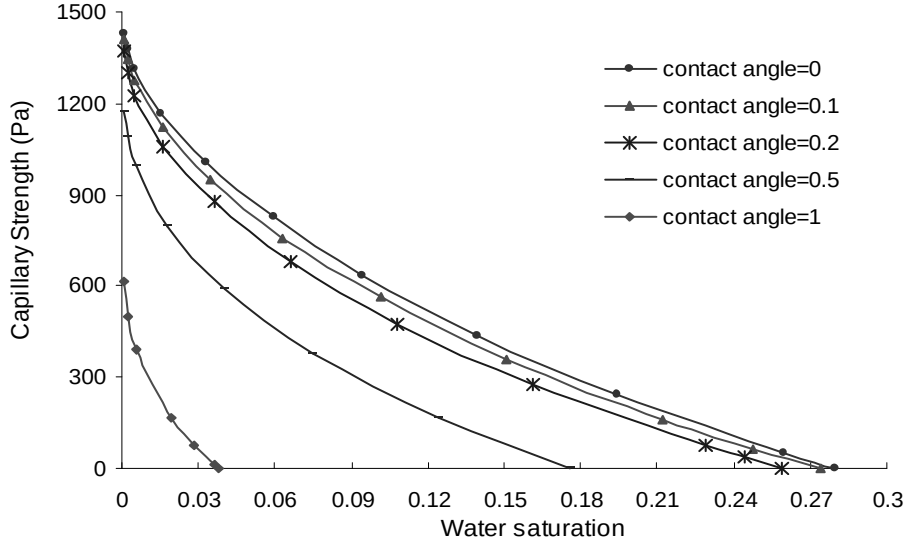

Fig.3-22: Capillary strength (UCS) for tangentially contacted particles

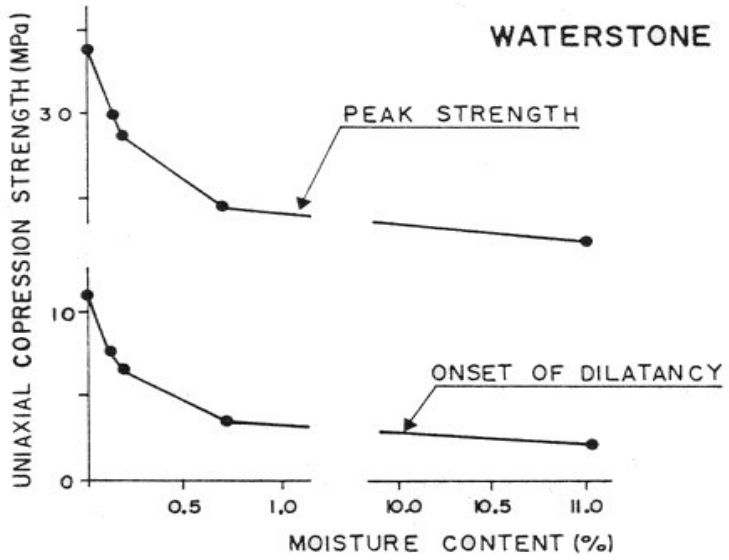

Fig. 3-23: Variations of rock strength with water saturation
(After Dyke and Dobereiner, 1991)

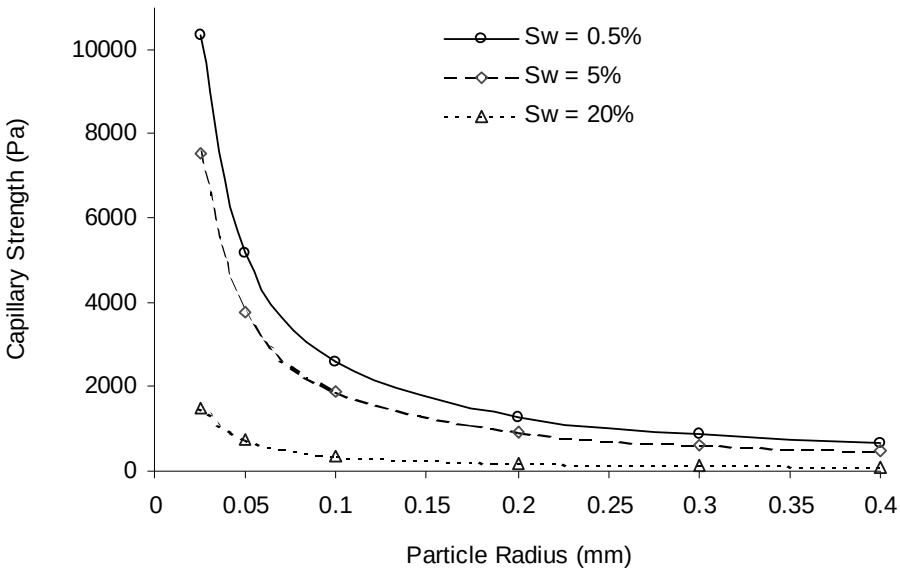

Fig. 3-24: Effect of particle size on capillary strength (UCS)

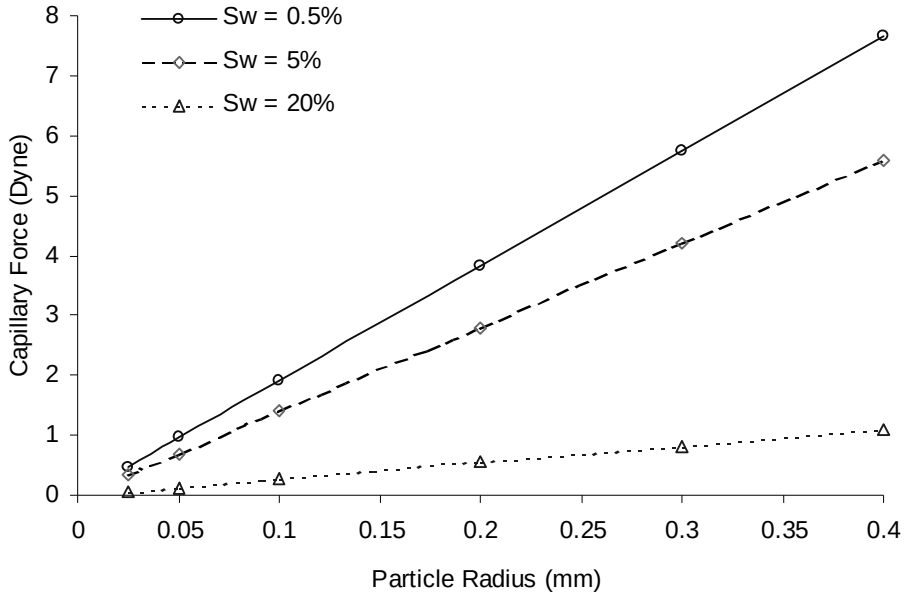

Fig. 3-25: Effect of particle size on capillary force

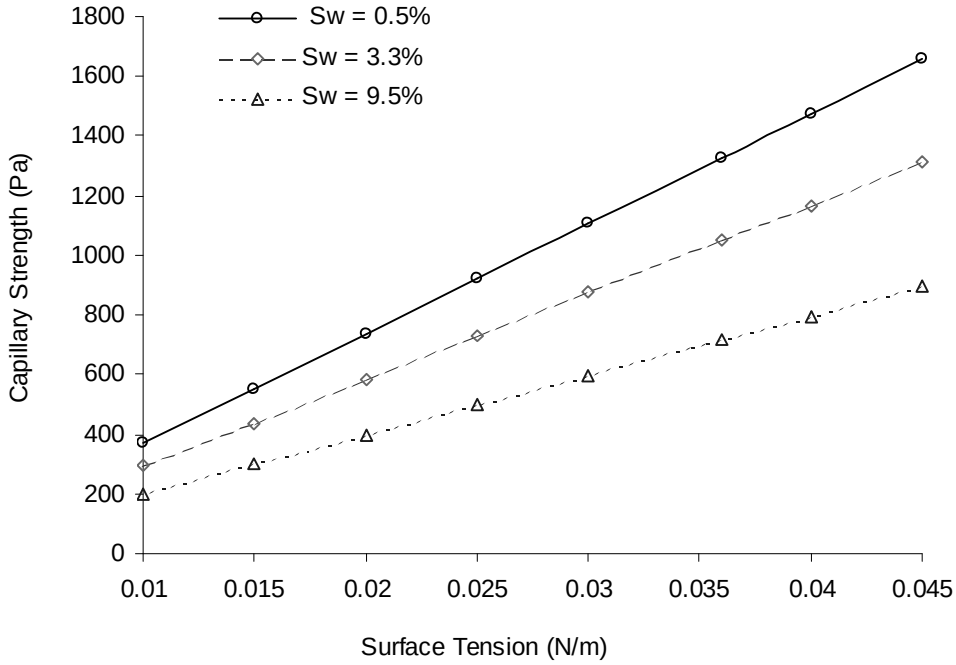

Fig. 3-26: Effect of surface tension on capillary strength (UCS)

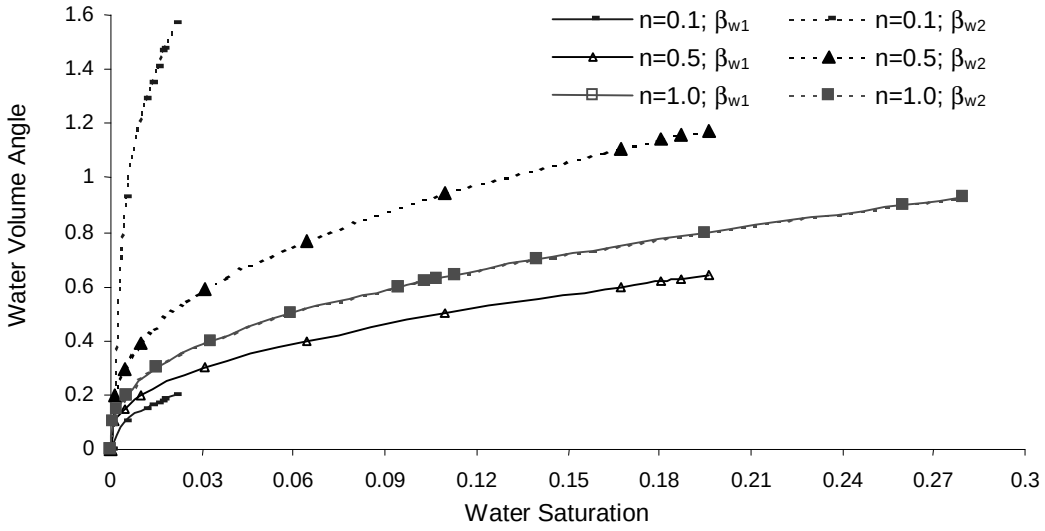

Fig. 3-27: Effect of non-uniform particle size on water volume angle

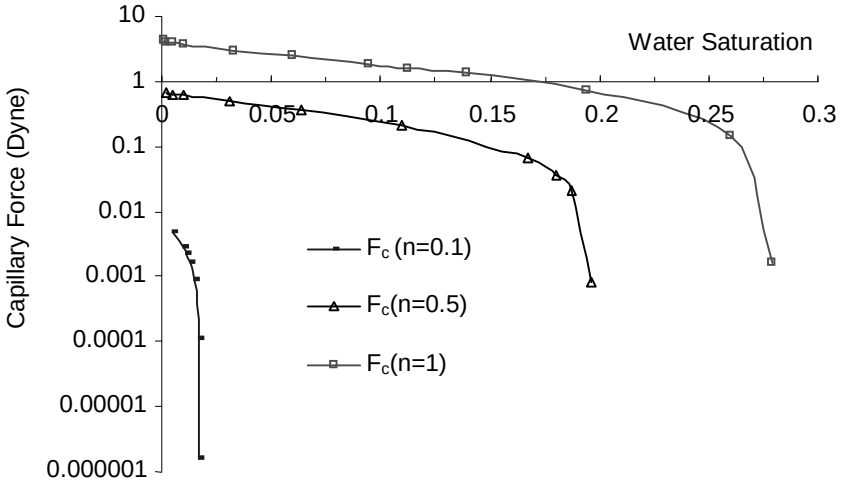

Fig. 3-28: Effect of non-uniform particle size on capillary force

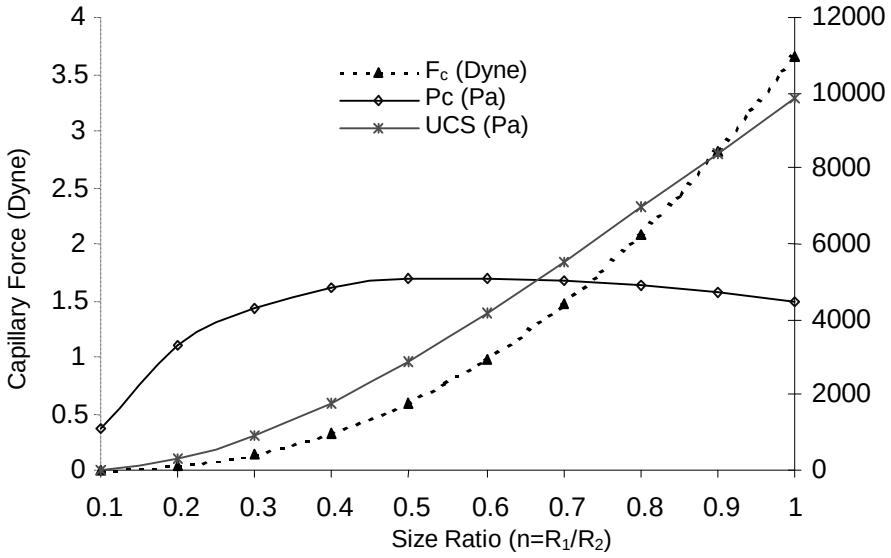

Fig. 3-29: Effect of size ratio on capillary strength (UCS) (S_w =1%)

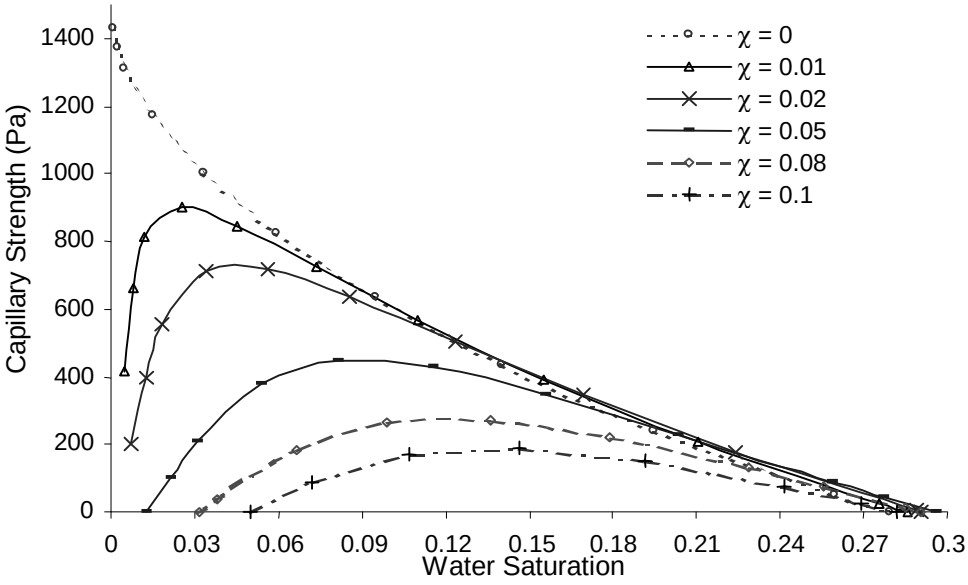

Fig. 3-30: Variations of capillary strength (UCS) in detached fabrics

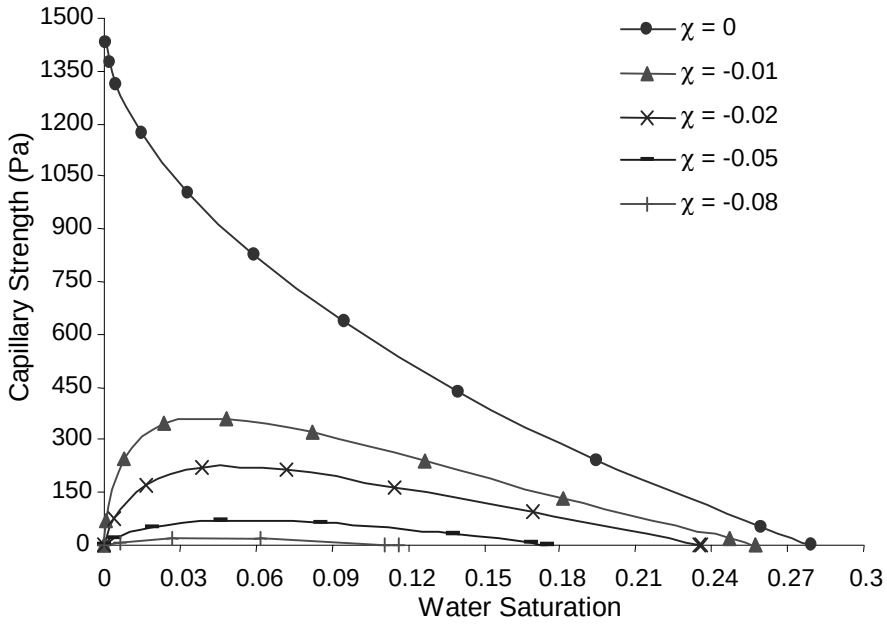

Fig.3-31: Variations of capillary strength (UCS) in squeezed fabrics

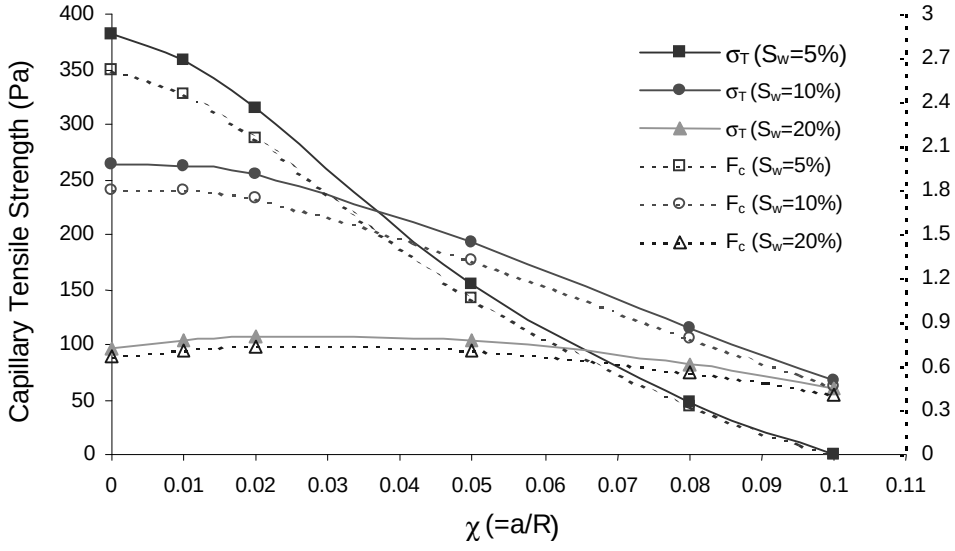

Fig. 3-32: Effect of detached extent on capillary strength

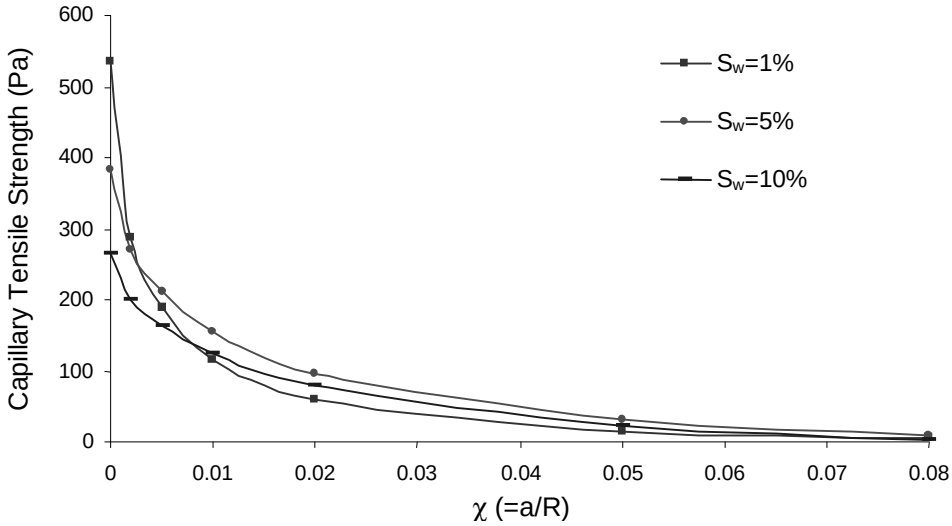

Fig. 3-33: Effect of squeezed extent on capillary strength

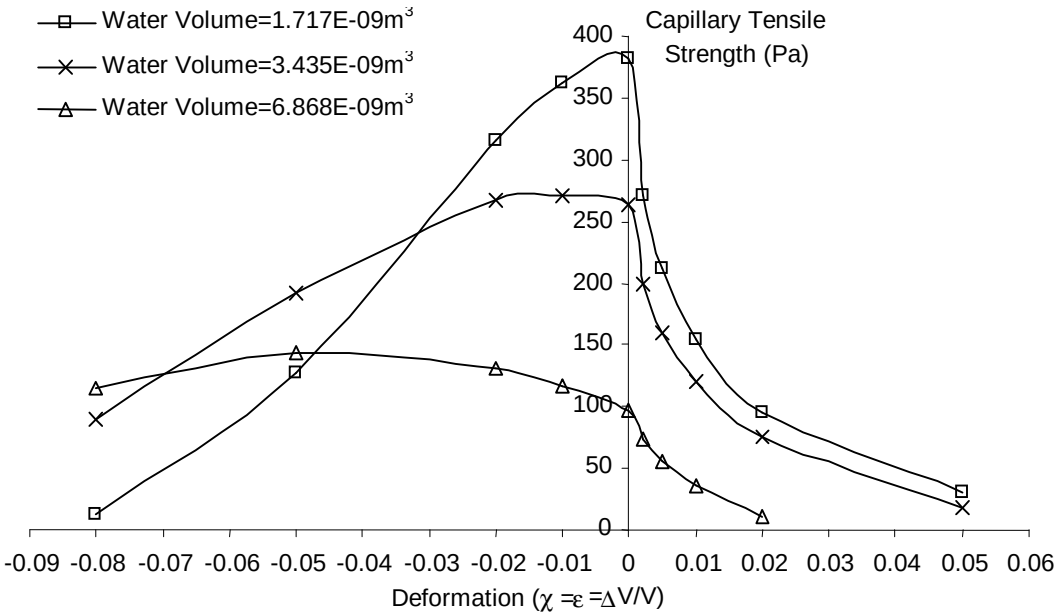

Fig.3-34: Behavior of capillary tensile strength with rock deformation

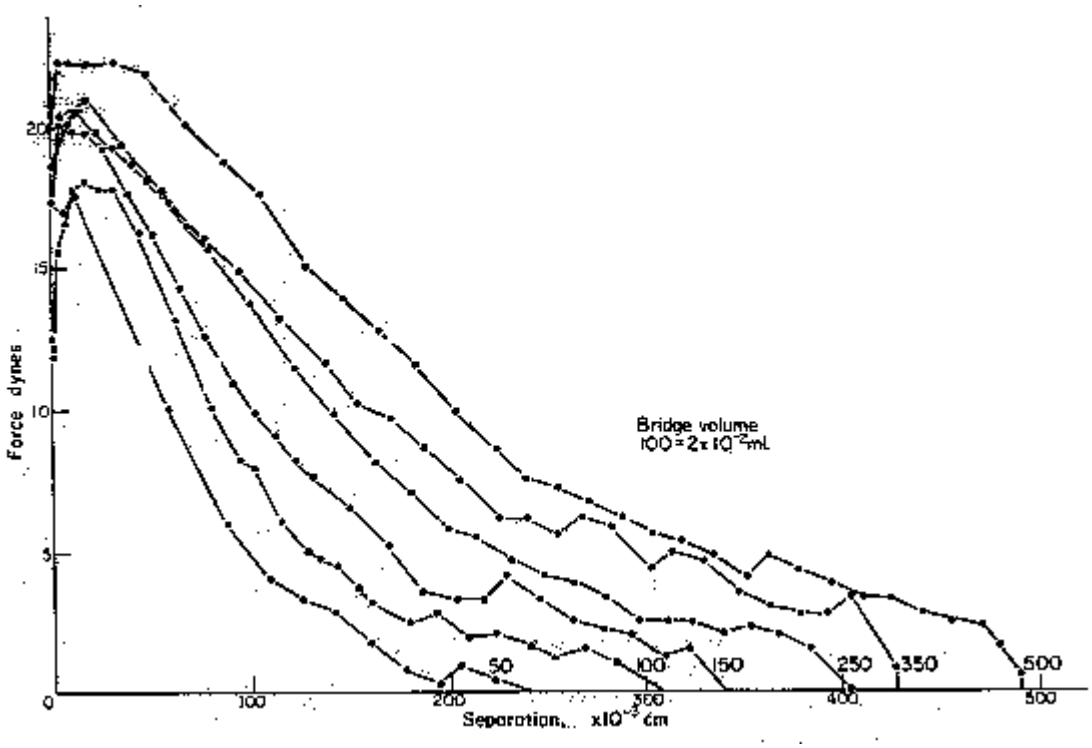

Fig. 3-35: Capillary force variations with the distance between particles
(After Mason and Clark, 1965)

Chapter 4 Coupled Stress Solutions for Water/Oil Fluid Flow

4.1 Geomechanics Model for Steady Monophase Flow

4.1.1 Coupled elastic stress model

For an elastic isotropic formation with a Biot coefficient of α, stress equilibrium in a one-dimensional cylindrical system can be expressed as

$$\frac{\partial \sigma_r}{\partial r} + \frac{\sigma_r - \sigma_\theta}{r} = 0 \tag{4.1}$$

or

$$\frac{\partial \sigma'_r}{\partial r} + \frac{\sigma'_r - \sigma'_\theta}{r} = \alpha \frac{\partial P}{\partial r} \tag{4.2}$$

where α is the negative Biot constant that is defined in Section 1.1.1. The negative sign is taken for mathematical convenience. Radial effective stress σ'_r and tangential effective stress σ'_θ can be determined by corresponding radial strain ε_r and tangential strain ε_θ relationships

$$\sigma'_r = (\lambda + 2G)\varepsilon_r + \lambda \varepsilon_\theta = (\lambda + 2G)\frac{du}{dr} + \lambda \frac{u}{r} \tag{4.3}$$

$$\sigma'_\theta = \lambda \varepsilon_r + (\lambda + 2G)\varepsilon_\theta = \lambda \frac{du}{dr} + (\lambda + 2G)\frac{u}{r} \tag{4.4}$$

where λ and G are the Lamé constants defined in Eq. (1.5), and

$$\varepsilon_r = \frac{du}{dr},\ \varepsilon_\theta = \frac{u}{r} \tag{4.5}$$

Substituting Eq (4.3), Eq. (4.4) into Eq. (4.2), the displacement, u, must satisfy

$$\frac{\partial^2 u}{\partial r^2} + \frac{1}{r}\frac{\partial u}{\partial r} - \frac{u}{r^2} = \alpha \frac{E(1-\nu)}{(1+\nu)(1-2\nu)}\frac{\partial P}{\partial r} \tag{4.6}$$

It should be noted that since the pore pressure is not only dependent upon radius but also on time ($P_p = P_p(r,t)$), so therefore is deformation ($u = u(r,t)$). The above equation can be rewritten as

$$\frac{\partial}{\partial r}\left(\frac{\partial u}{\partial r} + \frac{u}{r}\right) = \alpha \frac{(1+\nu)(1-2\nu)}{E(1-\nu)}\frac{\partial P}{\partial r} \tag{4.7}$$

Therefore

$$\frac{\partial u}{\partial r}+\frac{u}{r}=\int \alpha \frac{(1+\nu)(1-2\nu)}{E(1-\nu)}\frac{\partial P}{\partial r}dr \tag{4.8}$$

i.e. $$\frac{\partial u}{\partial r}+\frac{u}{r}=\alpha \frac{(1+\nu)(1-2\nu)}{E(1-\nu)}P+c_1 \tag{4.9}$$

The solution of this equation can be written as (see Appendix 1):

$$u=\frac{c_2(t)}{r}+c_1(t)r+\frac{\alpha}{r}\frac{(1+\nu)(1-2\nu)}{E(1-\nu)}\int^r rP_p(r,t)dr \tag{4.10}$$

where coefficients $c_1(t)$, $c_2(t)$ are variables only related to time and determined by boundary conditions. From Eqs. (4.3) and (4.4), the effective stresses can be shown to be

$$\sigma_r'=\alpha P(r,t)+\frac{Ec_1(t)}{(1+\nu)(1-2\nu)}-\frac{Ec_2(t)}{(1+\nu)}\frac{1}{r^2}-\frac{1-2\nu}{1-\nu}\frac{\alpha}{r^2}\int^r rP(r,t)dr \tag{4.11}$$

$$\sigma_\theta'=\alpha\frac{\nu}{1-\nu}P(r,t)+\frac{Ec_1(t)}{(1+\nu)(1-2\nu)}+\frac{Ec_2(t)}{(1+\nu)}\frac{1}{r^2}+\frac{1-2\nu}{1-\nu}\frac{\alpha}{r^2}\int^r rPdr \tag{4.12}$$

Total stresses can be expressed as ($\sigma = \sigma' - \alpha P$):

$$\sigma_r=\frac{Ec_1(t)}{(1+\nu)(1-2\nu)}-\frac{Ec_2(t)}{(1+\nu)}\frac{1}{r^2}-\frac{1-2\nu}{1-\nu}\frac{\alpha}{r^2}\int^r rP(r,t)dr \tag{4.13}$$

$$\sigma_\theta=\frac{Ec_1(t)}{(1+\nu)(1-2\nu)}+\frac{Ec_2(t)}{(1+\nu)}\frac{1}{r^2}+\frac{1-2\nu}{1-\nu}\left(\frac{\alpha}{r^2}\int^r rP(r,t)dr-\alpha P(r,t)\right) \tag{4.14}$$

If one assumes steady-state fluid flow, the pore pressure varies only with radius and follows Darcy's rule:

$$P(r)=P_1+\overline{K}\ln\left(\frac{r}{R_1}\right) \tag{4.15}$$

where $\overline{K}=\frac{Q\mu}{2\pi kh}$, R_1 is wellbore radius, P_1 is the bottom-hole flowing pressure, and Q is the production rate that is assumed to be constant for a formation with height h. Hence, the integration of pore pressure in Eq. (4.11) and Eq. (4.12) can be expressed as

$$\int^r rP(r)dr=\frac{r^2}{2}\left(P(r)-\frac{\overline{K}}{2}\right) \tag{4.16}$$

Therefore effective stresses in the equations can be written as

$$\sigma_r^{'} = \frac{0.5\alpha}{1-\nu}P + \frac{Ec_1}{(1+\nu)(1-2\nu)} - \frac{Ec_2}{(1+\nu)}\frac{1}{r^2} + \alpha\frac{0.5-\nu}{1-\nu}\cdot\frac{\overline{K}}{2} \tag{4.17}$$

$$\sigma_\theta^{'} = \frac{0.5\alpha}{1-\nu}P + \frac{Ec_1}{(1+\nu)(1-2\nu)} + \frac{Ec_2}{(1+\nu)}\frac{1}{r^2} - \alpha\frac{0.5-\nu}{1-\nu}\cdot\frac{\overline{K}}{2} \tag{4.18}$$

4.1.2 Discussion of boundary conditions

There are two types of boundary conditions currently used: one is at the outer boundary (R_2) where both tangential stress and radial stress are taken to be equal to the horizontal stress

BC1: $r = R_2,\ \sigma_r' = \sigma_\theta' = \sigma_h'\ (= \sigma_h + \alpha P);$ (4.19)

the other is that the effective radial stress is zero at the inner boundary and equals the horizontal effective stress at the outer boundary:

BC2: $r = R_1,\ \sigma_r' = 0\ ;\ \ r = R_2,\ \sigma_r' = \sigma_h'$ (4.20)

Both conditions are tried in this research, and results are compared.

From the first set of boundary conditions (BC1),

$$\sigma_h = -\alpha\frac{0.5-\nu}{1-\nu}(P_2 - \frac{\overline{K}}{2}) + \frac{Ec_1}{(1+\nu)(1-2\nu)} - \frac{Ec_2}{(1+\nu)}\frac{1}{R_2^{\ 2}} \tag{4.21}$$

$$\sigma_h = -\alpha\frac{0.5-\nu}{1-\nu}(P_2 + \frac{\overline{K}}{2}) + \frac{Ec_1}{(1+\nu)(1-2\nu)} + \frac{Ec_2}{(1+\nu)}\frac{1}{R_2^{\ 2}} \tag{4.22}$$

where P_2 is pore pressure at the outer boundary of the reservoir, and thus the two constants can be solved as

$$c_1 = \frac{(1+\nu)(1-2\nu)}{E}(\sigma_h + \alpha\frac{0.5-\nu}{1-\nu}P_2)\ ;\ c_2 = \alpha\frac{(1+\nu)(0.5-\nu)}{(1-\nu)E}\cdot\frac{\overline{K}R_2^2}{2} \tag{4.23}$$

Similarly, for the second boundary condition (Eq. 4.20), the stresses become

$$\sigma_h = -\alpha\frac{0.5-\nu}{1-\nu}P_2 + \alpha\frac{0.5-\nu}{1-\nu}\frac{\overline{K}}{2} + \frac{Ec_1}{(1+\nu)(1-2\nu)} - \frac{Ec_2}{(1+\nu)}\frac{1}{R_2^{\ 2}} \tag{4.24}$$

$$0 = \frac{0.5\alpha}{1-\nu}P_1 + \alpha\frac{0.5-\nu}{1-\nu}\cdot\frac{\overline{K}}{2} + \frac{Ec_1}{(1+\nu)(1-2\nu)} - \frac{Ec_2}{(1+\nu)}\frac{1}{R_1^{\ 2}} \tag{4.25}$$

and expressions for c_1, c_2 can be

$$c_1 = \frac{(1+\nu)(1-2\nu)}{E}\left[\frac{R_2^2}{R_2^2 - R_1^2}(\sigma_h + \alpha\frac{0.5-\nu}{1-\nu}P_2 + \frac{R_1^2}{R_2^2}\frac{0.5\alpha}{1-\nu}P_1) - \alpha\frac{0.5-\nu}{1-\nu}\cdot\frac{\overline{K}}{2}\right] \tag{4.26}$$

$$c_2 = \frac{1+\nu}{E}\cdot\frac{R_2^2 R_1^2}{R_2^2 - R_1^2}\left(\sigma_h + \alpha\frac{(0.5-\nu)P_2 + 0.5P_1}{1-\nu}\right) \tag{4.27}$$

With the input parameters listed in Table 4-1, these solutions are plotted in Fig. 4-1 and Fig. 4-2. Clearly, the results are strongly affected by the selection of boundary conditions: without the restraint of the inner boundary (such as BC1), stresses become wild and irrationally two orders higher than the one with the restraint (i.e. BC2). The results from BC2 seem more reasonable. In fact, although it is currently used, BC1 fails to meet the rigorous definition of boundary condition in mechanics (Charlez, 1991).

4.1.3 Poro-inelastic stress model

The above solutions are based on the assumption that the formation is linear elastic. However, weak or unconsolidated sandstones are more likely to be yielded and mobilized by stresses and fluid flow, which may lead to sand influx during fluid production. Bratli and Rinses demonstrated (1981) that there usually exists a "Coulomb zone" around the wellbore, a region characterized by low cohesion, low permeability and undergoing inelastic deformation. Hence, poroelastic solutions may be considered to be inaccurate as far as stress calculations concerned for most borehole cases. As a "rule-of-thumb", the boundary condition $\sigma_r' = 0$ @ r = R_1 should not be used to solve elastic equations, as long as a critical distance (R_c) defining the width of the Coulomb zone can be found. To avoid complexity of theoretical development, a simple approach to describe stress distributions inside the Coulomb zone is taken, which is called poro-inelastic stress model in this research because, comparing to current plasticity models, there is no strain-based flow rule involved.

The well-established Mohr-Coulomb failure criterion is used herein to stipulate the occurrence of shear failure, although the procedure is general and other yield criterion can be used. Assuming the rock stresses inside the Coulomb zone satisfy the Mohr-Coulomb failure criterion and stress equilibrium, the effective stress equilibrium equation (Eq. 4.2) becomes

$$\frac{d\sigma_r'}{dr} + \frac{1-\tan^2\beta}{r}\sigma_r' = \frac{2C_o\tan\beta + \alpha\overline{K}}{r} \tag{4.28}$$

and solutions can be found to be

$$\sigma'_r(r) = \frac{c_3}{\omega} r^{-\omega} + \frac{2C_o \tan\beta + \alpha\overline{K}}{\omega} \tag{4.29}$$

$$\sigma'_\theta(r) = \frac{c_3(1-\omega)}{\omega} r^{-\omega} + \frac{2C_o \tan\beta + \alpha(1-\omega)\overline{K}}{\omega} \tag{4.30}$$

where $\omega = 1 - \tan^2\beta$. Since at the inner boundary the rock radial effective stress must be zero, i.e $\sigma'_r(R_1) = 0$, a solution for the constant c_3 can be found:

$$c_3 = -\left(2C_o \tan\beta + \alpha\overline{K}\right) \cdot R_1^{\omega} \tag{4.31}$$

Therefore at the outer boundary of Coulomb zone, i.e., at r = R_c, the stresses should be

$$\sigma'_r(R_c) = \frac{c_3}{\omega} R_c^{-\omega} + \frac{2C_o \tan\beta + \alpha\overline{K}}{\omega} \tag{4.32}$$

$$\sigma'_\theta(R_c) = \frac{c_3(1-\omega)}{\omega} R_c^{-\omega} + \frac{2C_o \tan\beta + \alpha(1-\omega)\overline{K}}{\omega} \tag{4.33}$$

Furthermore, the radial stresses should be continuous across the elastic and Coulomb zone transition, i.e., at r = R_c, so that the stresses calculated from coupled poroelastic solutions (Eqs. 4.17 and 4.18) should equal those from Eqs. (4.32) and (4.33), i.e.

$$\frac{c_3}{\omega} R_c^{-\omega} + \frac{2C_o \tan\beta + \alpha\overline{\mathrm{K}}}{\omega} = \frac{0.5\alpha}{1-\nu} P_c + \frac{Ec_1}{(1+\nu)(1-2\nu)} - \frac{Ec_2}{(1+\nu)} \frac{1}{R_c^2} + \alpha \frac{0.5-\nu}{1-\nu} \frac{\overline{\mathrm{K}}}{2} \tag{4.34}$$

$$\frac{c_3(1-\omega)}{\omega} R_c^{-\omega} + \frac{2C_o \tan\beta + \alpha(1-\omega)\overline{\mathrm{K}}}{\omega} = \frac{0.5\alpha}{1-\nu} P_c + \frac{Ec_1}{(1+\nu)(1-2\nu)} + \frac{Ec_2}{(1+\nu)} \frac{1}{R_c^2} - \alpha \frac{0.5-\nu}{1-\nu} \frac{\overline{\mathrm{K}}}{2} \tag{4.35}$$

where P_c is pore pressure at R_c and can be expressed as $P_c = P_1 + \overline{K} \ln\left(\frac{R_c}{R_1}\right)$. Another boundary condition used is the assumption that, in the far field, the effective radial stress is equal to the horizontal effective stress (i.e. $\sigma'_r(R_2) = \sigma'_h$):

$$\sigma'_h = \frac{0.5\alpha}{1-\nu} P_2 + \frac{Ec_1}{(1+\nu)(1-2\nu)} - \frac{Ec_2}{(1+\nu)} \frac{1}{R_2^2} + \alpha \frac{0.5-\nu}{1-\nu} \frac{\overline{\mathrm{K}}}{2} \tag{4.36}$$

Finally, the three unknown constants R_c, c_1, c_2, in the above three equations can be solved:

$$c_1 = \frac{(1+\nu)(1-2\nu)}{E} \left(\sigma'_h - \frac{0.5\alpha}{1-\nu} P_2 + \frac{Ec_2}{(1+\nu)} \frac{1}{R_2^2} - \alpha \frac{0.5-\nu}{1-\nu} \frac{\overline{\mathrm{K}}}{2}\right) \tag{4.37}$$

$$c_2 = -\frac{1+\nu}{2E}\left(\frac{0.5\alpha}{1-\nu}\overline{\mathrm{K}} + c_3 R_c^{-\omega}\right)\cdot R_c^2 \tag{4.38}$$

$$\sigma_h' - \frac{2C_o\tan\beta + \alpha\overline{\mathrm{K}}}{\omega} + \frac{0.5\alpha}{1-\nu}\frac{\overline{\mathrm{K}}}{2} = \frac{c_3}{2R_2^{\,2}}R_c^{\,2-\omega} + \left(\frac{1}{\omega} - \frac{1}{2}\right)c_3 R_c^{\,-\omega} + \frac{0.5\alpha\overline{\mathrm{K}}}{1-\nu}\left[\frac{R_c^{\,2}}{2R_2^{\,2}} - \ln\left(\frac{R_c}{R_2}\right)\right] \tag{4.39}$$

Eq. (4.39) is a nonlinear equation of R_c, in the form of $f(R_c^{2-\omega}, R_c^{-\omega}, R_c^2, \ln(R_c)) = 0$, which can be easily solved with the aid of mathematical software (e.g. Matlab).

The stress solutions are plotted in Fig. 4-3. Comparing these to their poroelastic counterparts (dashed lines), the inelastic stresses shift the concentration of shear stress away from the wellbore. Directly applying elastic stress equations Eq. (4.17) and Eq. (4.18) into the Mohr-Coulomb failure expression Eq. (1-11), the equation of R_c will be

$$\frac{0.5\alpha}{1-\nu}(1-\tan^2\beta)P_c + (1-\tan^2\beta)\frac{Ec_1}{(1+\nu)(1-2\nu)} + (1+\tan^2\beta)\frac{Ec_2}{(1+\nu)}\frac{1}{R_c^{\,2}} -$$

$$(1+\tan^2\beta)\frac{0.5-\nu}{1-\nu}\frac{\alpha\overline{K}}{2} - 2C_o\tan\beta = 0 \tag{4.40}$$

with boundary condition BC2 (Eq. 4.20), the solution of R_c is 0.1393 m, appreciably smaller than the value determined by Eq. (4.39): R_c = 0.4327 m.

However, the poro-inelastic stress solutions treat the Coulomb zone as a zone with constant low cohesive shear strength (C_o). This obviously conflicts with the fact that sand becomes weaker with the extent of shear yield (plastic strain), leading to a non-constant reduced cohesion or even a cohesionless state after large plastic strain. Fig. 4-4 demonstrates the effect of cohesive strength on stress distributions inside the Coulomb zone: when C_o becomes small (C_o is from 0.5 to 0.178 MPa), stresses are lowered significantly at the same distance while the critical radius increases dramatically (i.e. the Coulomb zone is enlarged). Therefore Eq. (4.29) and Eq. (4.30) give the upper limit of stresses inside the plastic zone, and should be treated as conservative solutions.

One common approach to compensate for this is to add a plastic strain to the elastic strain calculated by Hooke's law, and this type of strain is defined by plastic theory. (Bradford and Cook, 1994; Wang, 2002). But as far as rock is concerned, those plasticity models need intensive calibrations before being applied in practice; in fact, many researchers believe that a nonlinear theory based on rock moduli and other properties that change with loading stresses is more

convincing and reasonable. Some developments have been made during the past few decades (Santarelli and Brown 1986; Nawrocki and Dusseault 1995; Vaziri 1995), but additional experiments are needed in order to determine the parameters, and this affects budgets and presents substantial challenges for geomechanics modelers. Damage theory (e.g. Cheng and Dusseault, 2002) is somewhat more useful in describing strength behaviors and rock property changes than classical plasticity theory, but the deformation parameters in most versions of damage mechanics theories are not linked to stress level.

Developing more comprehensive and mathematically advanced stress models is beyond the scope of this research, which focuses on the effect of water saturation on stress distributions and rock properties. The inelastic models developed above with appropriate boundary conditions are the basis for the stress calculations in this research.

4.2 Stress-Dependent Porosity and Permeability

4.2.1 Stress-dependent permeability and previous models

Concepts of stress-dependent permeability of porous media have attracted attention from production engineers and reservoir engineers for about 50 years (Fatt and Davis, 1952), as such a phenomenon could significantly affect well production rate, reserves estimates, profitability predictions and so on. For stress-sensitive materials such as low permeability lithic sandstones, collapsing chalk, or fractured rock, the reduction of permeability can be as high as 90% (Thomas and Ward, 1972; Jones and Owens, 1980; Yale, 1984; Kilmer et al., 1987), leading to losses of up to 50% of the production rate (Vairogs et al. 1971). Yale (1984) showed that the decrease of permeability could approach 5% for 500 - 1,000 mD permeability sandstones with an increase in isotropic effective (matrix) stresses from 3.45 to 34.5 MPa ($\Delta\sigma'_1 = \Delta\sigma'_2 = \Delta\sigma'_3$).

However, when stress changes are anisotropic (deviatoric) because of boundary conditions, depletion effects in the field, or a non-isotropic *in-situ* stress state and sand fabric, the behavior of permeability reduction with increasing stress is not yet clear. Holt (1990) reported that changes in permeability became more significant in the presence of non-isotropic stresses: up to 10% of its initial value (sample porosity 25% and initial permeability from 1 to 2.5 Darcies). King et al. (2001) found that permeability was 10% lower in their triaxial tests, compared to hydrostatic stress tests (initial permeabilities were 366 mD, 220 mD, 15 mD in the three principal stress directions).

It has been found that in triaxial compression tests a small permeability increase occurs when rock is compressed close to failure (Morita et al., 1984; Keaney et al., 1998), and therefore fluid flow is enhanced (Tronvoll and Fjær, 1994) because of shear dilation of microcracks or particle sliding. However, these reports were limited to low permeability samples (for Keaney's experiment, 3 μD; for Morita, 100 to 200 mD). Also, it is very challenging to model shear dilation, shear-induced grain crushing, or interstitial mineral grain mobilization within the scope of continuum theories.

Despite only a partial understanding of the complicated permeability behavior with stresses, some models have been proposed to quantify this phenomenon, most of which are "strain-dependent" (Chin et al., 2000; Wang and Xue, 2002); i.e., permeability calculations are based on the strain determined by a geomechanics stress-strain model. Even though it is mathematically convenient to relate porosity changes to volumetric strain, this type of model needs intensive laboratory calibrations before it can be applied in the field. This is because strain is sensitive to many factors such as stress (loading and confining stress) levels, stress path and anisotropy, loading rate and history, pressure depletion or increase, sample size, shape, and so on. There exist some empirical relationships between permeability and stress that have been developed from curve-fitting analysis of experimental data, requiring two (Ostensen, 1986) to four (Jones and Owens, 1980; Jones, 1998) coefficients. However, these are purely empirical relations, and the authors did not tried to generate more generalized stress-dependent porosity and permeability distributions around a wellbore, both of which should be input and output variables of a coupled geomechanics model to calculate stress level.

It is well accepted that there does not exist a unique relationship between permeability and stress (Fatt and Davis, 1952; Jamtveit and Yardley, 1997; Davies, 2001). Nevertheless, it is possible to develop a methodology to describe permeability alterations with rock stress as part of reservoir simulation or geomechanical analysis. In this section, based on a nonlinear theory and currently available empirical relations, a novel analytical method is developed to describe the distribution of stress-dependent porosity and permeability around a wellbore producing oil from high porosity (such as unconsolidated sand) reservoirs. As an application, a new criterion is proposed to evaluate whether porosity (or permeability) should be considered to be stress-dependent or a constant in a geomechanics analysis.

4.2.2 Porosity vs. stress

Applying four types of compressibilities defined by Zimmerman (1986) into geomechanics analysis, four stress-pressure related compressibilities can be defined:

Effective bulk compressibility $$C_{bc} = -\frac{\partial V_b}{V_b}\frac{1}{\partial \sigma} \tag{4.41}$$

Pseudo-bulk compressibility $$C_{bp} = \frac{\partial V_b}{V_b}\frac{1}{\partial P} \tag{4.42}$$

Formation Compaction Coefficient $$C_{pc} = -\frac{\partial V_p}{V_p}\frac{1}{\partial \sigma} \tag{4.43}$$

Effective pore compressibility $$C_{pp} = \frac{\partial V_p}{V_p}\frac{1}{\partial P} \tag{4.44}$$

In these definitions, σ and P are rock total stress and fluid pore pressure, and V_b and V_p are bulk and pore volume, respectively. The advantage of this classification is that rock volume change upon loading has been separated into bulk and pore volume changes affected by either total stress or pore pressure variations. These compressibilities follow certain relationships

$$C_{bc} = C_{bp} + C_m; \qquad C_{pc} = C_{pp} + C_m; \qquad C_{bp} = \phi C_{pc} \tag{4.45}$$

where C_m is rock matrix compressibility.

Porosity changes under loading condition are defined as:

$$d\phi = d(\frac{V_p}{V_b}) = \frac{dV_p}{V_b} - \phi\frac{dV_b}{V_b} \tag{4.46}$$

Substituting $dV_p = -C_{pc}V_p d\sigma + C_{pp}V_p dP$, and $dV_b = -C_{bc}V_b d\sigma + C_{bp}V_b dP$ into the above expressions gives

$$d\phi = -\phi C_{pc} d\sigma + \phi C_{pp} dP + \phi C_{bc} d\sigma - \phi C_{bp} dP \tag{4.47}$$

Using the relationships among compressibilities, the porosity changes are

$$d\phi = -[C_{bc}(1-\phi) - C_m]d\sigma' \tag{4.48}$$

where σ' is the difference between total stress and pore pressure ($\sigma' = \sigma$ - P). Similarly, the bulk volumetric strain ε_b can be calculated as

$$d\varepsilon_b = -\frac{dV_b}{V_b} = C_{bc}d\sigma - C_{pc}dP = C_{bc}d\sigma' + C_m dP \tag{4.49}$$

Combining with Eq. (4.48),

$$d\phi = -(1-\frac{C_m}{C_{bc}} - \phi)(d\varepsilon_v - C_m dP) \tag{4.50}$$

which is in agreement with Wang and Dusseault's work (1991), except for the negative sign because of a different sign convention. As far as unconsolidated and weakly consolidated sand are concerned, C_m is assumed to be small enough to be negligible; therefore Eq. (4.48) and Eq. (4.50) can be written as:

$$d\phi = -(1-\phi)d\varepsilon_v \tag{4.51}$$

an equation which has been widely used in coupled geomechanics models; and,

$$d\phi = -C_{bc}(1-\phi)d\sigma' \tag{4.52}$$

which is the form that will be used herein.

4.2.3 Compressibility vs. stress

The integration of Eq. (4.52) involves the expression of stress-dependent bulk compressibility, C_{bc}. As bulk compressibility is the easiest to measure in the laboratory, a common approach is to derive an empirical relationship based on experiment data, e.g. in the form of (Zimmerman, 1991)

$$C_{bc} = a_1 + a_2 e^{-a_3\sigma'} \tag{4.53}$$

or (Rhett and Teufel, 1992)

$$C_{bc} = \frac{b_1}{(1+b_2\sigma')^2} \tag{4.54}$$

or (Jones, 1998)

$$C_{pp} = \frac{d_3 e^{-\sigma'/d_1}}{d_1} + \frac{d_2}{1+d_2\sigma'} \tag{4.55}$$

where a_1, a_2, a_3, b_1, b_2, d_1, d_2 and d_3 are constants determined from curve-fitting analysis. Therefore, Eq. (4.52) can be integrated into the following forms:

$$\ln\left(\frac{1-\phi}{1-\phi_i}\right) = a_1(\sigma' - \sigma_i') - \frac{a_2}{a_3}(e^{-a_3\sigma'} - e^{-a_3\sigma_i'}) \tag{4.56}$$

$$\ln\left(\frac{1-\phi}{1-\phi_i}\right)=\frac{b_1}{b_2}\left(\frac{1}{1+b_2\sigma_i'}-\frac{1}{1+b_2\sigma'}\right) \tag{4.57}$$

$$\ln\left(\frac{1-\phi}{1-\phi_i}\right)=\ln\left(\frac{1+d_2\sigma'}{1+d_2\sigma_i'}\right)+d_3\left(e^{-\frac{\sigma_i'}{d_1}}-e^{-\frac{\sigma'}{d_1}}\right) \tag{4.58}$$

where ϕ_i and σ'_i are initial porosity and initial mean effective stress (i.e. far field in-situ mean effective stress).

The other way to calculate bulk compressibility is based on nonlinear theory. Bulk modulus can be expressed as (Duncan and Chang, 1970; Byrne et al., 1987; Vaziri, 1995)

$$B_K = nP_a\left(\frac{\sigma'}{P_a}\right)^m \tag{4.59}$$

where P_a is atmospheric pressure (for normalization), and m and n are the hyperbolic equation parameters. For soils, the parameter values have been determined (Byrne et al., 1987), e.g. m is usually taken as a constant of 0.25. Hence bulk compressibility can be expressed as

$$C_{bc} = \frac{1}{B_K} = \frac{P_a^{m-1}}{n}(\sigma')^{-m} \tag{4.60}$$

The integration of Eq. (4.52) gives

$$\int_{\phi_i}^{\phi}\frac{-1}{1-\phi}d\phi=\int_{\sigma_i'}^{\sigma'}\left[\frac{P_a^{m-1}}{n}(\sigma')^{-m}\right]d\sigma' \tag{4.61}$$

Hence

$$\ln\frac{1-\phi}{1-\phi_i}=\frac{P_a^{m-1}}{(1-m)n}\left[(\sigma')^{(1-m)}-(\sigma_i')^{(1-m)}\right] \tag{4.62}$$

or

$$\phi = 1-(1-\phi_i)e^{\frac{P_a^{m-1}}{(1-m)n}\left[(\sigma')^{(1-m)}-(\sigma_i')^{(1-m)}\right]} \tag{4.63}$$

As indicated in Eq. (4.63), porosity changes are solely related to the state of effective stress through application of these concepts.

The four methods of empirically including compressibility (i.e. Eqs. (4.53)-(4.55) and (4.60)) and porosity (Eqs. (4.56)-(4.58) and (4.62)) discussed above are compared in Fig. 4-5 and Fig. 4-6, with the input parameters listed in Table 4-2. The porosities used for this calculation

range from 0.10 (tight sand, Jones, 1998), 0.13 (North Sea sand, Rhett and Teufel, 1992), 0.16 (Bandera Sand, Zimmerman, 1991), 0.18 (Berea Sand, Zimmerman, 1991), 0.27 (Boise Sand, Zimmerman, 1991), to above 0.3 (unconsolidated sandstone, Eq. (4.63)). As shown in Fig. 4-5, the rock compressibility, and consequently the porosity, becomes small as effective stress increases (Fig. 4-6), while their decrease rates follow the same trend: less property changes occur when rock becomes more and more compacted (i.e. in high in-situ confining stress conditions). Furthermore, the lower the porosity and the higher the bulk compressibility, the larger the alterations of the stress-dependent porosity and compressibility: for Jones' model ($\phi < 0.1$), rock porosity loses about 20% with stress increases of less than 5 MPa; however, for high porosity rock (ϕ>30%), the porosity loss is almost negligible given the same stress variations.

In both figures, the porosity calculation based on nonlinear theory shows particular applicability to high-porosity (or unconsolidated) sandstones, probably because nonlinear theory was initially developed for soil, which is similar to unconsolidated sandstone. As around a wellbore there usually exists a zone of low cohesion and often damaged granular material in a relatively low stress environment (at least the radial stress, σ'_r, is low), the approximations that are commonly used in soil mechanics, such as soil strength being dominated by frictional behavior and geometrical relationships among individual particles, become just as valid as other assumptions, perhaps more so.

4.2.4 Permeability vs. porosity

Many approaches have been proposed to describe the relationship of permeability to porosity and other rock properties. These approaches can be classified into two categories (Dullien, 1979): geometrical permeability models that treat fluid flow in porous media as a network of conduits, and statistical permeability models in which a probability law is applied. Among the geometrical methods, the Carman-Kozeny model is popular because of its simplicity:

$$k = \frac{\phi^3}{5(1-\phi)^2 S^2} \tag{4.64}$$

where specific surface area, S, can be derived as $S = \sqrt{\frac{\phi_i^{\,3}}{5(1-\phi_i)^2 k_i}}$, and ϕ_i and k_i are porosity and permeability under initial conditions. It holds well for unconsolidated and weakly consolidated spherical particulate assemblies (Dullien, 1979; Holt, 1990). However, it should be noted that permeability can easily deviate from the description of Eq. (4.64), particularly if small amounts of fine-grained materials such as clays or silt are present in a coarser-grained assembly.

Also, relative permeability in multi-phase cases cannot easily be based on such a relationship. For example, Davies (2000) showed there is no consistent relationship of porosity with permeability for sand samples from the Gulf of Mexico and southern California when porosity exceeds 20%. As a matter of fact, permeability is not only dependent on porosity and specific surface area, but also on the size distribution, skewness, the topographical arrangement of capillaries, and the amount and location of interstitial fine-grained minerals. Even though Eq. (4.64) is used hereafter, other types of porosity-permeability relationships can also be applied, following similar steps discussed below, for specific cases where adequate laboratory information are available. This empiricism is necessary, given the complexity of the problem, but the use of such a relationship is attractive because semi-analytical solutions can be derived.

Fig. 4-7 shows the calculated variations of stress-dependent porosity and permeability with the nonlinear theory developed above. In the stress range of 0 to 40 MPa, porosity changes are magnified when interpreted as permeability variations: from 1% for porosity to 4.5% for permeability, which agrees with experimental observations (e.g. Mohuiddin et al., 2000).

4.2.5 Permeability vs. distance from wellbore

For the elastic zone, effective mean stress in Eq. (4.63) can be determined by Eq. (4.17) and Eq. (4.18):

$$\sigma_e' = \frac{\sigma_r' + \sigma_\theta'}{2} = \frac{0.5\alpha}{1-\nu} P(r) + \frac{Ec_1}{(1+\nu)(1-2\nu)} \tag{4.65}$$

For the Coulomb zone, it can be expressed as

$$\sigma_p' = \frac{c_3(1-\omega/2)}{\omega} r^{-\omega} + \frac{2C_o \tan\beta + (1-\omega/2)\alpha\overline{K}}{\omega} \tag{4.66}$$

Substituting Eqs. (4.65) and (4.66) into Eq. (4.52), the relationship between permeability and effective stress can be determined. It should be noted there are no time-dependent effects considered; rock properties are assumed to be independent of time.

Some arguments have been put forward suggesting that effective stress theory becomes questionable (or at least inadequate) when permeability-stress relationships are analyzed (e.g. Zoback and Byerlee, 1975). However, the experiments they performed with Berea Sandstone were executed with the assumption that pore pressure and confining stress can be changed independently, i.e. the magnitude of pore pressure increase or decrease equals the changes of effective stress ($\Delta\sigma' = \Delta P$) if constant confining stress and elastic rock state are assured. Unfortunately, the changes of effective stress, as shown in Eq. (4.65), are a function of the

variations of pore pressure but do not equal them. Pore pressure and effective stress are so closely interlaced that they can not be separately analyzed, let alone the additional effect of Biot's constant that should be considered when consolidated sand is concerned.

4.2.6 Should permeability be considered as stress-dependent?

Distributions of stress-dependent permeability and porosity around a wellbore producing oil from high-porosity sand are determined and plotted in Fig. 4-8. Comparing to the initial values, both permeability (solid line) and porosity (dashed line) decrease promptly inside the Coulomb zone, while beyond the critical radius the reduction rates are small. This is because of the nature of the stress distributions around the wellbore (Fig. 4-3): within the critical distance the mean effective stress (σ'_m) has a steep gradient, whereas it changes little in the elastic zone. It should be noted that the initial permeability and porosity are defined at atmospheric stress (i.e. 0.1 MPa), while the dimensionless variables, which are constantly below 1.0, are the ratios of the current property values to their original ones.

The variations of permeability and porosity are relatively small, about 3.2% and 0.7%, respectively. When reflected in pore pressure calculations, the stress-dependent permeability model only predicts about 1.6% change (solid line in Fig. 4-8), and much of this takes place near the wellbore. Zimmerman's model for Boise Sand, which has high porosity and is weakly consolidated, produces a similar effect (dashed line in Fig. 4-8): pore pressure variations are less than 1.8% of its original value. It is therefore concluded that for clean unconsolidated sand with parameters roughly similar to those listed in Table 4-2, the stress-dependent porosity and permeability may be negligible in practice. This conclusion is consistent with the experiments reported by Yale (1984) and Sarda et al. (1998).

However, these permeability calculations inside the Coulomb zone conflict with data showing that permeability has indeed been significantly lowered in many cases, e.g. cases where less than half of the original value has been left (Bratli and Rinses, 1980; Holt, 1990; Sarda et al., 1998). This is because the model above did not take account of changes of rock properties after shear yield. As pore throats in sand have been reshaped after sand particles rearrange and fracture occurs, specific surface area and pore throat apertures changes significantly, particularly under conditions of large stress changes. Even though some approaches are developed to describe permeability evolutions with plastic deformation (e.g. Simoni, 1999; Yale, 2002), a method based on reasonable physics simplifications remains a challenge, mainly because the rock in the Coulomb zone is little studied due to the limitations of core collection and experimentation.

There are some experiments that report obvious permeability variations in high-porosity sand (Holt, 1990; Morita, 1984), but the suitability of the experimental conditions as field analogues are in question. For example, the 10 - 95% permeability reduction in Holt's experiment (Fig. 4-10) was detected when rock samples were axially loaded up to 80 MPa, whereas the real (in-situ) effective stresses are only about $\sigma'_v \approx 15$MPa and $\sigma'_h \approx 7.5$MPa for that sandstone. From the shape of the response curve, it is obvious that massive grain crushing was initiated in the specimen.

4.2.7 Model limitations and suggestions for future research

Other than effective stress, there are many additional factors that may affect the permeability distributions around a wellbore, either in a positive (permeability enhancement) or a negative (formation damage) manner. For example, shear dilatancy (Dusseault and Rothenburg, 1988) and production of sand particles (Geilikman and Dusseault, 1997) can significantly increase permeability, whereas infiltration of drilling fluid, formation of mud cake, fabric perturbations caused by workovers, and accumulation of permeability-sensitive materials such as clay and asphaltenes will usually result in permeability reduction. Those factors may play more important roles than stress in their effects on permeability impairment, and some developments have been made to model those factors with respect to rock geomechanical responses (e.g. Wang and Dusseault, 1991; Zhang and Dusseault, 1997); however in this paper only stress is considered.

Besides the need to develop empirical relations for use in the model developed above, another big challenge is the lack of a description of permeability anisotropy. Crawford and Smart (1994) demonstrated that changes of vertical permeability are much less than those of horizontal permeability in triaxial compression tests, given the same mean stress increase. Because continuum theories face great challenges in macroscopically modeling permeability anisotropy in non-hydrostatic loading stress environment, particulate mechanics models may provide an alternative and more satisfactory approach in terms of describing pore structure changes at the grain scale level. Microscopically, when sand particles are loaded, several responses may occur:

- Particles undergo elastic deformation, such as changes in particle shape (Davies and Davies, 2001). Micas and shale fragments are minerals that can be easily altered in shape, whereas monomineralic fragments such as quartz and feldspar grains require higher load levels to evidence significant shape changes;
- Particles rotate, slip, and rearrange themselves, although this is most likely at low stress levels when particles are loosely packed and unconsolidated;

- Particles, particularly weak lithic fragments or coccoliths, experience fracturing and crushing as forms of plastic deformation. Pore throats are thereby "collapsed", and liberation of appreciable quantities of fine-grained particles tends to block intact pore throats, lead directly to sand production and even wellbore collapse; and,
- Interstitial clay and silicate particles are dislodged by shear strains, bridging across pore throats and affecting the permeability disproportionately. Interstitial minerals are often bound to the silicate substrate so lightly that small hydrodynamic forces, combined with geochemical and capillary changes or shear distortion, can mobilize them.

Hertz contact theory can only reach the first effect, i.e. particle elastic deformation (Wong and Li, 2000; Bai et al., 2002), and the other three situations remain to be explored quantitatively in future research.

4.3 Geomechanics Model for Two-Phase Flow

4.3.1 An optimized microscopic capillary model

Based on Chapter 3.3, it has been found that capillary strength:

- generally decreases with water saturation and eventually disappears after some specific saturation level that is affected by contact angle, size difference between particles, and contact fabric;
- increases linearly with increasing surface tension;
- increases with smaller particle diameters;
- decreases with large size differences;
- decreases with increase of contact angle; and,
- generally decreases with particle deformation, either extension or compression.

From a practical point of view, i.e. assuming that water breakthrough is relatively sudden and water saturation increases quickly to some level that makes capillary forces relatively small, a "safe" or conservative model should be selected to describe how significant is the impact of capillary force changes on rock stability after water breakthrough. Another consideration is the limitation in practice on system parameters; some parameters such as contact angle, surface tension, and grain size difference may not be available from routine petrophysical activities. Hence, a model that would account for a maximum change of capillary strength, but with modest input data requirements, should be considered. This leads to a set of analytical assumptions that would support such a conservative approach:

- Particles in the model should be set with as small a diameter as possible (linked to the lower limit of the available grain size data, perhaps D_{10});
- The value of surface tension should be the upper limit of available data;
- The contact angle should be set to zero, which maximizes capillary strength;
- A uniform particle size should be assumed; and,
- A tangential contact fabric should be assumed.

As a consequence, instead of pursuing complex particle combinations such as the one shown in Fig. 4-11, a more practical model is proposed in which particles have the same size, contact tangentially, and with a zero contact angle (Fig. 4-12).

Bearing in mind the limits on practical availability of input data, the models presented above have deliberately been developed to require a limited number of input parameters. For example, the capillarity model only needs two inputs: particle radius (R) and surface tension (γ), whereas parameter λ in Eq. (3.3) can be selected based on the distribution of particle size (Table 4-3). The surface tension between oil and water can be set as high as 0.036 N/m (which is the value for heavy oil and water), as capillary strength is linearly related to surface tension and the peak strength is needed for calculations. As a result, only particle radius is de facto required. The relation of oil and water relative permeabilities to water saturation (Table 4-4) is usually available for reservoir simulations. If capillary pressure data have been determined at the same time, calibration of the microscopic capillarity model is straightforward.

4.3.2 Pore pressure calculations

After water breakthrough, two pressures exist: water pressure and oil pressure. Assuming steady-state fluid flow in an infinite reservoir, they can be calculated by

$$P_w(r) = P_2 - \frac{Q_w \mu}{2\pi k k_{rw} h} \ln\left(\frac{R_2}{r}\right) \tag{4.67}$$

$$P_o(r) = P_2 - \frac{Q_o \mu}{2\pi k k_{ro} h} \ln\left(\frac{R_2}{r}\right) \tag{4.68}$$

where P_w, P_o are water and oil pressure at distance "r" from the wellbore, respectively; P_2 is far-field reservoir pressure; k is absolute permeability; k_{rw} is the relative permeability to water, and k_{ro} is the relative permeability to oil. The difference of the two pressures is equal to the capillary pressure:

$$P_w - P_o = -P_c \tag{4.69}$$

Following the development of effective stress theory by Bishop (1959) and Bishop et al. (1963), a relationship of the form $P(r) = P_w(r)S_w - P_o(r)(1-S_w)$ is conventionally used to determine pore pressure in multiphase environments (Simoni et al. 1999; Zhang et al. 2001; Shrefler and Scotta 2001). However, this has not been physically confirmed, as saturation is a concept of volume, compared to pore pressure, an areal concept. Furthermore, it is well known that when water saturation reaches a certain level (less than 100%), capillary bridges will collapse and capillary forces will disappear. This fact has been overlooked in current theories of pore pressure calculation. In the following development, a novel method based on physics is developed to calculate pore pressure at grain scale in two-phase fluid environment.

From Fig. 4-12, the force from pore fluid pressure acting on the particle surface is

$$P(r)A = P_w(r)A_w + P_o(r)A_o \tag{4.70}$$

where A_w, A_o are areas on which water and oil are acting, respectively, and A is particle surface area. The equation can be rewritten as

$$P(r) = P_w(r)\frac{A_w}{A} + P_o(r)\frac{A_o}{A} \tag{4.71}$$

The ratio of A_w/A and A_o/A can be derived within the dashed frame of Fig. 4-12:

$$A_w/A = 2\beta_w/\pi; \qquad A_o/A = 1 - 2\beta_w/\pi \tag{4.72}$$

After replacing $P_o(r)$ with $P_w(r)$ through Eq. (4.69), Eq. (4.72) becomes

$$P(r) = P_w(r) + P_c(1-\frac{2\beta_w}{\pi}) \text{ or } P(r) = P_o(r) - P_c\frac{2\beta_w}{\pi} \tag{4.73}$$

Finally, with constant production rate, the expression for pore pressure can be written as

$$P(r) = P_2 - \frac{Q\xi(S_w)}{2\pi kh}\ln\left(\frac{R_2}{r}\right) \tag{4.74}$$

where R_1 is wellbore radius, P_1 is bottom flowing pressure, Q is production rate assumed to be a constant ($Q = Q_w + Q_o$), and $\xi(S_w) = \frac{2\beta_w}{\pi}\frac{f_w}{k_{rw}/\mu_w} + \left(1-\frac{2\beta_w}{\pi}\right)\frac{f_o}{k_{ro}/\mu_o}$. Furthermore, f_w and f_o are water and oil cut in fluid production, respectively, and can be related to each other through $f_w = 1- f_o$. Water cut can be calculated through

$$f_w = \frac{Q_w}{Q} = \frac{-\frac{Akk_{rw}}{\mu_w}\frac{dP_w}{dr}}{-Ak(\frac{k_{rw}}{\mu_w}\frac{dP_w}{dr}+\frac{k_{ro}}{\mu_o}\frac{dP_o}{dr})} \tag{4.75}$$

With Eq. (4.69), considering capillary pressure as only related to water saturation (i.e. $dP_c/dr = 0$), the above equation becomes

$$f_w = \frac{1}{1+\frac{k_{ro}\mu_w}{k_{rw}\mu_o}} \tag{4.76}$$

Since the value of the water volume angle β_w is related to water saturation through Eq. (3.20) in Chapter 3.3.1, there will be a specific value of pore pressure P(r) for each value of water saturation. It should be noted that since β_w varies from zero to some level (Fig. 3-17), the above equation only holds within a certain range of β_w. Beyond it, the flow becomes monophasic again.

4.3.3 Stress calculations in oil/water environment

Assuming that water saturation is only a function of time (i.e. saturation is not linked to radius), applying pore pressure Eq. (4.74) into Eqs. (4.17) and (4.18), the effective stresses for multiphase fluid flow in elastic porous media are

$$\sigma_r^{'} = \frac{0.5\alpha}{1-\nu}P + \frac{Ec_1}{(1+\nu)(1-2\nu)} - \frac{Ec_2}{(1+\nu)}\frac{1}{r^2} + \alpha\frac{0.5-\nu}{1-\nu}\cdot\frac{\overline{K}(S_w)}{2} \tag{4.77}$$

$$\sigma_\theta^{'} = \frac{0.5\alpha}{1-\nu}P + \frac{Ec_1}{(1+\nu)(1-2\nu)} + \frac{Ec_2}{(1+\nu)}\frac{1}{r^2} - \alpha\frac{0.5-\nu}{1-\nu}\cdot\frac{\overline{K}(S_w)}{2} \tag{4.78}$$

where $\overline{K}(S_w) = \frac{Q\xi(S_w)}{2\pi kh}$, is a variable only related to water saturation.

As discussed in Chapter 3.1.2, the friction angle can be assumed to be constant after water breakthrough, while the decrease of cohesive strength can be divided into two parts (Han and Dusseault, 2002 a), one from chemical reactions, the other from changes in capillary force. If the effect of chemical reactions is neglected (e.g. for clean sands), the shear strength after water breakthrough can be approximately expressed as:

$$C_o(S_w) = C_{o\_init} + \sigma_T(S_w)\tan\varphi \tag{4.79}$$

or $$C_o(S_w) = C_{o\_init} + \lambda \tan\varphi \frac{1-\phi}{\phi} \frac{F_c(S_w)}{4R^2} \tag{4.80}$$

where C_{o_init} is the initial cohesive shear strength before water breakthrough.

Following the same steps illustrated in Chapter 4.13, inelastic stress solutions inside the Coulomb zone can be expressed as

$$\sigma'_r(r) = \frac{c_3}{\omega} r^{-\omega} + \frac{2C_o(S_w)\tan\beta + \alpha\overline{K}(S_w)}{\omega} \tag{4.81}$$

$$\sigma'_\theta(r) = \frac{c_3(1-\omega)}{\omega} r^{-\omega} + \frac{2C_o(S_w)\tan\beta + (1-\omega)\alpha\overline{K}(S_w)}{\omega} \tag{4.82}$$

where c_3 is

$$c_3 = -\left(2C_o(S_w)\tan\beta + \alpha\overline{K}(S_w)\right)\cdot R_1^{\omega} \tag{4.83}$$

Three unknown constants R_c, c_1, c_2, in Eqs. (4.34), (4.35), (4.36) can be solved as

$$c_1 = \frac{(1+\nu)(1-2\nu)}{E}\left(\sigma'_h - \frac{0.5\alpha}{1-\nu}P(R_2) + \frac{Ec_2}{(1+\nu)}\frac{1}{R_2^2} - \alpha\frac{0.5-\nu}{1-\nu}\frac{\overline{\mathrm{K}}(S_w)}{2}\right) \tag{4.84}$$

$$c_2 = -\frac{1+\nu}{2E}\left(\frac{0.5\alpha}{1-\nu}\overline{\mathrm{K}}(S_w) + c_3 R_c^{-\omega}\right)\cdot R_c^2 \tag{4.85}$$

$$\sigma'_h - \frac{2C_o(S_w)\tan\beta + \alpha\overline{\mathrm{K}}(S_w)}{\omega} + \frac{0.5\alpha}{1-\nu}\frac{\overline{\mathrm{K}}(S_w)}{2} =$$

$$\frac{c_3}{2R_2^2}R_c^{2-\omega} + \left(\frac{1}{\omega} - \frac{1}{2}\right)c_3 R_c^{-\omega} + \frac{0.5\alpha\overline{\mathrm{K}}(S_w)}{1-\nu}\left[\frac{R_c^2}{2R_2^2} - \ln\left(\frac{R_c}{R_2}\right)\right] \tag{4.86}$$

4.3.4 Redistributions of pore pressure and stresses with water

4.3.4.1 Pore pressure vs. water saturation

Before introducing relative permeability data, the water saturation in the microscopic model developed above should be calibrated to experimentally determined values. The saturation discrepancy between the model and reality results mainly from two sources that the microscopic model cannot address: one is connate water saturation (S_{wc}) and immobile oil saturation (S_{oi}); the

other is the wettability effect of irregular particle surfaces. If assuming water saturation remains as a constant (S_{wc}) until water breakthrough occurs, the calibration can be carried out as

$$S'_w = S_{wc} + S_w * (1 - S_{wc} - S_{oi}) / S_{w0} \tag{4.87}$$

where S_{w0} is the saturation at which capillary pressure becomes zero.

Fig. 4-13 shows the calculated pressure variations with water saturation at different distances from the wellbore (i.e. r = 0.2 m, 1.0 m, 2.55 m). Interestingly, pore pressure first decreases with saturation until some critical saturation (S_w = 0.45), and the decrease in magnitude can be as high as several megaPascals; then, it increases continuously to a value (when S_w = 0.734) even higher than the initial value (when S_w = 0.32). Correspondingly, the pressure distributions around the wellbore (Fig. 4-14) are first lowered by the increase of water saturation (e.g. from S_w = 0.34 to S_w = 0.507), but eventually become flat (e.g. S_w = 0.704). Physically, because water is a less viscous and more mobile fluid than oil, less energy (i.e. lower pressure drawdown) is needed to drive it into the wellbore; consequently, the increase of water relative permeability raises the pore pressure whereas that of oil relative permeability lowers it. The synthesis of both effects indicates that pore pressure in a water-dominant fluid system is relatively higher than in an oil-dominant fluid system.

The pressure difference between the new approach based on physics at the grain scale and the conventional method is plotted in Fig. 4-15 and Fig. 4-16. Both methods are confirmed to be precise enough to be applied in the pressure analysis: they agree very well when calculating both pressure variations with water saturation at a specific location (r = 2.5m) and pressure distributions with distance at a specific saturation (S_w = 34%).

4.3.4.2 Stress distribution vs. water saturation

Compared to the changes of pore pressure that first decrease, then increase with water saturation, the stress behavior around the opening is more complicated. Fig. 4-17 describes the redistribution of effective stresses around a wellbore producing oil and water simultaneously. To investigate the details, stresses in both the elastic zone near the shear yield front (R_c) and the plastic zone are presented in Fig. 4-18 and Fig. 4-19.

In the elastic zone close to the shear yield front (Fig. 4-18), the effective tangential stress (σ'_θ) increases to a peak before it declines with saturation, whereas the effective radial stress (σ'_r) does the opposite, it first decreases to its lowest value and then increases. Hence the difference between them (i.e. shear stress $\times$ 2) reaches a maximum at some specific saturation (around S_w =

0.45, connate water saturation is S_{wc} = 0.32). Thus, at the initial stage of water breakthrough, elastic sand is most likely to experience shear yield that breaks cementation among particles and propagates the yield front (R_c) away from the wellbore. If fluid flow forces are strong enough to carry yielded sand into the wellbore, sand production occurs. However, as shown in Fig. 4-17, in the elastic zone far from wellbore (i.e. $r/R_1 > 15$), the effective radial stress follows the same trend as the effective tangential stress: first it increases then decreases with saturation.

In the plastic zone (Fig. 4-19), both the effective tangential stress and the effective radial stress decrease with saturation, except that the former decreases more than the latter. This creates an even lower general confining stress environment around the wellbore after water breakthrough, which increases the possibility of fluid flow destabilizing sand.

4.3.5 Why does sand fail after water breakthrough?

Many arguments exist concerning which mechanism (capillarity changes, pore pressure decreases due to alteration of relative permeabilities, chemical reactions, etc.) is mainly responsible for sand failure when an oil well starts to produce water. However, most arguments are not convincingly supported by quantitative measures. For the first time, based on model calculations, the main mechanisms and their relative importance with respect to rock stability are analyzed and clarified. The variation of the critical radius (i.e. yield front R_c) at which the sand experiences Mohr-Coulomb shear yield is selected to evaluate the importance of each mechanism, as the radius is found to be positively and closely related with critical drawdown pressure (Morales et al., 2000) and the amount of produced sand (Vásquez et al., 1999).

4.3.5.1 Pore Pressure and Capillarity

Fig. 4-20 shows the propagation of R_c with saturation for rocks of different initial cohesive shear strengths (C_{o_init}). Clearly, saturation has a large impact on the size of the plastic yield zone: R_c rapidly increases with the increase of saturation, and furthermore, the lower the initial cohesive strength, the more significant the increase in critical radius. For example, for C_{o_init} = 0.4 MPa, the dimensionless critical radius (R_c/R_1) increases from 5 to 16 when saturation rises from 0.32 (connate saturation) to about 0.45, while R_c/R_1 changes from 4.2 to 7.3 for C_{o_init} = 0.5 MPa and from 2.7 to 3.2 for C_{o_init} = 1 MPa. Thus the initial rock strength greatly affects the extent of water breakthrough on sand stability. The decrease of the critical radius after S_w = 0.45 is related to the increase of pore pressure (see Fig. 4-13) as a higher water percentage leads to a lower energy requirement (i.e. pressure drawdown) to flow through the porous media. However, it should not be necessarily interpreted as a stabilizing factor because if sand starts to fail and the

yield front propagates, geometrical changes require re-definition of the boundary conditions used in the geomechanics model, an issue that is too complicated to be discussed in this research. Even if the sand can sustain stress increases, this stress fluctuation may progressively damage the rock fabric and therefore leave the sand weaker and easier to mobilize.

Compared to pore pressure, the variations of capillary strength with water saturation are much simpler (see Fig. 4-21, where the effect of connate saturation is not considered). The solid lines in Fig. 4-22 describe the relationship between dimensionless critical radius and saturation when capillary strength changes are taken into account. Comparing to the dashed lines that treat rock strength as a constant, i.e. no capillary strength appears and rock stability changes only result from pore pressure variations by virtue of relative fluid permeability changes, the capillary effect that varies the rock strength through changing water-oil menisci is far less significant than the effect of relative permeabilities unless initial rock strength is relatively low (e.g. C_{o_init} = 0.4 MPa). Considering that the magnitude of capillary strength (on the order of kPa) is much lower than rock strength (on the order of MPa), this defines when capillary strength plays an important role in stabilizing sand: after the rock experiences shear yield and most of its initial strength has been destroyed. Only at this time can the effect of capillarity strength variations become a significant destabilizing factor.

4.3.5.2 Chemical Reactions

The above discussions assume that the rock is not chemically sensitive to formation water and that the microstructures have not been altered by water breakthrough. However, this assumption is very tentative because chemical reactions, such as chemical quartz hydrolysis, ferruginous deposition, carbonate dissolution, shale swelling, etc., can not only lower the strength magnitude, but also alter the original geometric structure maintained by particle-particle bonds, and therefore increase local drawdown. In fact, the significant loss of strength in water-saturated rock (in the magnitude of MPa) discovered in the laboratory may be mainly due to those reactions, rather than capillarity (usually in the magnitude of kPa for sandstones).

Another characteristic of chemical reactions is that they can continue even after the rock is fully saturated, instead of quickly diminishing with water saturation like capillarity and pore pressure. Fig. 4-23 shows an experimental relationship of shear strength with time for fully saturated sand and shale (Tamada, 1970): the main strength reduction occurs within the first 20 hours, then the strength remains almost unchanged for many days. An empirical approach using a time-exponential relationship is recommended for incorporating chemically reduced strength (C_{o_ch}) into stress calculations:

$$C_{o\_ch} = C_{o\_final} + a\exp(-bt) \tag{4.89}$$

where C_{o_final} is the remaining rock strength after chemical reaction; a and b are coefficients through curve fitting and t is time

Even though it is hard to rigorously quantify chemical reactions in terms of rock strength changes (Han and Dusseault 2002*a*), one qualitative way is to consider a reduced initial cohesive shear strength (C_{o_init}), as shown in Fig. 4-20. When the rock initial strength is decreased from 0.5 to 0.4 MPa because of supposed chemical reactions, the dimensionless critical radius (r/R_1) can increase from 7.3 to 16 at $S_w = 0.45$. When interpreting this effect in terms of effective stresses distributions around a wellbore (Fig. 4-24), the magnitude of stress changes is highly significant and can be comparable in magnitude to the effect of pore pressure changes (Fig. 4-17) caused by relative permeabilities alterations. Furthermore the lower the strength, the larger the plastic zone.

4.3.5.3 When will each mechanism play a role in destabilizing sand?

In general, the increase of effective stresses due to the changes of water/oil relative permeabilities ends as soon as pore pressure stops declining at a specific saturation (e.g. $S_w = 45\%$ in Fig. 4-13, considering the effect of connate water saturation); capillarity disappears around $S_w = 65\%$ (Fig. 4-21), and chemical reactions may continue even after rock is fully saturated (e.g. as long as 20 hours). Based on these calculations and observations, some interesting conclusions can be made:

- For unconsolidated or weakly consolidated sand with little water-sensitive cementation material, chemical reactions can be neglected when rock failure is analyzed after an oil well starts to produce water. Pore pressure variations seem to be largely blamed for sanding initiation at an early stage of water breakthrough, while capillarity reduction contributes but is not significant until saturation reaches some point, at which effective stresses start to decrease due to recovery of pore pressure.
- For weak or consolidated sand with water-sensitive cementation, the effect of chemical reactions may be more dominant and may continue for much longer than that of other mechanisms; indeed, many experiments have suggested that the extent of rock strength decrease with saturation can be easily in the MegaPascal range. Combining with stress elevations (from pore pressure decrease) that also reach the magnitude of MPa, weakened rock is further loaded beyond its original state, where the loading results from the introduction of the wellbore.

- Capillarity should be considered in stress analysis when the rock strength is low or becomes low due to shear damage or chemical reactions. There are some cases in which capillarity can be neglected, e.g. when the rock has experienced considerable compaction and particles overlap each other to a great extent, when particle radius is large, or when the surface tension of the oil-water interface is relatively low. However, as a cohesive force among particles, the capillary force is comparable in magnitude to the fluid seepage force (discussed in Chapter 3.4.3). This indicates that after rock experiences shear failure capillarity becomes a dominant factor to stabilize disintegrated particles as long as water saturation is not high.

4.4 Conclusions

The conditions assumed in stress models are demonstrated to be a critical aspect of solutions. Two types of conditions (BC1 and BC2) commonly used in solving poroelastic stresses are inaccurate as long as a Coulomb zone can be found, in which case the assumptions of continuous stresses across the Coulomb zone should be applied along with the restraints at the outer and inner boundaries. Based on these conditions, a simple analytical poroinelastic model is presented, and its limitations are discussed. The solutions can be used as input to analyze stress-dependent aspects of rock permeability.

Based on nonlinear theory and existing empirical relationships, a general analytical approach to calculation of stress-dependent porosity and permeability is developed. Comparing the calculations to available published data, it is shown that nonlinear theory has good applicability for clean unconsolidated or weakly consolidated sandstones that do not undergo grain crushing. As an application of the theory, the distributions of stress-dependent permeability and porosity around a wellbore producing oil from a weakly consolidated sand are described, and their effects are evaluated in terms of pore pressure variations. The calculations suggest that, given minimal grain crushing and lack of interstitial fine-grained minerals that can be mobilized by shear distortion, the stress-dependent aspect of porosity and permeability may be trivial as far as stress analysis is concerned. With the input of different stress-compressibility relationships for different rocks, the developed model can be used to help screen those reservoirs for which the effect of stress on permeability should be considered during geomechanical analysis, incorporating issues such as sand production predictions, reservoir stress arching and shear, plasticity onset, etc. Furthermore, the model can be applied to evaluate the extent of formation compaction resulting from the variations of stress-dependent porosity.

Although this solution is found to be useful, the limitations of the continuum analytical approach have been emphasized, and it is believed that a micromechanics approach based on particulate mechanics may be valuable for future research.

Based on a simplified microscopic model that needs only two input parameters (particle radius and water saturation) to physically describe capillary strength behavior with water saturation, a coupled poro-inelastic model is developed to evaluate the effect of different mechanisms on rock stability after an oil well starts to produce free water. According to model calculations, it is found that:

- Because of changes in oil and water relative permeabilities, pore pressure first decreases with saturation until some critical point, and the magnitude of decrease can be as high as several MegaPascals; then it increases continuously to a value (e.g. when $S_w = 0.734$) even higher than in the initial state (where only oil exists).
- In the elastic zone close to the shear yield front, the effective tangential stress increases to a maximum before declining with saturation, whereas the effective radial stress first decreases to its lowest value and then increases. Thus, at the initial stage of water breakthrough, elastic sand is most likely to experience shear yield that breaks cementation among particles and moves the yield front outward from the well.
- For the plastic zone, both the effective tangential stress and effective radial stress decrease with saturation. This creates a lower stress condition around the wellbore after water breakthrough, which makes fluid erosion of sand easier.
- In terms of the plastic radius, several mechanisms such as pore pressure changes due to variations of oil and water relative permeabilities, capillary effects, and strength loss due to chemical reactions, are evaluated as for water-related rock stability. Water saturation is shown to have a large impact on changes in the plastic yield zone, and this impact increases with the increase of saturation. The magnitude of the initial shear strength plays a vital role in evaluating the relative importance of those mechanisms: when the initial strength is low, the increase of the plastic radius with saturation becomes significant, and so does the contribution of the capillarity to stress calculations; otherwise, the effect of capillarity is trivial compared to that of relative permeabilities (pore pressure variations).
- If cemented materials are water-sensitive, the effect of chemical reactions on rock stability through the lowering of the rock strength is more dominant and lasts longer than those of other mechanisms. The magnitude of stress alterations by this effect is high enough to match the result from pore pressure changes caused by relative permeability alterations.

- The fact that the magnitude of the capillary cohesive force is comparable to that of the fluid seepage force indicates that after rock experiences shear failure, capillarity becomes the only dominant factor to stabilize disintegrated particles as long as water saturation is not high. (Gillespie and Settineri, 1967).

Based on the microscopic model developed in this work, the conventional method to calculate pore pressure in a multiphase environment is confirmed to be precise enough to apply in pressure analysis. The geomechanics model facilitates the understanding of why and how rock becomes unstable after water breakthrough into an oil well, and can be used as a foundation to evaluate sand production risk in multiphase fluid environments.

4.5 Tables and Figures

Table 4-1: Parameters used in geomechanics (stress) model

Rock Mechanical Properties					Reservoir Flow Properties						Geometry Parameters		
E (Pa)	ν	σ_h (Pa)	C_o (Pa)	φ	ϕ_i	k_i (m^2)	P_2 (Pa)	μ (Pa/s)	μ_w (Pa/s)	Q (m^3/s)	R_2 (m)	R_1 (m)	h (m)
3×10^9	0.25	28×10^6	0.5×10^6	30°	0.3	0.3×10^{-12}	10×10^6	0.01	0.001	1.157×10^{-3}	50	0.1	10

Table 4-2: Coefficients used in four compressibility models

	Zimmerman			Rhett&Teufel (ϕ_i =0.13)		Jones (ϕ_i =0.1)			Nonlinear (ϕ_i =0.3)	
	$a_1(\times10^{-4})$	$a_2(\times10^{-4})$	a_3	b_1	b_2	d_1	d_2	d_3	m	n
Bandera (ϕ_i =0.16)	0.82	5.35	0.120							
Berea (ϕ_i =0.18)	1.05	6.35	0.211	8.9×10^{-4}	3.1×10^{-2}	13.8	0.44×10^{-3}	0.1	0.25	2.4×10^4
Boise (ϕ_i =0.27)	0.95	2.79	0.143							

Table 4-3: Input parameters for capillarity model

R (m)	γ (N/m)	λ
1×10^{-4}	0.036	10

Table 4-4: Relative permeabilities vs. saturation

S_w	k_{rw}	k_{row}
0.32	0	1
0.375	0.003	0.653
0.415	0.008	0.436
0.4555	0.017	0.311
0.495	0.028	0.214
0.535	0.057	0.14
0.575	0.091	0.089
0.615	0.134	0.049
0.655	0.184	0.019
0.694	0.242	0.001
0.734	0.301	0

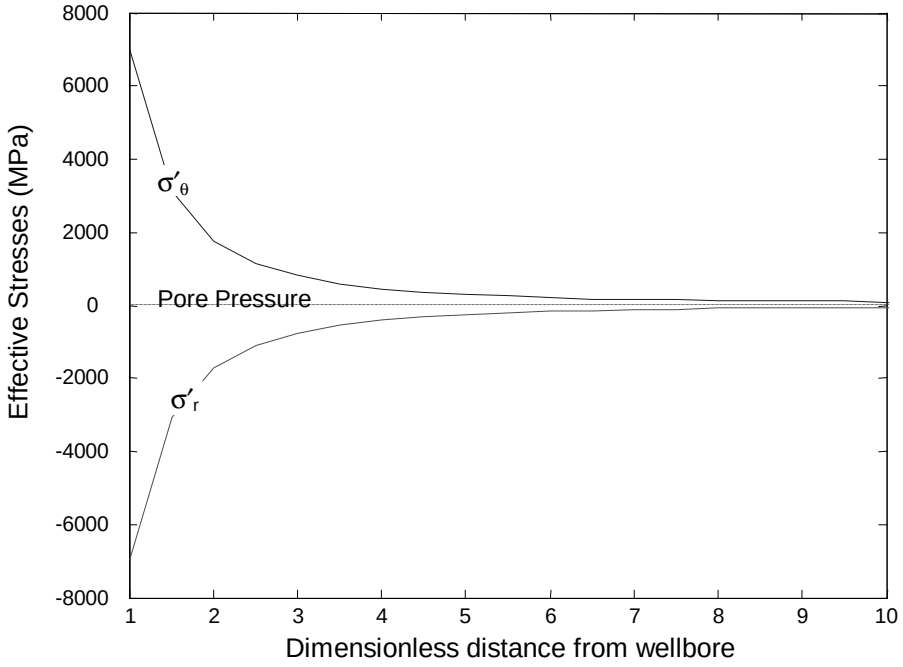

Fig. 4-1: Stress solutions with BC1

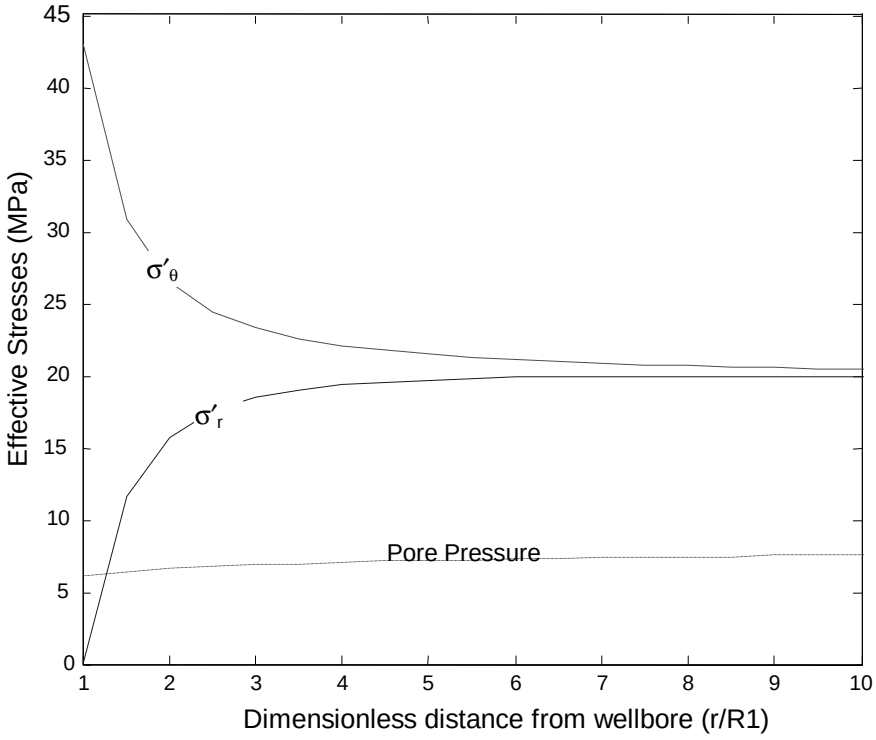

Fig. 4-2: Stress solutions with BC2

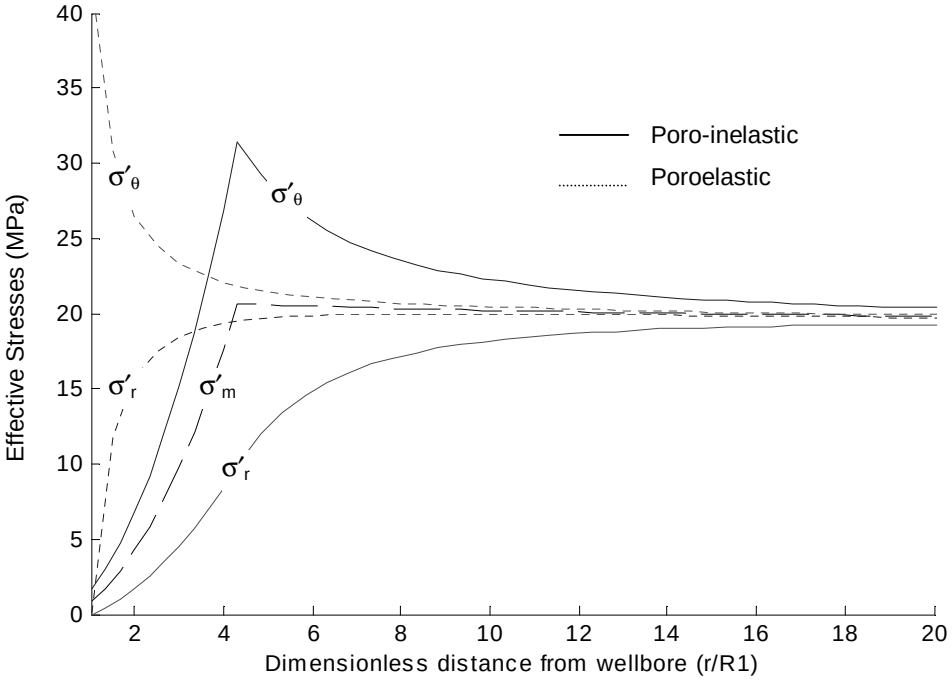

Fig. 4-3: Stress solutions under different boundary conditions

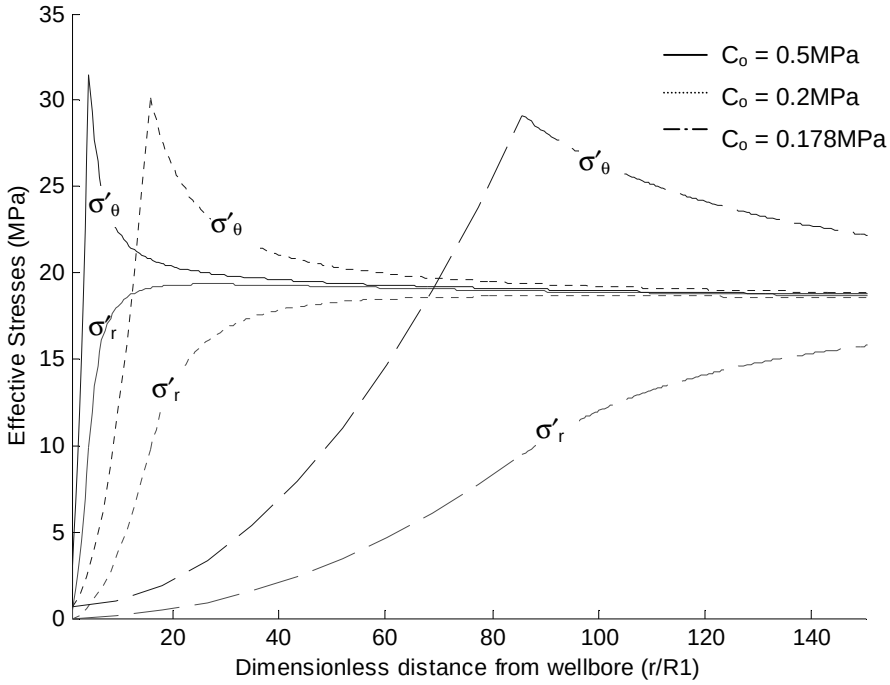

Fig. 4-4: Effect of cohesive shear strength on stress distributions

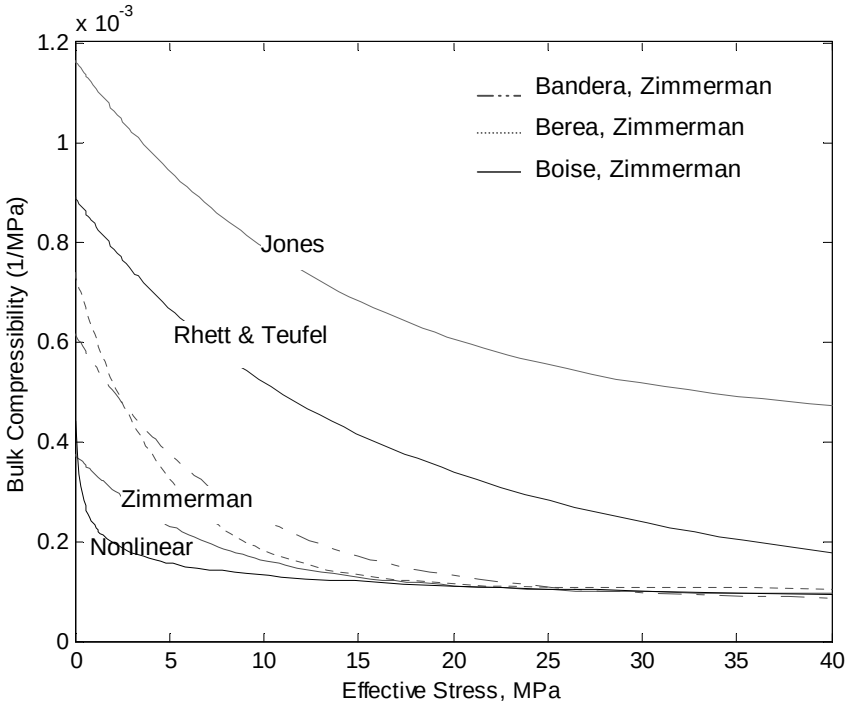

Fig. 4-5: Different models for stress-dependent bulk compressibility

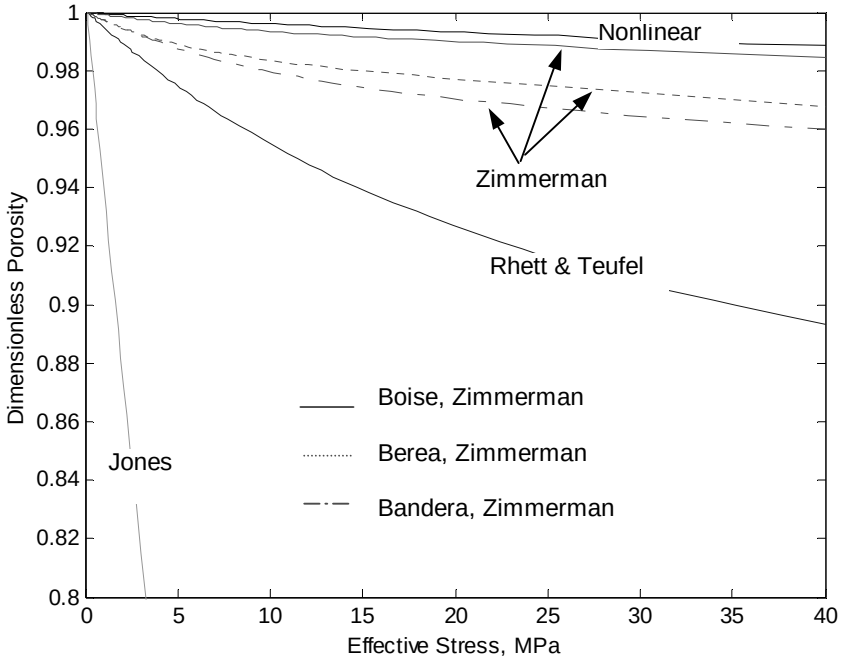

Fig. 4-6: Influence of effective stress on porosity
(dimensionless porosity = $\phi(\sigma')/\phi_i$)

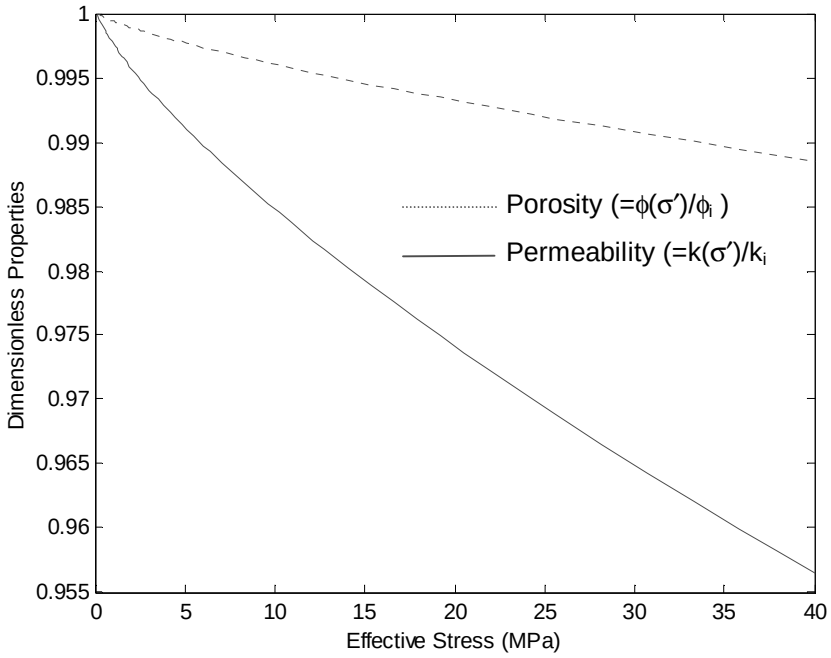

Fig. 4-7: Stress-dependent porosity and permeability for unconsolidated sand

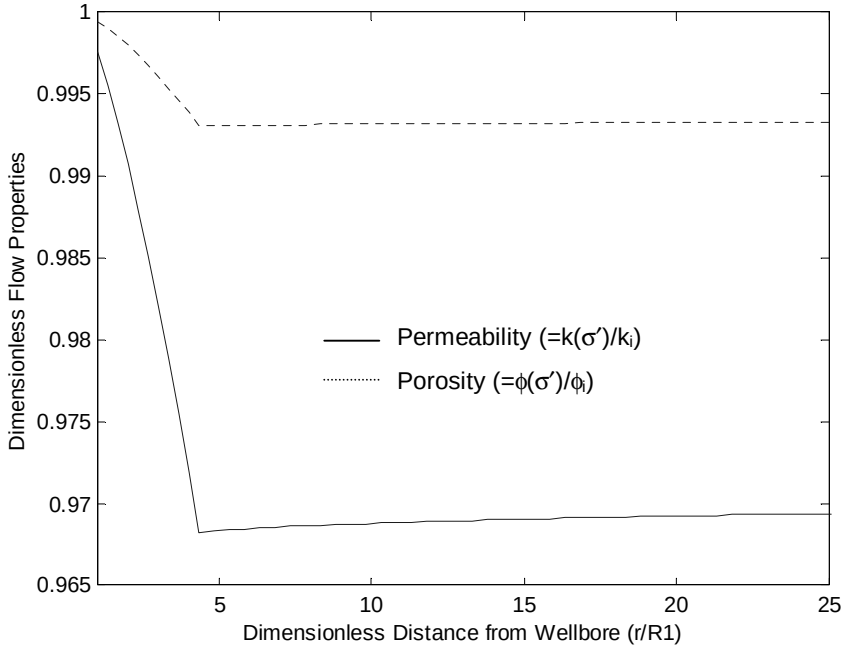

Fig. 4-8: Stress-dependent porosity and permeability around a wellbore

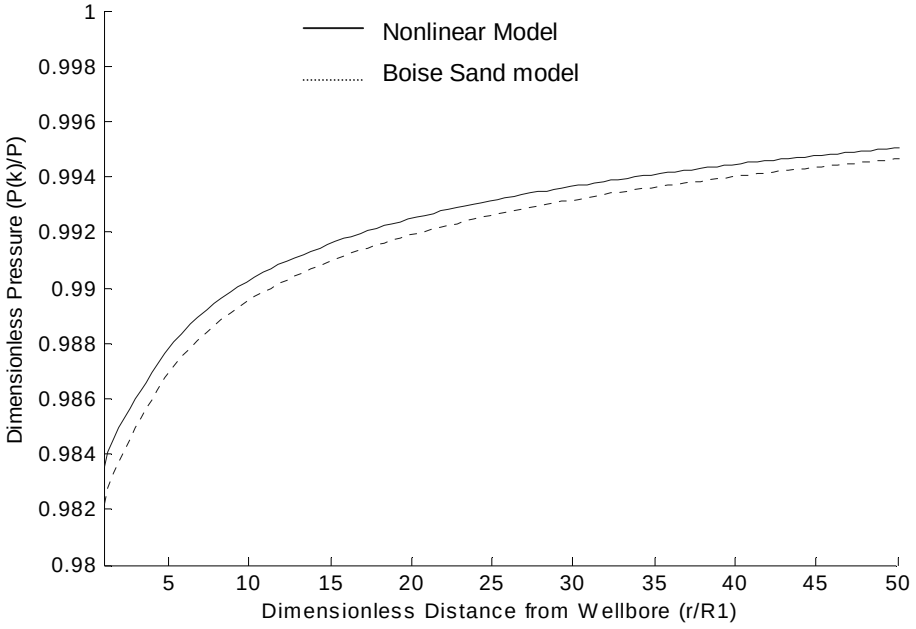

Fig. 4-9: Pore pressure variations with stress-dependent permeability for high-porosity sands

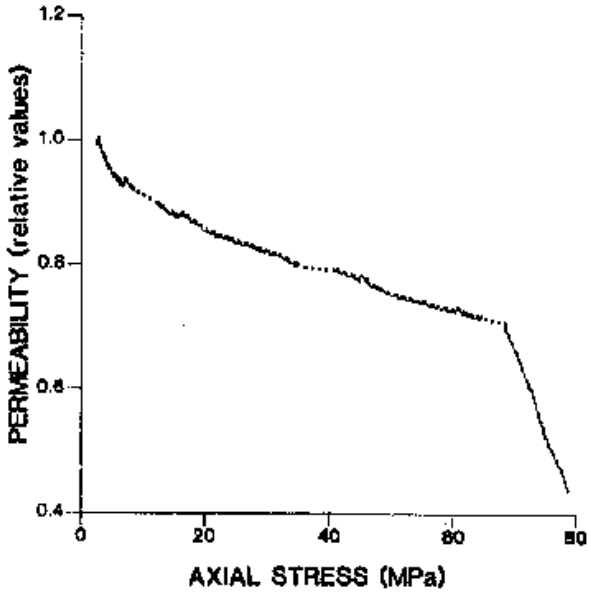

Fig. 4-10: Permeability vs. axial stress in non-hydrostatic test of Red Wildmoor sandstone (after Holt, 1990).

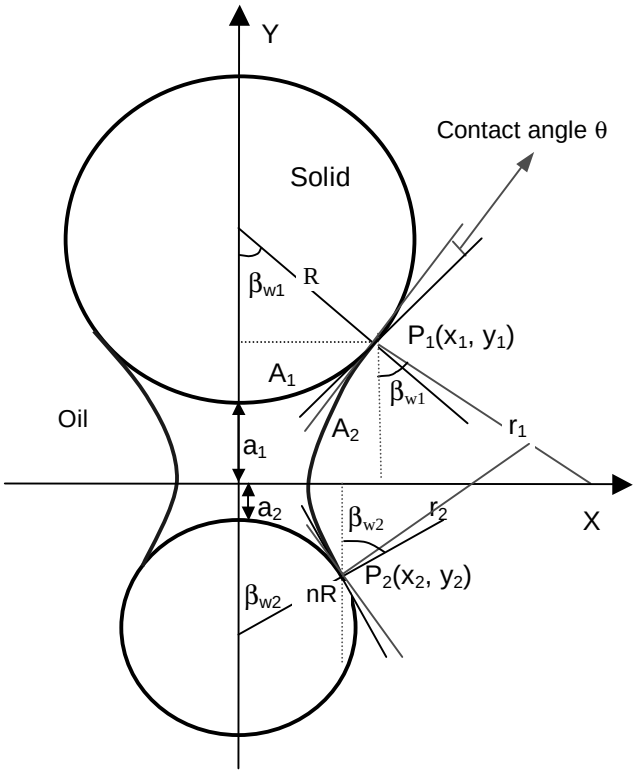

Fig. 4-11: The most sophisticated situation for capillary strength

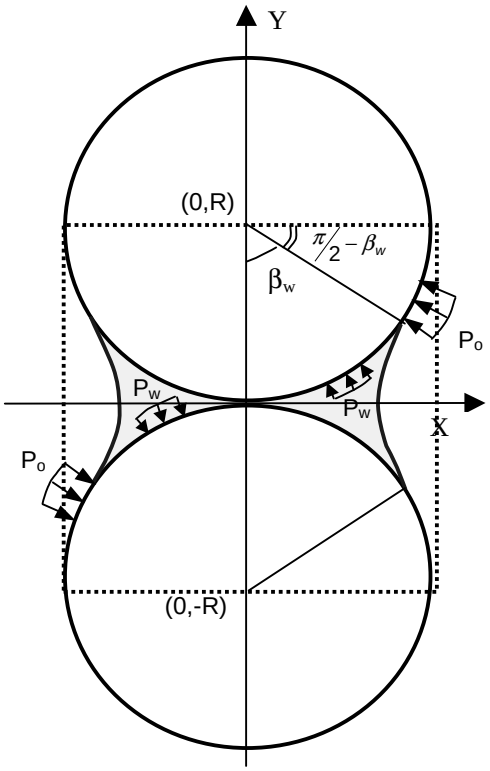

Fig. 4-12: Sketch of pore pressure calculations

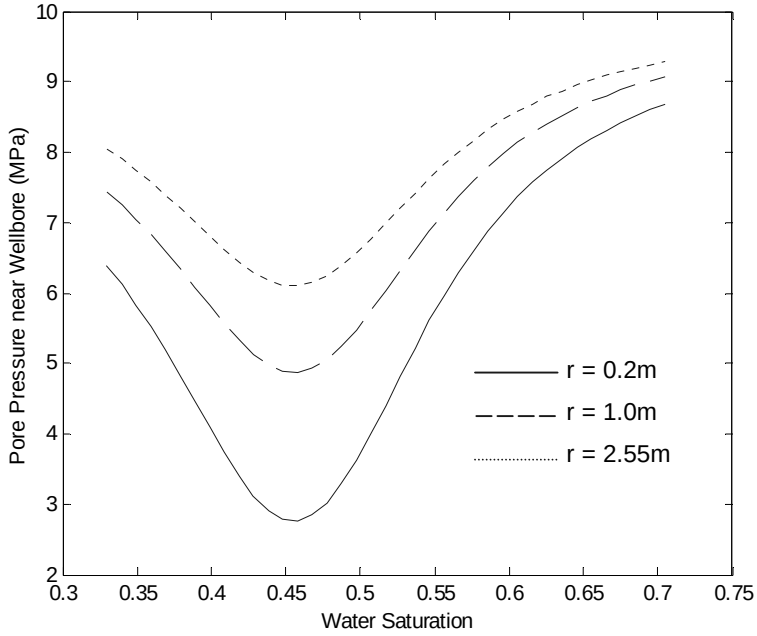

Fig. 4-13: Variations of pore pressure at different locations with saturation

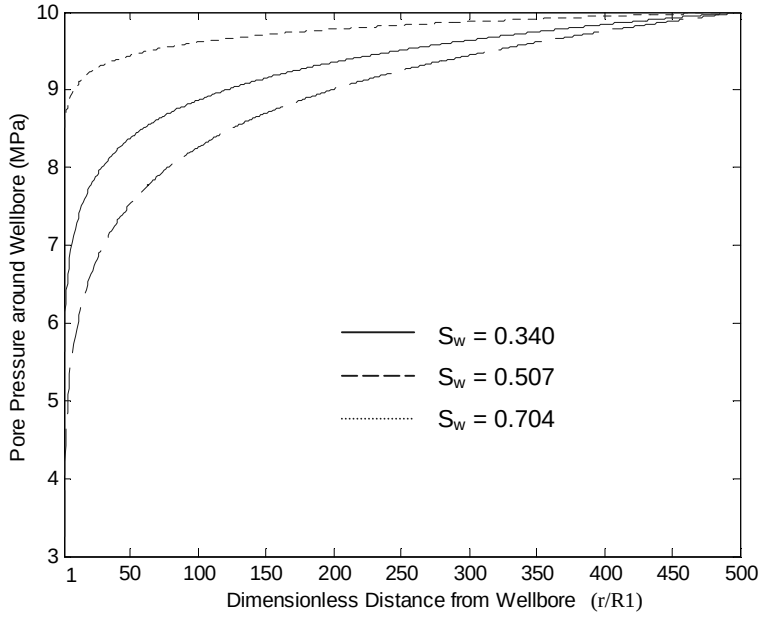

Fig. 4-14: Pressure distributions around a wellbore after water breakthrough

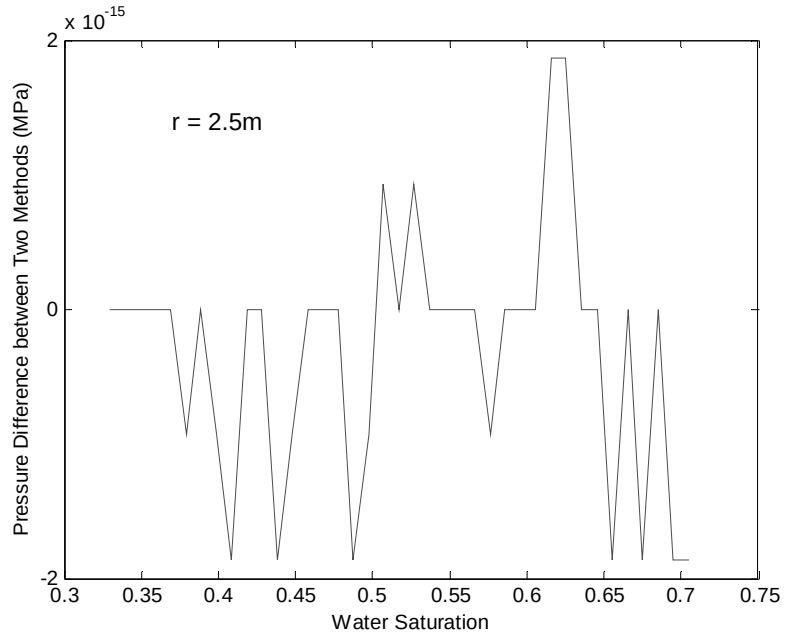

Fig. 4-15: Difference of pressure variations calculated by two methods

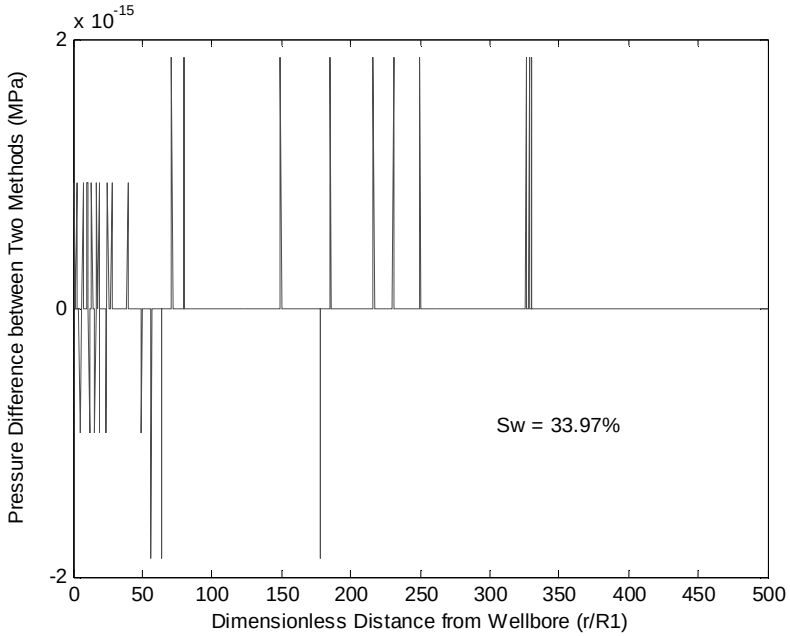

Fig. 4-16: Difference of pressure distributions calculated by two methods

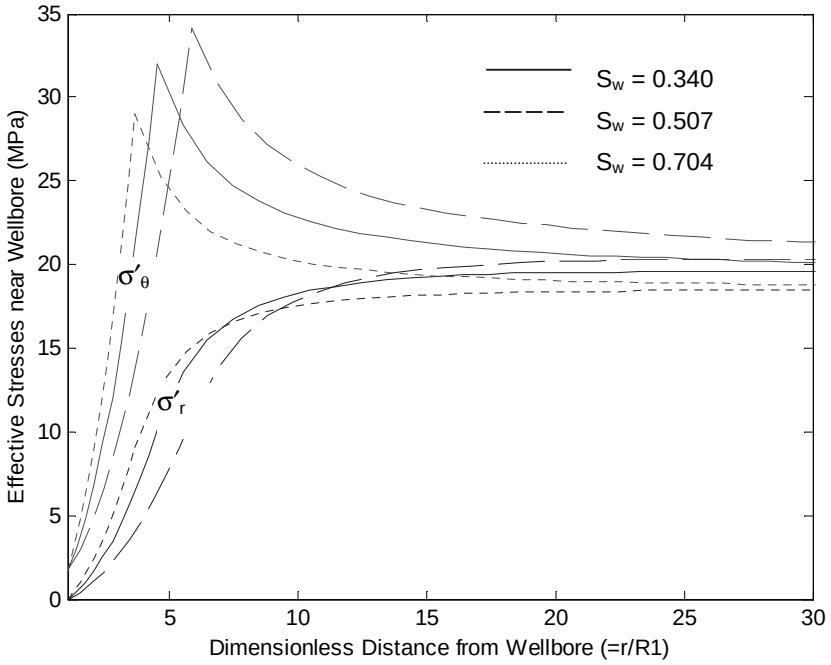

Fig. 4-17: Variations of effective stresses with water saturation

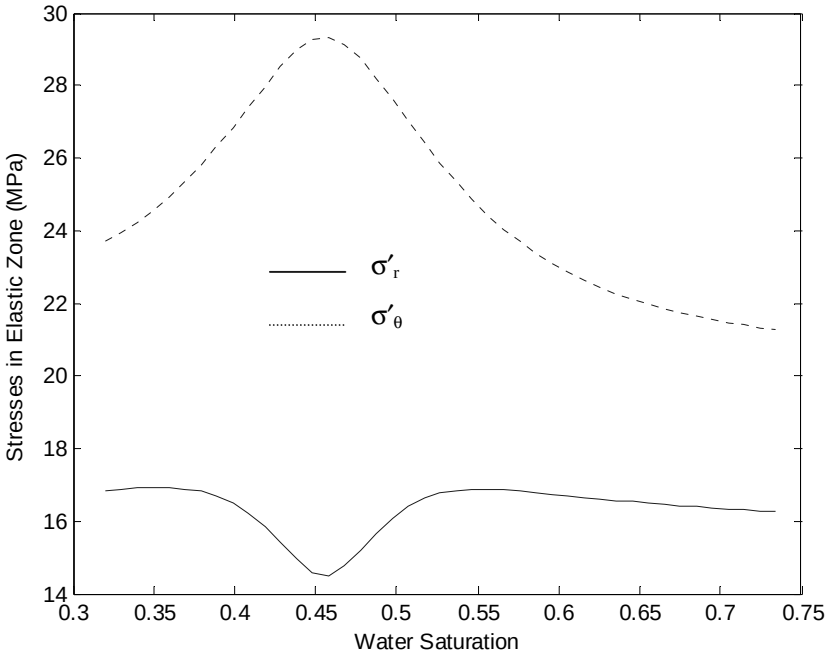

Fig. 4-18: Variations of elastic stresses with water saturation (r/R1 = 8)

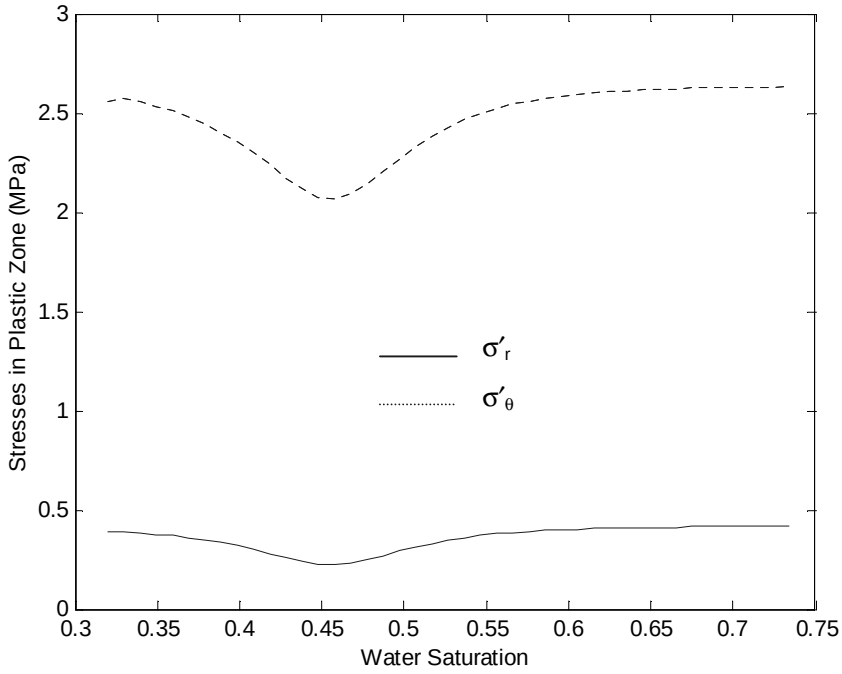

Fig. 4-19: Variations of plastic stresses with water saturation (r = 0.131m)

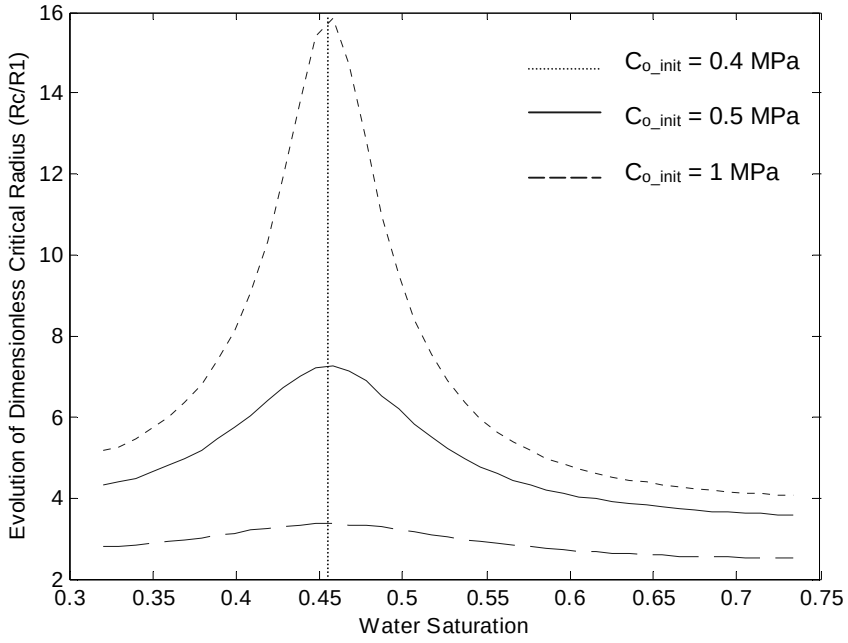

Fig. 4-20: Variations of plastic yield front (Rc) with water saturation

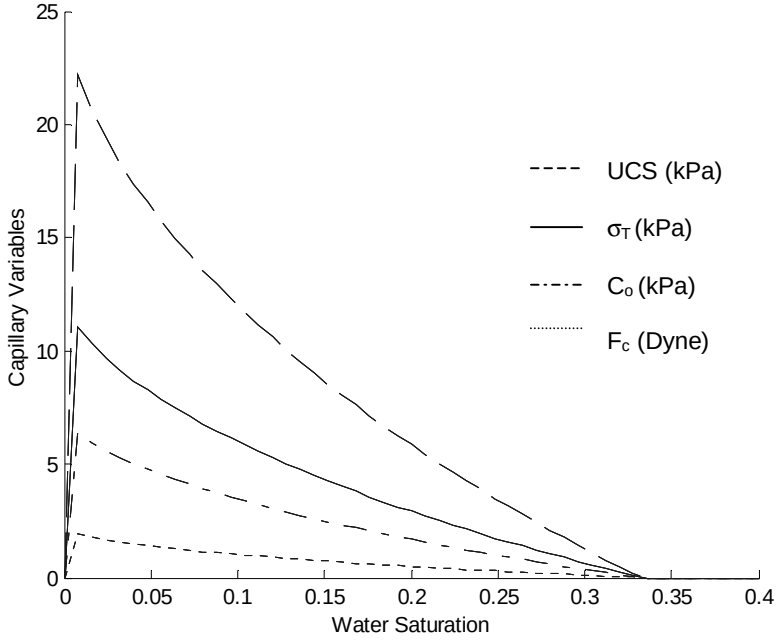

Fig. 4-21: Variations of capillary force and strengths with water saturation
(without the effect of connate water saturation)

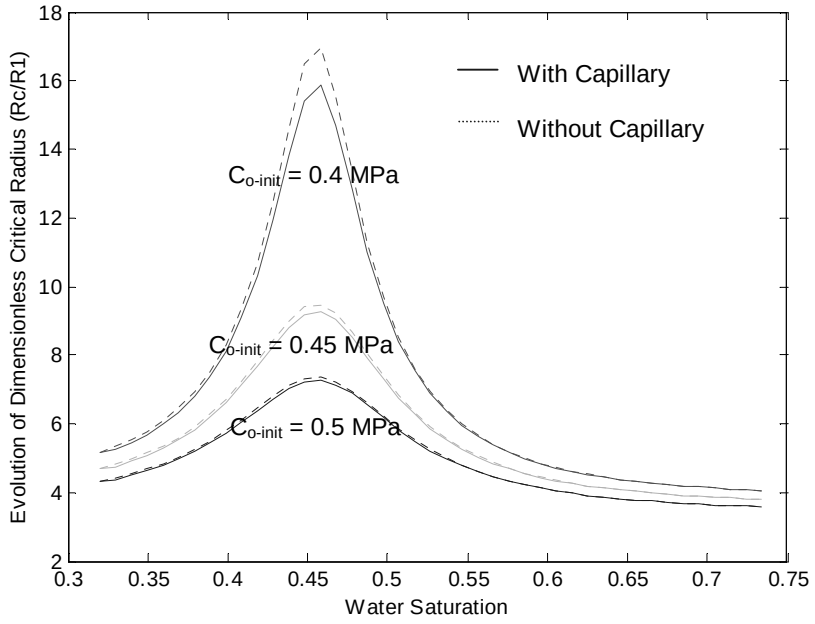

Fig. 4-22: Effect of capillary strength on plastic yield front
(with the effect of connate water saturation)

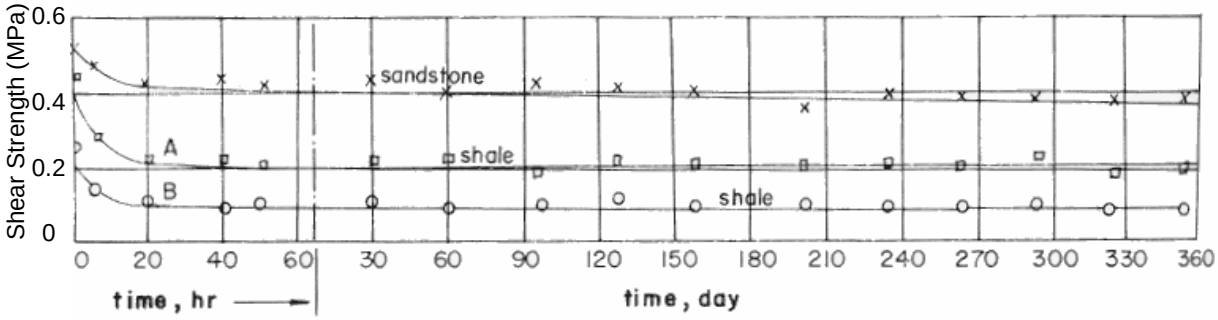

Fig. 4-23: Evolutions of water-related shear strength with time
(after Tamada, 1970)

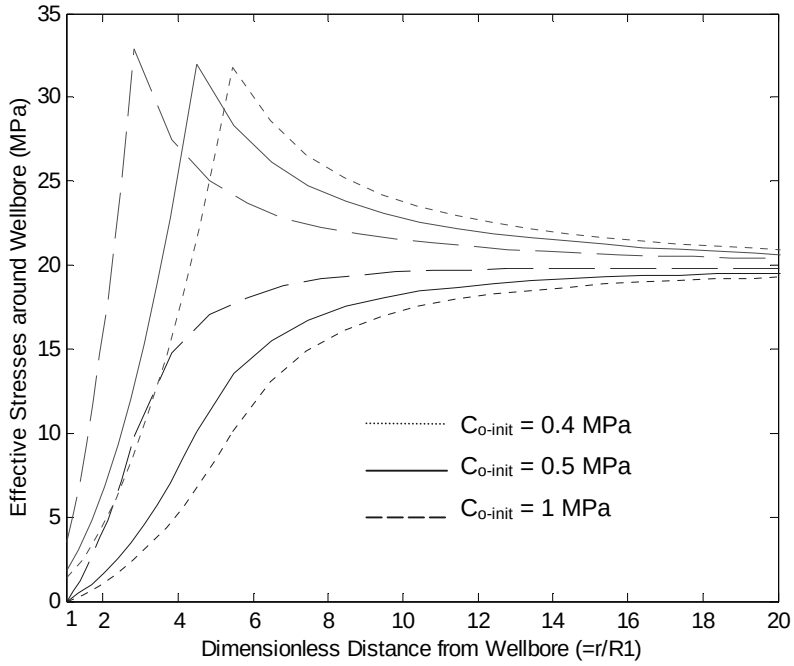

Fig. 4-24: Effect of chemical reactions on stress distribution (S_w = 0.34)

Chapter 5 Nonlinear Rock Properties in Stressed and Oil/Water Environments

5.1 Introduction: Stress- and Water-Induced Nonlinearities

It is generally agreed in geomechanics that rock nonlinearity may lead to significant stress differences compared to elastic calculations (Santarelli, 1986; Wang, 1990; Vaziri, 1995; Nawrocki, 1998). There are mainly two parts of a rock stress-strain curve that shows nonlinear trends upon loading (Fig. 5-1): when the rock is initially loaded, and when the load exceeds a certain level and the rock starts to yield and behave plastically. At the grain scale level, the initial stress increase may result in the closure of existing fractures and rearrangement of sand particles in order to form a more compacted agglomerate, whereas the latter involves irreversible behaviors such as grain sliding, breaking of cementation, generation of micro-fissures, grain deformation, and even crushing at elevated stress levels. Some reservoir problems involve only one mechanism, e.g. for reservoir compaction the dependency of moduli on confining stress should be of primary concern. However, for other situations such as wellbore stability and sand production, both non-linear mechanisms are expected because stresses around wellbore can be as low as zero (such as the effective radial stress at the wellbore), or as high as many MPas (such as the effective radial stress at the boundary between elastic and plastic zones).

Besides stress-dependent nonlinearity, changes of water saturation also can lead to significant alternations of rock strength (as discussed in Chapter 3) and elastic properties such as Young's modulus and Poisson's ratio (Fig. 5-2). Based on experiment results, it is found that

- Young's modulus generally decreases with increase of water saturation (Burshtein, 1969; Van Eeckhout and Peng, 1975; Gregory, 1976; Rao et al., 1987; Hadizadeh and Law, 1991; Hawkins and McConnell, 1992; Papamichos et al., 1997). The variation in tangent modulus at 50% of ultimate strength, the E_{50}, with water saturation is found to be similar to that observed in strength: it decreases with an increase in water content, and becomes minimum when full saturation is attained (Table 5-1).

- The behaviour of Poisson's ratio in oil/water environments is not as clear as that of Young's modulus: depending on rock type, mineralogy, and heterogeneity, it may monotonously increase with water saturation, or decrease slightly before a general increase takes place (Priest and Selvakumar, 1982; Van Eeckhout and Peng, 1975; Hawkins and McConnell, 1992; Rao et al., 1987), or remain constant (Papamichos 1997).

Corresponding to changes in elastic properties, rock may behave quite differently upon loading (Fig. 5-3). Unfortunately, this type of rock nonlinearity is often neglected in geomechanical models to predict rock or soil stability in multi-phase fluid flowing systems.

5.2 Nonlinear Theories

5.2.1 Literature review

There are many types of nonlinear elasticity theories developed to include the stress-related nonlinear behavior in rock properties such as Young's modulus, bulk modulus, Poisson's ratio, etc. They can be briefly summarized as follows:

- Duncan and Chang (1970) developed a stress-difference dependent rock modulus for soil description based on an assumption of a hyperbolic stress-strain relationship. Vaziri (1995) showed its value in the stress analysis of oil sands, which is largely treated as a friction-dominated soil.
- Based on their experiments, Santarelli et al. (1986) proposed a confining-stress dependent Young's modulus for stress calculations in rock mechanics. The method only considers the effect of confining stress and is empirical; therefore it lacks the advantage of relationships based on fundamental physical processes. The recommended formula is straightforward and simple, but many experiments are needed to determine the power parameters.
- Nawrocki et al. (1998) developed strain-dependent and radius-dependent Young's modulus models for stress calculations around a wellbore. While the use of a strain-based Young's modulus, in a manner similar to strain-based failure criteria (see Section 2.3.1), reduces modeling difficulties greatly, the approach faces great challenges as it needs intensive calibration before practical application, because

strain is sensitive to many factors such as stress levels (loading and confining stresses), stress path and anisotropy, loading rate and history, pressure depletion or increase, and even laboratory sample size and shape. Radius-dependent approaches assume that the relationship of Young's modulus with radius from the wellbore either fulfills an exponential law or power law, which has not yet been justified. The author believes that because rock stresses are not monotonously increasing with distance from the wellbore (e.g. stress deviation first increases to a peak and then decreases, as shown in Fig. 2-3), a simple relationship such as an exponential or power law may be not suitable.

In this research, stress-dependent rock nonlinearity is analyzed in two categories: one is based on confining-stress; the other is based on rock failure. Stemming from the physical mechanisms for rock property changes in oil/water environments, a new modified nonlinear theory is proposed with consideration of the effects of both stress and water saturation around a wellbore.

5.2.2 Failure-based nonlinearity

5.2.2.1 Young's modulus

It is assumed that a typical triaxial stress-strain curve for sandstone fits a hyperbolic expression (Duncan and Chang, 1970), in the form of

$$\sigma_1' - \sigma_3' = \frac{A_E \varepsilon}{1 + B_E \varepsilon} \tag{5.1}$$

where A_E, B_E are constants derived from curving fitting, and their ratio A_E/B_E is the maximum stress the rock can sustain, and σ'_1 and σ'_3 are the maximum effective stress (axial stress) and the minimum effective stress (confining stress), respectively. For the axisymmetric in a uniform stress field, $\sigma'_\theta = \sigma'_1$ and $\sigma'_r = \sigma'_3$. The derivation of stress with strain results in the tangent Young's modulus (Rothenburg, 2002),

$$E = \frac{d(\sigma_\theta' - \sigma_r')}{d\varepsilon} = \frac{A_E}{(1 + B_E \varepsilon)^2} \tag{5.2}$$

Rearranging Eq. (5.1)

$$\frac{1}{1+B_E\varepsilon} = 1 - \frac{\sigma'_\theta - \sigma'_r}{A_E / B_E} \tag{5.3}$$

Substituting it into Eq. (5.2), the Young's modulus can be expressed as

$$E = A_E \left(1 - \frac{\sigma'_\theta - \sigma'_r}{A_E / B_E} \right)^2 \tag{5.4}$$

Since A_E/B_E is the maximum stress the rock can sustain (i.e. $(\sigma'_\theta - \sigma'_r)|_{max}$), it fulfills the Mohr-Coulomb failure criterion, $\sigma'_\theta = 2C_o \frac{\cos\varphi}{1-\sin\varphi} + \sigma'_r \frac{1+\sin\varphi}{1-\sin\varphi}$:

$$(\sigma'_\theta - \sigma'_r)\big|_{\max} = 2C_o \frac{\cos\varphi}{1-\sin\varphi} + 2\sigma'_r \frac{\sin\varphi}{1-\sin\varphi} \tag{5.5}$$

Substituting A_E/B_E by Eq. (5.5), Eq. (5.4) becomes

$$E = A_E \left(1 - \frac{R_f (1-\sin\varphi)(\sigma'_\theta - \sigma'_r)}{2C_o \cos\varphi + 2\sigma'_r \sin\varphi} \right)^2 \tag{5.6}$$

where R_f is a parameter accounting for residual strength after stress reaches the peak. Based on Eq. (5.6), Fig. (5-4) shows that Young's modulus generally decreases with plastic deformation, as more and more shear-induced microcracks (i.e. damage) occur. Also, the residual value of modulus depends on the residual strength.

5.2.2.2 Poisson's ratio

Following similar development steps, Kulhawy and Duncan (1972) proposed an equation for alteration of Poisson's ratio by shear damage. Assume that tangential strain (ε_θ) is related hyperbolically with radial strain (ε_r),

$$\varepsilon_\theta = \frac{\varepsilon_r}{A_\nu + B_\nu \varepsilon_r} \tag{5.7}$$

where A_ν, B_ν are constants derived from curve fitting. Now, the tangent Poisson's ratio can be expressed as

$$\nu = \frac{d\varepsilon_r}{d\varepsilon_\theta} = \frac{(A_\nu + B_\nu \varepsilon_r)^2}{A_\nu} \tag{5.8}$$

Rewriting Eq. (5.7) as

$$\frac{A_\nu}{1-B_\nu\varepsilon_\theta} = A_\nu + B_\nu\varepsilon_r \tag{5.9}$$

and substituting it into Eq. (5.8), Poisson's ratio becomes

$$\nu = \frac{A_\nu}{(1-B_\nu\varepsilon_\theta)^2} \tag{5.10}$$

where the tangential strain ε_θ can be calculated by rearranging Eq. (5.1)

$$\varepsilon_\theta = \frac{\sigma'_\theta - \sigma'_r}{A_E\left(1-\dfrac{R_f(1-\sin\varphi)(\sigma'_\theta-\sigma'_r)}{2C_o\cos\varphi+2\sigma'_r\sin\varphi}\right)^2} \tag{5.11}$$

Plotting Eq. (5.10) into Fig. 5-5, it is found that Poisson's ratio increases with shear stress, and the increase rate becomes faster if the rock is largely damaged: i.e., the rock becomes more deformable when plastic effects accumulate (as more microfissures are developed), which agrees with the observations by Walsh and Brace (1966), as shown in Fig. 5-6, and has been proved to be efficient for soil analysis by Kulhawy and Duncan (1972).

5.2.3 Confining-stress-based nonlinearity

When a wellbore is created in an isotropic formation, in-situ stress is disturbed in a way that at some location it is elevated, likely leading to shear damage, while at other locations a decreased confining stress (σ'_r) results in relaxation of rock stiffness and increase of rock deformability. Therefore, according to each value of confining stress, rock properties such as Young's modulus, Poisson's ratio, bulk modulus, friction angle, and so on, have to be recalculated.

5.2.3.1 Young's modulus

In Eq. (5.6), A_E can be treated as the initial Young's modulus (E_i) from which E starts to decrease. The value at atmospheric pressure (P_a) is taken in soil mechanics since soil is exposed on the surface (Duncan and Change 1970; Vaziri, 1995):

$$E_i = K_E P_a \left(\frac{\sigma'_3}{P_a} \right)^n \tag{5.12}$$

which implies that soil will lose its stiffness when the confining stress is zero. Because rock always remains some stiffness regardless of the level of confining stress, Eq. (5.12) is not suitable for stress analysis in rock. Santarelli et al. (1986) developed another empirical relation based on their triaxial compression tests on carboniferous sandstones (Fig.5-7)

$$E_i = E_o \left(1 + m_E \sigma'^{n_E}_3 \right) \tag{5.13}$$

where E_o is rock Young's modulus at atmospheric pressure, and m_E and n_E are constants determined from curve fitting (e.g. $m_E = 0.043$ and $n_E = 0.78$ for the carboniferous sandstone, as shown in Fig. 5-8). There are other different empirical expressions for stress-dependent rock stiffness (e.g. King, 1969; Brady, 1969; McLean, 1987), but Eq. (5.13) is used in this study, as it agrees with Tronvoll's experiments with Red Wildmoor sandstone (1993): i.e., the relation of Young's modulus to confining stress is fitted to a power law function.

5.2.3.2 Poisson's ratio

Similarly, A_ν in Eq. (5.10) can be treated as initial Poisson's ratio (ν_i), which is related to confining stress through a semi-logarithmic equation (Kulhawy and Duncan, 1972)

$$\nu_i = \nu_0 - D_\nu \log\left(\frac{\sigma'_3}{P_a}\right) \tag{5.14}$$

where ν_0 is the rock Poisson's ratio at atmosphere pressure, D_ν is the rate of ν_i change with confining stress σ'_3, and P_a is atmosphere pressure (same units as stress). Fig. 5-9 plots the calculations from Eq. (5.14) and

shows that the rock becomes less deformable when confining stress increases to certain level, which agrees with many rock experiment results (Schmidt, 1926 (Fig. 5-10); Lama and Vutukuri, 1978; Tronvoll, 1993). Due to experimental difficulties and the complex behavior of ν, there are few publications available for unconsolidated sand, except that Lama and Vutukuri (1978) suggested that an increase of effective confining stress lowers Poisson's ratio for weaker rocks, but for stronger rocks its effect is not significant.

5.2.3.3 Friction angle and bulk modulus

Other rock properties such as friction angle (φ) and bulk modulus (B) have been studied and their relations with confining stress are expressed in the form of (e.g. Byrne et al., 1987)

$$\varphi = \varphi_0 - D_\varphi \log(\frac{\sigma_3'}{P_a}) \tag{5.15}$$

and

$$B = K_B P_a \left(\frac{\sigma_3'}{P_a}\right)^n \tag{5.16}$$

where φ_0 is friction angle at atmosphere pressure, D_φ is the rate of φ change with confining stress, and K_B, n are constants derived from curve-fitting. Since friction angle becomes almost constant after confining stress increases to some level (e.g. 10 MPa in Fig. 5-11), and reservoir rock is usually restrained by high in-situ stresses, the friction angle is assumed to be stress-independent in this research.

5.2.4 Incorporating nonlinear properties into stress calculations

For axisymmetric problems such as wellbore stress analysis, radial strain (ε_r) and tangential strain (ε_θ) can be expressed as

$$\varepsilon_r = \frac{du}{dr} \tag{5.17}$$

and

$$\varepsilon_\theta = \frac{u}{r} \tag{5.18}$$

where u is the radial deformation and r is the distance from the wellbore. Substituting Eq. (5.18) into Eq. (5.17) to eliminate the variable u, a strain compatibility relation can be derived

$$\varepsilon_r = \frac{d(r\varepsilon_\theta)}{dr} = \varepsilon_\theta + r\frac{d\varepsilon_\theta}{dr} \tag{5.19}$$

i.e. $$\frac{d\varepsilon_\theta}{dr} = \frac{\varepsilon_r - \varepsilon_\theta}{r} \tag{5.20}$$

Meanwhile, the total stress equilibrium is

$$\frac{d\sigma_r}{dr} = -\frac{\sigma_r - \sigma_\theta}{r} \tag{5.21}$$

Combining Eq. (5.20) with Eq. (5.21), stress can thus be related to strain through

$$\frac{d\sigma_r}{d\varepsilon_\theta} = -\frac{\sigma_r - \sigma_\theta}{\varepsilon_r - \varepsilon_\theta} \tag{5.22}$$

We assume that strain is a function of the effective stresses, i.e.

$$\varepsilon_r = \varepsilon_r(\sigma'_r, \sigma'_\theta);\ \varepsilon_\theta = \varepsilon_\theta(\sigma'_r, \sigma'_\theta) \tag{5.23}$$

where σ'_r and σ'_θ are the effective radial and the tangential stresses, respectively. For porous media with fluid flow the incremental elastic plane stress-strain relations are

$$d\varepsilon_r = \frac{1+\nu}{E}\left[(1-\nu)d\sigma'_r - \nu d\sigma'_\theta\right] \tag{5.24}$$

$$d\varepsilon_\theta = \frac{1+\nu}{E}\left[(1-\nu)d\sigma'_\theta - \nu d\sigma'_r\right] \tag{5.25}$$

Therefore the total differential ε_θ can be

$$d\varepsilon_\theta = \frac{\partial\varepsilon_\theta}{\partial\sigma'_r}d\sigma'_r + \frac{\partial\varepsilon_\theta}{\partial\sigma'_\theta}d\sigma'_\theta \tag{5.26}$$

Substituting $d\varepsilon_\theta$ into Eq. (5.22), the Biot equation can be developed (Biot, 1974)

$$\frac{d\sigma_r}{d\sigma_\theta} = -\frac{\partial\varepsilon_\theta/\partial\sigma_\theta}{\frac{\varepsilon_r - \varepsilon_\theta}{\sigma_r - \sigma_\theta} + \partial\varepsilon_\theta/\partial\sigma_r} \tag{5.27}$$

This has served as the theoretical basis of analytical nonlinear stress models (Santarelli et al., 1986; Santarelli and Brown, 1987; Wang, 1990).

Eq. (5.25) - Eq. (5.24) gives

$$\frac{\varepsilon_r - \varepsilon_\theta}{\sigma_r - \sigma_\theta} \equiv \frac{\varepsilon_r - \varepsilon_\theta}{\sigma_r' - \sigma_\theta'} = \frac{1+\nu}{E} \tag{5.28}$$

Replacing it in Eq. (5.22) yields

$$\frac{d\varepsilon_\theta}{d\sigma_r} = -\frac{E}{1+\nu} \tag{5.29}$$

By assuming the tangent Poisson's ratio is a constant and the tangent Young's modulus is a function of radial stress only, i.e. $E = E(\sigma_r)$, from Eq. (5.25)

$$\frac{\partial\varepsilon_\theta}{\partial\sigma_\theta'} = \frac{(1+\nu)(1-\nu)}{E(\sigma_r')} \tag{5.30}$$

and

$$\frac{\partial\varepsilon_\theta}{\partial\sigma_r'} = -\frac{(1+\nu)(1-\nu)}{E(\sigma_r')^2}\sigma_\theta'\frac{dE(\sigma_r')}{d\sigma_r'} - (1+\nu)\nu\left(\frac{1}{E(\sigma_r')} - \frac{\sigma_r'}{E(\sigma_r')^2}\frac{dE(\sigma_r')}{d\sigma_r'}\right) \tag{5.31}$$

Using the above three equations, Eq. (5.27) becomes

$$\frac{d\sigma_\theta}{d\sigma_r} = \left(\sigma_\theta - \frac{\nu}{1-\nu}\sigma_r\right)\frac{1}{E(\sigma_r)}\frac{dE(\sigma_r)}{d\sigma_r} - 1 \tag{5.32}$$

i.e.

$$\frac{d\sigma_\theta}{d\sigma_r} - \left(\frac{1}{E(\sigma_r)}\frac{dE(\sigma_r)}{d\sigma_r}\right)\sigma_\theta = -\frac{\nu}{1-\nu}\frac{1}{E(\sigma_r)}\frac{dE(\sigma_r)}{d\sigma_r}\sigma_r - 1 \tag{5.33}$$

This is a first-order linear inhomogeneous equation, in the form of

$$y'(x) + P(x)y(x) = f(x) \tag{5.34}$$

where $x = \sigma_r$, $y = \sigma_\theta$, $P(x) = -\left(\frac{1}{E(\sigma_r)}\frac{dE(\sigma_r)}{d\sigma_r}\right)$, $f(x) = -\frac{\nu}{1-\nu}\frac{1}{E(\sigma_r)}\frac{dE(\sigma_r)}{d\sigma_r}\sigma_r - 1$. The solution of this type of equation is (Bender and Orszag, 1978)

$$y(x) = \frac{C}{I(x)} + \frac{1}{I(x)}\int^x f(t)I(t)dt \tag{5.35}$$

where C is a constant determined by the boundary conditions, and

$$I(x) = \exp\int^{\sigma_r}\left(-\frac{1}{E(t)}\frac{dE(t)}{dt}\right)dt = E^{-1}(\sigma_r) \tag{5.36}$$

Correspondingly the tangential stress can be expressed as

$$\sigma_\theta(\sigma_r) = CE(\sigma_r) + E(\sigma_r)\int^{\sigma_r}(-\frac{\nu}{1-\nu}\frac{1}{E(t)}\frac{dE(t)}{dt}t - 1)E^{-1}(t)dt \tag{5.37}$$

i.e
$$\sigma_\theta(\sigma_r) = CE(\sigma_r) + \frac{\nu}{1-\nu}\sigma_r - \frac{E(\sigma_r)}{1-\nu}\int^{\sigma_r}E^{-1}(t)dt \tag{5.38}$$

which agrees with Santarelli and Brown's work ($\sigma_\theta = \frac{\nu}{1-\nu}\sigma_r - \frac{E(\sigma_r)}{1-\nu}\int\frac{d\sigma_r}{E(\sigma_r)}$, 1987). Applying a boundary condition, such as BC1 in Section 4.1.2, into the above equation, the constant C can be solved as

$$C = \frac{1-2\nu}{1-\nu}\frac{\sigma_h}{E_o} + \frac{\int^{\sigma_{hr}}E^{-1}(t)dt}{1-\nu} \tag{5.39}$$

With input of different forms of $E(\sigma_r)$, the tangential stress σ_θ can be determined from Eq. (5.38) and Eq. (5.39). Substituting it into Eq. (5.21), a first-order differential equation of total radial stress is derived, which may yield stress solutions.

5.2.5 Validity of nonlinear theories for rock analysis

Even though the equations in Sections 5.2.2 and 5.2.3 show that rock becomes more compacted and stiffer with increase of confining stress, i.e. higher moduli, smaller Poisson's ratio, and smaller friction angle, the determination of constants may require numerous experiments. Furthermore, nonlinear theories were initially designed for soil in civil engineering, and their applications to reservoir rock may require further developments.

Kulhawy (1975) demonstrated the validity of a hyperbolic form of Young's modulus and Poisson's ratio for various types of rock from shale to sandstone and summarized experimental values of different input parameters, e.g. $R_f = 0.73$ in Eq. (5.6) for Berea sandstone. For rock stress calculations, because the friction angle can be treated as constant at high confining stress (e.g. 10MPa in Fig. 5-11), only nonlinear E

and ν values are involved. Moreover, since the development of failure-based nonlinearities has not introduced any limitation from soil mechanics, Eqs. (5.6) and (5.10) are promising for reservoir rock. Besides describing the physical changes of loaded rock, another attraction of the theory is that only two curves are needed to determine A_E in Eq. (5.6) and A_ν, B_ν in Eq. (5.10): a stress-strain curve and tangential-radial strain curve, which are usually available in rock triaxial test data. Furthermore, due to cohesion degradation (or loss) in the plastic zone around the wellbore, the rock behaves more like soil than it initially does. This highlights the value of the nonlinear theory in stress analysis around a wellbore.

The author believes that the greatest challenge of nonlinear theory comes from the analytical solution of the stress equations rather than the limitations inherited from soil mechanics. The stress derivations in Section 5.2.3 have to assume that modulus only depends on confining stress (i.e. $E=E(\sigma_r)$), Poisson's ratio is a constant, and leave aside the effect of pore pressure (as it is the effective stresses that should be used in Eq. (5.24) and Eq. (5.25)). Even with those assumptions, only certain forms of $E(\sigma_r)$ are demonstrated to be solvable (Brown et al., 1989). Analytical stress solutions with both stress-dependent modulus and stress-dependent Poisson's ratio present more prohibitive mathematical challenges. Those limitations jeopardize the applicability of nonlinearity theory to a considerable extent in practical applications.

Instead of analytical approaches, numerical methods of stress calculations with nonlinear rock properties are used, such as the Finite Element Method that enables nonlinear descriptions of element properties at each iteration (Vaziri, 1995). The application of FEM into stress analysis is not carried out in this research as physics and analytical approaches are the main focus. However the following description of water-related property changes can be served as a basis for further numerical analysis.

5.3 Modelling Rock Properties after Water Breakthrough

5.3.1 Incorporation of the water effect

Based on the discussions in Chapter 4, water breakthrough into an oil producer can affect rock stability in three ways:

- Strength weakening. Both chemical reactions and capillarity can reduce shear strength with respect to water saturation and time, which can be described mathematically by Eq. (4.81);
- Stress elevation. Due to the changes of oil/water relative permeabilities, pore pressure first declines to a minimum, leading to the increase of rock effective stresses; and,
- Stress oscillations. The viscosity difference between water and oil results in less energy consumed by fluid flow at later stages of water breakthrough. Therefore pore pressure starts to increase after the initial minimum, and loading stress (i.e. effective stress) is released. Fig. 5-12 shows stress loading (from S_w = 34% to S_w = 50%) and unloading processes (from S_w = 50% to S_w = 70%) in terms of shear stress redistributions around the wellbore. Stress fluctuations may significantly affect rock stability (Han et al., 2002 *b*).

Introducing Eq. (4.81) for strength and Eqs (4.78) and (4.79) for stresses into nonlinear equations for Young's modulus and Poisson's ratio, the effect of water breakthrough on rock behavior can be evaluated.

5.3.2 Nonlinear Young's modulus

Rock behavior in the plastic zone where rock has been damaged by shear failure and only residual strength exists is complex and not amenable to detailed analytical modeling, so a simplified approach with a constant strength in the zone is taken in the following discussions.

Following the stress distributions, Fig. 5-13 shows Young's modulus monotonously decreasing from the far field to the near wellbore, and then stays almost constant within the plastic zone. The rate of decrease becomes much faster near the plastic boundary (r/R1, where R1 is wellbore radius): rock modulus lost is about 80% within 1 meter for a typical borehole diameter. Also, varying parameter R_f from 0.73 (Fig. 5-14) to 0.5 (Fig. 5-15) demonstrates that the minimum value of Young's modulus depends strongly on the magnitude of rock residual strength, as rock remains stiffer if its fabric has been less damaged by shear failure.

The effect of confining stress on the modulus is studied by varying the slope of Eq. (5.13) (i.e. m_E) while other parameters are kept unchanged. Comparing Fig. 5-13 (m_E = 0.043) with Fig. 5-14 (m_E =

0.0043), the effect is very limited for a wellbore situation, even though Fig. 5-8 shows that variation of m_E from 0.043 to 0.0043 can result in a significant difference in the Young's modulus. This suggests that failure-based mechanisms play a more important role in reducing rock stiffness around the wellbore than confining-stress-based mechanisms.

Initial rock strength greatly affects the distribution of shear stress (Fig. 5-16). The stronger the rock is, the more the stress is concentrated towards the wellbore, which in turn decreases Young's modulus much faster (Fig. 5-17). Therefore, consolidated rock may lose most of its stiffness within a very short distance from the well, within the yielded zone. For example, 90% of the modulus is lost within 0.6 meter when rock initial cohesive shear strength is 1 MPa, whereas about 1.7 meter is needed to reduce the same amount of modulus when rock strength is 0.4 MPa.

Based on model calculations, different mechanisms for rock stiffness reduction after an oil well starts to produce free water, such as chemical reactions, capillarity, and pore pressure changes, are evaluated and compared:

- Largely due to the changes of oil/water relative permeabilities, shear stress is elevated significantly with water saturation: it increases from 6 MPa to 14 MPa at a location of $r/R_1 = 7.5$ when S_w changes from 32% of connate saturation to about 45% and cohesive strength is 0.4 MPa (Fig. 5-18). Correspondingly, the rock Young's modulus decreases from 2.3 GPa to 1.3 GPa, a loss of about 45%, before it regains part of stiffness because of stress release (Fig. 5-19). Furthermore, the magnitude of modulus loss and stress increase with water saturation depends on location in the rock (r/R1 = 7.5, 15) and its initial strength (C_o = 0.4MPa, 0.45MPa, 0.5MPa): the farther the rock is located away from the well, and the stronger the rock, the less the modulus loss and the stress increase. This confirms the experimental observations that weaker rock is more sensitive to changes in moisture content (Dyke and Dobereiner, 1991).
- Following a method similar to that in Chapter 4.3.5, the effect of chemical reactions on rock stiffness can be evaluated by manually inputting a reduced strength. If rock cementation is chemically sensitive and the rock strength is weakened from 0.5 MPa to 0.4 MPa (Fig. 5-19) by reactions, Young's modulus

is reduced to 1.3 GPa instead of 2 GPa at the location of r/R1 = 7.5. Meanwhile shear stress level reaches a maximum of 14 MPa (C_o = 0.4 MPa in Fig. 5-18) compared to the value of 9.5 MPa when no chemical reactions are assumed (C_o = 0.5 MPa in Fig. 5-18). Therefore the effects of chemical reactions leave the rock more deformable.

- As it is in the magnitude of several kPa, diminishing of capillary strength with saturation plays a very limited role in shear stress magnitude (Fig. 5-20), Young's modulus (Fig. 5-21), and plastic radius (Fig. 5-22). Comparing solid lines (without capillarity) with dotted lines (with capillarity) in those figures, at the critical water saturation (i.e. S_w = 45%) capillary strength can cause a maximum change of several 100 KPa in shear stress, several tens of MPa in Young's modulus, and one or two units in dimensionless plastic radius.

5.3.3 Nonlinear Poisson's ratio

Fig. 5-23 shows the effect of Poisson's ratio on plastic radius. When the Poisson's ratio changes from 0.15 to 0.45, critical radius varies little (similar to the effect of capillarity), which may validate the assumption that Poisson's ratio can be treated as a constant when stresses around a yielding wellbore are calculated. This is consistent with Cristescu (1989)'s statement that "Poisson's ratio … is generally of little use in determining a reasonably accurate constitutive equation for rocks", and also reinforces the conclusions made by Morita (1989). However for compaction analysis or strain calculations, on which some failure criteria of sand production are proposed, this assumption is invalid. For example, in elastic analysis thermal cases (i.e. substantial changes in volume from heating or cooling), the stress and strain values are quite sensitive to Poisson's ratio.

5.4 Conclusions

Water breakthrough into an oil well can lead to significant stress redistributions and strength variations, upon which rock elastic properties such as Young's modulus and Poisson's ratio are dependent. Unfortunately, none of them is carefully studied in current sand production prediction efforts. Based on an improved nonlinear theory, which considers both a failure-based mechanism (Section 5.2.2) and a

confining-stress-based mechanism (Section 5.2.3), a strength model that accounts for strength weakening from capillarity and chemical reactions, and a coupled inelastic stress model, the effect of water breakthrough on rock properties is, for the first time, analytically addressed. Influential factors such as pore pressure changes, chemical reactions, and capillarity are analyzed and their relative importance to sand stability is compared.

The mechanisms for rock nonlinearity are analyzed in two categories: one is based on shear failure that damages rock fabric and leaves the rock softer and more deformable; the other depends on confining stress that compacts and stiffens the rock. There are many different equations developed for various materials and properties, among which appropriate forms should be carefully selected, modified, and verified for rock analysis around the wellbore in specific cases and specific rock types. The derivation of analytical stress models with nonlinear rock properties faces prohibitive mathematical challenges. Very few solutions can be achieved under the assumption that rock stiffness solely relies on confining stress in some simple, specific way. Numerical methods such as finite element analysis are recommended in order to more generally incorporate nonlinear rock properties into stress and strain calculations.

Based on calculations using the proposed models, new conclusions are made with regard to the distributions of stress-dependent rock moduli around a wellbore:

- Corresponding to shear stress distribution, which increases rapidly to a peak at the boundary between plastic and elastic zones, Young's modulus rapidly decreases to a minimum at the boundary (for the case studied, rock modulus loss was about 80% within 1 meter) and increases with the distance in the far field. Within the plastic zone where the rock has already been damaged by shear failure, the modulus remains low. The magnitude of the residual modulus depends on rock residual strength: the more the residual strength, the more the residual modulus;
- Yield mechanisms play a more important role in reducing rock stiffness around the wellbore than confining-stress-based mechanisms;

- Rock initial strength greatly affects the distributions of both shear stress and stiffness: stronger rock results in the stress being more concentrated near the wellbore, and therefore a more precipitous decrease of Young's modulus in that region;
- Mainly due to the changes of oil/water relative permeabilities, shear stress increases significantly with water saturation and then gradually decreases. Correspondingly, the loss of rock Young's modulus can be as high as 45% before it regains part of its stiffness because of pressure recovery and stress release. Furthermore, the magnitude of stiffness loss and stress increase with saturation is related to the rock location and its initial strength: the stronger rock located far away from the well results in less modulus loss and stress increase;
- For water-sensitive cemented rock, chemical reactions, along with changes of fluid relative permeabilities, play dominant roles in reducing modulus: the more the strength is chemically lost, the greater the decrease of Young's modulus with water saturation;
- The effect of capillarity on rock elastic properties is very limited; and,
- Nonlinear Poisson's ratio is modeled as depending on both stress and strength. However for all possible values of sand, Poisson's ratio affects the magnitude of effective stress and plastic radius very little. This indicates that Poisson's ratio can be treated as a constant when stresses around wellbore are analyzed.

These new studies of nonlinear rock behavior facilitates the understanding of rock behavior in oil/water environments, and may explain why current predictive models for sand production are "invalid when the well being analyzed produces free water" (Ghalambor et al., 1994). The models can be served as a basis for a new sand prediction tool in oil industry.

5.5 Tables and Figures

Table 5-1. Variation of E_t and ν with Humidity for the Sandstones Tested

(After Rao et al., 1987)

Relative Humidity (%)	Kota sandstone		Jamrani Sandstone		Singrauli Sandstone		Jhingurda Sandstone	
	$E_t \times 10^2$ MPa	ν	$E_t \times 10^2$ MPa	ν	$E_t \times 10^2$ MPa	ν	$E_t \times 10^2$ MPa	ν
0	1.5304	0.0784	0.546	0.2857	0.44	0.1364	0.3053	0.1316
35	1.825	0.125	0.546	0.2461	0.4583	0.125	0.2174	0.1087
60	1.1896	0.1034	0.4106	0.25	0.4255	0.1489	0.1864	0.1818
85	1.1123	0.1579	0.3879	0.4697	0.3654	0.1154	0.1842	0.1579
95	1.037	0.2407	0.3539	0.4444	0.425	0.1542	0.21	0.3
100	0.9505	0.2667	0.3193	0.4386	0.3091	0.2545	0.1524	0.24
Saturated	0.9091	0.3182	0.2724	0.5345	0.2633	0.3167	0.1154	0.2309

Note: tangential modulus E_t is taken at the 50% of peak strength.

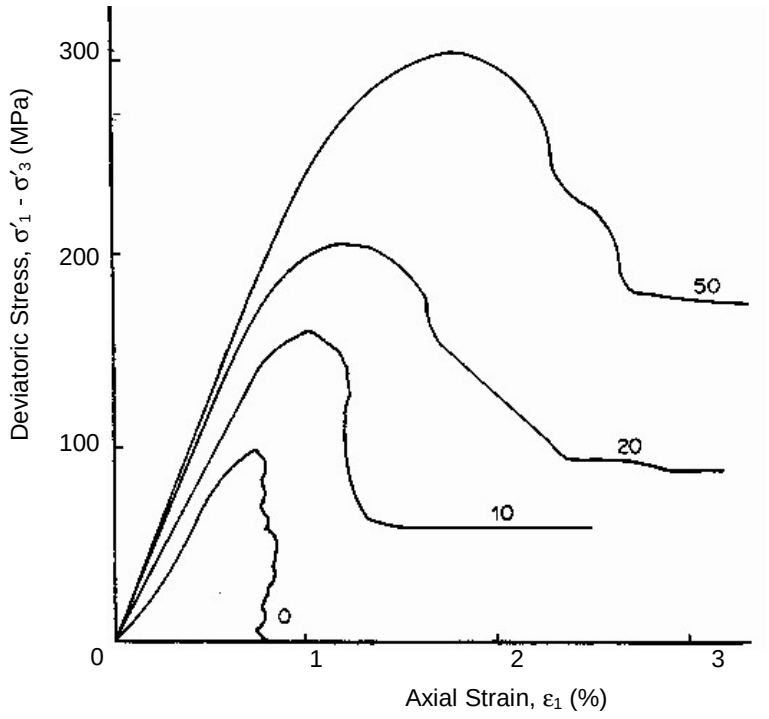

Fig. 5-1: Stress-strain curves for triaxial compression tests on a sandstone under different confining stresses (in MPa) (after Santarelli et al., 1986)

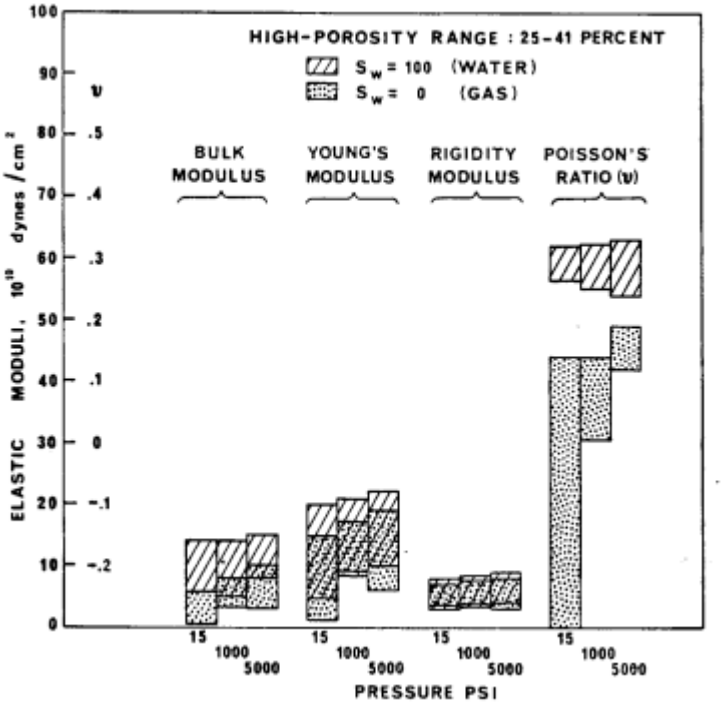

Fig. 5-2: Effects of confining stress and fluid saturation on elastic moduli of high-porosity rock
(After Gregory, 1976)

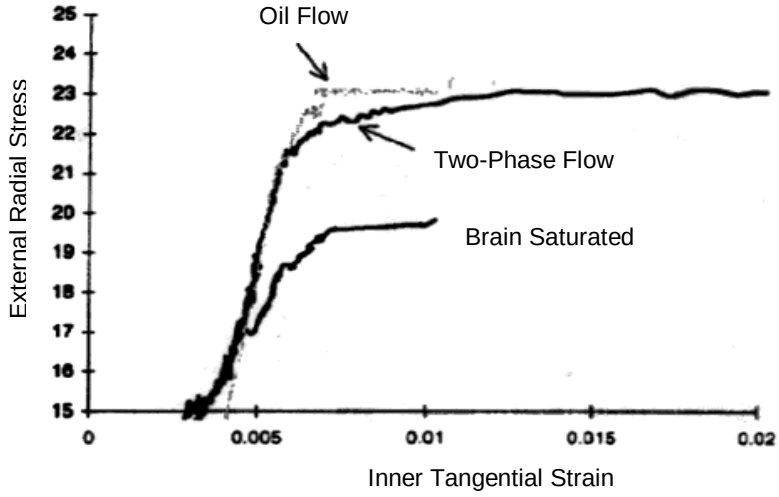

Fig. 5-3: Stress-strain curves under different water saturations in a hollow cylinder test with fluid flow (after Skjærstein et al., 1997)

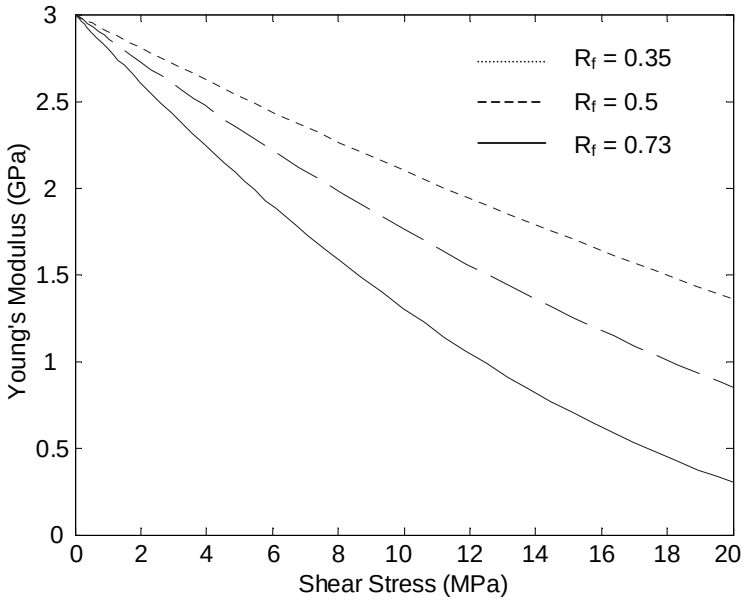

Fig. 5-4: Effect of shear stress on Young's modulus (σ'_3 = 10MPa)

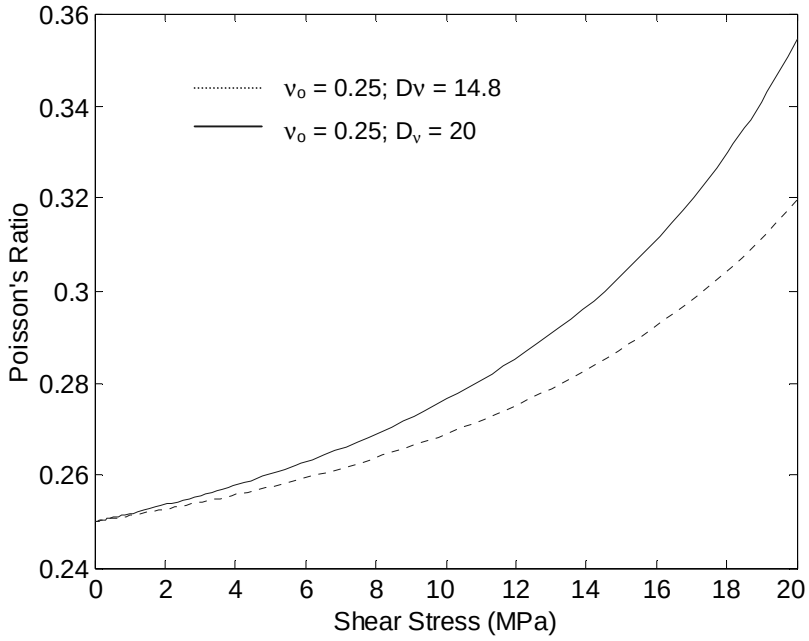

Fig. 5-5: Effect of shear stress on Poisson's ratio

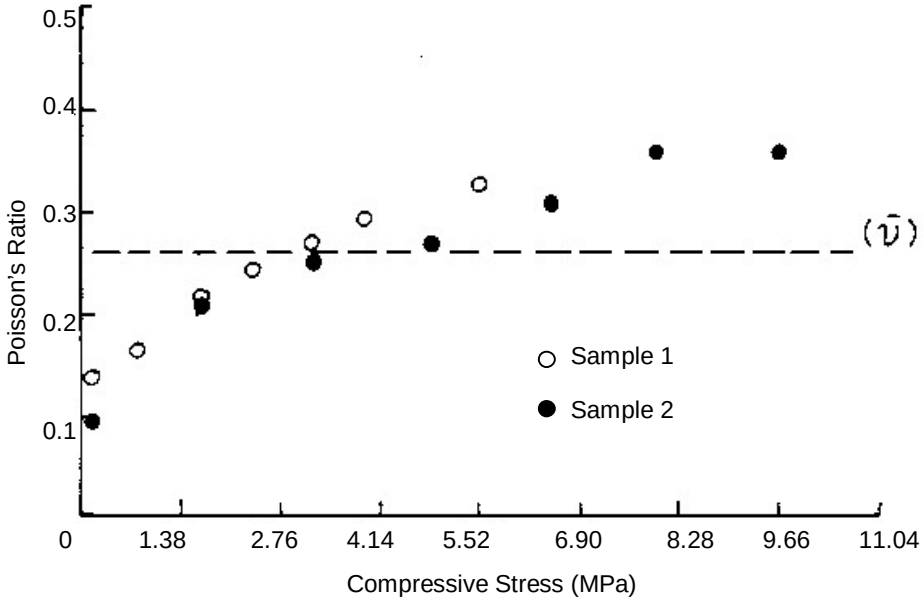

Fig. 5-6: Poisson's ratio vs. compressive stress for a rock
(after Walsh and Brace, 1966)

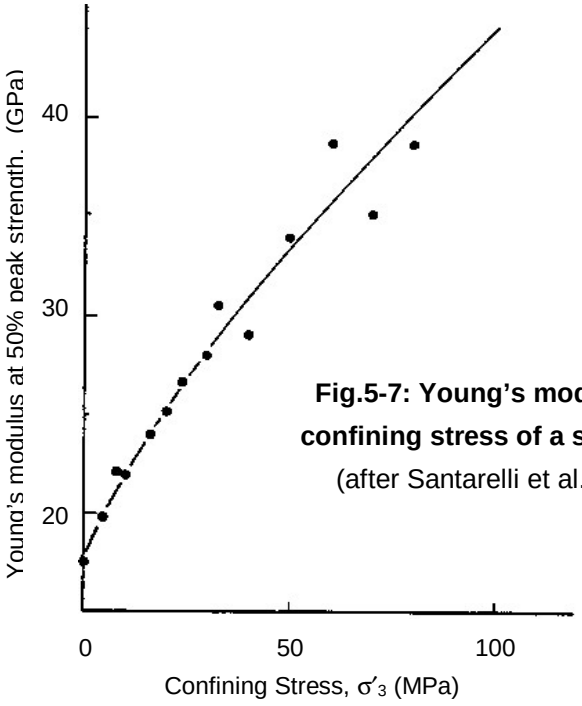

Fig.5-7: Young's modulus vs. confining stress of a sandstone
(after Santarelli et al., 1986)

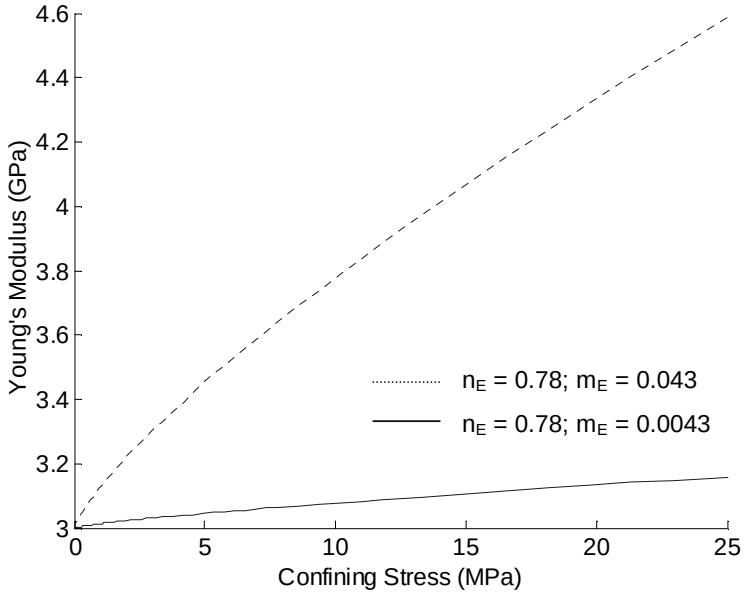

Fig. 5-8: Effect of confining stress on Young's modulus

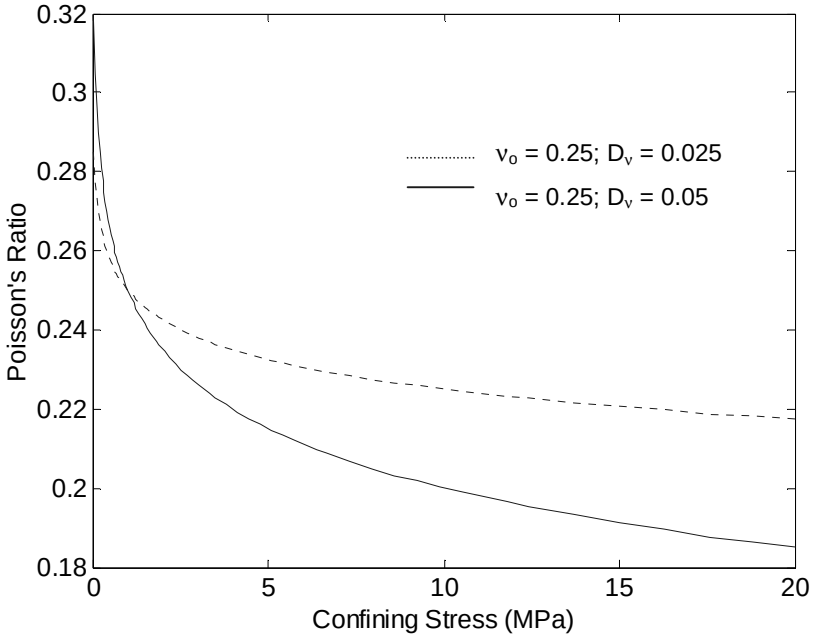

Fig. 5-9: Effect of confining stress on Poisson's ratio

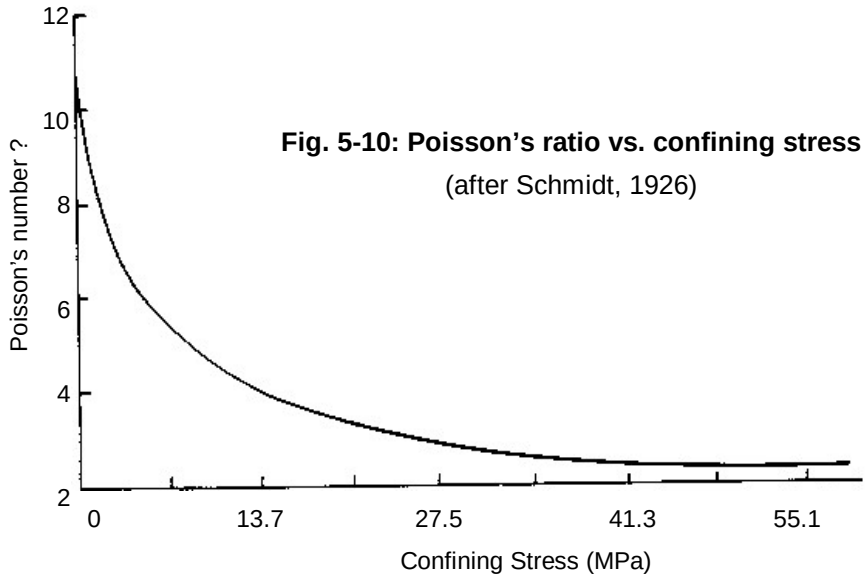

Fig. 5-10: Poisson's ratio vs. confining stress
(after Schmidt, 1926)

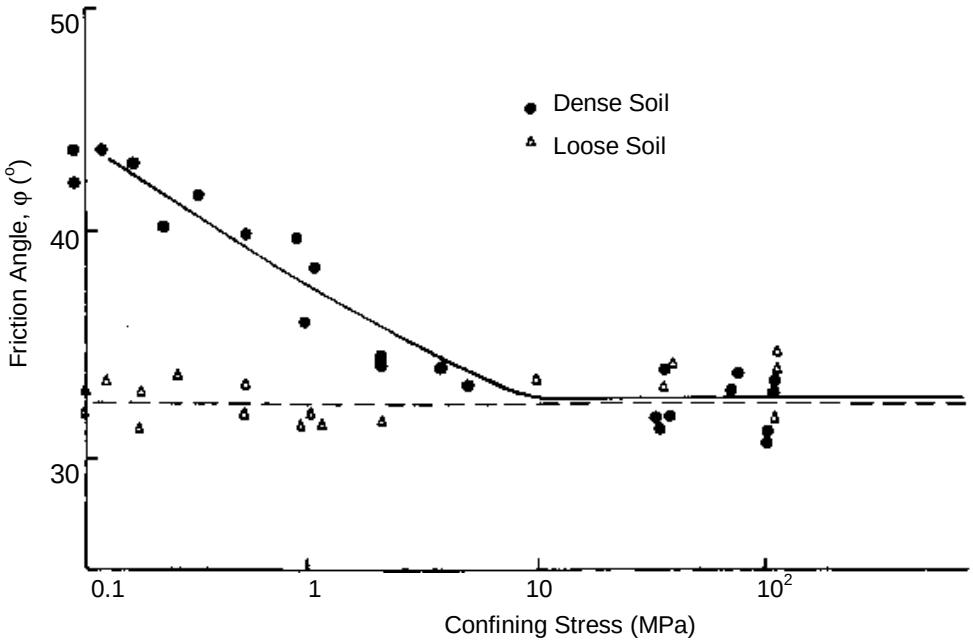

Fig. 5-11: Friction angle vs. confining stress of dense and loose soil
(after Vesic and Clough, 1986)

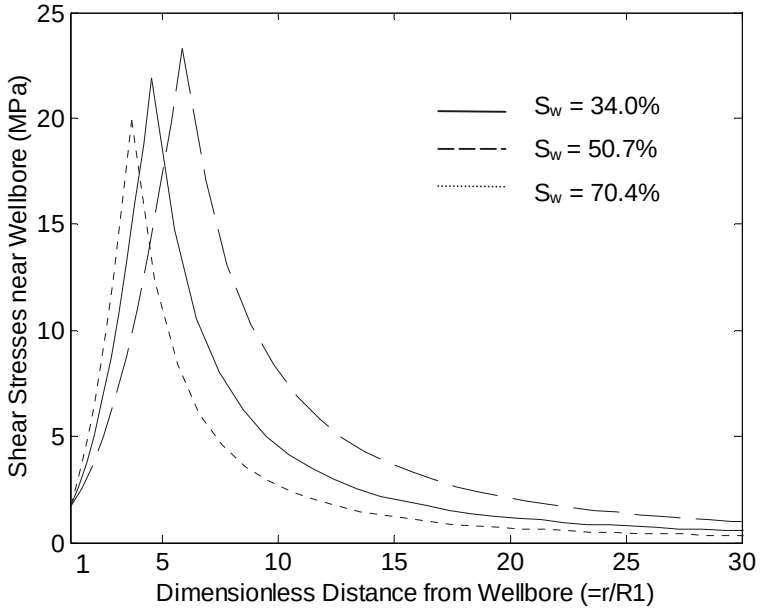

Fig. 5-12: Distributions of shear stress around the wellbore

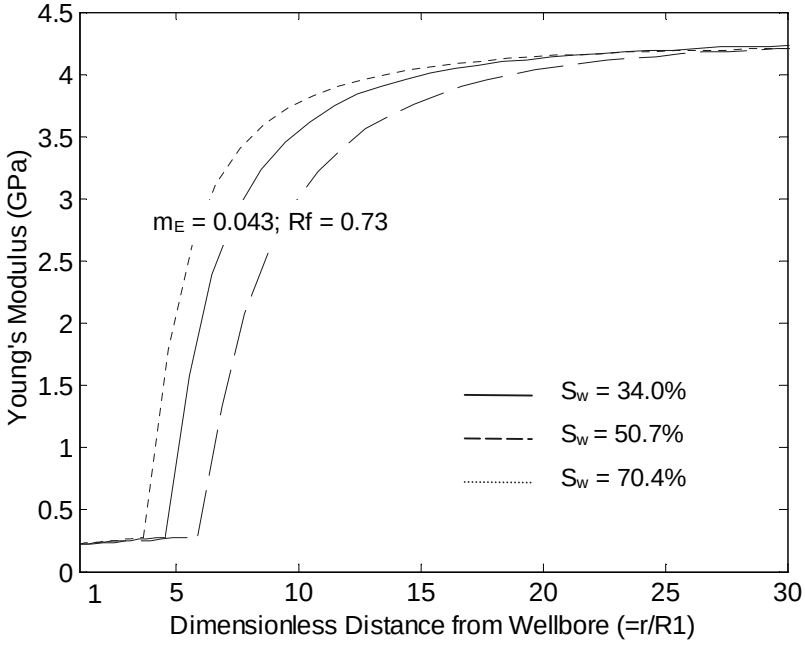

Fig. 5-13: Distributions of stress-dependent Young's modulus around wellbore

(m_E = 0.043; Rf = 0.73)

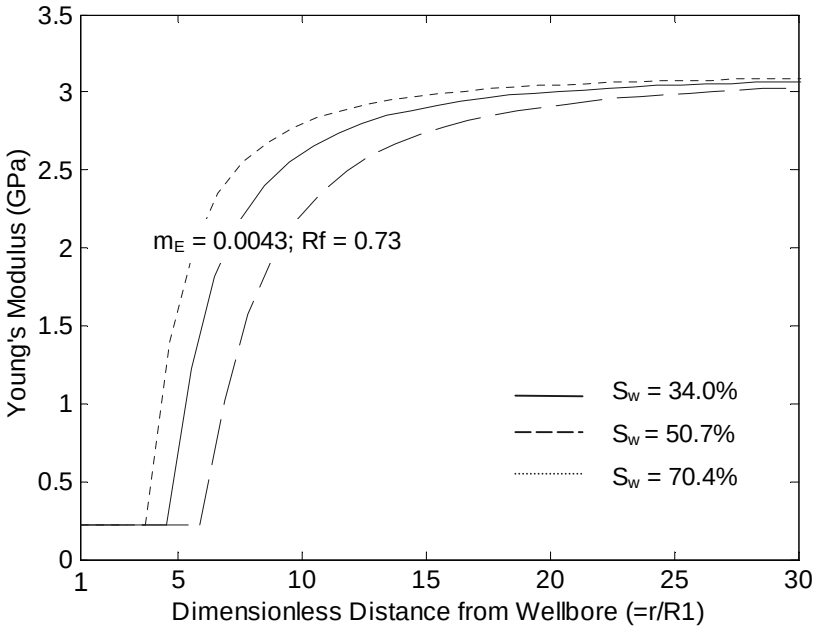

Fig. 5-14: Distributions of stress-dependent Young's modulus around wellbore

(m_E = 0.0043; Rf =0.73)

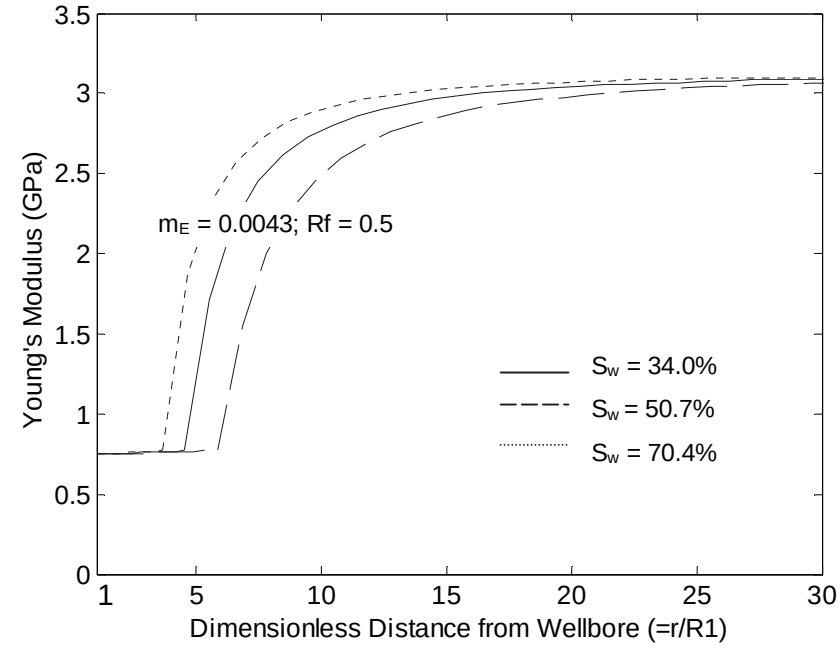

Fig. 5-15: Distributions of stress-dependent Young's modulus around wellbore

(m_E = 0.0043; Rf =0.73)

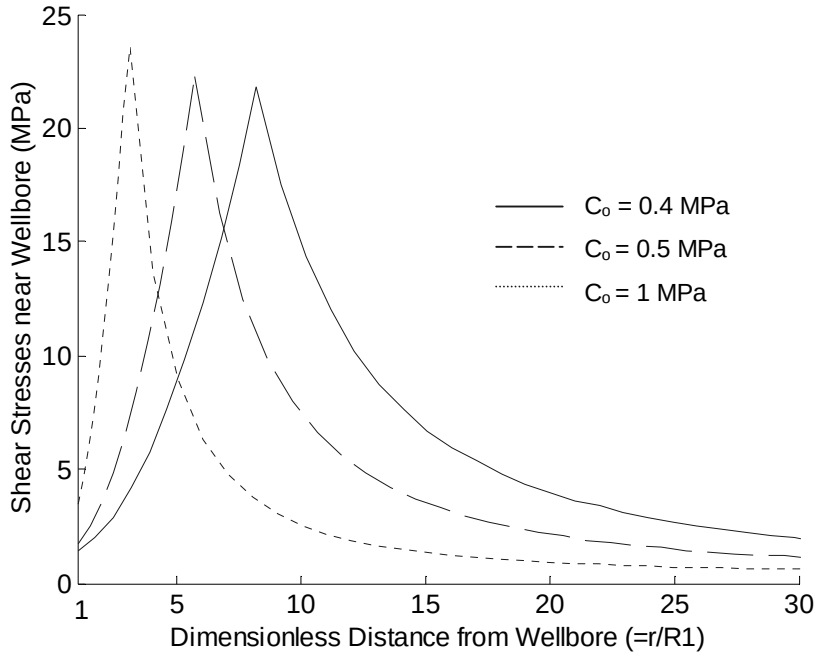

Fig. 5-16: Effect of rock strength on shear stress distributions

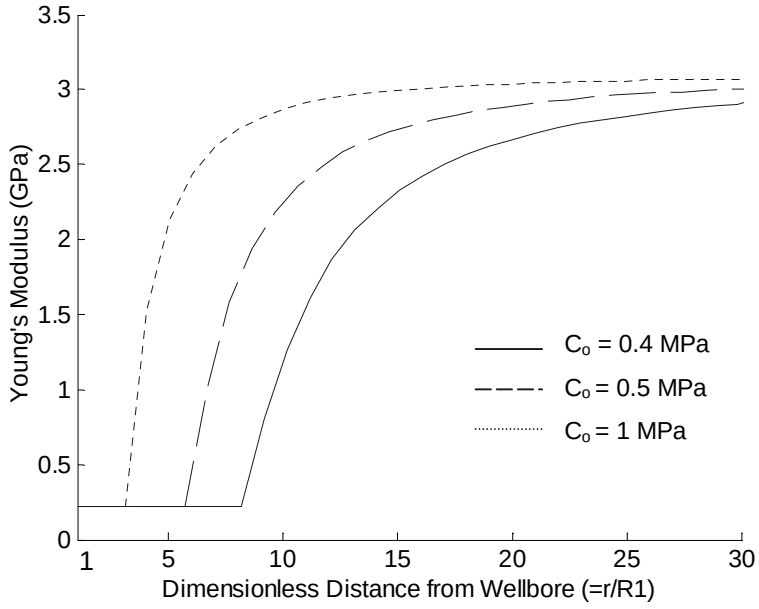

Fig. 5-17: Effect of rock strength on Young's modulus distributions

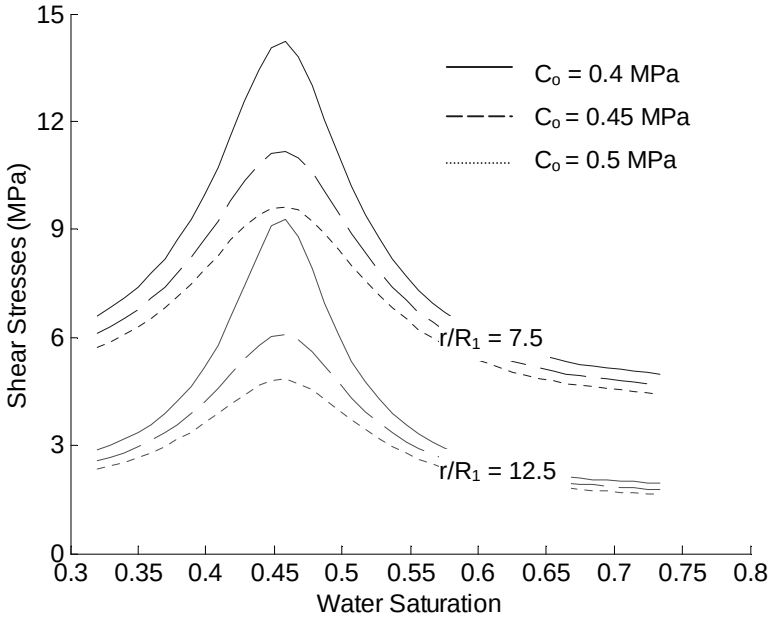

Fig. 5-18: Variations of shear stress after water breakthrough

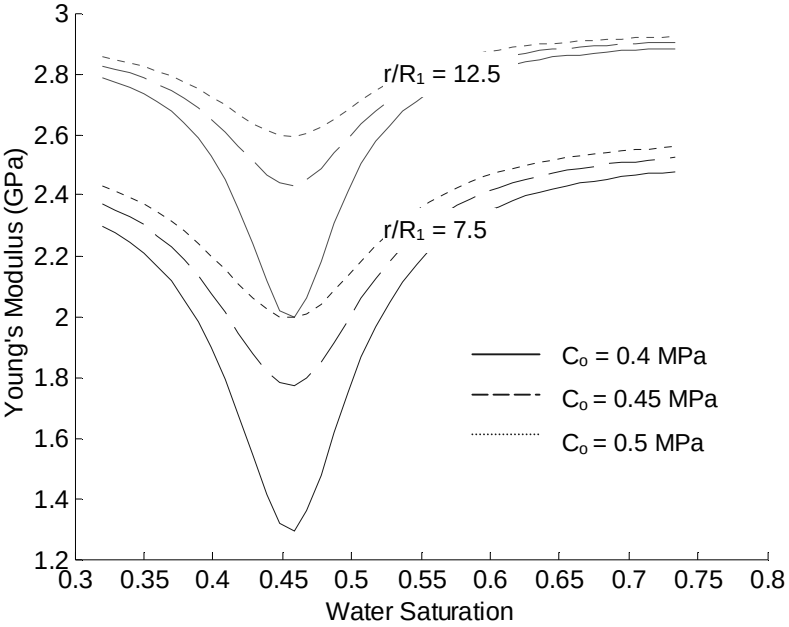

Fig. 5-19: Evolutions of Young's modulus after water breakthrough

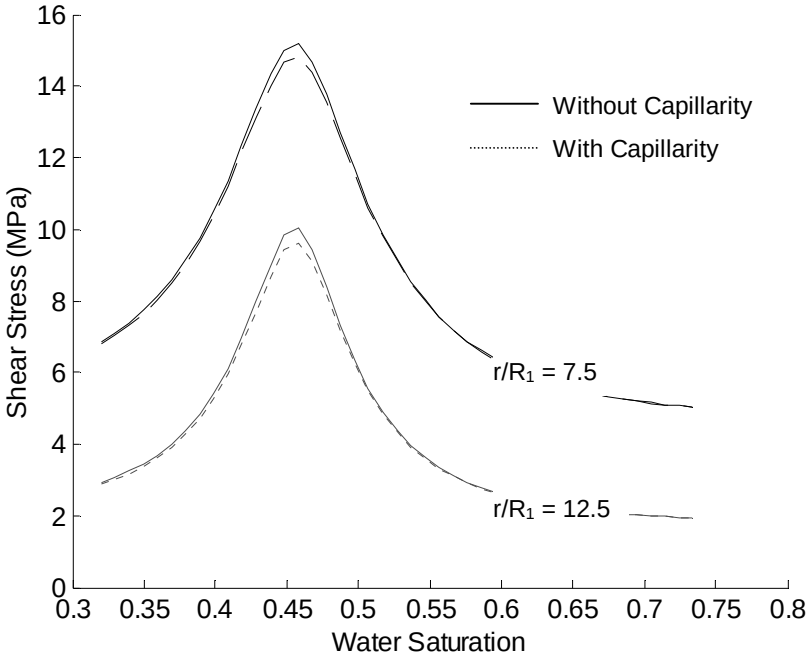

Fig. 5-20: Effect of capillary strength on shear stress distributions

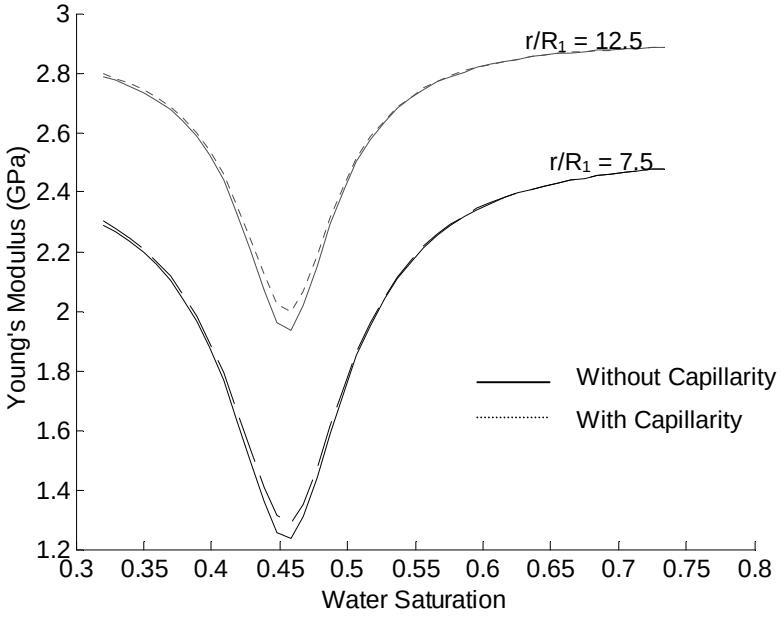

Fig. 5-21: Effect of capillary strength on Young's modulus distributions

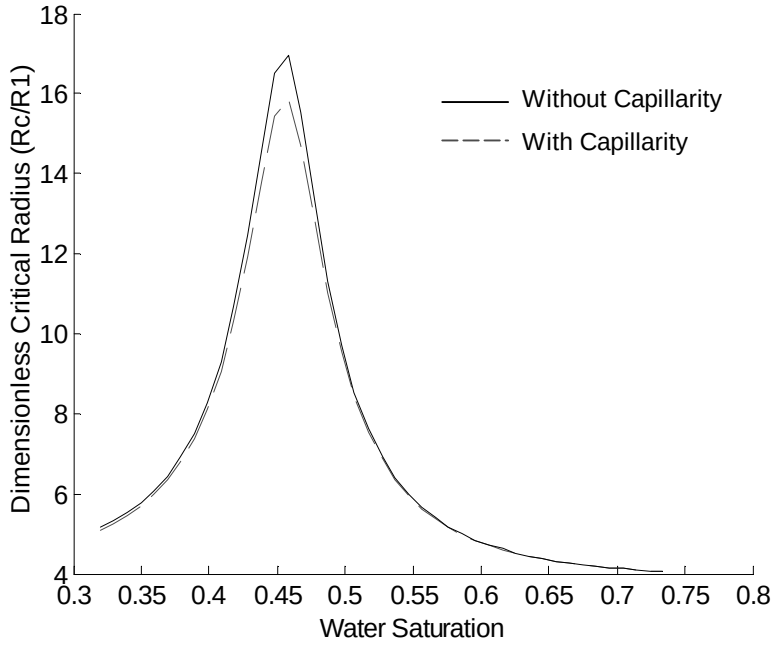

Fig. 5-22: Effect of capillary strength on sand stability

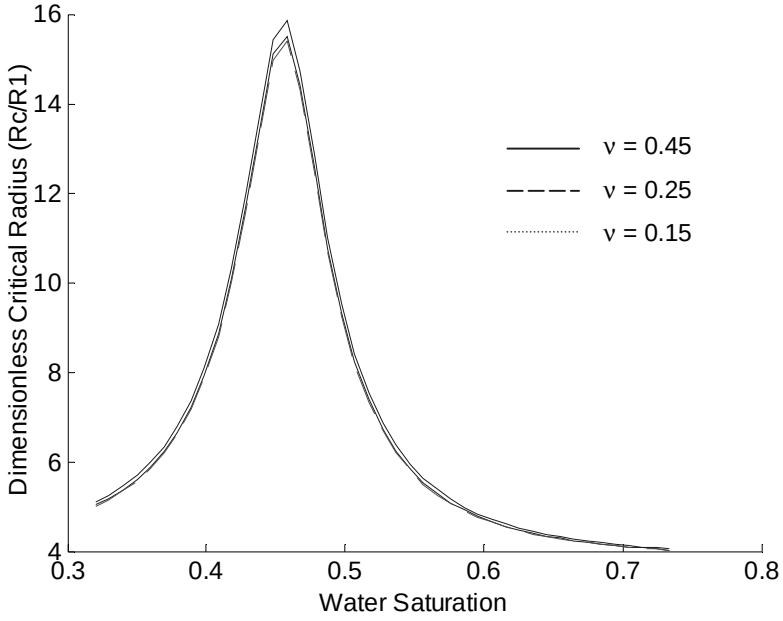

Fig. 5-23: Effect of Poisson's ratio on sand stability

Chapter 6 Geomechanics Models for Unsteady Fluid Flow

6.1 Introduction

Dynamic pressure fluctuations near a wellbore in a reservoir can, in principle, lead to rock instability; however, there is little quantitative field documentation available. Santarelli et al. (1998) reported injectivity decline of some water injectors in the Norwegian sector of the North Sea after well shut-in. Dusseault *et al.* (2000) developed a new workover method to clean up wellbore damage based on a strong dynamic pressure pulse method, clearly demonstrating that dynamic pressure perturbation can re-initiate sand influx in heavy oil wells that use sand production as a means of recovery. Santos (2002) has indicated that during the well drilling process, pressure oscillation at bottom-hole not only can destabilize sand but also shale.

The lack of more extensive documentation of dynamic pressure pulse induced instability may be due to several reasons: first, monitoring rapid downhole pressure fluctuations has traditionally been difficult; second, the presence of gas in the oil dampens the effect of pressure oscillations; and third, the impact of dynamic effects on sand instability has not been widely understood. It should be noted that the practical solution to this problem is, in principle, relatively simple: smooth (i.e. slow) production or injection reductions can be easily implemented to avoid abrupt pressure changes.

However, it is valuable to evaluate rock stability before a production strategy is chosen, and a thorough understanding of mechanisms and quantitative analysis of their potential effects should be pursued.

When production (or injection) is adjusted at the wellhead, or when the drilling string is moved up or down during drilling, pressure fluctuations will appear within the wellbore. This is also known as the water hammer effect in Civil Engineering, where, for example, massive pressure waves in hydroelectric water tunnels can arise through rapid shut-down of water flow. Through the open part of the wellbore, a pressure wave will transfer its energy to the adjacent rocks like ocean waves transfer their energy to the shore. As a result, stresses in the rock will dynamically redistribute to accommodate the energy input, while also experiencing a quasi-static change resulted from pressure recovery processes in the reservoir after shut-in. Moreover the dynamic stress fluctuations will not cease until the pressure wave attenuates, and this results in a cyclic as well as a dynamic load.

In this chapter, the cases of rapid shut-down of a producing well or an injection well are studied, both of which will lead to a water hammer. First, a quasi-steady pressure model is developed to account for pressure recovery in the reservoir around the wellbore; then, a water hammer model is used to provide the boundary conditions for the stress model, which is coupled through induced fluid pressure. Since the model originates from effective stress theory instead of introducing stress as factor of compressibility into the pressure equilibrium equations (e.g. Chen et al., 1995), it may be viewed as a coupled model that directly captures the stress changes due to fluid pressure fluctuations.

6.2 Model Development

6.2.1 Pressure recovery in reservoir after well shut-in

Suppose there is a well steadily producing oil from a bounded isotropic reservoir (e.g. in a fault block). One day, it may be shut down, and as a consequence, the pore fluid pressure will recover and eventually reach a constant value. Assuming both fluid and formation are slightly compressible, fluid flow is linear, and temperature is constant, the pressure model describing the problem in the domain $R_w \le r \le R_e$ is

$$\frac{k}{\mu C_t}\left(\frac{\partial^2 P}{\partial r^2}+\frac{1}{r}\frac{\partial P}{\partial r}\right)=\frac{\partial P}{\partial t} \tag{6.1}$$

, where formation total compressibility C_t (= $\phi C_l + C_m$) measures the liquid volume squeezed out of pore space due to compression of rock skeleton and fluid expansion when reservoir is depleted. It should be noted that the effect of quadratic gradient terms, as discussed by Wang and Dusseault (1991), is not considered in this research. The initial conditions at t = 0 can be assumed to be

$$\frac{\partial P(r)}{\partial r}=-\frac{Q\mu}{2\pi khr} \tag{6.2}$$

When time becomes infinite, there will be no flow in the reservoir, and the reservoir pressure is constant

$$\partial P(r,t)/\partial r = 0 \tag{6.3}$$

$$\overline{P} = P_e - \frac{P_e - P_w}{2\ln(R_e/R_w)} \tag{6.4}$$

There will be no flux across the boundaries after shut-in

$$@\ r = R_w,\ \partial P(r,t)/\partial r = 0 \tag{6.5}$$

$$@\ r = R_e,\ \partial P(r,t)/\partial r = 0 \tag{6.6}$$

After grouping parameters into dimensionless groups and applying the boundary and initial conditions, the final solution for pressure can be analytically shown to be (Appendix 6-A)

$$P(r,t) = P_e\left[A + B\sum_{n=1}^{\infty} C_n D_n(t) J_0(\lambda_n \frac{r - R_w}{R_e})\right] \tag{6.7}$$

where

$$A = 1 - \frac{1}{2}\cdot\frac{1 - P_w/P_e}{\ln(R_e/R_w)} \qquad B = \frac{Q\mu}{\pi k h P_e}$$

$$C_n = \frac{1 - J_0(\lambda_n)}{\lambda_n{}^2 J_0(\lambda_n) J_2(\lambda_n)} \qquad D_n(t) = \exp(-\frac{kR_e{}^2}{C_t\mu}\lambda_n{}^2 t) \tag{6.8}$$

where J_0 and J_2 are Bessel function of the first kind of the order zero and of the second order.

Equation (6.1) with initial conditions Eq. (6.2) and boundary conditions Eq. (6.5) and Eq. (6.6) can also be solved numerically, e.g. with finite difference method. After discretization, Eq. (6.1) becomes

$$\frac{dP_i}{dt} = \frac{k}{\mu C}\left[\frac{P_{i+1}^j - 2P_i^j + P_{i-1}^j}{(\Delta r)^2} + \frac{1}{(i-1)\Delta r}\frac{P_{i+1}^j - P_{i-1}^j}{2\Delta r}\right] \tag{6.9}$$

where $\Delta r = (R_e - R_w)/n$, and n is the number of discrete segments (n=50 in the model) within (0, $R_e - R_w$), where i =1, 2, …, n. Since $\lim_{r\to 0}\frac{1}{r}\frac{\partial P}{\partial r} = \frac{\partial^2 P}{\partial r^2}$, the pressure distribution at the wellbore is

$$\frac{dP_1}{dt} = \frac{2k}{\mu C_t}\cdot\frac{1}{(\Delta r)^2}(P_2^j - 2P_1^j + P_0^j) \tag{6.10}$$

Thus, at the boundaries (@ r = 0), Eq. (6.9) becomes

$$\frac{dP_1}{dt} = \frac{4k}{\mu C_t}\cdot\frac{1}{(\Delta r)^2}(P_2^j - P_1^j) \tag{6.11}$$

and at $r = R_e - R_w$

$$\frac{dP_n}{dt} = \frac{2k}{\mu C_t}\cdot\frac{1}{(\Delta r)^2}(P_{n-1}^j - P_n^j) \tag{6.12}$$

Combining Eqs. (6.9), (6.11), (6.12) and using the method of characteristics, a numerical solution can be achieved. Calculated results from Eq. (6.7) and Eq. (6.9) are presented as dashed lines in Fig. 6-1. Note that the numerical solutions for the pressure distributions (part b) are pictured at time t = 21 s (blue dash), 94 s (red dash), and 463 s, for comparison with the times t = 20 s (blue solid), and 100 s (red solid) for the analytical solutions.

6.2.2 Coupled geomechanics model

Fluid pressure plays a fundamental role in rock stability. It not only provides a driving force to mobilize sand (liquefaction and entrainment), but also serves as one of the supportive force for natural and induced loads; i.e., the effective stress in the rock matrix is affected by pressure changes in the manner of $\sigma' = \sigma + \alpha P$, where α is the negative Biot constant. As a rule of thumb, the stress analysis should always be coupled to the fluid pressure through volume changes as far as the reservoir situation is concerned. To focus on the physical mechanisms and simplify this theoretical development, a linear elastic material is considered hereafter. However it should be noted that inelastic stresses could be incorporated in a similar way.

From the development in Section 4.1, the integration of pore pressure is

$$\int^{r} rPdr = P_e\left[\frac{A}{2}r^2 + B\sum_{n=1}^{\infty} C_n D_n(t)\frac{R_e}{\lambda_n}\cdot rJ_1(\lambda_n\frac{r-R_w}{R_e})\right] \tag{6.13}$$

Applying boundary conditions

$r = R_w$, $\sigma'_r = 0$;

$r = R_e$ (when $R_e >> R_w$), $\sigma'_r = \sigma_h - \alpha P_e(t)$ (6.14)

the two unknown parameters $C_1(t)$, $C_2(t)$ in Eqs. (4.11) and (4.12) can be solved:

$$C_1(t) = \frac{(1+\nu)(1-2\nu)}{E}\left[-\alpha P_w(t) + \frac{EC_2(t)}{(1+\nu)}\frac{1}{R_w^2} + \frac{1-2\nu}{1-\nu}\frac{A}{2}\alpha P_e\right] \tag{6.15}$$

$$C_2(t) = \frac{1+\nu}{E}\left[\sigma_h + \alpha P_w(t) + \alpha B P_e\frac{1-2\nu}{1-\nu}\sum_{n=1}^{\infty}\frac{C_n D_n(t)}{\lambda_n}J_1(\lambda_n\frac{R_e-R_w}{R_e})\right]\cdot\frac{R_w^2 R_e^2}{R_e^2 - R_w^2} \tag{6.16}$$

where, from Eq. (6.7),

$$P_w(t) = P_e\left[A + B\sum_{n=1}^{\infty} C_n D_n(t)\right] \tag{6.17}$$

Therefore the redistribution of the effective radial and tangential stresses after well shut-down can be determined with the integration part of P(r,t) and parameters $C_1(t)$ and $C_2(t)$ expressed by Eqs. (6.13), (6.15), and (6.16).

6.2.3 Pressure wave inside wellbore

For transient fluid flow inside a vertical wellbore, the equation of motion can be expressed as (Wylie and Streeter, 1984)

$$g\frac{\partial H}{\partial z}+v\frac{\partial v}{\partial z}+\frac{\partial v}{\partial t}+\frac{fv|v|}{2D_{iw}}=0 \tag{6.18}$$

and the equation of continuity is

$$v\frac{\partial H}{\partial z}+\frac{\partial H}{\partial t}+\frac{a_w{}^2\partial v/\partial z}{g}=0 \tag{6.19}$$

The friction factor f is determined by the Reynolds number and the relative roughness (Moody, 1941). If we assume laminar flow in the wellbore, it is (Orkiszewski, 1967)

$$f = 64\,\mu/(\rho D_{iw} v) \tag{6.20}$$

and "a_w" is the wave speed calculated by (Záruba, 1993)

$$a_w{}^2=\frac{K_o/\rho}{1+(K_o/E_{iw})(D_{iw}/e)C_1} \tag{6.21}$$

where C_1 can vary depending on how the tubing is anchored.

This problem is difficult to solve analytically (Streeter and Wylie, 1967). In this research the method of characteristics is used, and the solution is (Appendix 6-B)

$$H_i^{j+1}=\frac{H_{i-1}^j+H_{i+1}^j}{2}+M\left(\frac{Q_{i-1}^j-Q_{i+1}^j}{2}\right)-N\left(\frac{Q_{i-1}^j|Q_{i-1}^j|-Q_{i+1}^j|Q_{i+1}^j|}{2}\right) \tag{6.22}$$

where Q_i^{j+1} can be expressed as

$$Q_i^{j+1}=Q_{i-1}^j+\frac{1}{M}(H_{i-1}^j-H_i^{j+1}-NQ_{i-1}^j|Q_{i-1}^j|) \tag{6.23}$$

where $M=\frac{a_w}{gA_{iw}}$ and $N=\frac{f\Delta z}{2gD_{iw}A_{iw}^2}$. Note that the piezometric head H can also be written in terms of the fluid pressure, $P = \rho g(H-z)$.

Assuming that at the wellhead the production rate reduces to zero rapidly; then

$$H_1^{j+1} = H_2^j - MQ_2^j + NQ_2^j\left|Q_2^j\right| \tag{6.24}$$

Consistent with the boundary condition used in the pore pressure model (Eq. 6.5), at the well bottom this equation becomes:

$$H_n^{j+1} = H_{n-1}^j + MQ_{n-1}^j - NQ_{n-1}^j\left|Q_{n-1}^j\right| \tag{6.25}$$

With an assumption of steady flow inside the wellbore, i.e. fluid pressure only varies with the coordinate z, the initial pressure distribution before shut-in can be easily derived from the Darcy-Weisbach Equation (Wylie and Streeter, 1984):

$$H_{i+1}^0 = H_i^0 - \frac{8f\Delta zQ|Q|}{g\pi^2 D_{iw}^5} \tag{6.26}$$

6.3 Model Calculations and Discussions

6.3.1 Model simplifications

As a comprehensive and complicated topic that incorporates many concepts from production engineering (wellbore pressure), reservoir engineering (reservoir pressure), and rock mechanics (effective stresses), quantitative analysis of shut-in effects on rock stresses involves a total of 18 parameters, including 6 for the wellbore, 4 for the oil, and 8 for the reservoir (Table 6-1), all of which are usually available in the field.

However, as a tradeoff, some simplifications have to be made in order to achieve analytical solutions, such as:

- quasi-steady pressure state in a bounded homogeneous reservoir before the well shuts down (a reasonable initial condition for a well that has been on production for some time);
- immediate shut-in boundary conditions for water hammer and pressure recovery model (this gives the most conservative results);
- a single phase fluid (note that in a real case, if there is any free gas in a producing wellbore, water hammer effects are dramatically weakened due to the increased fluid compressibility); and,
- Cyclic fatigue effects on failure are not included in the rock model.

Furthermore the fluid pressure fluctuation is constrained within the wellbore and its effect on reservoir fluid has not been considered at this stage.

6.3.2 Rock stability when pressure fluctuates

Calculations of the wellbore pressure are plotted in Fig. 6-4. Due to the boundary assumption that there is no cross flow from the reservoir to the wellbore in the perforated section after shut-in, the calculated pressure cannot reach the same level as that determined by the reservoir recovery model Eq. (6.4). Physically, this assumption is not valid until energy equilibrium is reached between the wellbore and the reservoir. Before that, the effects of wellbore storage and pressure fluctuations lead to fluid continuously flowing back and forth across the interface, which is too difficult to quantify. As a simplified approach to approximately describe how much energy has been added to the wellbore from the reservoir after shut-in, the pressure difference between Eq. (6.17) and Eq. (6.25) is added at the n^{th} node of the wellbore. Fig. 6-5 illustrates the adjusted pressure fluctuations at the well bottom after shut-in. Comparing to Fig. 6-4, the pressure is building up along the path of static recovery (dashed line), while fluctuations of up to 600 KPa take place because of the hammer effect.

The fluctuation period calculated by the above hammer model (about 10s) agrees with the descriptions in Fig. 6-6, which is a field record of an injector being shut down. Compared to the production well, pressure in the injector is much higher than that in the reservoir, which results in fluid gradually flowing into the reservoir instead of the opposite direction for the producer. Consequently, the magnitude of pressure fluctuations in the injector is higher (about 4.3 MPa); furthermore, hammer energy is quickly consumed by wellbore friction (or fluid loss in some part of the well): only 2.5 MPa is left for the second half of the period.

Fig. 6-7 shows the effect of the pressure wave inside the wellbore on the effective stresses in reservoir rock (0.1 m from the wellbore). The dashed lines are stress curves under the condition of no pressure fluctuation, i.e. the stress-coupled pressure is obtained only from a quasi-static pressure recovery model. Clearly, a water hammer leads to an oscillation of effective stresses, while the overall stress trend still follows the static part (dashed line). Furthermore, the strongest hammer effect occurs in the rock around wellbore: as high as 200 kPa at r =0.2 m (Fig. 6-7), while it diminishes to about 30 kPa if distance increases to 0.5m (Fig. 6-8). As a result, the rock exposed to the wellbore is most likely failed first if stress fluctuations exceed rock strength.

There are three ways that the stress oscillations can affect rock stability:

- Shear failure. Fig. 6-8 illustrates the shear stress variation at r = 0.2 m from the wellbore. With the model data listed in Table 6-1, the magnitude of shear stress variation can be as high as 300 kPa. Thus the cementation of formerly consolidated rock may be damaged or even

broken if shear stress exceeds the limitation defined by the Mohr-Coulomb criterion (or any similar yield criterion);

- Induced tensile failure. For rock that has already been damaged by shear failure, oscillations of the effective radial stress may result in rock particles being plucked out of the rock skeleton if the stress is larger than the rock tensile strength; and,
- Cyclic fatigue. The stress fluctuations result in the rock being loaded and unloaded periodically. As shown in Fig. 6-10, cyclic loading can decrease rock strength greatly before total failure occurs as long as the rock deformation is nonlinear (i.e. partly elastoplastic, indicating accumulating damage). Therefore even though the shear stress may not lie above the Mohr-Coulomb criterion, the rock still can fail due to cyclic loading.

6.4 Conclusions

Three models are developed to describe the effect of well shut down (or sharp change of production rate) on rock stress distributions. Analytical solutions for quasi-static pressure recovery processes in a bounded oil reservoir are coupled with a poro-elastic geomechanics model, while pressure fluctuations inside the wellbore provide a boundary condition to the formation outside the wellbore. By resorting to analytical solutions, direct relationship among fluid properties, rock properties and production parameters can be established. These stress fluctuations can then be examined in the context of rock stability changes arising from the dynamic loading, perhaps, for example, by examining the peak dynamic shear stress. Model calculations demonstrate that the fluctuations of effective stresses and shear stress may reach several hundred kPa due to pressure wave created by water hammer inside a wellbore.

The models provide a method to quantify the effect of pressure oscillation, resulting from operation at the surface, on the stability of the rock. However, the lack of information on the dynamic response of unconsolidated sandstones to rapidly oscillating pressures, largely because operators do not collect this type of data, will still impede the use of these solutions in practice. The author hopes this deficiency could be overcome in the future with the advent of “smart well” technology that incorporates precise and rapid response bottom-hole pressure transducers in wells that are prone to sanding.

Finally, noting that the motivation for this analysis was to addresses issues related to sand production, it can be said that a method of analysis for water hammer effects can help quantify the deterioration in rock resistance, and therefore be of some value in a general sand production management strategy.

6.5 Tables and Figures

Table 6-1: Input data for the developed model

Wellbore		Oil		Reservoir	
D_{iw}	0.06 m	μ	0.01 Pa·s	R_e	50 m
e	5×10^{-4} m	ρ	900 kg/m^3	k	1×10^{-12} m^2
E_{iw}	200×10^{11} Pa	Q	100 m^3/day	h	10 m
ν_{iw}	0.3	K_o	1.5×10^{9} Pa	P_e	10×10^{6}Pa
L	500 m			$k/\mu C_t$	1
R_w	0.1m			E	3×10^{9} Pa
				ν	0.25
				σ_h	40×10^{6} Pa

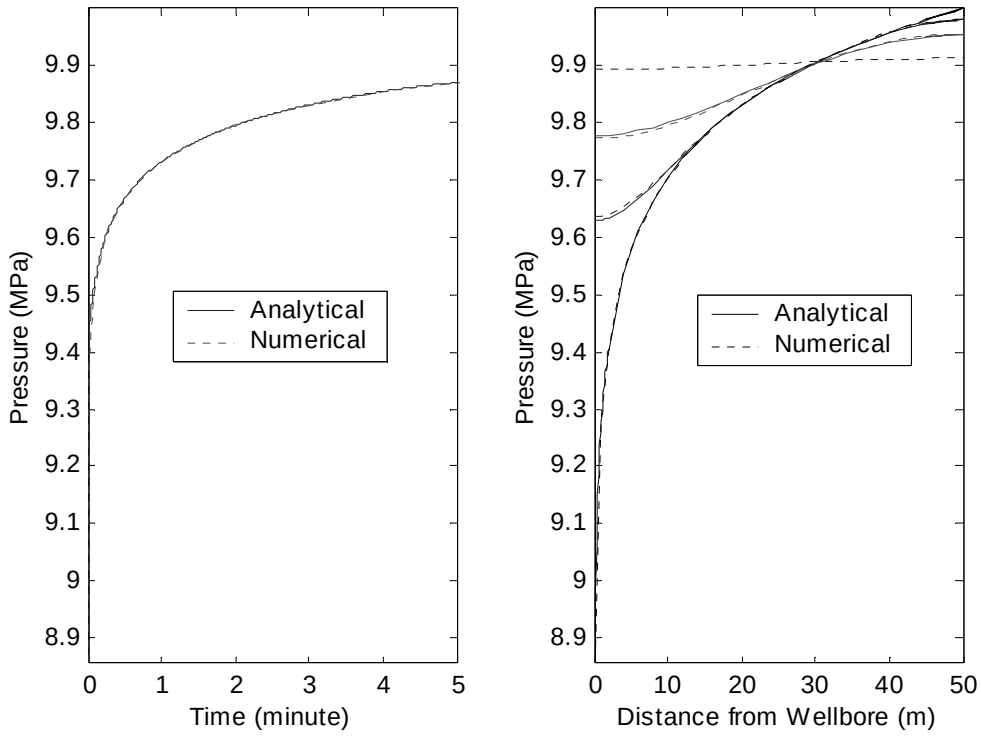

a):Pressure Variations at Wellbore b): Pressure Distributions

Fig. 6-1: Pressure recovery (analytical vs. numerical)

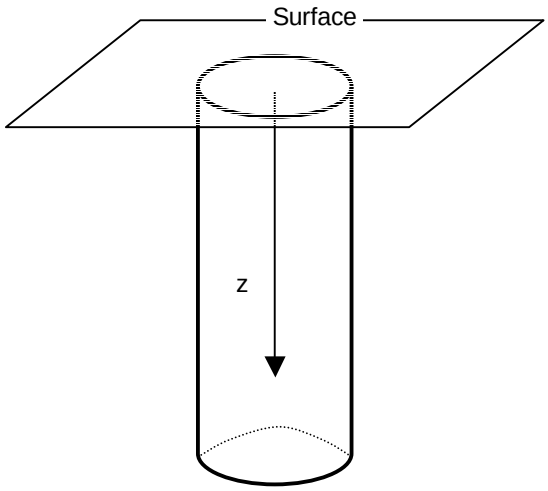

Fig. 6-3: Sketch of wellbore

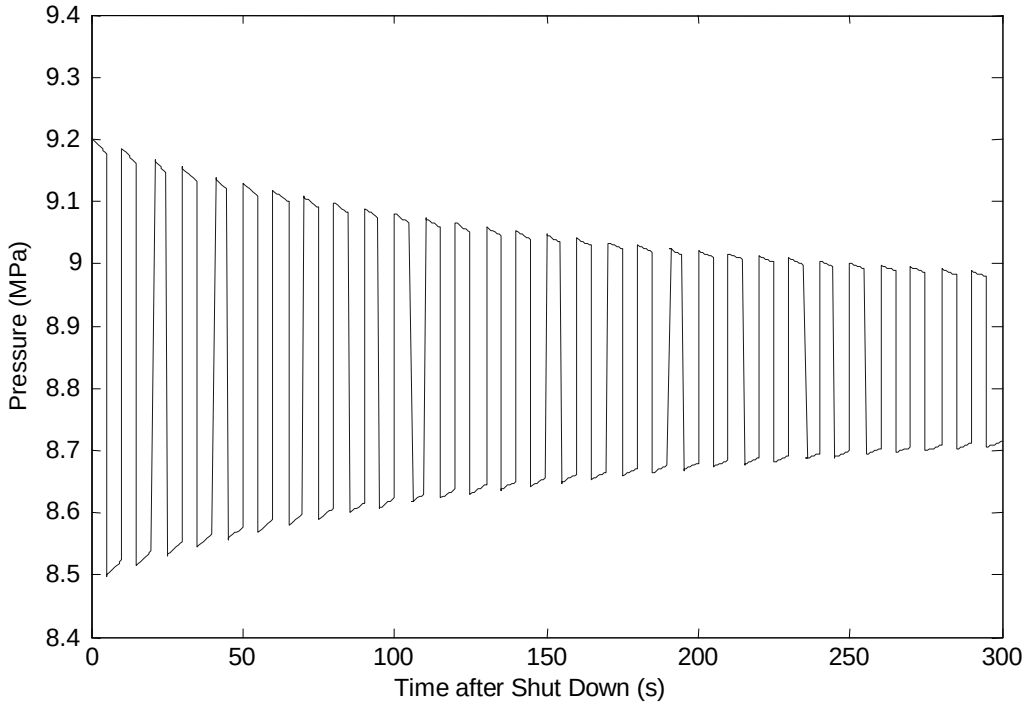

Fig. 6-4: Water hammer effect on wellbore pressure (unadjusted)

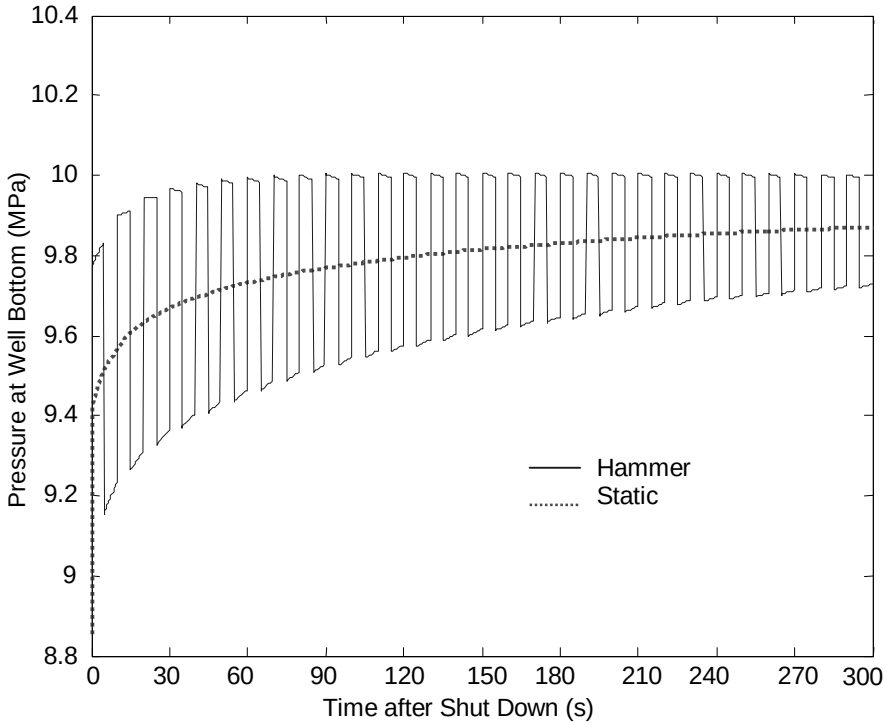

Fig. 6-5: Water hammer effect on wellbore pressure recovery (adjusted)

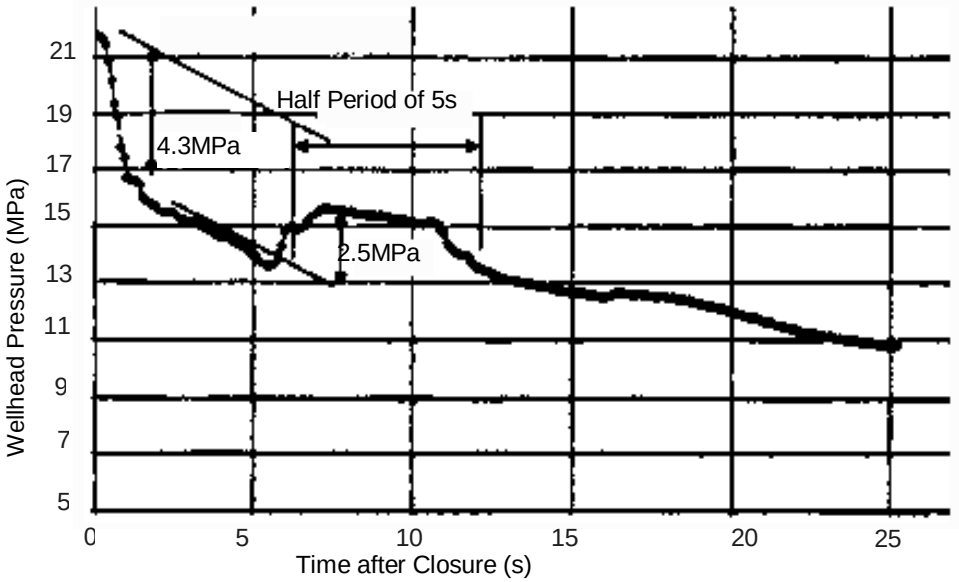

Fig. 6-6: Pressure wave inside wellbore after shutting down injectors
(After Santarelli, 1998)

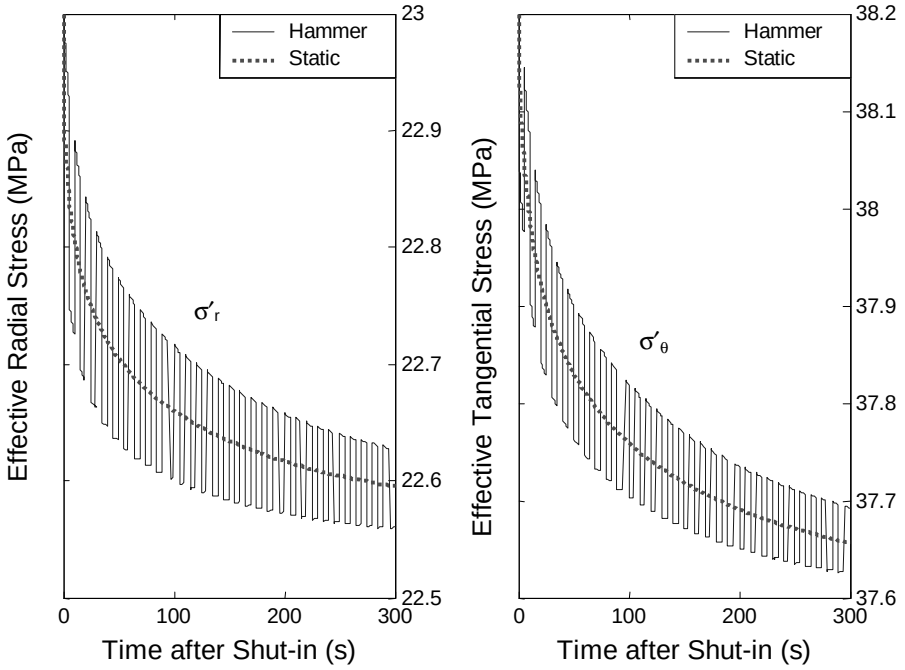

Fig. 6-7: Effective stress redistributions at r = 0.2m from wellbore

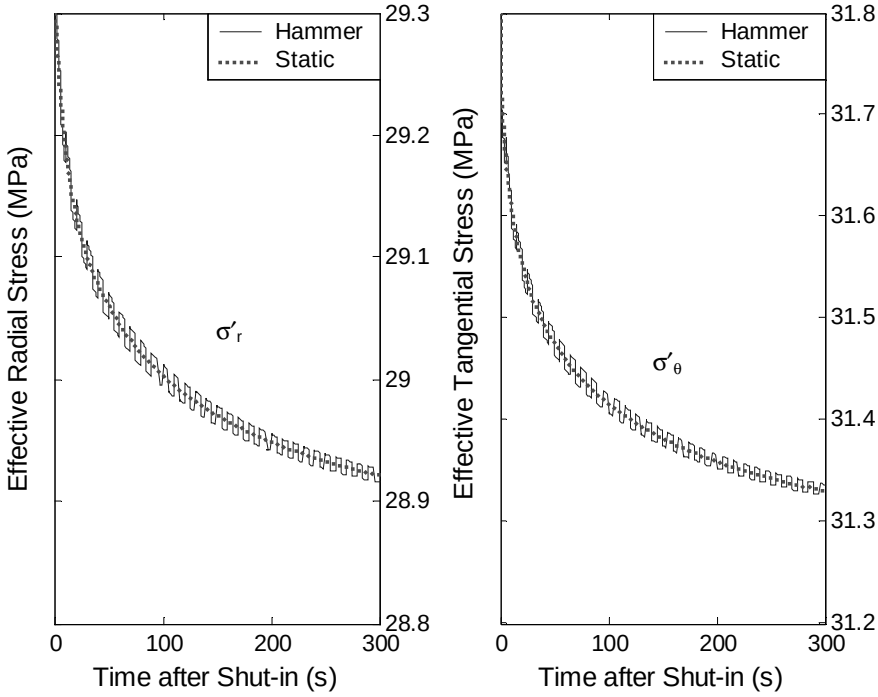

Fig. 6-8: Effective stress redistributions at r = 0.5m from wellbore

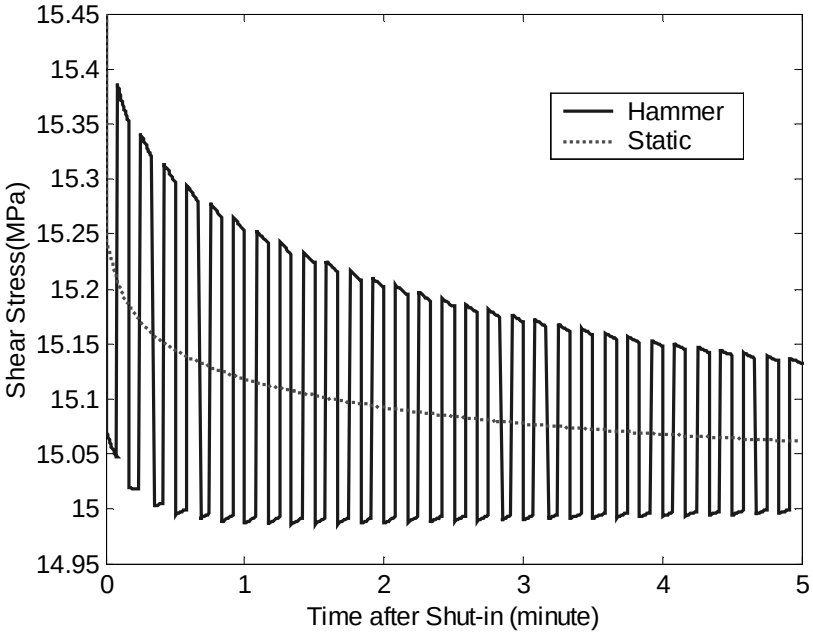

Fig. 6-9: Shear stress fluctuations after shutting down the well (r=0.2m)

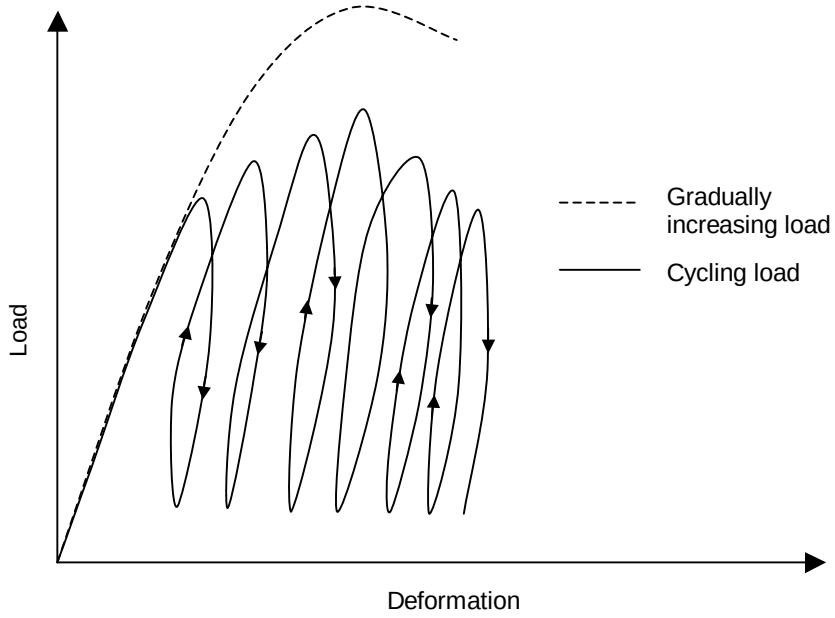

Fig. 6-10: Effect of cyclic loading on rock strength

Chapter 7 Summaries, Conclusions, and Recommendations

7.1 Summary of efforts

It is widely known in the oil industry that changes in fluid flow conditions such as water breakthrough or unsteady flow due to well shut-in can lead to sand destabilization, with a possible consequent sand production event. This occurs mainly in unconsolidated and weakly consolidated sand, from whence seventy percent of world oil production is achieved (Bianco and Halleck, 2001). Though many issues are unclear and controversial, it is generally believed that the disturbance caused by drilling activities, workover operations, or production strategies leads to stress alterations in the formations near the well. After stresses reach the rock strength, failure (or fabric deterioration) occurs, and fluid flow can start to erode and carry failed and disaggregated sands into the wellbore. Hence, sand production can be divided into two processes: sand failure and failed sand transportation. In this research the first process is focused upon, involving strength weakening, stress overloading, and decrease of rock stiffness when fluid conditions vary from monophasic to biphasic, or from steady-state to unsteady-state flow.

As the most important factor in stability analysis, strength behavior after an oil well starts to produce water is investigated in detail. Two main mechanisms exist for strength weakening, chemical reactions of rock with formation water and variations of rock capillary strength, are identified and analyzed, both qualitatively and quantitatively. Inspired by theories from particle mechanics, rock mechanics, and interfacial science, and based on published laboratory and field findings, four capillarity models are developed and verified to analytically capture the macroscopic physical implications of capillary strength phenomena at the grain scale. A better understanding of sand behavior is achieved, based on the model calculations.

A simplified capillarity model is developed to quantify capillary strength conservatively but efficiently using only two input parameters (i.e. particle radius and water saturation). Based on the microscopic model, a new method is proposed and verified to physically calculate pore pressure in a

multiphase environment. More importantly, for the first time, the redistributions of effective stresses around a wellbore after water breakthrough are solved with a coupled inelastic stress model. Also, the effect of different mechanisms, such as capillarity changes, chemical reactions, pore pressure decreases due to alteration of relative permeabilities, etc., are quantified and compared in order to clarify when and how they contribute to sand production in two-phase fluid environments. Meanwhile, in the stress models, different conditions currently used in geomechanics analysis are compared and their limitations are discussed.

The nonlinearities of rock properties in stressed and biphasic fluid environments are analytically addressed, based on an improved nonlinear theory, which considers both a failure-based mechanism (Section 5.2.2) and a confining-stress-based mechanism (Section 5.2.3), a strength model that accounts for strength weakening from capillarity and chemical reactions, and a coupled stress model. The calculations demonstrate the distributions of stress-dependent rock stiffness around a wellbore and its evolution with increase of water saturation, clarify the relative importance of each mechanism in reducing rock stiffness, and fundamentally explain why current predictive technologies are invalid when water appears in a flowing wellbore. The stress-dependent characteristics of rock transport properties such as porosity and permeability are also modeled (Section 4.2). With input of different relations of compressibility and stress, the proposed method can depict stress-dependent transport properties for different types of rock. As an application, a new approach for unconsolidated sand is formulated based on nonlinear theory.

Three models are developed to describe the effect of well shut down (or sharp change of production rate) on rock stress distributions. Analytical solutions for quasi-static pressure recovery processes in a bounded oil reservoir are coupled with a poro-elastic stress model, while pressure fluctuations inside the wellbore provide a boundary condition to the formation outside the wellbore. As a comprehensive and complicated topic that incorporates many concepts from production engineering (wellbore pressure), reservoir engineering (reservoir pressure), and rock mechanics (effective stresses), quantitative analysis of shut-in effects on rock stresses involves only a total of 18 parameters (Table 6-1), all of which are usually available in the field. By resorting to analytical solutions, direct relationships among fluid properties, rock

properties and production parameters are established. The mechanisms for rock failure after well shut-in, including shear stress elevation, seepage force increase, and cyclic fatigue, are elucidated.

7.2 Conclusions

7.2.1 Why does sand fail after water breakthrough?

In general, with increase of water saturation, sands tend to become weaker (strength weakening) and softer (stiffness reduction) while the loading stresses (the effective stresses and shear stress) are elevated and the maximum shear stress moves outward into the reservoir (i.e. more and more rocks are affected). As a result, the rock is more likely to experience shear failure that destroys or damages the cohesive or interlocked fabric among rock particles. Furthermore, the sands are more easily detached from the rock matrix due to a decrease of the rock tensile capillary strength with an increase of water saturation. Since the capillary strength only depends on water saturation if the rock and fluid properties are fixed, the sanding rate for each saturation will be constant until destabilizing forces are changed, which leads to so-called episodic sand production after water breakthrough (Bruno et al., 1996; Tronvoll et al., 2001).

There are mainly two kinds of chemical reactions between rock and formation water that are likely to lower rock strength when water breakthrough into an oil well occurs: quartz hydrolysis and carbonate dissolution that lower the surface energy of rock; and ferruginous deposition and shale swelling that change the rock pore structure and affect local fluid gradients, thereby enhancing seepage forces that may destabilize the sand. Since the rock strength changes from these reactions are environmentally dependent and are related to numerous parameters that cannot realistically be determined, it will be extremely hard to quantify the effects of those reactions.

Besides chemical reactions, the reduction of capillary force and strength through changing water-oil menisci also plays a role in weakening rock strength in two-phase fluid environments. More specifically,

- At the grain scale, capillary cohesive forces among the particles can reach the order of kPa and are one to three orders of magnitude higher than fluid seepage forces when the fluid gradient is about 1 psi/ft.

The smaller the particles, the greater the effect; therefore capillary forces should not be neglected in the analysis of sand instability, especially for unconsolidated sand.

- Capillary induced strength, such as UCS or tensile strength resulting from capillary force, can decrease quickly with water saturation, from several kPa to near zero within only a 5% change of saturation.
- The magnitude and behavior of capillary strength are affected by several factors:
    - It increases linearly with increasing surface tension of the interface between the fluids.
    - Contact angle affects both the magnitude of capillary strength and its variation with saturation. At the same saturation, the larger the contact angle, the smaller the strength, and the faster the strength decrease with increasing saturation.
    - If the particle size is uniform, small particle size results in high capillary strength. If particles have different size, the smaller the size difference, the higher the capillary strength and the faster its decrease.
    - For detached and squeezed contact fabrics, the capillary strength first increases to a peak with water saturation, then decreases after a critical saturation, in contrast to the tangential contact fabric where capillary force always decreases with water saturation. The peak strength is closely related to the distance between particles, contact angle, and size homogeneity of particles. At the same saturation, the strength decrease becomes more significant for squeezed particles than for detached ones.
    - Capillary strength is also found to vary greatly with rock deformation: it reaches a maximum when particles are tangentially contacted and generally decreases no matter whether the rock is compressed or extended. Comparing with particles subjected to extensional deformation, the strength of compressed particles decreases much faster with saturation.

Because of strength weakening and variations of fluid relative permeabilities, pore pressure and effective stresses will redistribute after the well starts to produce free water:

- Pore pressure first decreases with saturation until some critical point, and the magnitude of decrease can be as high as several MPa; then it increases continuously to a value (e.g. when $S_w = 0.734$) even higher than in the initial state (where only oil exists).
- In the elastic zone close to the shear yield front, the effective tangential stress increases to a maximum before declining with saturation, whereas the effective radial stress first decreases to its lowest value and then increases. Thus, at the initial stage of water breakthrough, elastic sand is most likely to experience shear yield that breaks cementation among particles and moves the yield front outward from the well.
- For the plastic zone, both the effective tangential stress and effective radial stress decrease with saturation. This creates a lower stress environment around the wellbore after water breakthrough, which makes fluid erosion of sand easier.
- In terms of the plastic radius that defines the range of failed sands, water saturation has a large impact on its magnitude, and this impact increases with the increase of saturation. Several mechanisms such as pore pressure changes, capillary effects, and strength loss due to chemical reactions, are responsible for the expansion of failed region. The magnitude of the initial shear cohesive strength plays a vital role in evaluating the relative importance of those mechanisms: when the initial strength is low, the increase of the plastic radius with saturation becomes significant and so does the contribution of the capillarity to stress calculations; otherwise, the effect of capillarity is trivial compared to that of relative permeabilities (pore pressure variations). If cementation materials are water-sensitive, the effect of chemical reactions on rock stability through lowering of rock strength is more dominant and lasts longer than those of other mechanisms. The magnitude of stress alterations by this effect is high enough to match the result from pore pressure changes.

Another significant effect of water breakthrough on rock stability is a reduction in rock stiffness.

- Corresponding to the shear stress distribution, which increases rapidly to a peak at the boundary between plastic and elastic zones, Young's modulus rapidly decreases to a minimum at the boundary (for the case studied, rock modulus loss was about 80% within 1 meter) and increases with the distance

in the far field. Within the plastic zone where the rock has already been damaged by shear failure, the modulus remains low. The magnitude of the residual modulus depends on rock residual strength: the more the residual strength, the more the residual modulus.

- Rock initial strength greatly affects the distributions of both shear stress and stiffness: stronger rock results in the stress being more concentrated near the wellbore, and therefore a more precipitous decrease of Young's modulus in that region.
- Mainly due to the changes of oil/water relative permeabilities, the loss of rock Young's modulus can be as high as 45% before it regains part of its stiffness because of pressure recovery and stress release. Furthermore, the magnitude of modulus loss and stress increase with saturation is related to the rock location and its initial strength: the stronger rock located far away from the well results in less modulus loss and stress increase.
- For water-sensitive cemented rock, chemical reactions, along with changes of fluid relative permeabilities, play dominant roles in reducing modulus: the more the strength is chemically lost, the greater the decrease of Young's modulus with water saturation.
- The effect of capillarity on rock elastic properties is very limited.
- For all possible values for sand, Poisson's ratio affects the magnitude of effective stress and plastic radius very little. This indicates that Poisson's ratio can be treated as a constant when stresses around wellbore are analyzed in order to avoid prohibitive mathematical challenges.

The fact that the magnitude of the capillary cohesive force is comparable to that of the fluid seepage force indicates that after rock experiences shear failure, capillarity becomes a dominant factor to stabilize detached particles as long as water saturation is not high. With increase of water saturation the sands become more easily detached from the rock matrix due to decrease of the rock tensile capillary strength.

Since the capillary strength only depends on water saturation if rock and fluid properties such as surface tension, particle size, porosity, friction angle, etc., are fixed, it will be unique with each value of water saturation. Therefore, the sanding rate for each saturation will be constant until destabilizing forces,

e.g. fluid seepage force and loading force resulting from deviatoric stresses, are changed, which leads to so-called episodic sand production after water breakthrough (Bruno et al., 1996; Tronvoll et al., 2001).

7.2.2 Why does sand production often happen after a well is abruptly shut-in?

Because of the pressure wave created by a water hammer inside the wellbore, fluctuations of effective stresses and shear stress in an oil reservoir may reach several hundred kPa (Fig. 6-8). Furthermore, the strongest hammer effect occurs in the rock adjacent to the wellbore and diminishes outward. As a result, the rock exposed to the wellbore is most likely failed first.

There are three ways that the stress oscillations can affect rock stability:

- Shear failure. If shear stress exceeds the limitation defined by the Mohr-Coulomb criterion (or other appropriate yield criterion), the cementation of formerly consolidated rock may be damaged or even broken.
- Induced tensile failure. For rock that has already been damaged by shear failure, oscillations of the effective radial stress may result in rock particles being plucked out of the rock skeleton if the stress is larger than the rock tensile strength.
- Cyclic fatigue. The stress fluctuations result in the rock being loaded and unloaded periodically. Because cyclic loading can decrease rock strength greatly before total failure occurs if the rock deform elastoplastically and damage accumulates (Fig. 6-9), the rock still can fail even though the shear stress may not lie above the Mohr-Coulomb criterion.

7.3 Model Limitations and Recommendations

7.3.1 Capillarity models

Assumptions made during the development of capillary models should be clearly restated, such as:

- The pore structure is stable while the collapse of rock cementation is neglected even though it can change the radius of capillary menisci (Papamichos et al., 1997);
- The liquid bridge formed between spherical particles can be described as a toroid;

- The variable bond strength between particles can be replaced by a mean value that is applicable throughout the whole rock mass;
- The water content is distributed evenly inside the particulate rock mass; and,
- The particles deform elastically upon compressive loading (without crushing).

Whereas these may be viewed as limitations to the models' applicability, the author believes that because the models capture the essential physics, adjustments and calibrations can easily be incorporated so as to give useful results in practice.

7.3.2 Permeability models

The model developed in Section 4.2 did not account for permeability changes after shear failure. As pore throats have been reshaped after sand particles rearrange and fracture occurs, specific surface area and pore throat apertures change significantly, particularly under conditions of large stress changes. Even though some approaches are developed to describe permeability evolutions with plastic deformation (e.g. Simoni, 1999; Yale, 2002), a straightforward method based solidly on widely accepted physical principles remains elusive, mainly because the rock in the Coulomb zone is little studied due to the limitations of core collection and experimentation. Because continuum theories face great challenges in macroscopically modeling permeability anisotropy in non-hydrostatic loading stress environments, particulate mechanics models may provide an alternative and more satisfactory approach in terms of describing pore structure changes at the grain scale level. Hertz contact theory can only address the effect of elastic deformation (Wong and Li, 2000; Bai et al., 2002), and the plastic situations involving shear slip remain to be explored quantitatively in future research.

Other than effective stress, there are many other factors that may affect the permeability distributions around a wellbore such as solids production, infiltration of drilling fluid, formation of mud cake, fabric perturbations caused by workovers, etc. Those factors may play more important roles than stress in their effects on permeability impairment; however in this research only stress is considered.

7.3.3 Nonlinear models

The author believes that the greatest challenge of nonlinear theory comes from the analytical solution of the stress equations with stress-dependent modulus. The stress derivations in Section 5.2.3 have to assume that modulus only depends on confining stress (i.e. $E=E(\sigma_r)$), Poisson's ratio is a constant, and leaving aside the effect of pore pressure (as it is the effective stresses that should be used in Eq. (5.24) and Eq. (5.25)). Even with those assumptions, only certain forms of $E(\sigma_r)$ are demonstrated to be solvable (Brown et al., 1989). Analytical stress solutions with both stress-dependent modulus and stress-dependent Poisson's ratio present more prohibitive mathematical challenges. Those limitations jeopardize the applicability of nonlinearity theory to a considerable extent in practical applications.

Instead of analytical approaches, numerical methods of stress calculations (e.g. Finite Element Method) with nonlinear rock properties enable nonlinear descriptions of element properties at each iteration (Vaziri, 1995). The application of FEM into stress analysis is not carried out in this research as physics and analytical approaches are the main focus. However the research results can serve as a basis for further numerical analysis.

7.3.4 Stress models for sand production prediction

To achieve analytical solutions, poro-inelastic stress models in Section 4.1.3 treat the Coulomb zone as a zone with constant low cohesive shear strength, which conflicts with the fact that sand becomes weaker with the extent of shear yield (plastic strain), leading to a non-constant reduced cohesion or even a cohesionless state after large plastic strain. Therefore the solutions give the upper limit of stresses inside the plastic zone, and should be treated as conservative solutions.

Because plastic theory is a correlated-empirical theory instead of one based on precise descriptions of physical changes in the rock mass fabric, it needs intensive calibrations. The author believes that a nonlinear theory based on rock moduli and other properties that change with loading stresses is more convincing and reasonable, as strength weakening, stiffness reduction, and stress redistributions are so

physically interlaced that neglect or separation of any of them would be inaccurate in terms of stability analysis in multiphase fluid environment.

7.3.5 Water hammer models

As a tradeoff of the pursue of analytical solutions, which enables the establishment of direction relationship among fluid properties, rock properties and production parameters, some simplifications have to be made during the development of water hammer models:

- quasi-steady pressure state in a bounded homogeneous reservoir before the well shuts down;
- immediate shut-in boundary conditions for pressure oscillation and pressure recovery models;
- a single phase fluid (note that in a real case, if there is any free gas in a producing wellbore, water hammer effects are dramatically weakened);
- The fluid pressure fluctuation is constrained within the wellbore and its effect on reservoir fluid has not been considered at this stage; and,
- static rock properties, such as the Mohr-Coulomb yield criterion.

Those simplifications result in conservative results. Their relaxations are recommended for future study.

Appendix 6-A

Set dimensionless variables of pressure, radius and time as $\Phi = \frac{P(r,t)}{P_e}$, $\xi = \frac{r - R_w}{R_e}$, $\varpi = \frac{tk/\mu C}{R_e^{\ 2}}$,

then the model becomes

$$\frac{\partial^2 \Phi}{\partial \xi^2} + \frac{1}{\xi}\frac{\partial \Phi}{\partial \xi} = \frac{\partial \Phi}{\partial \varpi} \tag{A-1}$$

Correspondingly, Eqs. 6.2-6.6 can be transformed to dimensionless expressions. Note, if $R_e >> R_w$, Eq. (6.6) can be simplified as

$$\text{if } \xi=1,\ \partial\Phi(\xi,\varpi)/\partial\xi = 0 \tag{A-2}$$

The steady state part of Eq. (A-1) is

$$\frac{\partial^2 \Phi}{\partial \xi^2} + \frac{1}{\xi}\frac{\partial \Phi}{\partial \xi} = 0 \tag{A-3}$$

therefore Φ can be in the form of

$$\Phi = B_1 \ln \xi + B_2 \tag{A-4}$$

where B_1 and B_2 are unknown. Assuming $\Phi(\xi,\varpi) = \mathrm{E}(\xi)\mathrm{T}(\varpi)$, the transient part of Eq. (A-1) satisfies

$$\frac{1}{T}\frac{dT(\varpi)}{d\varpi} = \frac{1}{E}\left(\frac{dE^2(\xi)}{d\xi^2} + \frac{1}{\xi}\frac{dE(\xi)}{d\xi}\right) \equiv -\lambda^2 \tag{A-5}$$

where λ is a constant. Thus T can be expressed as:

$$T = C_1 e^{-\lambda^2 \varpi} \tag{A-6}$$

while $\mathrm{E}(\xi)$ is a combination of Bessel functions $J_0(x)$ and $Y_0(x)$:

$$E(\xi) = D_1 J_0(\lambda\xi) + D_2 Y_0(\lambda\xi) \tag{A-7}$$

where C_1, D_1 and D_2 are unknown constants. Because $Y_0(x)$ is minus infinity as ξ approaches zero, D_2 has to be zero to limit dimensionless pressure (Φ) as a finite variable. Therefore the expression for Φ becomes:

$$\Phi = F e^{-\lambda^2 \varpi} J_0(\lambda\xi) + B_1 \ln \xi + B_2 \tag{A-8}$$

where F (=C_1D_1), and B_1, B_2 are constants to be determined. Since at infinite time there is no flow at all and pressure approaches the constant value determined in Eq. (6.4), B_1 should be zero, and $B_2 = 1 - \frac{1}{2} \cdot \frac{1 - P_w / P_e}{\ln(R_e / R_w)}$. From Eq. (A-8), the derivative of Φ, $\partial\Phi / \partial\xi = -Fe^{-\lambda^2 \varpi} J_1(\lambda\xi)$ satisfies the inner boundary condition Eq. (6.5), and it should also satisfy Eq. (6.6), i.e.

$$J_1(\lambda) = 0 \tag{A-9}$$

There are infinite eigenvalues of first order Bessel functions, e.g. λ_1=3.833, λ_2=7.016, λ_3=10.174, λ_4=13.324, λ_5= 16.427, … each of which corresponds to a solution $\Phi(\xi)$. Therefore $\Phi(\xi)$ is actually a combination of many solutions:

$$\Phi = \sum_{n=1}^{\infty} F_n e^{-\lambda_n{}^2 \varpi} J_0(\lambda_n \xi) + 1 - \frac{1}{2} \cdot \frac{1 - P_w / P_e}{\ln(R_e / R_w)} \tag{A-10}$$

In order to determine F_n, the initial condition is applied

$$\left.\frac{\partial \Phi}{\partial \xi}\right|_{\varpi=0} = -\sum_{n=1}^{\infty} F_n \lambda_n J_1(\lambda_n \xi) = -\frac{Q\mu}{2\pi k h P_e} \cdot \frac{1}{\xi} \tag{A-11}$$

Multiplying both sides with the weighting function, $\xi J_1(\lambda_m \xi)$, where λ_m is an eigenvalue of $J_1(\lambda)$=0, and integrating ξ from 0 to 1:

$$\int_0^1 \sum_{n=1}^{\infty} F_n \lambda_n \xi J_1(\lambda_n \xi) J_1(\lambda_m \xi) d\xi = \int_0^1 \frac{Q\mu}{2\pi k h P_e} \cdot \frac{1}{\xi} \cdot \xi J_1(\lambda_m \xi) d\xi \tag{A-12}$$

Since the eigenvalues are orthogonal to each other, the product of $J_1(\lambda_m \xi)$ $J_1(\lambda_n \xi)$ will be zero unless n = m. The left side of Eq. (A-12) will be (Gradshteyn and Ryzhik, 1994)

$$\int_0^1 \sum_{n=1}^{\infty} F_n \lambda_n \xi J_1(\lambda_n \xi) J_1(\lambda_m \xi) d\xi = \frac{1}{2} F_n \lambda_n J_0(\lambda_n) J_2(\lambda_n) \tag{A-13}$$

and the right side will be

$$\int_0^1 \frac{Q\mu}{2\pi k h P_e} \cdot \frac{1}{\xi} \cdot \xi J_1(\lambda_m \xi) d\xi = \frac{Q\mu}{2\pi k h P_e} \cdot \frac{1 - J_0(\lambda_n)}{\lambda_n} \tag{A-14}$$

Then Eq. (A-12) becomes

$$\frac{1}{2} F_n \lambda_n J_0(\lambda_n) J_2(\lambda_n) = \frac{Q\mu}{2\pi k h P_e} \cdot \frac{1 - J_0(\lambda_n)}{\lambda_n} \tag{A-15}$$

Therefore F_n can be obtained as

$$F_n = \frac{Q\mu}{\pi khP_e} \cdot \frac{1 - J_0(\lambda_n)}{\lambda_n{}^2 J_0(\lambda_n) J_2(\lambda_n)} \tag{A-16}$$

The solution for dimensionless pressure is finally derived as:

$$\Phi = A + \sum_{n=1}^{\infty} B \cdot C_n \cdot e^{-\lambda^2 \varpi} J_0(\lambda \xi) \tag{A-17}$$

where A, B, C_n are defined in Eq. (6.8). By replacing dimensionless variables, Eq. (6.7) is derived.

Appendix 6-B

Eq. (6.18) + C_3*Eq. (6.19) results in

$$gH_z + C_3 H_t + v_t + \frac{\lambda a^2}{g} v_z + \frac{fv|v|}{2D_{iw}} = 0 \tag{B-1}$$

i.e $$C_3 \left(\frac{g}{C_3} H_z + H_t\right) + \left(v_t + \frac{C_3 a^2}{g} v_z\right) + \frac{fv|v|}{2D_{iw}} = 0 \tag{B-2}$$

Note that $\frac{dH}{dt} = H_z \frac{dz}{dt} + H_t$ and $\frac{dv}{dt} = v_z \frac{dz}{dt} + v_t$. When $\frac{dz}{dt} = \frac{g}{C_3} = C_3 \frac{a^2}{g}$, Eq. (B-2) becomes

$$C_3 \frac{dH}{dt} + \frac{dv}{dt} + \frac{fv|v|}{2D_{iw}} = 0 \tag{B-3}$$

and Eq. (6.18) and Eq. (6.19) can be transformed from two PDEs to two ODEs:

$$c^+: \text{ if } \frac{dZ}{dt} = a, \ \frac{g}{a}\frac{dH}{dt} + \frac{dv}{dt} + \frac{fv|v|}{2D_{iw}} = 0 \tag{B-4}$$

$$c^-: \text{ if } \frac{dZ}{dt} = -a, \ -\frac{g}{a}\frac{dH}{dt} + \frac{dv}{dt} + \frac{fv|v|}{2D_{iw}} = 0 \tag{B-5}$$

which can be graphically expressed in Fig. B-1. Multiplied by $a\frac{dt}{g}(=\frac{dx}{g})$, the above equations become

$$c^+: dH + \frac{a}{gA_{iw}} dQ + \frac{f}{2gD_{iw}A_{iw}^2} Q|Q| dZ = 0 \tag{B-6}$$

$$c^-: dH - \frac{a}{gA_{iw}} dQ - \frac{f}{2gD_{iw}A_{iw}^2} Q|Q|dZ = 0 \qquad \text{(B-7)}$$

Differentiating both equations results in

$$c^+: H_i^{j+1} = H_{i-1}^j - M(Q_i^{j+1} - Q_{i-1}^j) - NQ_{i-1}^j \left|Q_{i-1}^j\right| \qquad \text{(B-8)}$$

$$c^-: H_i^{j+1} = H_{i+1}^j + M(Q_i^{j+1} - Q_{i+1}^j) + NQ_{i+1}^j \left|Q_{i+1}^j\right| \qquad \text{(B-9)}$$

Therefore H_i^{j+1} and Q_i^{j+1} can be derived.

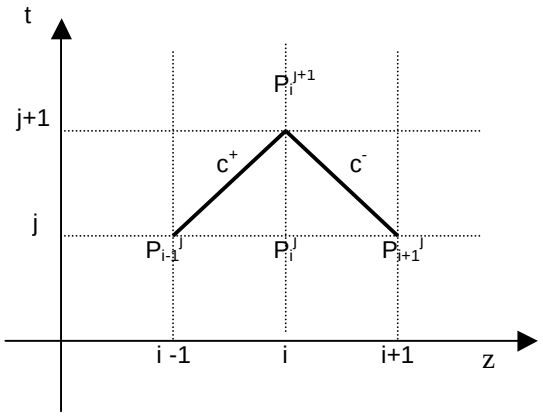

Fig. B-1: Sketch of Characteristic Method

Chapter 8 Bibliography

Adamson, A.W., 1982. Physical Chemistry of Surfaces, 4th Edition, John Wiley and Sons, Toronto, Canada.

Alonso, E.E., Gens, A., and Josa, A. 1990. A constitutive model for partially saturated soils. Géotechnique, 40(3): 405-430.

Appelo, C.A.J., and Postma, D., 1993. Geochemistroy, Goundwater and Pollution, A.A.Balkema, Rotterdam, Netherlands, 253-255, 279.

Bai, M., Meng, F., Roegiers, J.-C., and Green, S., Oct. 2002. Improved determination of stress-dependent permeability for anisotropic formations. SPE 78188, the SPE/ISRM Rock Mechanics Conference, Irving, TX, USA.

Bailey, B., Crabtree, M., Tyrie, J., Kuchuk, F., Romano, C., and Roodhart, L., 2000. Water control, Oil Field Review, 30-50.

Bianco, L.C.B., and Halleck, P.M., May 2001. Mechanisms of arch instability and sand production in two-phase saturated poorly consolidated sandstones. SPE 68932, the SPE European Formation Damage conference, Hague, Netherlands.

Biot, M.A., 1974. Exact simplified nonlinear stress and fracture analysis around cavities in rock, Int. J. Rock Mech. Min. Sci. & Geomech. Abstr., 11: 261-266.

Bishop, A.W., 1959. The principle of effective stress. Teknisk Ukeblad, 39: 859-863.

Bishop, A.W., and Blight, G.E., 1963. Some aspects of effective stress in saturated and partly saturated soils. Géotechnique, 13(3): 177-197.

Bolzon, G., Schrefler, B.A., and Zienkiewicz, O.C., 1996. Elastoplastic soil constitutive laws generalized to partially saturated sates. Géotechnique, 46(2): 279-289.

Boretti-Onyszkiewicz, W., 1966. Joints in the Flysch sandstones on the ground of strength examinations. Proc. of 1st Cong. of Int. Soc. of Rock Mech., 1: 153-157, Lisbon, Portugal.

Brace, W.F., 1963. Behavior of quartz during indentation. J. Geology, 71: 581-595.

Bradford, I.D.R., and Cook, J.M., Aug. 1994. A semi-analytic elastoplastic model for wellbore stability with applications to sanding. SPE 28070, the SPE/ISRM Rock Mechanics in Petroleum Engineering Conference, Delft, Netherlands.

Brady, B.T., 1969. The non-linear behavior of brittle rock. Int. J. Rock Mech. & Min. Sci., 6: 301-310.

Brady, B.H.G., and Brown, E. T., 1985. Rock Mechanics for Underground Mining. George Allen & Unwin Ltd, London, 162-167.

Bratli, R.K. and Risnes, R.R., Apr. 1981. Stability and failure of sand arches. SPE 8427, SPE Journal, 236-248.

Brignoli, M., Santarelli, F.J., and Papamicos, E., 1995. Capillary effects in sedimentary rocks: application to reservoir water-flooding. Proceedings of the 35th US Rock Mechanics Symposium, 619-625.

Brignoli, M., Santarelli, F.J., and Righetti, C., 1994. Capillary phenomena in an impure chalk. *Eurock '94*, 837-843, Balkema, Rotterdam.

Brown, E.T., Bray, J.W., Santarelli, F.J., 1989. Influence of stress-dependent elastic moduli on stresses and strains around axisymmetric boreholes. Rock Mech.& Rock Eng., 22: 189-203.

Bruno, M.S., Bovberg, C.A., and Meyer, R.F., 1996. Some influences of saturation and fluid flow on sand production: laboratory and discrete element model investigations. SPE 36534, the 1996 Annual Technical Conference and Exhibition, Denver, Colorado.

Burshtein, L.S., 1969. Effect of moisture on the strength and deformability of sandstone. Soviet Mining Science, N4: 573-576.

Burton, R.C., Davis E.R., Morita, N., and Mcleod, H.O., Sept. 1998. Application of reservoir strength characterization and formation failure modeling to analyze sand production potential and formulate sand

control strategies for North Sea gas reservoirs. SPE 48979, the 1998 SPE Annul Technical Conference and Exhibition, New Orleans, USA.

Byrne, P.M., Cheung, H., and Yan, L., 1987. Soil parameters for deformation analysis of sand masses. Can. Geotech. J., 24: 366-376.

Capes, C.E., 1980. Particle Size Enlargement. Handbook of Powder Technology (vol.1), Elsevier Scientific Publishing Company, 23-26.

Chalaturnyk, R.J., and Wagg, B.T., Feb. 1992. The mechanisms of solids production in unconsolidated heavy-oil reservoirs. SPE 23780, the SPE International Symposium on Formation Damage Control, Lafayette, LA, USA.

Chang, J., 2000. System Dynamics Approaches for Sand Production Simulation and Prediction (a Semi-Analytical Implementation), Master thesis, University of Waterloo.

Charlez, Ph. A., 1991. Rock Mechanics, v.1, Theoretical Fundamentals. Imprimerie Chirat, France, 30.

Chen, H.Y., Teufel, L.W., and Lee, R.L., 1995. Coupled fluid flow and Geomechanics in reservoir study – I. Theory and Governing Equations. SPE 30752, SPE Annual Technical Conference and Exhibition, Dallas, USA.

Cheng, H.B., and Dusseault, M.B., Oct. 2002. Continuum damage theories and petroleum geomechanics. SPE 78198, SPE/ISRM Rock Mechanics Conference, Irving, TX, USA.

Chin, L.Y., Raghavan, R., and Thomas, L.K., Mar. 2000. Fully coupled geomechanics and fluid-flow analysis of wells with stress-dependent permeability. SPE 48857, SPE Journal, 32-45.

Coates, G.R., and Denoo, S.A., Jun. 1981. Mechanical properties program using borehole analysis and Mohr's circle. SPWLA 22nd Annual Logging Symposium.

Colback, P.S.B., and Wiid, B.L. 1965. The influence of moisture content on the compressive strength of rocks. Proceedings of 3rd Canadian Symposium of Rock Mechanics, 65-83.

Cook, J., 2000. Personal communications.

Costin, L.S., 1987, Time-dependent deformation and failure, Fracture Mechanics of Rocks (B.K. Atkinson Ed.), Academic Press, London, 167-216.

Crawford, B.R., and Smart, B.G.D., Sept.1994. The influence of stress anisotropy on horizontal well performance predicted via special core analysis under true triaxial conditions. SPE 28452, the 69th SPE Annual Technical Conference and Exhibition, New Orleans, LA, USA.

Cristescu, N., 1989. Rock Rheology, Kluwer Academic Pulishers, The Netherlands.

Davies, J.P., and Davies, D.K., Jun. 2001. Stress-dependent permeability: characterization and modeling, SPE 71750, SPE Journal, 224-235.

Dube, A.K., and Singh, B, Jan.1972. Effect of humidity on tensile strength of sandstone. Journal of Mines, Metals and Fuels, 20(1): 8-10.

Dullien, F.A.L., 1979. Porous Media: Fluid Transport and Pore Structure, Academic Press, New York, 75 - 139.

Dumoré, J.M., and Schols, R.S., Oct.1974. Drainage capillary-pressure functions and the influence of connate water. SPE 4096, SPE Journal.

Duncan, J.M., and Chang, C., Sept. 1970. Nonlinear analysis of stress and strain in soils, Journal of the Soil Mechanics and Foundations Division. Proceedings of the American Society of Civil Engineers, SM5: 1629-1652.

Dunning, J.D., Aug.1983. The effects of aqueous chemical environments on crack by hydraulic fracture propagation and morphologies. J. Geophy. Res., 88(B8): 6491-6499.

Dusseault, M.B., 1979. Undrained volume and stress change behavior of unsaturated very dense sands. Can. Geotech. J., 16: 627-640.

Dusseault, M.B., and Rothenburg, L., 1988. Shear dilatancy and permeability enhancement in oil sands. Proceedings of the 4th UNITAR Conference Heavy Crude and Tar Sand, 3: 55-66.

Dusseault, M.B., and Santarelli, F. J., 1989. A conceptual model for massive solids production in poorly consolidated sandstone. Proceedings of the International Symposium on Rock at Great Depth, A.A.Balkema, Rotterdam, 789-797.

Dusseault, M.B., 2000. Geomechanics, Course notes, University of Waterloo.

Dusseault, M.B., Tronvoll, J., Sanfilippo, F., and Santarelli, F.J., 2000. Skin self-cleaning in high-rate oil wells using Sand Management. SPE 58786, the SPE International Conference on Formation Damage, Lafayette, LA, USA.

Dyke, C.G., and Dobereiner, L., 1991. Evaluating the strength and deformability of sandstones. Quart. J. Eng. Geol., 24: 123-134.

Edwards, D.P., Sharma, Y., and Charron, A., Mar. 1983. Zones of sand production identified by log-derived mechanical properties: a case study. Proceedings of the SPWLA 8th European Formation Evaluation Symposium, London, UK.

Fatt, I., and Davis, D.H., Dec.1952. Reduction in permeability with overburden pressure. J. Pet. Tech., Trans., AIME, 195.

Fjær, E., Holt, R.M., Horsrud, P., Raaen, A.M., and Risnes, R., 1992. Petroleum Related Rock Mechanics. Elsevier Science Publishers B.V., The Netherlands, 48.

Forsans, T.M., and Schmitt, L., 1994. Capillary force: the neglected factor in shale stability, Proc. Eurock'94, 71-84, Delft.

Ghalambor, A., and Hayatdavoudl, A., Apr. 1994. A study of sensitivity of relevant parameters to predict sand production. SPE 27011, the III Latin American/Caribbean Petroleum Engineering Conference, Buenos Aires, Argentina.

Geilikman, M.B., and Dusseault, M.B., 1997. Fluid-rate enhancement from massive sand production in heavy oil reservoirs. J. Pet. Sci. Eng., 17: 5-18.

Gillespie, T., and Settineri, W.J., 1967. The effect of capillary liquid on the force of adhesion between spherical solid particles. Journal of Colloid Interface Science, 24: 199.

Gregory, A.R., Oct. 1976. Fluid saturation effects on dynamic elastic properties of sedimentary rocks. Geophysics, 41(5): 895-921.

Griffith, A.A., 1924. Theory of rupture. The 1st International Congress on Applied Mechanics, Delft, Netherlands, 55-63.

Griggs, D.T., 1967. Hydrolytic weakening of quartz and other silicates. Geophys. J. R. Astr. Soc., 14: 19-31.

Griggs, D.T., and Blacic, J.D., 1965. Quartz: anomalous weakness of synthetic crystals. Science, 147: 292-295.

Gutierrez, M., Øino, L.E., and Høeg, K., 2000. The effect of fluid content on the mechanical behaviour of fractures in chalk. Rock Mech. & Rock Eng., 33(2): 93-117.

Hadizadeh, J., and Law. R.D., 1991. Water-weakening of sandstone and quartzite deformed at various stress and strain rates. Int. J. Rock Mech. Min. Sci. & Geomech. Abstr., 28(5): 431-439.

Hall, C.D., and Harrisberger, W.H., Jul. 1970. Stability of sand arches: a key to sand control. J. Pet. Tech., 821-829.

Han, G., and Dusseault, M.B., Feb.2002, *a*. Quantitative analysis of mechanisms for water-related sand production. SPE 73737, the SPE Int. Symposium and Exhibition on Formation Damage Control, Lafayette, LA, USA.

Han, G., and Dusseault, M.B., Sept.2002, *b*. Strength variations with deformation in unconsolidated rock after water breakthrough. SCA 2002-22, Proceedings of the 2002 Symposium of SCA (Society of Core Analysis), Monterey, CA, USA.

Han, G., Dusseault, M.B., and Cook, J., Oct.2002, *a.* Quantifying rock capillary strength behavior in unconsolidated sandstones, SPE 78170, the SPE/ISRM Rock Mechanics Conference, Irving, TX, USA.

Han, G., Ioannidis, M., and M. Dusseault, Jun. 2002, *b.* Analytical solutions for the effect of well shut down on rock stability. paper# 2002-050, Proceedings of the 2002 Canadian International Petroleum Conference, Calgary, Canada.

Hawkins, A.B., and McConnell, B.J., 1992. Sensitivity of sandstone strength and deformability to changes in moisture content. Quart. J. Eng. Geol., 25: 115-130.

Holt, R.M., Dec.1990. Permeability reduction induced by a nonhydrostatic stress field. SPE 19595, SPE Formation Evaluation, 444-448.

Holt, R.M., 2001. In situ porosity from cores: the rock mechanics approach to overburden correction. SCA 2001-09, the 2001 Symposium of Core Analysts, Edinburgh, Scotland.

Homand, S., Shao, J.F., and Schroeder, Ch., Jul. 1998. Plastic modelling of compressible porous chalk and effect of water injection. SPE 47585, the SPE/ISRM Eurock'98, Trondheim, Norway.

Horn, H.M., and Deere, D.W., 1962. Frictional characteristics of minerals. Géotechnique, 12: 319-335.

Hotta, K., Takeda, K., and Iinoya, K., 1974. The capillary binding force of a liquid bridge, Powder Technology, 10, 231-242.

Jaeger, J.C., and Cook, N.G.W., 1979. Fundamentals of Rock Mechanics. Chapman and Hall, London, UK.

Jamtveit, B., and Yardley, B.W.D., 1997. Fluid Flow and Transport in Rocks: Mechanisms and Effects, Chapman and Hill Co., London, UK, 319.

Jones, S.C., Mar.1998. Two-point determinations of permeability and PV vs. net confining stress. SPE Formation Evaluation. 235-240.

Jones, F.O., and Owens, W.W., Sept.1980. A laboratory study of the low permeability gas sands. J. Pet. Tech., 1631-1640.

Kan, M., and Roegiers J.-C., 1998. A neural approach to sand production prediction in wells. Int. J. Rock Mech. & Min. Sci., 35(4/5): 489.

Keaney, G.M.J., Meredith, P.G., and Murrell, S.A.F., Jul. 1998. Laboratory study of permeability evolution in a 'tight' sandstone under non-hydrostatic stress conditions. SPE 47265, the SPE/ISRM Eurock '98, Trondheim, Norway.

Keith, D.C., Harrison, W., and Wendlandt, R.F., 1998. Mineralogical response of siliciclastic carbonate-cemented reservoirs to steamflood enhanced oil recovery. Applied Geochemistry, 13(4): 491-507.

Kilmer, N.H., Morrow, N.R., and Pitman, J.K., 1987. Pressure sensitivity of low permeability sandstones. J. Pet. Sci. Eng., 1: 65-81.

King, M.S., 1969. Static and dynamic elastic moduli of rocks under pressure, Rock Mechanics: Theory and Practice, Proceedings of the 11th Symposium of Rock Mechanics, Society of Mining Engineers, AIME, New York, 329-351.

King, M.S., Al-Harthy, S., and Jing, X.D., 2001. Petrophysical studies of sandstones under true-triaxial stress conditions. SCA 2001-10, the 2001 Symp. of Core Analysts, Edinburgh, Scotland.

Knutson, C.F., and Bohor, B.F., 1963. Reservoir rock behavior under moderate confining pressure. The 5th Symposium on rock mechanics, University of Minnesota. MacMillan, New York, 627-659.

Kulhawy, F.H., 1975. Stress deformation properties of rock and rock discontinuities. Eng. Geol., 9: 327-350.

Kulhawy, F.H., and Duncan, J.M., Jul. 1972. Stress and movements in Oroville dam. Journal of the Soil Mechanics and Foundations Division, Proceedings of the American Society of Civil Engineers, SM7: 653-665.

Lama, R.D., and Vutukuri, V.S., 1978, a. Handbook on Rock Properties of Rocks (II), Trans Tech Publications, Clausthal, Germany.

Lama, R.D., and Vutukuri, V.S., 1978, b. Handbook on Rock Properties of Rocks (VI), Trans Tech Publications, Clausthal, Germany.

Larsen, L., Fjær, E., Renlie, L., Zhang, Z., et al., Jul. 1998. The effects of porosity and stress on dilatancy in sandstone. SPE 47199, the SPE/ISRM Eurock '98, Trondheim, Norway.

Lazzer, A.de, Dreyer, M., and Rath, H.J., 1999. Particle-surface capillary forces, Langmuir, 15: 4551-4559.

Li, X., Zienkiewicz, O.C., and Xie, Y.M., 1990. A numerical model for immiscible two-phase fluid flow in a porous medium and its time domain solution. Int. J. Num. Anal. Meth. Geomech., 30: 1195-1212.

Lian, G., Thornton, C., and Adams, M.J., 1993. Effect of Liquid Bridge Forces on Agglomerate Collisions. Powders & Grains 93, 59-64.

Lord, C.J., Johlman, C.L., and Rhett, D.W., Jul. 1998. Is capillary suction a viable cohesive mechanism in chalk? SPE 47310, the SPE/ISRM Eurock '98, Trondheim, Norway.

Marmur, A., 1993. Tip-surface capillary interactions. Langmuir, 9: 1922-1926.

Mason, G., and Clark, W.C., 1965. Liquid bridges between spheres. Chem. Eng. Sci., 20: 859.

Mclean, M.R., 1987. Wellbore Stability Analysis, PhD Thesis, University of London.

McLatchie, L.S., Hemstock, R.A., and Young, J.W., 1958. The effective compressibility of reservoir rock and its effects on permeability. SPE AIME Trans., 213: 386-388.

Mohiuddin, M.A., Korvin, G., Abdulraheem, A., Awal, M.R., Khan, K., Khan, M.S. and Hassan, H.M., 2000. Stress-dependent porosity and permeability of a suite of samples from Saudi Arabian sandstone and limestone reservoirs. SCA2033, the 2000 Symposium of Core Analysts, Abu Dhabi, UAE.

Morales, R.H., Webb, T.R., and Hollier, R., Feb. 2000. Borehole failure: safe drawdown pressures and wellbore damage radius. SPE 58789, the SPE International Symposium on Formation Damage Control, Lafayette, LA, USA.

Morita, N., Gray, K.E., Srouji, F.A.A., and Jogi, P.N., Sept.1984. Rock property change during reservoir compaction. SPE 13099, the SPE Annual Technical Conference and Exhibition, Houston, TX, USA.

Morita, N., Whitfill, D.L., Fedde, O.P., and Levik, T.H., Feb. 1989. Parameter study of sand-production prediction: analytical approach, SPE Production Engineering, 25-33.

Mühlhaus, H.-B., and Vardoulakis, I., 1987. The thickness of shear bands in granular materials. Géotechnique, 37(3): 271-283.

Nadeau, P.H., 1990. The petrophysical effects of dispersed diagenetic clay minerals on reservoir sands: an experimental study. Abstract and Program, 27th Annual Clay Minerals Society, 95.

Nawrocki, P.A., Dusseault, M.B., and Bratli, R.K. 1995. Addressing the effects of material non-linearities on wellbore stresses using stress- and strain-dependent elastic moduli. 1995 USRM Symposium, Lake Tahoe, Nevada.

Nawrocki, P.A., Dusseault, M.B., and Bratli, R.K., 1998. Use of uniaxial compression test results in stress modeling around openings in nonlinear geomaterials, J. Pet. Sci. Eng., 21: 79-94.

O'Brien, G., Bean, C.J., and McDermott, F., 2000. Numerical and experimental modelling of fluid-rock interactions with heterogeneous porosity. J. Geochem. Explor., 69-70, 119-125.

Orowan, E., 1949. Fracture and strength of solids. Reports on Progress in Physics, 12: 185-232.

Ostensen, R.W., Jun. 1986. The effect of stress-dependent permeability on gas production and well testing. SPE 11220, SPE Formation Evaluation, 227-235.

Papamichos, E., Brignoli, M., and Santarelli, F.J., 1997. An experimental and theoretical study of a partially saturated collapsible rock. Mechanics of Cohesive-Frictional Material, 2: 251-278.

Papmichos, E., and Vardoulakis, I., 1993. The effect of confining pressure on shear band formation in sand. Submitted to Géotechnique.

Perkins, E.H., Sept. 2001, Personal communications.

Plummer, L.N., Wigley, T.M.L., and Parkhurst, D.L., 1978, The kinetics of calcite dissolution in CO_2 – water system at 5° to 60° and 0.0 to 1.0 atm CO_2. Am. J. Sci. 278: 179-216.

Powers, J., Jun. 15, 2000. Halliburton and Geomechanics International announce strategic partnership. 2000 Press Releases of Halliburton, Dallas, TX, USA.

Priest, S.D., and Selvakumar, S. 1982. The failure characteristics of selected British rocks. Transport and Road Research Laboratory Report.

Raaen, A.M., Hovern, K.A., Jøranson, H., and Fjær, E., Oct. 1996. FORMAL: a step forward in strength logging. SPE 36533, the 1996 SPE Annual Technical Conference and Exhibition, Denver, Colorado, USA.

Rabinowica, E., 1965. Friction and Wear of Materials, New York, John Wiley and Sons, 302.

Rao, K.S., Rao, G.V., and Ramamurthy, T., Jun. 1987. Strength of sandstones in saturated and partially saturated conditions. Geotechnical Engineering, 18(1): 99-127.

Rhett, D.W., and Teufel, L.W., Oct.1992. Effect of reservoir stress path on compressibility and permeability of sandstones. SPE 24756, the 67th SPE Annual Technical Conference and Exhibition, Washington, DC, USA.

Rothenburg, L., and Bruno, M.S., 1997. Micromechanical modeling of sand production and arching effects around a cavity, Int. J. Rock Mech. & Min. Sci., 34 (3-4), Paper #068.

Rothenburg, L., 2002. Course note of Theoretical Soil Mechanics, University of Waterloo.

Rowlinson J.S., and Widom, B., 1982. Molecular Theory of Capillarity, Oxford, Clarendon Press, 5-29.

Ruistuen, H., Teufel, L.W., and Rhett, D., Oct. 1996. Influence of reservoir stress path on deformation and permeability of weakly cemented sandstone reservoirs. SPE 36535, the SPE Annual Technical Conference and Exhibition, Denver, USA.

Rumpf, H., 1962. The strength of granules and agglomerates. in W.A. Knepper (Ed.), Agglomeration, Interscience, New York, 379-414.

Risnes, R.R., Bratli, R.K., and Horsrud, P., Dec. 1982. Sand stresses around a wellbore. SPE Journal, 883-898.

Santarelli, F.J., Brown, E.T., and Maury, V., 1986. Analysis of borehole stresses using pressure-dependent linear elasticity, Int. J. Rock Mech. Min. Sci. & Geomech. Abstr., 23(6): 445-449.

Santarelli, F.J., and Brown, E.T., 1987. Performance of deep wellbores in rock with a confining pressure-dependent elastic modulus, Proceedings of the 6th International Congress on Rock Mechanics, Montreal, II: 1217-1222.

Santarelli, F.J., Skomedal, E., and Markestad, P., et al., Jul. 1998. Sand Production on Water Injectors: Just How Bad Can It Get? SPE 47629, the SPE/ISRM Eurock '98, Trondheim, Norway.

Santos, H., 2002. Personal Communications. Impact Engineering Solutions, United Kingdom.

Sarda, J.P., Kessler, N., Emmanuelle Wlcquart, Kevin Hannaford, and J-P. Deflandre, Oct. 1993. Use of porosity as a strength indicator for sand production evaluation. SPE 26454, the SPE Annual Technical Conference and Exhibition, Houston, TX, USA.

Sarda, J-P., Ferfera, F.M.R., Vincké, O., Boutéca, M., and Longuemare, P., 1998. Experimental study of the stress paths influence on monophasic permeability evolution. SCA 9827, the 1998 Symposium of Core Analysts, Hague, Netherlands.

Schmidt, H., 1926. Statische Probleme des Tunnel- und Druckstollenbaues, Berlin, Germany.

Schrefler, B.A., and Scotta, R. 2001. A fully coupled dynamic model for two-phase fluid flow in deformable porous media. Comput. Meth. Appl. Mech. Eng., 3223: 3223-3246.

Schubert, H., 1975. Tensile strength of agglomerates, Powder Technology, 11: 107-119.

Schuyler, J., and Dunning, J., 1982. Effects of aqueous chemical environments on hydraulic fracture morphology and fracture strength of flathead sandstone. Geol. Soc. Am. Program Abstr., 14(7): 612.

Schubert, H., 1984. Capillary forces – modelling and application in particulate technology. Powder Technology, 47: 105-116.

Settari, A., and Walters, D.A., Sept.2001. Advances in coupled geomechanical and reservoir modeling with applications to reservoir compaction. SPE 51927, SPE Journal.

Skjærstein A., Tronvoll, J., Santarelli, F.J., and Jøranson, H., Oct. 1997. Effect of water breakthrough on sand production: experimental and field evidence. SPE 38806, the SPE Annual Technical Conference and Exhibition, San Antonio, TX, USA.

Simoni, L., Salomoni, V., and Schrefler, B.A. 1999. Elastoplastic subsidence models with and without capillary effects. Comput. Meth. Appl. Mech. Eng., 171: 491-502.

Stein, N., and Hilchie, D.W., Sep.1972. Estimating the maximum production possible from friable sandstones without using sand control. J. Pet. Tech., 1157-60, Trans. AIME, 253.

Suri, P., Azeemuddin, M., Zaman, M., Kukreti, A.R., and Roegiers, J.-C., 1997. Stress-dependent permeability measurement using the oscillating pulse technique. J. Pet. Sci. Eng., 17: 247-264.

Swolfs, H.S. Dec. 1971. Chemical effects of pore fluids on rock properties. Underground Waste Management and Environmental Implications, Proceedings of Symposium of American Association of Petroleum Geologists (AAPG), Memoir 18: 224-233.

Takamura, K., and Isaacs E.E., 1989. Interfacial properties. AOSTRA Technical Handbook on Oil Sands, Bitumens and Heavy Oils, Chapt.5, edited by Hepler, L.G. and His, C., AOSTRA Technical Publication Series #6.

Tamada, B., 1970. Studies on the collapse phenomenon of sedimentary rock by absorption of water at landslide area. Rock Mechanics, in Japan, 1: 68-70.

Taylor, J.M., 1950. Pore space reduction in sandstone. Bull. Am. Assoc. Pet. Geol., 34: 701-716.

Thomas, R.D., and Ward, D.C., Feb.1972. Effect of overburden pressure and water saturation on gas permeability of tight sandstone cores. J. Pet. Tech., 120-124.

Tremblay, B., Oldakowski, K., and Settari, A., Jun. 1997. Geomechanical properties of oil sands at low effective stress. 48th Annual Technical Meeting of the Petroleum Society, Calgary, Canada.

Tremblay, B., Sedgwick, G., and Vu, D., Aug.1999. A review of cold production in heavy oil production. EAGE-10th European Symposium on Improved Oil Recovery, Brighton, UK.

Trixier, M.R., Loveless, G.W., and Anderson, R.A., Mar.1975. Estimation of formation strength from the mechanical properties log. J. Pet. Tech., 283-93.

Tronvoll, J., 1993. Investigation of Cavity Failures for Sand Production Prediction. University of Trondheim, Norway, 20-48.

Tronvoll, J., and Fjær, E., 1994. Experimental study of sand production from perforation cavities. Int. J. Rock Mech. Min. Sci. & Geomech., 31(5): 393-410.

Vairogs, J., Hearn, C.L., Dareing, D.W., and Rhoades, V.W., Sept. 1971. Effect of rock stress on gas production from low-permeability reservoirs. J. Pet. Tech., 1161-1167.

Van Den Hoek, P.J., Hertogh, G.M.M., Kooijman, A.P., de Bree, Ph., Kenter, C.J., and Papamichos, E., Dec. 2000. A new concept of sand production prediction: theory and laboratory experiments, SPE Drilling and Completion, 15(4): 261-273.

Van Eeckhout, E.M., and Peng, S.S., 1975. The effect of humidity on the compliance characteristics of coal mine shales. Int. J. Rock Mech. & Min. Sci., 12: 335-340.

Vásquez H., A.R., Sánchez D., M.S., Yánez, R.L., Poquioma, W., Rampazzo, M., and Chirity, K. El, Apr. 1999. The diagnosis, well damage evaluation and critical drawdown calculations of sand production problems in the Ceuta Field, Lake Maracaibo, Venezuela. 1999 SPE Latin American and Caribbean Petroleum Engineering Conference, Caracas, Venezuela.

Vaziri, H.H., 1995. Analytical and numerical procedures for analysis of flow-induced cavitation in porous media. Computers and Structures, 54(2): 223-238.

Vaziri, H.H, Phillips, R., and Hurley, S., 1997. Physical modeling of sand production. Int. J. Rock Mech. & Min. Sci., 34(3-4): 323.

Vaziri, Hans, Barree, B., Xiao Y., Palmer, I., and Kutas, M., Oct. 2002. What is the magic of water in producing sand? SPE 77683, the SPE Annual Technical Conference and Exhibition, San Antonio, TX, USA.

Veeken, C.A.M., Davies D. R., Kenter C. J., and Kooijman A. P., Oct. 1991. Sand production prediction review: developing an integrated Approach. SPE 22792, the 66th SPE Annual Technical Conference and Exhibition, Dallas, Texas, USA.

Vesic, A.B., and Clough, G.W., 1986. Behavior of granular material under high stresses. Journal of Soil Mechanics and Foundation Division, ASCE, 94 (SM3): 661-688.

Vutukuri, V.S., Lama, R.D., and Saluja, S.S., 1974. Handbook on Mechanical Properties of Rocks, First edition, 2 (1), Trans Tech Publications.

Walton, I.C., Oct. 2000. Optimum Underbalance for the Removal of Perforation Damage, the 2000 SPE Annual Technical Conference and Exhibition, Dallas, TX.

Wang, Y., 1990. 2-D Circular Borehole Solutions in Saturated Non-Isothermal Porous Media and Their Application to Borehole Stability and Stress Measurements, PhD Thesis, University of Waterloo.

Wang, Y., and Dusseault, M.B., Dec. 1991. The effect of quadratic gradient terms on the borehole solution in poroelastic Media. Water Resources Research, 27(12): 3215-3223.

Wang, Y., Scott, J.D., and Dusseault, M.B., 1994. Borehole rupture from plastic yield to hydraulic fracture – a nonlinear model including elastoplasticity. J. Pet. Sci. Eng., 12: 97-111.

Wang, Y., and Xue. S., Feb. 2002. Coupled reservoir-geomechanics model with sand erosion for sand rate and enhanced production prediction. SPE 73738, the SPE International Symposium and Exhibition on Formation Damage Control, Lafayette, LA, USA.

Walsh, J.B., and Brace, W.F., 1966. Cracks and pores in rocks. Proceedings of the 1st Congress of International Society of Rock Mechanics, Lisbon, 1: 643-646.

West, G., 1994. Effect of suction on the strength of rock. Quart. J. Eng. Geol., 27: 51-56.

Wibberley, C., 1999. Are feldspar-to-mica reactions necessarily reaction-softening processes in fault zones? Journal of Structural Geology, 21: 1219-1227.

Wintsch, R.P., Christoffersen, R., and Kronenberg, A.K., Jul. 1995. Fluid-rock reaction weakening of fault zones, J. Geophy. Res., 100 (B7): 13021-13032.

Wintsch, R.P., Sept. 2001. Personal communications.

Wong, R.C.K., and Li, Y., June 2000. A deformation-dependent model for permeability changes in oil sand due to shear dilation. Canadian International Petroleum Conference, Calgary, Canada.

Yale, D.P., 1984. Network Modeling of Flow, Storage and Deformation in Porous Rocks. PhD dissertation, Stanford University, Standford, CA, USA.

Young, G., and Busch, T., 1960. Immersion calorimetry of the interaction of water with silica surfaces. Journal of Colloid Science, 15: 361-369.

Yuan, J.Y., Babchin, A., and Tremblay, B., 2000. Modelling wormhole flow in cold production. J. Can. Pet. Tech., 39(4): 40-45.

Zhang, H.W., Deeres, O.M., Borst, R.de, and Schrefler, B.A., 2001. Implicit integration of a generalized plasticity constitutive model for partially saturated soil. Engineering Computations. 18(1/2): 314-336.

Zhang, L., and Dusseault, M.B., 1997. Formation alteration characterization from well test interpretation. IACMAG 9th Int. Conf. Comp. Meth. & Advances in Geomech, Wuhan, P.R.China, 2299-2306.

Zhang, L. and Dusseault, M. B., Nov. 2000. Sand production simulation in heavy oil reservoir. SPE 64747, the SPE International Oil and Gas Conference and Exhibition, Beijing, China.

Zimmerman, R.W., 1991. Compressibility of Sandstones. Developments in Petroleum Science, 29, Elsevier, New York.

Zoback, M.D., and Byerlee, J.D., 1975. Permeability and effective stress. AAPG Bulletin, 59: 154-158.